Characterization of a scalable fabrication process for supported or suspended devices made of CVD graphene

Omur Isıl Aydin

UNIVERSITÉ DE GRENOBLE

THÈSE

Pour obtenir le grade de

DOCTEUR DE L'UNIVERSITÉ DE GRENOBLE

Spécialité **: Nanoélectronique et Nanotechnologies**

Arrêté ministériel : 7 août 2006

Présentée par

Ömür Işıl AYDIN

Thèse dirigée par **Mireille/MOUIS**

préparée au sein d'**IMEP-LAHC**
dans **l'École Doctorale EEATS**

Étude et caractérisation d'un procédé intégrable pour la fabrication de composants supportés ou suspendus à base de graphène CVD

Thèse soutenue publiquement le **29.09.2014**,
devant le jury composé de :

Mme. Mireille MOUIS
Directeur de Recherches, CNRS, IMEP-LAHC, Grenoble (Directeur de thèse)
Mr. Henri HAPPY
Professeur, IEMN, Université Lille, Lille (Rapporteur)
Mr. Max LEMME
Professeur, Universität Siegen, Siegen (Rapporteur)
Mr. Franz BRUKERT
Professeur, LMGP, Grenoble INP, Grenoble (Examinateur)
Mr. Georg, DUESBERG
Professeur, CRANN, Trinity College, Dublin (Invité)

ABSTRACT

We propose a high-yield (~ 90%) fabrication route to obtain suspended graphene devices. Importantly, we focus on the scalability of the process as well as its compatibility with existing Si technologies. To address these issues, we developed a fabrication scheme based on graphene grown by chemical vapor deposition (CVD).

The most crucial step in the fabrication process relates to the etching of the underlying SiO2 substrate to suspend the graphene ribbons. It is often reported in the literature that at this stage, capillary forces can lead to the collapse of the graphene beams. We have found that apart from this effect, the quality of the interface between the etch mask and the substrate is key to successfully suspend graphene devices. Only when the quality of this interface was improved, were we able to achieve remarkably high yields of approximately 90%. Characterization by Raman spectroscopy, scanning electron microscopy (SEM) and atomic force microscopy (AFM), performed after each step of fabrication, attested that our methodology does not impact the quality of the graphene.

We have subsequently employed Raman spectroscopy to investigate doping and strain in our CVD graphene devices. While we did observe a strong p-type doping of graphene supported on SiO2 in air, doping alone cannot account for the observed spectra. Instead, we conclude that the measured graphene samples display a compressive internal strain, which does not fully relax during fabrication. We attribute this strain to the large temperature budget of the CVD process and to the rigid transfer polymer.

Finally, we have studied the electrical characteristics of our devices at room temperature as well as at low temperatures. The measurements confirmed the strong p-type doping of graphene, and as a result, back-gating only resulted in a weak current modulation. Magneto-transport measurements performed at 4 and 20 K were used to extract the carrier density and the mobility of devices supported on SiO_2. Low mobility values are attributed to scattering through grain boundaries. At low magnetic fields, we have observed signatures of weak localization, which implies that intervalley scattering is the dominant mechanism in our samples. At higher magnetic fields, the longitudinal resistivity showed temperature-robust oscillations which could be identified as Landau levels.

CONTENT

Chapter 1

INTRODUCTION

Graphene has entered research fields through the wonders of a scotch-tape. As it is simply one of the many layers which make up graphite, it should not be surprising that it was isolated simply by rubbing an adhesive tape full of cleaved graphite pieces against a Si wafer. Yet, it was surprising. Despite of how simple it sounds, its isolation was not trivial considering that it could not be achieved until 2004. It was even once proven by Landau that it cannot exist on its own to begin with. In fact, graphene had been part of various theoretical studies since the study of graphite by Wallace in 1937 with several predictions on its properties. Thus, its experimental isolation brought excitement since scientists finally had the possibility to study its remarkable electrical, mechanical, optical and thermal properties of this first truly two dimensional material not only in theory, but also in experiments. The wondrous material awarded the Manchester team with the Nobel Prize in 2010.
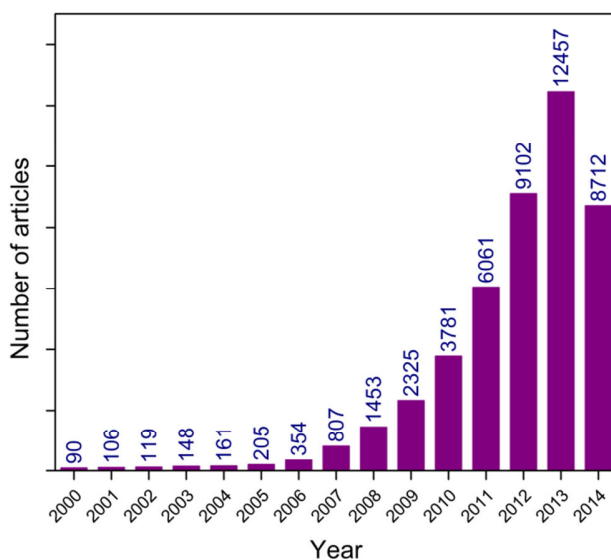
Figure 1. The number of articles within the topic "graphene" shown for every year between 2000 – 2014. The number for the year 2014 is recorded in August 2014 and is therefore incomplete. All data is taken from Web of Science.

Figure 1 gives an idea on how the field grew with the discovery of the isolation method in 2004 and the support that came in later years by wafer-scale synthesis techniques. As simple as the procedure was in theory, it should be noted that the sudden avalanche of the number of studies on graphene is significantly owed to the presence of clean room facilities, ebeam lithography and the existing knowledge of fullerenes.

In this chapter, we firstly would like to introduce you the different types of carbon and the emergence of graphene followed by presenting its various exceptional properties and the possible applications that can be developed from them.

1.1. Carbon allotropes

Carbon is the basis of all kinds of life forms. This originates from its unique position in the periodic table granting it four valence electrons. Depending on the hybridization, it is capable of single, double and triple bonds. This freedom gave way to the diversity of the possible forms of carbon, man-made as well as found in nature.

Pure atomic orbitals of central atom	Hybridization of the central atom	Number of hybrid orbitals	Shape of hybrid orbitals
s,p	sp	2	Linear
s,p,p	sp2	3	Trigonal Planar
s,p,p,p	sp3	4	Tetrahedral
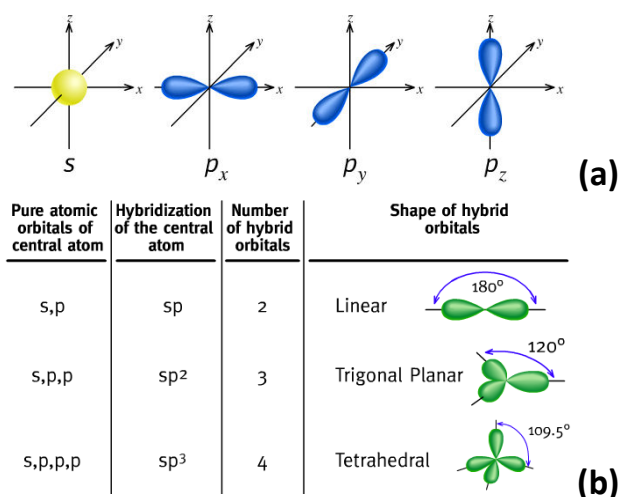
Figure 2. a) The atomic orbitals s, p_x, p_y and p_z. **b)** sp, sp^2 and sp^3 hybridization and the bond angles they lead to. **[1]**

The electron configuration of carbon goes as $1s^2\ 2s^2\ 2p^2$. The four valence electrons take part in the chemical bonds. Due to the small energy difference between the 2s and 2p ($2p_x$, $2p_y$ and $2p_z$) orbitals, (Figure 2a) their wave functions easily mix and create new orbitals in the form of sp, sp^2 or sp^3, depending on the number of p atomic orbitals participating in the mixing with the s atomic orbital. (Figure 2b) The phenomenon is first introduced by Pauling [2] as hybridization. Hybridization is the origin of the diverse geometries possible for C-C bonding. This unique ability allows carbon to form 0D, 1D, 2D as well as 3D structures.

The two most common allotropes of carbon are diamond and graphite. Diamond has a face-centered cubic unit cell as a result of sp^3 hybridization giving way to bonding angles of 109.5°. (Figure 2b and Figure 3a) The C-C covalent bond is one of the strongest bonds in nature and thus leads to a high Young's modulus and high thermal conductivity. As diamond is the hardest natural mineral known to man, it generally finds use in industry in the fields of drilling and cutting. Graphite, on the other hand, is the result of sp^2 bonding with bond angles of 120°. (Figure 2b) This, along with the interaction of the p_z orbitals leads to a set of stable hexagonal layers as in Figure 3b. Each individual layer is called graphene. A noticeable from Figure 3b, these layers are strong in the lateral direction where the atoms are chemically bonded and they can, at the same time, slide past each other. Van der Waals interaction is responsible for the weak vertical bonding. Graphene is not just a layer from the most thermodynamically stable form of carbon, it is a good electrical conductor through the delocalization of the electrons in π orbitals. Diamond, on the other hand, is an electrical insulator with a band gap of ∼ 5.5 eV. Carbon can also come in a non-crystalline form, as the so-called "amorphous carbon". (Figure 3g) While one can find entirely amorphous carbon, it is also

possible to produce the type preserving short-range order which is comprised of small crystallites of graphite or diamond. [3] [4]
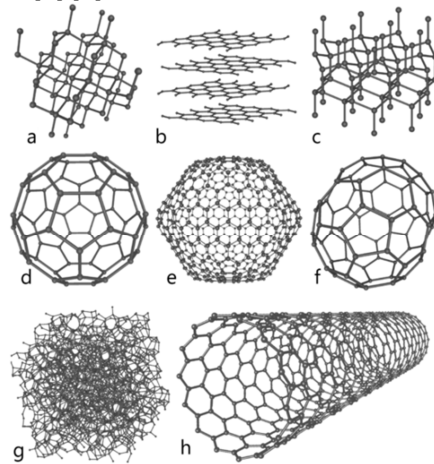
Figure 3. Sketches of several allotropes of carbon:
a) diamond,
b) graphite,
c) lonsdaleite,
d) C_{60} (buckyball),
e) C_{540}, **f)** C_{70},
g) amorphous carbon,
h) single-walled carbon nanotube.
[4]

The not-so-common forms of carbon have been studied heavily since 1985 with the discovery of buckminsterfullerenes or "buckyballs", by a team of scientists from Rice University and the University of Sussex. [5] The buckyball clusters are 0D crystals of carbon, the smallest of which can consist of 20 carbon atoms forming the C_{20}. Figure 3d depicts the most well-known form, the C_{60} which awarded the scientists with a Nobel Prize in 1996.

The studies on 0D fullerenes led to an interest on their 1D derivatives, the carbon nanotube (CNT). A CNT is a sheet of graphene, rolled up into a cylinder capped with half buckyballs as in Figure 3h. Even though there is evidence that the CNTs had been observed by several scientists earlier, the CNTs owe the buzz to the work by Ijima et al. in 1991. [6] With the extraordinary electrical and mechanical properties, the field quickly grew. The CNTs have dominated the research headlines in the 90s and 00s.

Graphene, the 2D carbon crystal, is simply one layer isolated from the stacking of graphite as in Figure 3b. The σ bonds in the hexagonal plane serve as the rigid backbone while the atomic p_z orbitals are responsible for the electrically conducting nature. In fact, for a long time its isolated existence was thought to be impossible. Landau has shown in 1937 that strictly 2D crystals were thermodynamically unstable. [7] As a 2D material and the consequent remarkable properties, graphene has always been interesting to scientists. However, the challenge in isolating a single graphene sheet had prevent it study until 2004.

A series of papers in 2004/5 by the Manchester [8], Columbia [9] and Georgia Tech [10] groups has brought graphene into spotlight. The researchers developed an impressively simple method to isolate graphene layers from graphite. A freshly cleaved highly ordered pyrolytic graphite (HOPG) was rubbed against a Si wafer. Owing to the thin film interference effects, the correct oxide thickness (∼ 300 nm) helped differentiating between single layer and the multilayer graphene pieces on the oxide under the optical microscope. [8] With all the experience that existed in the scientific groups who have been working with CNTs and fullerenes, all that know-how could be easily transferred into graphene research with minimal investment in time and resources.

Today, there are two more main sources for pristine graphene; graphene on SiC and CVD graphene. Films of graphene can be formed by evaporating Si atoms from either the C or Si terminated side of the SiC wafer. [11] And highly monolayer films can be grown on metal catalytic surfaces by chemical vapor deposition (CVD). [12] Other sources such as reduced graphene oxide can be discontinuous, have embedded oxygen or be comprised of more than one layer. We will present graphene sources in Chapter 2, Device fabrication, more in detail.

1.2. Properties of graphene

1.2.1. The band structure of graphene

Each carbon in the honeycomb-like graphene lattice is bonded to 3 other sp^2 hybridized carbon. All atoms lie in-plane with an angle of 120°. The atomic structure and the unit vectors $\vec{a_1}$ and $\vec{a_2}$ of the graphene lattice are depicted in Figure 4. The unit cells make an angle of 60° and enclose the area of the unit cell which has two atoms, A and B from each sublattice. The nearest-neighbor distance is $a_0 = 1.42$Å. Reciprocal vectors $\vec{b_1}$ and $\vec{b_2}$ can be derived from the unit vectors. [13]
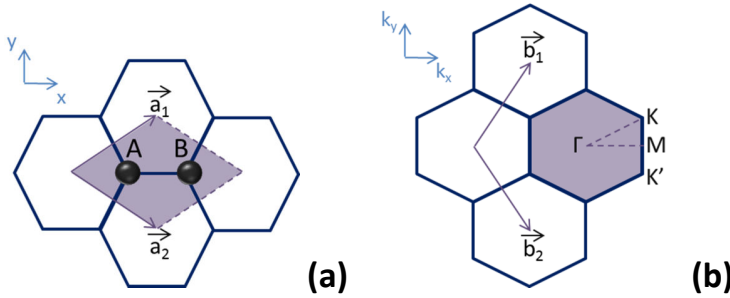
Figure 4. a) Graphene unit cell in real space with unit vectors $\vec{a_1}$ and $\vec{a_2}$. The unit cell encompasses two atoms, one from each sublattice. **b)** Reciprocal lattice with the reciprocal lattice vectors $\vec{b_1}$ and $\vec{b_2}$. The first Brillouin zone is highlighted with the high symmetry points Γ, K and K'.

Only the electrons from the p_z orbitals contribute to transport in graphene by forming the π and π* bands. Regular transport experiments only probe the vicinity of the Dirac point. For low energies, the dispersion relation of the π and π* can be well-approximated by tight binding calculations. The result is the following when the second nearest neighbor hopping is incorporated:

$$E_{\mp}(\vec{k}) = \mp t \sqrt{3 + f(\vec{k})} - t' f(\vec{k}) \qquad (1.1)$$

with

$$f(\vec{k}) = 2 \cos(\sqrt{3} k_y a_0) + 4 \cos\left(\frac{\sqrt{3}}{2} k_y a_0\right) \cos(\frac{3}{2} k_x a_0) \qquad (1.2)$$

where t is the nearest neighbor hopping energy and t' is the next nearest neighbor hopping energy. Figure 5 is the resulting band structure of graphene. As we can observe, the π and π* bands touch each other at K and K' points, at the corners of the Brillouin zone, at Dirac points. The dispersion relation close to the K point is linear. For $\vec{k} = \vec{K} + \vec{q}$ with $|\vec{q}| \ll |\vec{K}|$ and $t' = 0$ the following holds true:

$$E_{\mp} \approx \mp \hbar v_F |\vec{q}| + O[(|\vec{q}|/\vec{K})^2] \qquad (1.3)$$

4

where $v_F = \frac{3ta}{2} \approx 1 \; x \; 10^6 \; m/s$. In the case of an ideal and undoped graphene, the Fermi energy is found exactly at the Dirac point, where the valence and conduction bands touch each other thus, making the so-called "zero-gap semiconductor". The lack of a parabolic band structure and a real gap in-between the bands is the main difference of graphene from a regular semiconductor. The linear band structure makes it possible to describe the electrons in graphene as massless Dirac fermions at low energies. [14]
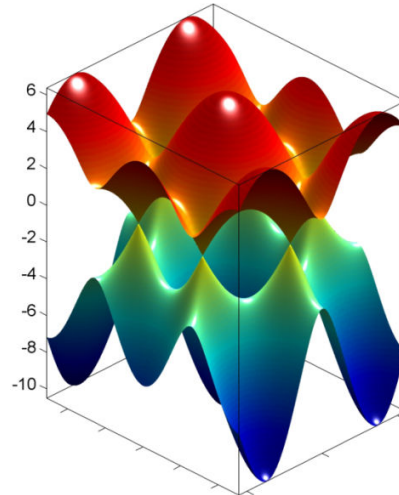
Figure 5. The electronic band structure of graphene (courtesy of by A. Cresti in 2012.)

1.2.2. Electrical properties

Before graphene, there have been 2D systems in electronic research. Even though these were not truly 2D materials, two dimensional electron gases provided ways to study 2D systems. A two-dimensional electron gas (2DEG) is a system where electrons can freely move in two dimensions, but are confined in the third. This system is commonly encountered in MOSFETs. The knowledge paved the basis for investigating the electrical properties of graphene.

The electron transport in graphene is directed by the relativistic Dirac equation. Charge carriers act as massless relativistic particles with a "speed of light" of $\sim 10^6$ m/s. [15] Figure 6 is the plot from one of the first gated devices made of graphene. One characteristic that draws the attention right away of is the ambipolarity of charge carriers. Novoselov et al. showed in 2004 that graphene FET on SiO_2 has ambipolar characteristics with electron and hole concentrations of 10^{13} cm^{-2} and a mobility of 10 000 cm^2/Vs at room temperature. That is to say, it is possible to continuously tune charge carriers from electrons to holes and vice versa. Secondly, as expected from the lack of the band gap, graphene shows little change in resistivity between the on and off stage of the transistor. [8] [15]

Another consequence of charge carriers posing as Dirac fermions is the high carrier mobility. Mobility of graphene on SiO_2 can reach 15 000 cm^2/Vs with a corresponding sheet resistivity of $\sim 10^6 \, \Omega$ cm. [8] To put in perspective, we should note that this value is lower than the resistivity of silver, the material with lowest resistivity at room temperature. [16] [8] And when there is no substrate to interfere with the transport properties, i.e. for the case of suspended graphene,

mobility can reach 40 000 cm^2/Vs at room temperature and even 200 000 cm^2/Vs at low temperature. [17] [18] Furthermore, the first measurements of graphene on SiO$_2$ devices have presented ballistic transport at submicron distances. Later studies showed that the mean free path of charge carriers can reach up to 0.5 mm. [19]
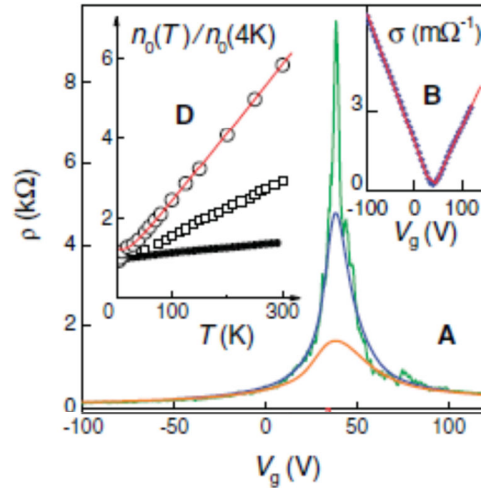
Figure 6. The change in the resistivity of few layer graphene with gate voltage. The image is adapted from reference. **[8]**

In addition to the favorably high values for mobility, graphene shows low electronic noise from thermal agitation of charge carriers in an electrical conductor at equilibrium, regardless of the voltage applied. Combined with the high values for mobility, it is interesting for graphene to participate in nanoelectromechanical systems (NEMS).

Graphene FETs are tainted with the low on/off ratio. For graphene to ever participate in logic applications, a band gap is needed. Therefore, there have been various studies on how to open a band gap. Two main methods have been suggested; graphene nanoribbons (GNRs) or bilayer graphene. In contrast to the massless Dirac fermions in monolayer graphene, bilayer graphene has massive Dirac fermions. A gate voltage introduces asymmetry between the layers and forms an energy gap. [20] [21] The second way to create an energy gap is through a lateral quantum confinement; i.e. patterning graphene into very narrow ribbons. Depending on their configuration, GNRs show different electronic properties; zigzag GNRs are, in theory, metallic while the armchair GNRs can be either semiconducting or metallic. The energy gap is inversely proportional to their width. [16] For real applications, however, GNRs need to have smooth edges which has been a great challenge in GNR research so far. Several approaches have been presented which involve top-down etching techniques as well as bottom up CNT opening. [22] [23] Yet edge defects still appear to dominate the experimental results related to the realization of possible GNR FETs. Moreover, it was also shown that it is possible to open a band gap of 0.26 eV in epitaxial graphene grown on SiC. The origin of the band gap is attributed the interaction of graphene with the substrate. [24]

6
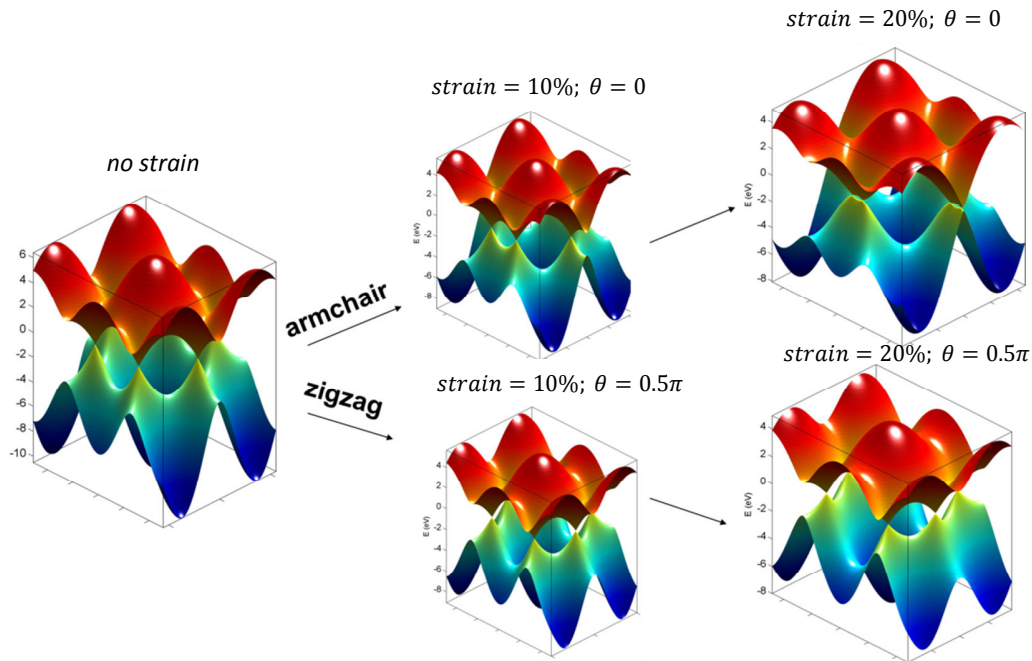
Figure 7. Change in the band structure of graphene with strain in the indicated directions. (Courtesy of A. Cresti, 2012)

Another way to open up a band gap is strain. Figure 7 , shows how strain modifies the electronic structure of graphene by breaking the sublattice symmetry. The two carbon sublattices are inequivalent under uniaxial strain. When one is tensed, the other contracts. A large uniaxial strain in the armchair direction can open an effective band gap as in Figure 7.

Strain is relevant not only for researchers aiming to open a band gap in graphene, but for electronic applications in general. It clearly modifies the electronic structure of graphene; consequently it will have an effect on electrical properties as well. We discussed externally applied strain, but synthesis and fabrication can lead to a built-in strain in the final graphene device. Therefore, it is important to study the evolution of strain in the graphene device and its consequences. We will investigate this in the next chapters more in detail.

1.2.3.   Mechanical properties

The strength of graphene has been modeled by atomistic simulation method and measured by nanoindentation technique. A Young's modulus of ca. 1.0 TPa, which corresponds to the theoretically calculated value, [25] has been deduced from a measured 2D elastic stiffness of 340 N/m. [26] The interlayer spacing of graphite is customarily taken as the sheet thickness. Moreover, a breaking strength of 42 N/m has been measured which translates into a bulk value of 130 GPa. [26] Graphene owes these remarkable values to the strong C-C covalent bond.

1.2.4.   Optical properties

The unique electronic properties of graphene generate an unexpectedly high opacity for one atomic monolayer in spite of a rather low white light absorption of 2.3%. [27] The light adsorption increases linearly with the number of layers. [28] The contrast of graphene on 300 nm SiO_2 increases

with the layers as well which was the key in locating single layer graphene during mechanical exfoliation.

1.2.5. Thermal properties

Most materials expand upon heating and contract upon cooling, i.e. they have positive thermal expansion coefficients (TEC). Ultra-thin suspended films, on the other hand, have the opposite situation. Many compounds in the form of a layer have a negative TEC which stems from the fact that the frequency of the out-of-plane acoustic phonons increases when the inter-atomic distance is increased. [29] Already before measurements, graphene was predicted to demonstrate a negative TEC. [30] The TEC determined experimentally exceeded theoretical predictions by 2 - 3 times as $\sim 7 \times 10^{-6} \, K^{-1}$ at room temperature. This value is larger than the in-plane TEC of graphite. [29]

Through the strong C-C covalent bond and the high phonon speed ($\sim 2 \times 10^{4}$ m/s), phonons dominate the thermal conductivity of graphene at room temperature. The thermal conductivity of suspended graphene is estimated as $\sim$ 2000 - 5000 W/mK around room temperature. [31] [32] To put these values in perspective, the thermal conductivity of Cu is ~ 400 W/mK and of Si ~ 150 W/mK. Not only the electrical properties, but also thermal properties of graphene degrade on a substrate. Phonon leakage to the substrate and scattering reduce the thermal conductivity of graphene down to ~ 600 W/mK. [33]

1.3. Potential applications

Here, we present an outlook on potential applications of graphene. These are neither exhaustive nor in industrial production. That is to say, we aim to give examples of the incorporation of graphene into different fields. The applications are not yet maturely developed such that graphene is in an industrial product. A vast amount of research is done to uncover its properties and still an extensive research into the understanding and control of these properties is necessary to translate them into real applications.

1.3.1. Logic devices vs RF devices

The very commonly known Moore's law states that the number of transistors on a chip doubles once every two years driven by the demand for faster and more affordable computers and mobile devices. Now that the Si technology is reaching its limits, two new fields emerged in which the semiconductor industry is investing in heavily: Beyond CMOS and More than Moore. Beyond CMOS covers all the technologies that might replace CMOS in future and More than Moore focuses on incorporating new functionalities into existing device architectures.

Carbon electronics have the advantage of retaining FET architecture but replacing the conductive channel with a carbon nanomaterial. Graphene transistors can be divided into two categories; logic devices and RF devices. They have quite different design demands. Logic applications must have low energy consumption in static state. This translates into that the graphene device must be switched off completely to a non-conducting state, i.e. it needs to have a band gap. Another necessary yet debated phenomenon is the current saturation. It is argued that electron-electron interactions in graphene might make velocity saturation impossible. Additionally,

high current bias is demonstrated to cause hot spots which interfere with current transport into non-uniformity. [34] [35]
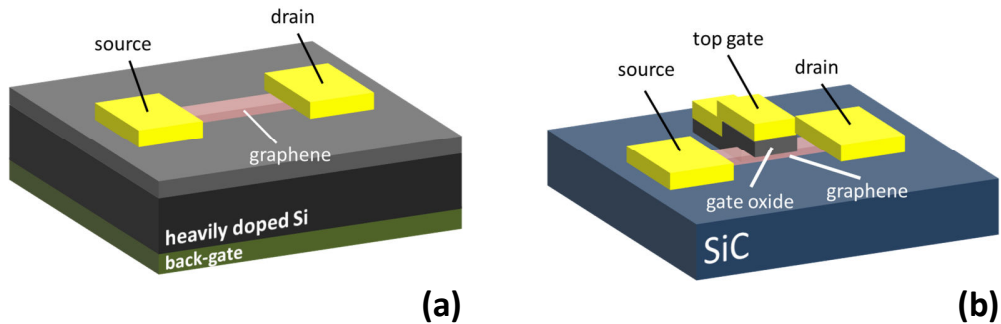
Figure 8. Examples of **a)** back-gated and **b)** top-gated graphene field effect devices.

As we mentioned, the zero band gap does not permit graphene to be employed in logic applications. In fact, IBM stated that it is unlikely for graphene to replace Si technology in future. [34] Yet again, studies on graphene primarily focused on graphene FETs. Generally, it is simpler to fabricate the transistor with a back-gate for research purposes by choosing the underneath layer as heavily doped Si. (Figure 8a) In that case, graphene is separated from the gate by the dielectric, (mostly a 300 nm of) SiO_2. The large parasitic capacitance of the 300 nm oxide interferes with measurements, thus top-gated devices have been fabricated as in Figure 8b.

For graphene to have a share in logic applications, it needs to beat CMOS in the parameters of room temperature operation, speed, scalability, size, device gain and cost. For RF devices, however, there is less requirement for a complete device switch-off. Instead, high speed and low noise are demanded. RF transistors play a key role in wireless communication by amplifying signals and offer gain at high frequencies. They commonly experience problems from series resistance and short channel effects. These could be overcome by employing graphene since it has intrinsically an atomically thin channel which improves electrostatistics.
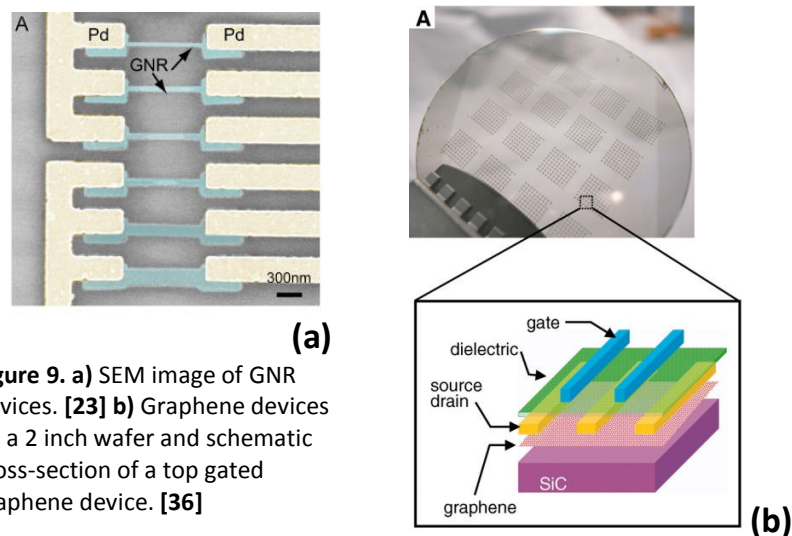
Figure 9. a) SEM image of GNR devices. **[23] b)** Graphene devices on a 2 inch wafer and schematic cross-section of a top gated graphene device. **[36]**

Beyond academic research [37] [38], companies such as IBM [23] [39] (Figure 9a) Samsung [40] (Figure 11b) and Intel [11] [41] have been doing research in the field of graphene field effect

transistors. IBM presented a 100 GHz graphene transistor on SiC with a higher cut-off than Si MOSFETs of the same length. [36] (Figure 9b)

1.3.2.   NEMS sensors

The field of NEMS looks into shrinking device dimensions since low dimensions improve resonant frequency, sensitivity of force and mass. [42] At the same time, narrowing the dimensions can degrade device characteristics and make transduction difficult. The well-known technologies of Si make it an eligible material to fabricate clamped beams and cantilevers by top-down approach. [43] [44] In recent years, nanowires and nanotubes have caught interest in the field of NEMS as a bottom-up approach. Graphene is intrinsically nanoscale and it can be fabricated over large areas allowing for standard lithographic techniques. Thus, it brings together top-down and bottom-up approaches.

(a)

(b)

(c)
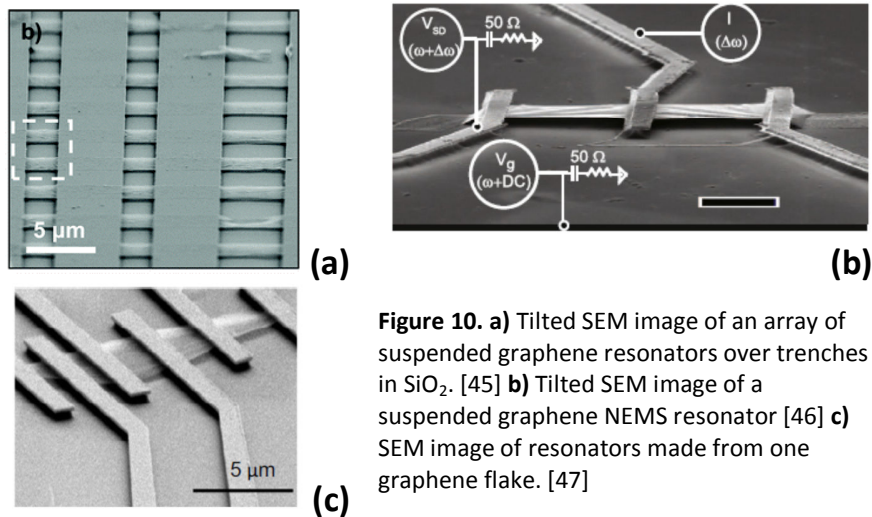
Figure 10. a) Tilted SEM image of an array of suspended graphene resonators over trenches in SiO_2. [45] **b)** Tilted SEM image of a suspended graphene NEMS resonator [46] **c)** SEM image of resonators made from one graphene flake. [47]

Graphene has a combination of properties that makes it well-suited for NEMS. It is chemically inert which enables atomically thin devices. Its high stiffness and low mass result in high resonant frequencies. Furthermore, its frequency is tunable over a large range due to its extraordinary values of strength. Graphene NEMS which have a small built-in tension can be employed in applications which require frequency tuning and a high force sensitivity. Devices which have a large built-in strain, on the other hand, can serve in mass sensing applications which require a high frequency and high quality factor. [47] [46] [45] Examples of graphene made into NEMS devices are given in Figure 10.

Combining extraordinary electrical properties with low thermal noise makes graphene devices excellent candidates for sensors. Considering that it is entirely made of surface, its 2D nature makes it very efficient in detecting adsorbed molecules. Adsorbed molecules act as donors or acceptors and alter the local carrier concentration which then appears as a change in the resistance. Gases such as CO, H_2O, NH_3 and NO_2 were successfully detected by micro-level gas sensor in the form of the truly 2D NEMS made of graphene. [48] [49] Moreover, another study demonstrated that dinitrotoluene (DNT) can also be detected which is of interest in terms of explosive detecting. [50] Next to chemicals, graphene has potential employment in the detection of biological substances as

well. One study showed the possibility of glucose sensing by graphene through an enzyme model of glucose oxidase. [51] Additionally, a study demonstrated graphene as a viable dopamine and serotonine sensor just as its predecessor, the CNT was. [52] Another study focused on Cadmium detection, which is a substance commonly used in several industrial areas while being severely damaging to human body. [53]

1.3.3.   Transparent electrodes

Transparent electrodes are in demand for in touchscreens, liquid crystal displays, organic photovoltaic cells and organic light-emitting diodes. The combination of the electrical conductivity with high optical transparency promotes the employment of graphene as transparent conducting electrodes as presented in Figure 11b. [16] [40] At the moment, indium tin oxide (ITO) dominates the industry as a conducting transparent material. However, it is brittle, high-cost and scarce in nature. This has driven the research into finding ITO replacements, preferably of flexible nature. Graphene is a promising candidate for this job considering that it is inert to water and oxygen while having high surface area and mobility. [40] [54] [55] An example was given as a dye-sensitized solar cell made of reduced graphene oxide has already been presented. [55] Transparent films made of graphene have also been used in organic solar cells. (Figure 11a) [56]

(b)

Figure 11. a) Synthetic nanographene is cross-linked and fused into larger graphene sheets. The resulting transparent film of graphene serves as window electrodes in solar cells. [56] **b)** Graphene transferred onto PDMS substrates demonstrating its use as a transparent and flexible electrode. [40]

(a)
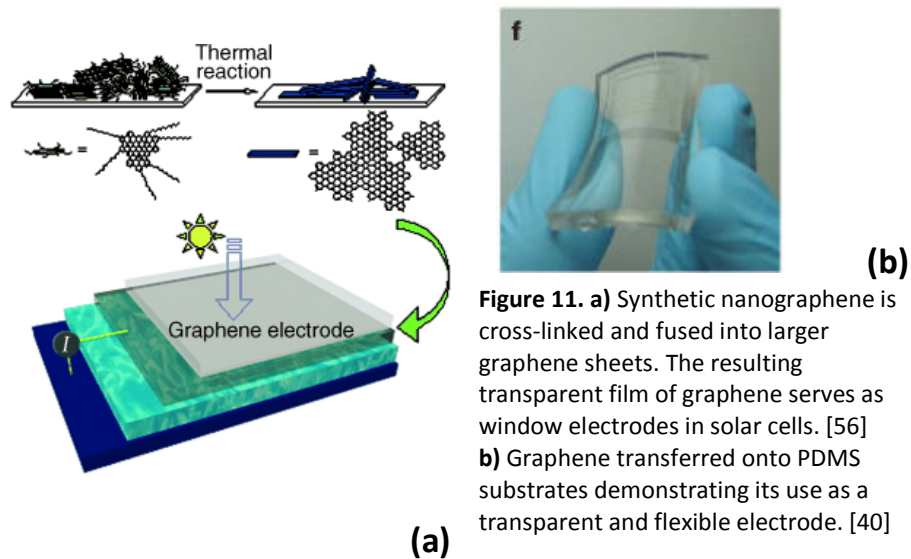
1.3.4.   Photonics

Optical transitions of graphene can be tuned by gate voltage. This and the electrical injection have the potential towards graphene-based optoelectronic devices such as tunable IR detectors, modulators and emitters. [57] Furthermore, when the zero gap is combined with the large surface area, graphene FETs can be used as ultrafast photodetectors. (Figure 12) [58]
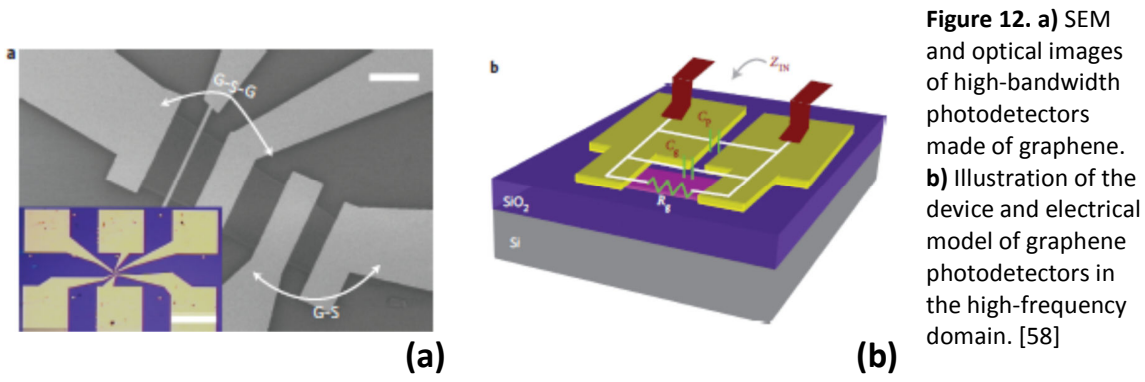
Figure 12. a) SEM and optical images of high-bandwidth photodetectors made of graphene. **b)** Illustration of the device and electrical model of graphene photodetectors in the high-frequency domain. [58]

(a)   **(b)**

1.3.5. Biotechnology

Graphene is searching for its way in biotechnological applications. The fact that it can be functionalized easily has prompted its use in biotechnology. One research made an effort to understand its interaction with DNA nucleobases and nucleosides. [59]

1.3.6. Electrochemistry

Few-layer graphene has been proposed as a part of composite electrodes in Li-ion batteries. Graphite and activated carbon are already embedded in electrochemical systems since they are reversible materials with reasonable specific capacity. And graphene displayed equal or better kinetics for the same task. It possesses superior in conductivity, surface area and chemical tolerance. Thus, it has the potential to replace such materials in energy storage devices such as batteries and supercapacitors. (Figure 13) [60] [61]
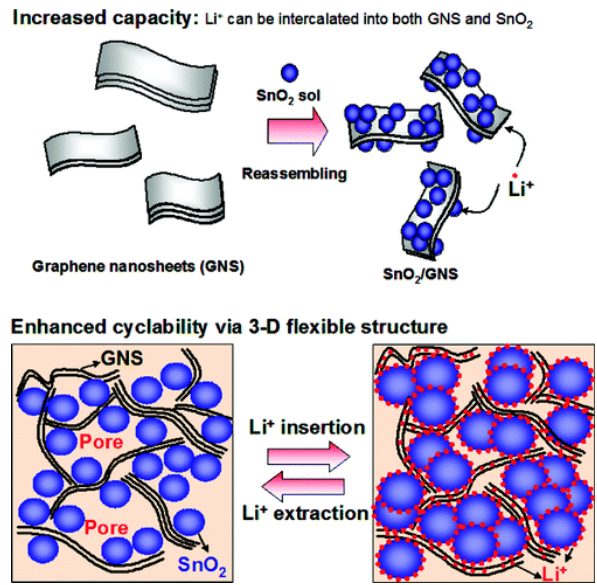
Figure 13. Schematics for the synthesis and the structure of SnO$_2$/graphene nanosheets to demonstrate the possible incorporation of graphene into Li ion batteries. [60]

1.4. Objective of this thesis

Its various potential applications in diverse fields have proven graphene to be worthy of more detailed studies for the behavior of its extraordinary properties and large-scale manufacturing capabilities. CVD technique made it possible for graphene to be a serious candidate to integrate in electronic applications by providing i)wafer-scale continuous material and ii) the possibility of transfer onto a desired substrate. Since the beginning of our thesis work, CVD techniques have been improved to produce wafer-scale, high-quality and highly-monolayer graphene. However, there are still issues to be addressed for the safe transfer of graphene into the industrial world.

The desire is to exploit the outstanding electronic properties of graphene to the fullest. For that, graphene sheet must be isolated; in other words the substrate interaction needs to be eliminated. Furthermore, in the field of NEMS, which can profit additionally from the exceptional mechanical properties of graphene, a suspended structure is required.

A reliable and reproducible fabrication route of suspended graphene devices with a high output is vital for graphene employment in industry. Most of the works on suspended graphene so far have been interested in assessing an extraordinary property. There are not many studies which study the interference of synthesis and fabrication techniques with the resulting device. Because of their immediate impact, the first two main factors which we addressed are the residual compressive strain from CVD techniques and beam collapse due to the fabrication route.

This thesis aims to study the fabrication of suspended and supported graphene devices and develop a high yield route within a realistic approach to the integration of graphene in industry. To that end, we employ CVD graphene which we obtain through our collaboration with Prof. Duesberg's team in CRANN, Dublin. The thesis is organized as follows:
In Chapter 2, we start by reviewing the existing fabrication techniques for suspended graphene ribbons to this date. We follow by the issues which, following our experience, interfere with suspension. We analyze their origin and explain the high-yield process that we developed. Characterizations by scanning electron microscopy (SEM) and atomic force microscopy (AFM) were used to assess morphological quality and suspension. We continue by investigating the strain and electrical properties in our devices.

For that, we devote an entire chapter to Raman measurements, where we discuss the effects of doping and strain in our devices and how they are influenced from temperature.

We finish by presenting the electrical properties such as contact resistance, carrier density and mobility as well as temperature-dependent resistivity and quantum interference and confinement effects under magnetic field.

The dissertation ends with conclusions and outlook of future work.

Chapter 2

DEVICE FABRICATION FROM GRAPHENE

This thesis concentrates on the successful fabrication of graphene devices, both supported and suspended, with an emphasis on how to achieve suspended graphene. Substrates are known to shadow over the extraordinary thermal and electrical properties of graphene; not to mention the fact that most mechanical properties cannot be accessed unless graphene is suspended. In this chapter, we present the details of the fabrication route for supported and suspended graphene devices, the latter of which poses greater challenge.

We start by reviewing the state of art for the fabrication of suspended graphene devices. As the reader will see, there is great variety in presented fabrication methods. The first experiments on suspended graphene dates back to as early as 2007. Thus, there exists a series of publications which studied the characteristics of suspended graphene. However, at the same time, we see that some researchers have gone to great lengths to find creative techniques to achieve batch fabrication of free-standing graphene. This on its own is evidence enough that repeatable mass-production of suspended graphene devices is not as a trivial process as it appears.

Throughout the chapter, there is an emphasis towards the methods involving mechanical exfoliation and chemical vapor deposition (CVD). This stems simply from the fact that our graphene of choice is CVD graphene. And the fabrication techniques of exfoliated graphene are transferrable to CVD graphene. Therefore, the fabrication routes proposed for these two types of graphene is our interest.

Fabrication techniques for suspended graphene devices have inherited basic techniques from NEMS technologies and modified them to its needs. Firstly, we present some of the existing methods for obtaining graphene and fabricating it into suspended devices. We then introduce our graphene source and present the route we propose for high-yield fabrication of devices with free-standing graphene, at the same time being scalable and compatible with existing Si technologies. Additionally, we demonstrate the characterization of the fabrication stages.

2.1. Different sources of graphene

In Chapter 1: Introduction, we mentioned that there are different methods developed for obtaining graphene by now. The main techniques for mostly single layer, pristine and/or continuous sheets come from i) mechanical exfoliation from highly ordered pyrolytic graphite (HOPG), ii) graphene from sublimation of Si atoms on SiC wafer and iii) graphene from chemical vapor deposition on catalytic metal substrates, listed in historical order. There have been other sources presented such as the "so-called" chemical exfoliation which involves intercalation compounds on graphite and reducing graphene oxide. However, we concentrate on methods that result in rather continuous films with little flaws. This is generally required for electronic applications. Reducing an already oxidized graphene, for example, does not fit this criterion since a 100% reduction is not quite possible from graphene oxide.

2.1.1.   Mechanical Exfoliation

The best quality graphene is obtained by mechanical exfoliation of highly oriented pyrolytic graphite (HOPG). In 2004, Novoselov et al. obtained few layer graphene by repeatedly peeling highly ordered pyrolytic graphite (HOPG). Firstly, the authors prepared mesas of 5 µm on the platelets in squares of different sizes. The patterned surface was pressed against a glass substrate with photoresist on it and baked. Baking helped attaching layers from the HOPG onto the resist. A scotch tape was used to peel off layers on the resist into fewer layers. Resist is removed in acetone where flakes from the resist were left floating in the solution. Si wafer with an oxide of 300 nm was dipped in the solution and flakes landed on the wafer. Layer thickness is determined by optical microscopy, electron microscopy and AFM. Graphene on a 300 nm oxide wafer gives a particular color contrast which helped the scientists to locate few layer graphene non-invasively via optical lithography such as in Figure 14. [8] [62] The method has spread in the scientific community fast due to its simplicity leading to a boom in graphene-related research in physics, chemistry and biology.
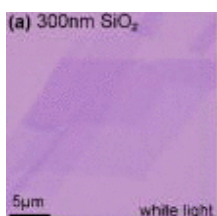
Figure 14. Graphene of different number of layers placed on a Si wafer with a 300 nm oxide layer under an optical microscope illuminated by white light. There is a clear contrast between graphene and the oxide layer due to constructive interference effects for certain oxide thicknesses and it changes with the number of graphene layers. This helped scientists to isolate single layer graphene at the start of the research. [62]

2.1.2.   Chemical Exfoliation

Another method for graphene fabrication is derived from colloidal suspensions of graphite and graphite oxide. Graphite can be oxidized with strong acids and oxidants. The oxidation level is defined by type of method, reaction conditions and the graphite precursor. By sonicating graphite oxide, it is possible to obtain homogeneous colloidal suspensions of graphene oxide in a variety of organic solvents. In contrast to graphene, graphene oxide is hydrophilic and can therefore be dispersed in water as well as several polar solvents. Additionally, these suspensions enable chemical modifications to graphene oxide through organic molecules. [63]

The resulting graphene oxide is electrically insulating. Its thermal, UV-assisted or chemical reduction through products such as hydrazine, dimethylhydrazine, hydroquinone and NaBH leads to an electrically conducting material, the so-called "reduced graphene oxide". Combustions analysis uncovered continuing presence of significant amount of oxide; thus reduced graphene oxide is not the same thing as graphene. It is difficult to remove the remaining hydroxyl groups. [63]

2.1.3.   Graphene synthesis from SiC

SiC is a wide gap semiconductor suited to high temperatures and high electric fields. It has many crystalline forms out of which two types stand out for electronic applications: the hexagonal 4H and 6H polytypes. They are formed from stacks from alternating bilayers of Si and C. [11] [64] Epitaxial growth of graphene is demonstrated from SiC(0001) wafers through sublimation of Si

16

atoms and graphitization of C atoms when the substrate is annealed at temperatures 1000 – 1800°C. (Figure 15) Multilayer epitaxial graphene on SiC is reported to have high mobility. [65] Devices made of SiC graphene were generally made on a SiC wafer. Transferring graphene from SiC onto another substrate is difficult since SiC is chemically inert to most etchants therefore cannot be easily etched away. Also, the dry techniques that involve peeling are not suitable either due to the great adhesion between the SiC and graphene.
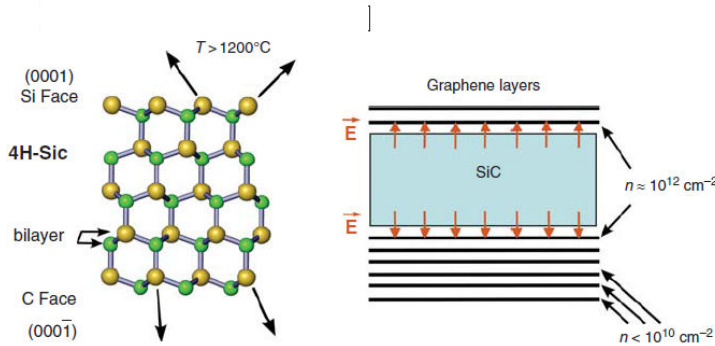
Figure 15. Illustration of graphene growth on SiC with a side-view representation of a SiC wafer. Yellow and green spheres are Si and C atoms, respectively. At high temperatures, the Si atoms evaporate indicated by arrows. This results in graphene sheets in the form of few-layers on the Si-terminated side and multilayers on the C-terminated side. [64]

2.1.4. Graphene synthesis by chemical vapor deposition

To this date, the best quality graphene comes from mechanical exfoliation. However, this method is without doubt not appropriate for mass production. The flake size is limited to tens of micrometers; neither the location nor the number of layers can be controlled. Chemical vapor deposition (CVD) has great potential to address these problems.

During experiments to grow diamond via CVD on metal catalysts in 1991, scientists unintentionally synthesized multilayers of graphene. The experiments used Cu surfaces after carbon implantation. The substrates were heated to 800 - 1000°C to diffuse carbon out and form graphite. In fact, graphite formation with all known metal catalysts has been heavily studied since 1960s for the need of high quality graphite as moderators in nuclear reactors. [65]

First attempts on graphene synthesis via CVD were reported by Somani et al. in 2006, which by now has developed into a technique to yield large-area, highly monolayer graphene. [66] Research on the CVD technique focuses on controlling domain size, number of layers and presence of defects.

The CVD technique activates gaseous reactants followed by a chemical reaction which leads to the deposition of the solid product over a substrate. The deposition can be of powder form as well as thin films depending on the nature of the reactions which can come either in homogeneous gas-phase form or heterogeneously on a surface. Since graphene is a thin film, we are interested in heterogeneous reactions on a substrate.

Carbon source

There have been studies on liquid and solid phase sources for carbon to fabricate graphene. While the choice of liquid source is toluene with its weak bonds to the advantage, polymer films,

evaporated solids, even food, insects and waste have been demonstrated as a solid source to synthesize graphene. [67] As more conventional solid sources, PMMA, fluorine or sucrose deposited on Cu at temperatures 800°C - 1000°C leading to graphene synthesis have been reported. However,the essential carbon source for CVD is in gas phase and mostly methane. In fact, Graphene thickness is directly governed by the gas flow rate. [68]

Description of chemical vapor deposition process for graphene production
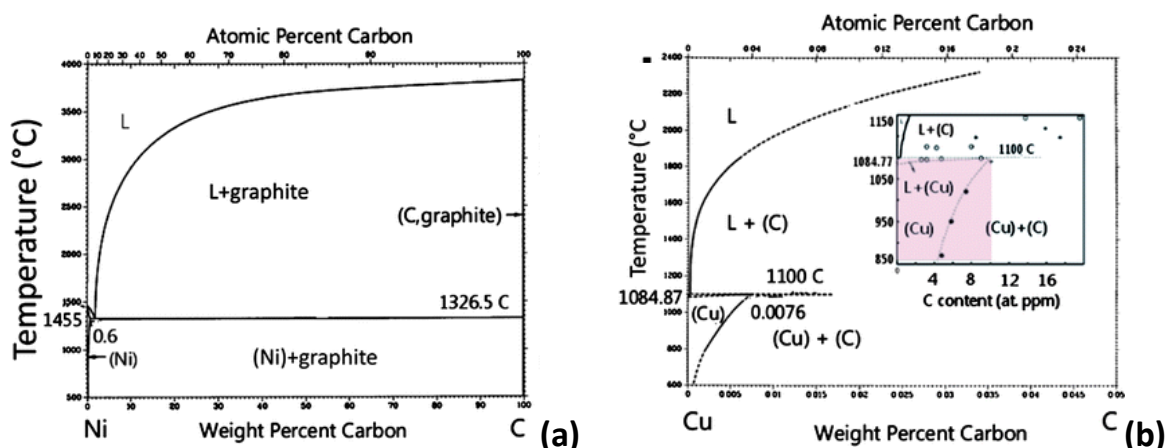
Figure 16. Binary phase diagram of **a)** Ni – C; **b)** Cu – C. L stands for the liquid phase. The x-axis of both phase diagrams describe the amount of carbon in copper in terms of weight percentage. "Ni + graphite" or "Cu + C" means that the metal and graphene are present in the system as separate entities, i.e. they do not form a solution. We also should draw attention to the fact that the x-scale of the two graphs are not the same. The low solubility of carbon in Cu is further emphasized in **b)** by showing the 0.008% solubility of carbon in Cu at 1084°C. That is to say, carbon is a part of a solution in Cu up to a weight percentage of only 0.008% even at a temperature as high as 1084°C. Any additional amount will precipitate out. [65]

A typical carbon source for CVD graphene is methane (CH_4). C-H bonds are strong (440 kJ/mol) and therefore require temperatures higher than 1200°C to decompose which is over the temperature range of a typical CVD furnace. To decrease the reaction temperature to values lower than 900°C, transition metal surfaces are employed as catalyst. If the reaction mainly takes place on the surface, it comes to an end after monolayer graphene coverage due to catalyst poisoning. That is to say, for a surface-based reaction, once the entire surface is covered with a layer of graphene, there are no longer eligible sites available for the reaction to occur. The nature of such surface reactions, therefore, prevents the formation of additional layers after the first one. Transition metals are commonly used as catalysts for CVD reactions. Among different transition metals such as Ni, Pd, Pt, Ir and Cu; copper is favored due to its catalytic ability and carbon solubility. The "self-limiting" system we just described is observed in the case of Cu as catalyst which is so far the only metal leading to highly monolayer CVD graphene. On other transition metals, of which Ni is heavily studied, graphene growth happens via bulk diffusion, i.e. not on the surface, since carbon is highly soluble in Ni. This is revealed in the phase diagram of Ni and C (Figure 16a) Graphene formation on Ni is therefore a diffusion-precipitation process. [65] Thus, the product graphene depends heavily on the reaction kinetics where a fast cooling is exercised to suppress the formation of multilayers. [40] [69] The phase diagram of Cu and C on the other hand (Figure 16b) shows a lower solubility of C. The low reactivity is related to the fact that Cu has a filled 3d shell. Therefore C can bond to Cu softly only by charge transfer from π of the sp^2 hybridized carbon into the empty 4s orbitals of Cu. [65]

18

We firstly focus on metals with a low carbon solubility such as Cu. As the catalyst, the properties of the metal of choice play a role in modifying the CVD process. The size and orientation of the metal grains, for instance, are thought to have significant influence on the defect density of graphene. Large grain sizes lead to better quality in graphene. [70] Furthermore, the crystallographic orientation of the metal affects graphene growth as well. It is reported that the (111) orientation of Cu results in pristine monolayer graphene. [71] Therefore, it is important to anneal Cu surface to the lowest energy (111) facets. Clearly, the properties of the surface have likewise strong impacts on graphene growth. The surface roughness of the metal can interfere with the uniformity of CVD graphene. Electro-polishing Cu surface helps the growth of a uniform graphene film. [72] Furthermore, it is known that graphene first nucleates at the impurities and imperfections of the surface. Thus, decreasing the amount of surface impurities, i.e. decreasing the number of nucleation sites increases the domain size of the synthesized graphene. [73] The little interaction between C and Cu leads to a polycrystalline yet continuous film expanding over the grain boundaries of the substrate. [65]

Growth on Ni

The metal choice has an impact not only through its carbon solubility, but also through its lattice parameters. Lattice mismatch between graphene and Co(0001) and Ni(111) is less than 1% whereas the lattice of Cu(111), Pt(111), Pd(111) and Ir(111) differs from graphene by more than 1%. [65] Fast cooling rates are essential for suppressing carbon migration into bulk in the case of high solubility metals such as Ni. For both high and low solubility metals, the temperature gradient during cooling has a direct impact on the number of layers as well as their quality. [74] [75]
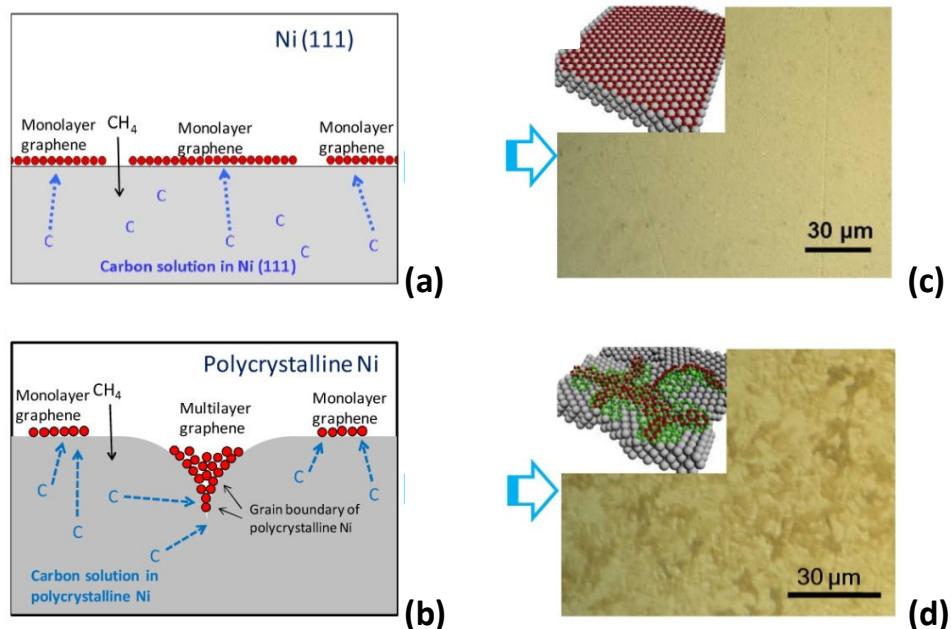
Figure 17. Graphene growth mechanism on **a)** Ni(111); **b)** polycrystalline Ni. Optical image of graphene grown **c)** on Ni(111) and **d)** on polycrystalline Ni. [76]

For the case of polycrystalline Ni films as catalyst, which have a high carbon solubility, the film is first annealed in Ar/H$_2$ at elevated temperatures such as 900 - 1000°C to expand grains which is then followed by gas flow of H$_2$/CH$_4$. The carbon decomposes and diffuses into the film followed by a precipitation during cooling. Precipitation principally occurs at grain boundaries and leads to multilayer graphene especially at these regions as depicted in Figure 17b and d [76] Therefore employing a single crystal Ni instead of a polycrystalline one can significantly improve the suppression of multilayer formation as shown in Figure 17a, c. For the case of Cu, polycrystalline films can be used. The Cu film is first annealed in hydrogen at 1000°C followed by a gas flow of H$_2$/CH$_4$ to grow graphene. The surface reaction is illustrated in Figure 18 for comparison. [76]
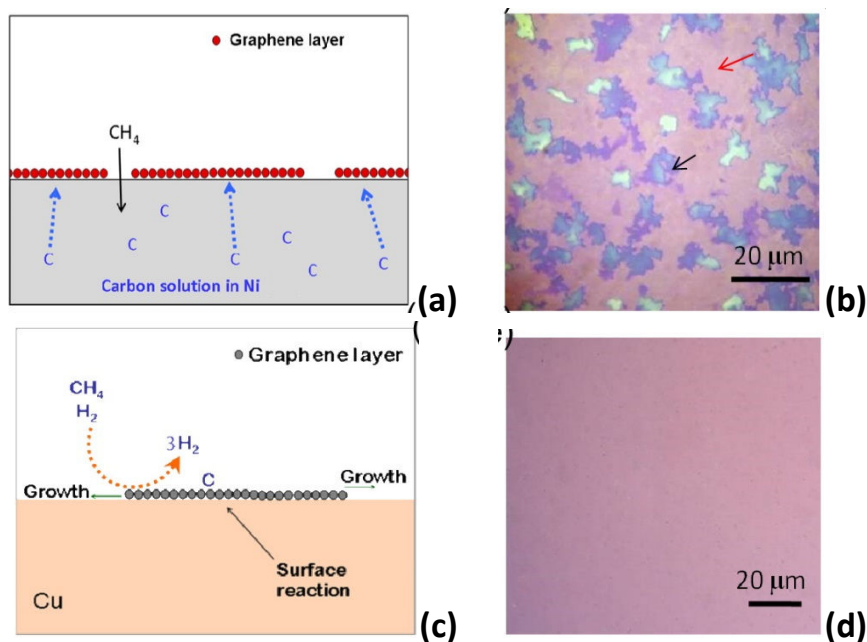
Figure 18. Graphene growth mechanism on **a)** Ni and **c)** Cu. Optical images of graphene transferred to SiO$_2$/Si **b)** from Ni and **d)** from Cu. [76]

The effect of hydrogen

Just as the carbon source, hydrogen content of the recipe is equally important. Hydrogen is employed to clean and crystallize metal substrates during annealing and oxygen reduction as well as to dilute the carbon precursor. Its interaction with the substrate plays a role in the chemisorption kinetics of the following methane in the sense that hydrogen can i) diffuse in the metal and change solubility for methane, ii) remove hydrogen from the surface if it comes in the atomic form and create adsorption sites for methane, iii) passivate defects and grain boundaries where nucleation is thought to start. Thus, the hydrogen flow needs to be optimized for monolayer CVD graphene recipe. [77] [78]

2.2. Graphene transfer & transfer-free processes:

In general, CVD graphene is transferred with the help of polymers onto a dielectric substrate. The routine procedure is depicted in Figure 19. A polymer, commonly PMMA, is

spincoated on graphene on metal and heated to evaporate the solvent. The metal layer underneath is then chemically etched leaving a structure of PMMA on graphene. Acid residues are cleaned in water. Without the polymer layer, graphene alone would disintegrate into flakes during transfer. With the help of the polymer, the floating form has sufficient structural integrity for transfer from water over the desired substrate. The substrate of choice is generally an oxidized Si wafer for in the field of graphene for electronic applications. The PMMA/graphene/oxidized wafer stack is heated to dispose of the probable water stuck in-between the layers. This is followed by the final step, the PMMA stripping in acetone. The resulting structure is graphene on a dielectric. [76] [79]
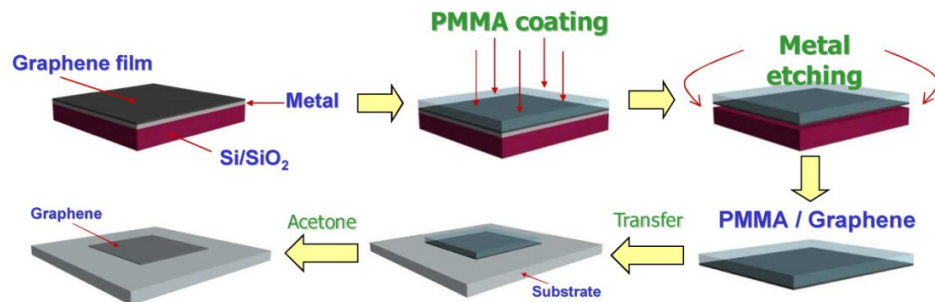
Figure 19. CVD graphene transfer. [76]

While this is a very neat method to have large-scale graphene on a dielectric, there are several reports on the contamination of graphene from the transfer polymer. The general consensus is that polymers cannot be cleaned off of the graphene surface completely. Thus, it is of great interest to grow graphene directly on dielectric substrates. [80] [81] [82] So far, there have been several attempts to fabricate graphene on SiO$_2$; however it has been difficult to synthesize continuous and highly conductive films. One method is proposed by Ismach et al. by using a sacrificial Cu layer. Customarily, thick copper foils are used for CVD. However, for the sake of direct growth on dielectrics, a thin film of Cu is deposited on the dielectric of choice. One primary challenge with this process is the control of the film thickness. Films that are too thin will experience dewetting at high temperatures. [65] One study, on the other hand, proposed to turn this issue into their advantage. They use dewetting to remove Cu completely from the dielectric by applying long processing times. However, the obtained graphene showed defects and graphitic-like material at places. That is to say, the idea is interesting to start a discussion, but the results are not yet competing with polymeric transfer of CVD graphene. [83] Another idea is to etch the Cu layer on the dielectric chemically and land graphene directly on the dielectric. The issue with this approach is the fact that Cu films are not stable at temperatures higher than 800°C, i.e. at temperatures of CVD process. Cu diffuses into SiO$_2$/Si, thus diffusion barriers such as W, Cr, Ni, Al$_2$O$_3$ are required to be put in-between Cu and the wafer. In any case, a complete suppression has not been possible until now. [84] Plasma-assisted growth decreases synthesis temperature and is therefore promising for such applications. [85]

2.3. Wrinkle and fold formation in CVD graphene

CVD graphene is known to have wrinkles, ripples or folds after transfer on a substrate or after device fabrication. For the sake of identifying the different forms, we use the wrinkle, ripple and fold as indicated in Figure 20. These structures, especially sharp folds, have been predicted to modify the electronic properties and chemical reactivity of graphene. [86] Therefore, it is important to understand them and control their formation, if possible.
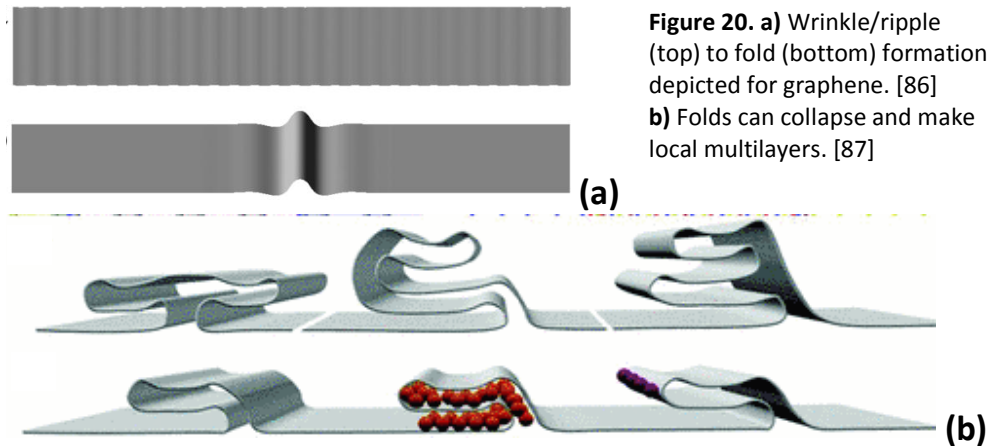
Figure 20. a) Wrinkle/ripple (top) to fold (bottom) formation depicted for graphene. [86] **b)** Folds can collapse and make local multilayers. [87]

Zhang et al. showed that folds originate from the nonlinearity in the van der Waals interaction between the graphene and the substrate. They characterized fold formations in term of adhesion and friction parameters and conclude that friction is the selecting factor for the separation between folds. They based this on the fact that the formation of folds which are far apart from each other would cost friction work. [86]

CVD graphene on a substrate typically shows networks of folds. CVD graphene is acknowledged to show wrinkles. These are generally attributed to the difference in the thermal expansion coefficients of the metal ($\alpha_{Ni} = 12.89 - 21.0 * 10^{-6}/K$ for $T = 0 - 1000°C$; $\alpha_{Cu} = 24 * 10^{-6}/K$) and graphene ($\alpha_{Graphene} = -6 * 10^{-6}/K$ at $T = 27°C$) [88] [89] [90] The folds primarily form during transfer and generally argued to depend on the transfer type and the topography and polycrystallinity of the growth metal. [86]

Considering that the substrate is planar, any fold formation must include delamination. The uniform spacing in-between folds was argued to be due to friction. Transition of a wrinkled state to a localized fold state happens through the sliding of the graphene sheet. Folds that are separated by a large distance were argued to be energetically favorable to smaller folds that are closer to each other. But they would have to spend a larger frictional work. That is to say, adhesion, i.e. the potential energy and frictional work are competing. In a rectangular graphene with a given length, the most energetically favorable number of folds are determined by friction. For instance, the lack of friction can favor the formation of one fold while high friction values would favor bi- or tri-fold formations. Furthermore, the folds can differ in size. When the strain was increased further, they did not move but grew in size. [86]

2.4. Device fabrication: State of art

Our devices are made from CVD graphene due to its scalability and compatibility with existing Si technologies. Here we focus on mainly fabrication techniques for exfoliated or CVD graphene since methods for exfoliated graphene are directly applicable on CVD fabrication techniques.

2.4.1. Transfer over existing trenches

While basic clean room techniques can engineer graphene devices supported on a substrate effortlessly, caution is called for when the device has to be suspended. First generation of free-standing graphene devices was fabricated through mechanical exfoliation over existing trenches. Trenches were pre-patterned in SiO_2 in a wafer followed by electrode realization next to trenches. Resulting devices looked as in Figure 21a-b. The adhesion between SiO_2 and graphene is high; the van der Waals forces keep the graphene attached to the substrate with no additional clamping required. These first devices were intended as resonators. Vibrations in MHz frequencies were optically and electrically actuated and detected optically by interferometry. This type of fabrication has no additional processing done on graphene, i.e. it keeps graphene as clean as possible. The disadvantage is though that the exfoliation method has little control over the beam size and is not applicable large scale. [48] [91] Still, it is the best method to show a certain physical property of graphene. Therefore even after scalable synthesis methods are discovered, scientists keep using this method as in the example of the work by Xu et al. in 2010. After patterning a gate electrode followed by PECVD of a gate oxide layer, Xu et al. opened a trench between the source and drain electrodes. Graphene is then exfoliated over this trench to investigate radio frequency electrical readout of mechanical resonators. [92]

(a)

(c)

(b)
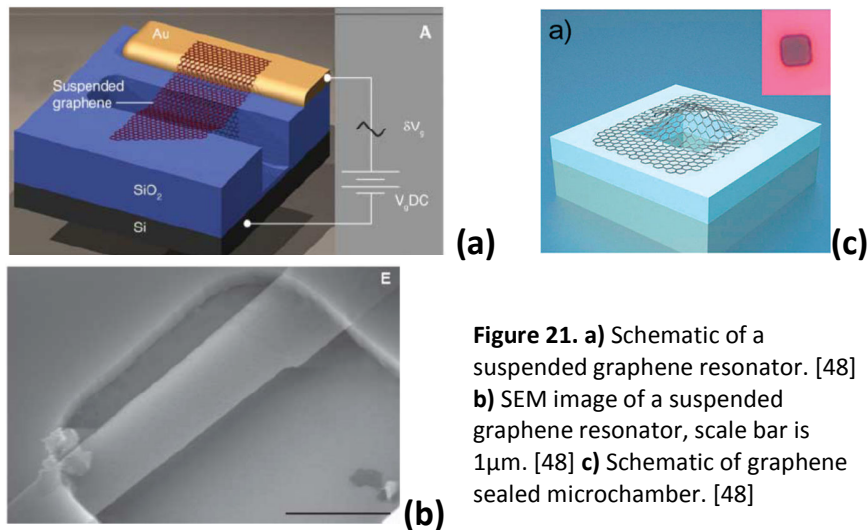
Figure 21. a) Schematic of a suspended graphene resonator. [48] **b)** SEM image of a suspended graphene resonator, scale bar is 1µm. [48] **c)** Schematic of graphene sealed microchamber. [48]

Frank et al. attempted to increase the control over suspended device fabrication from mechanical exfoliation. To that end, they employ a "pencil". Kish graphite is comprised of flakes which are few mm on a side. The authors attached these flakes to a probe which is then acting as a "pencil". As the graphite is cleaved, an atomically smooth surface on the tip of the surface is released. This is followed dragging this pencil over SiO_2 trenches leaving exfoliated pieces. The suspended sheets appear as "vivid shades of purple" under optical microscope. [93]
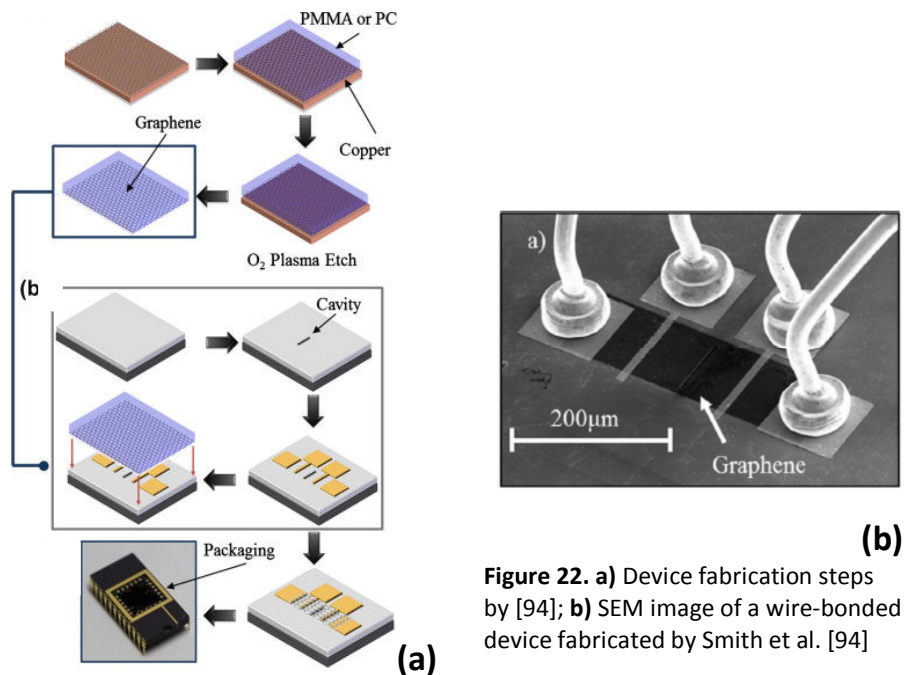
Figure 22. a) Device fabrication steps by [94]; **b)** SEM image of a wire-bonded device fabricated by Smith et al. [94]

Besides resonators, pressure sensors are made from exfoliated graphene during the early stages of the research. The application relied on the gas impermeability of graphene. To that purpose, graphene was mechanically exfoliated such that it covers an entire trench as in Figure 21c. [95]

Within the objective of suspended graphene devices, CVD graphene inherited the technique of predefined trenches from exfoliated graphene. Similar to the case of Bunch et al. 2008, Smith et al. etched trenches in SiO_2 with electrical contacts to realize pressure sensors from graphene as demonstrated in Figure 22. CVD graphene is transferred over trenches and contacts followed by patterning by lithography and oxygen plasma. [94]

Generally, lithography techniques are utilized if there is a desire to pattern graphene into a certain geometry. Morin et al. presented an unconventional method using focused ion beam (FIB). [96] The authors carved nanopores into suspended graphene sheets via a gallium ion beam after a work of direct patterning of low dimensional and high quality nanobeam structures down to 20 nm by gallium ions. [97] SEM images of the resulting free-standing ribbons are shown in Figure 23c .The origin of graphene is HOPG exfoliation. Additionally, they report rolling at beam edges. [96]

We brought up before how CVD graphene inherited fabrication techniques from exfoliated graphene. Zhang et al. apply the process of FIB patterning to CVD graphene. The authors transferred CVD graphene over a groove array in Si realized by deep reactive ion etching (DRIE). The transfer was followed by patterning of suspended graphene by FIB as explained in Figure 23a leading to SEM images in Figure 23b, d. [98]

24
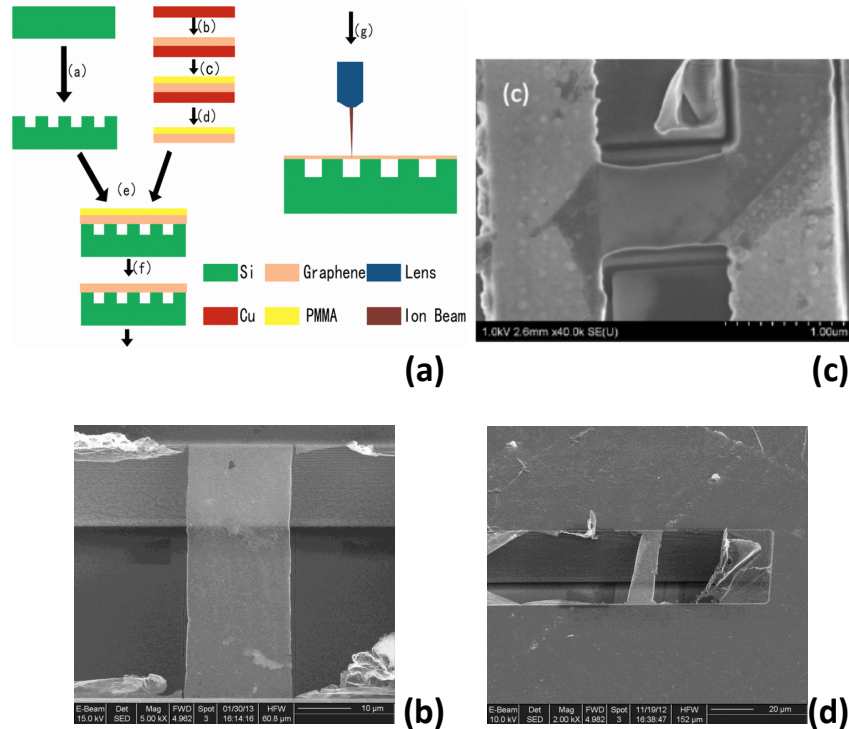
Figure 23. a) FIB patterning of graphene a)a. ICP etching of array, b. Graphene growth on Cu by CVD, c. Spincoating PMMA, d. Cu etching, e. Transfer to substrate, f. PMMA removal, g. Graphene patterning by FIB [98]; **b, d)** SEM images of free-standing CVD graphene ribbon fabricated via FIB [98]; **c)** SEM images of free-standing exfoliated graphene ribbon fabricated via FIB [96]

2.4.2. Suspending by substrate etch

Another method employed since the early stages of the study of suspended graphene was the simple idea of removing partially the substrate underneath graphene. Removing the SiO_2 layer with the objective of free-standing beams is no news to the MEMS community. Since exfoliated graphene was the monopoly of graphene sources for many years, the first free-standing graphene by substrate etch was done on mechanically exfoliated graphene. The process started by firstly locating single layer flakes from mechanically exfoliated graphene over SiO_2/Si. Electrodes were realized at these points. The oxide layer underneath was etched chemically which was followed by drying in critical point dryer (CPD). CPD is employed, in general, to eliminate surface tension which would collapse the beam during the phase transition of water, i.e. during drying. In fact, CPD is no news to the MEMS community either; it is quite often used to realize free-standing beams. During chemical etching, the electrodes acted as etch mask and they were, therefore, also etched underneath as seen in Figure 24a-b. [47] If the electrodes are fully suspended, they can buckle under pressure. [46] Thus, if the electrodes are intended to serve as a chemical etch mask, too, it is important to fabricate sufficiently large and thick electrodes to add to the rigidity of the structure. As we mentioned, if demonstrating a particular property of graphene is the goal of the study, exfoliated graphene is preferred over CVD graphene since the latter involves a polymer assisted transfer process. Similarly, to prevent graphene having contact with the polymeric resists of lithography, graphene patterning was particularly avoided in early studies. Patterning can introduce

not only polymeric impurities, but also additional defects and dangling bonds at the edges. Instead, rectangular shaped flakes suitable for fabrication were selected. [18]

Figure 24. a) SEM image of several resonators made from a single graphene flake. [47] **b)** Angled SEM image of a suspended graphene device and the electrical contacts for actuation and detection of the mechanical motion of the membrane. [46]
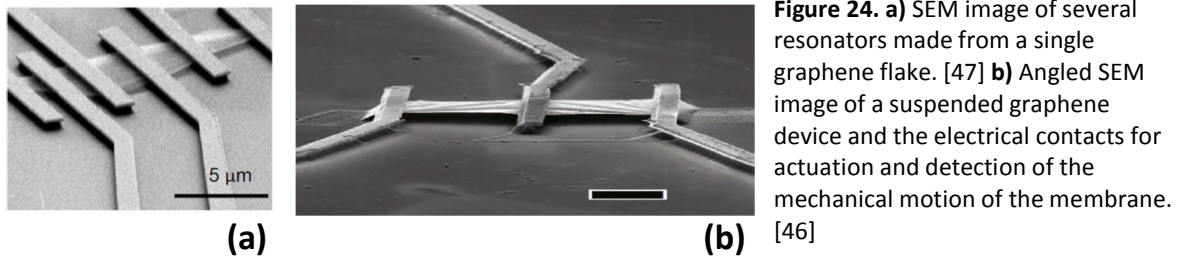
Dorgan et al. used the same method to fabricate devices both from mechanical exfoliation and CVD graphene. After exfoliating or transferring the graphene over Si wafer with an oxide layer of 300 nm, graphene was patterned into rectangles by e-beam lithography followed by oxygen plasma etch. Metal contacts of Cr/Au were realized. The device was then dipped in buffered HF (or more commonly known as BOE as in buffered oxide etching) followed by rinsing in deionized water. Water was slowly replaced by isopropanol and the sample is transferred to CPD. The suspended sample was annealed at 200°C in vacuum. [99]

Figure 25. a) SEM image of suspended graphene device by Tombros et al. after current annealing in vacuum at 4.2 K along with the schematic representation of its cross-section. The scale is 2 μm. [100] **b)** Suspended graphene device technique via LOR developed by Tombros et al. [101]
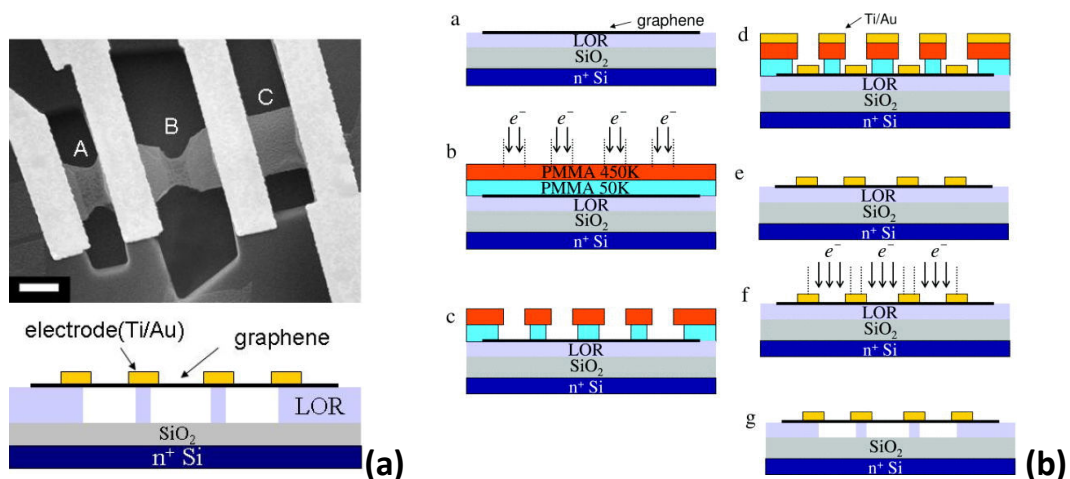
Tombros et al. aimed at demonstrating the quantized conductance of graphene at low temperature. As others have done before them, they chose exfoliated graphene as the source. However, they developed a different technique from two of the initial basic ideas; transferring over trenches in SiO$_2$ or chemically removing the SiO$_2$. Instead, they developed a polymer-assisted method for suspending. (Figure 25a) [100] This technique is mainly developed to avoid metal restriction in suspending graphene devices. Most methods involve etching the SiO$_2$ layer in HF, i.e. the electrode metals are exposed to HF. Only a handful of metals such as Au, Pd, Pt, Cr and Nb are resistant to HF. The idea makes use of a polymer as a spacer layer which is then sacrificed in an organic solvent to release graphene. (Figure 25b) The chosen polymer needs to resist to a wide range of solvents and to high temperature to able to use lithography resist during the process. LOR

is a suitable polymer for this purpose. It was spin-coated on a SiO$_2$/Si wafer with a thickness of 1.150 μm which provided a good visibility for graphene. Graphene was exfoliated from HOPG onto LOR. Electrodes were realized by ebeam lithography and evaporation. Lift-off was done at hot xylene at 80°C which at this temperature dissolves PMMA, the ebeam resist, but does not attack the LOR. Finally, LOR was exposed by ebeam and dissolved in hexane releasing graphene. The sample was dried in nitrogen. [101]
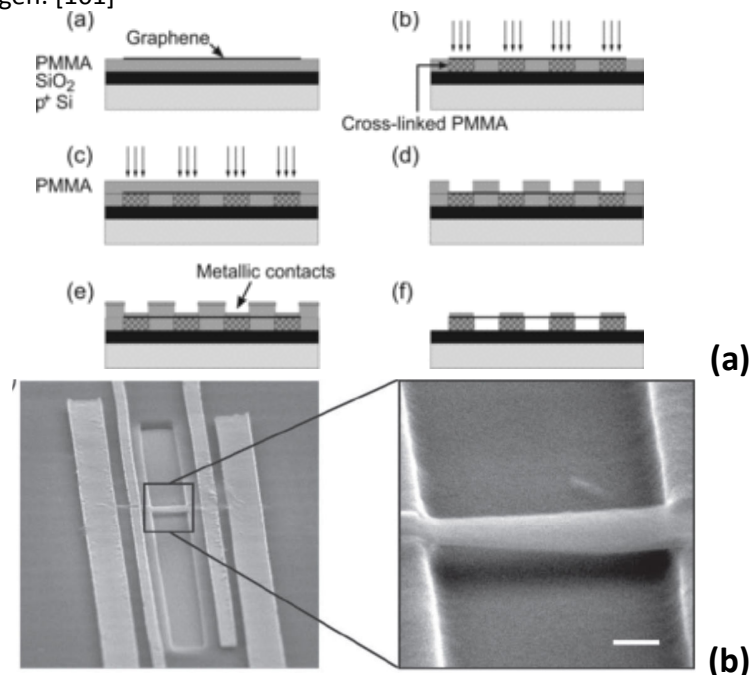
Figure 26. a) Fabrication process of suspended graphene devices by Neumann et al. **b)** SEM image of a suspended graphene device by Neumann et al. [102]

Substrate etching is usually done by exposing the device to powerful acids. And not all metals can survive this exposure. This is not an issue for electrical studies, i.e. there are several resilient metals eligible for electrical application. However, for spintronic applications, the eligible metals are also the ones that are attacked by HF. Thus, using spintronic electrodes as an etch mask is not possible. Having this in mind, Neumann et al. propose a different route to suspend graphene for spintronic applications. They exfoliated graphene onto an oxidized Si wafer with PMMA spun on top. The appropriate flakes were localized with the help of optical microscope and Raman spectroscopy. Subsequently, PMMA was overexposed by ebeam which then acts as negative resist at large doses, i.e. certain areas of PMMA are cross-linked as in Figure 26a. A second layer of PMMA was spincoated to realize metal electrodes by ebeam whose positions coincide with the PMMA pillars from the first layer of resist. During the step of lift-off, PMMA at both layers are removed except for the cross-linked areas. The graphene was thus suspended over the cross-linked pillars. (Figure 26b) Furthermore, the authors reported that CPD was unnecessary for drying. The authors claimed that this method is superior to the method involving LOR due to two main reasons: i) Graphene area to be suspended is exposed to high doses of ebeam in the case of LOR process. This can induce damage to graphene or deposit amorphous carbon. The deposited amorphous carbon cannot be removed by current annealing; instead, it is crystallized leading to the formation of multilayer graphene. ii) The device is exposed to chemicals of a regular fabrication process instead of additional foreign chemicals such as LOR [102].
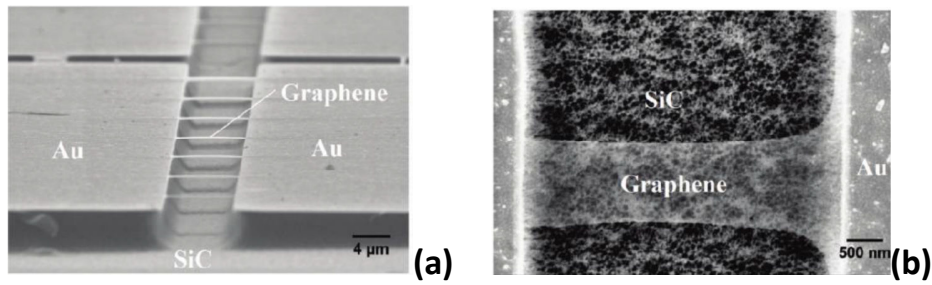
Figure 27. a-b) SEM image of suspended epitaxial graphene on SiC. [103]

Suspended structures were formed from epitaxial graphene on SiC as well. Graphene grown on 4H-SiC was suspended by wet etching of SiC. In fact, wet etching of SiC is not common. SiC is conventionally etched by plasma techniques which in this case would clearly damage graphene. Shivaraman et al. have used a wet etching technique developed by Kato et al., 2003 [104]. Firstly, they realized metal contacts on each side of the patterned graphene beam serving as etch masks. Graphene was patterned into ribbons by lithography and oxygen plasma. SiC was afterwards etched in the electrolyte KOH (1%) under a 100 W UV lamp for 4 h releasing the graphene beams as in Figure 27a-b. [103]

The first extensive study focusing on the various methods of fabrication of suspended devices from CVD graphene was done by van der Zande et al. in 2010. The authors employed several techniques and compared the results. The first type of membrane they fabricated is patterned by oxygen plasma while graphene is still on Cu foil, i.e. before transfer. The graphene strips are patterned by contact lithography and then transferred on predefined trenches in SiO_2. A second type of membranes was square and fully clamped on all sides. For this type, CVD graphene is transferred unpatterned onto a silicon nitride membrane with square holes. The PMMA is baked off at 300°C in air for 2 h. This suspending process did not involve liquids. A third type of membranes was suspended over electrical contacts. Graphene was transferred unpatterned over a wafer and patterned into small bars followed by electrode deposition. The bars were suspended by wet etching the oxide in BHF followed by critical point drying. Authors presented the SEM images of successfully suspended samples as in Figure 28a-b as well as of possible types of failures that occurred for the first set of suspended beams in Figure 28c. [45]
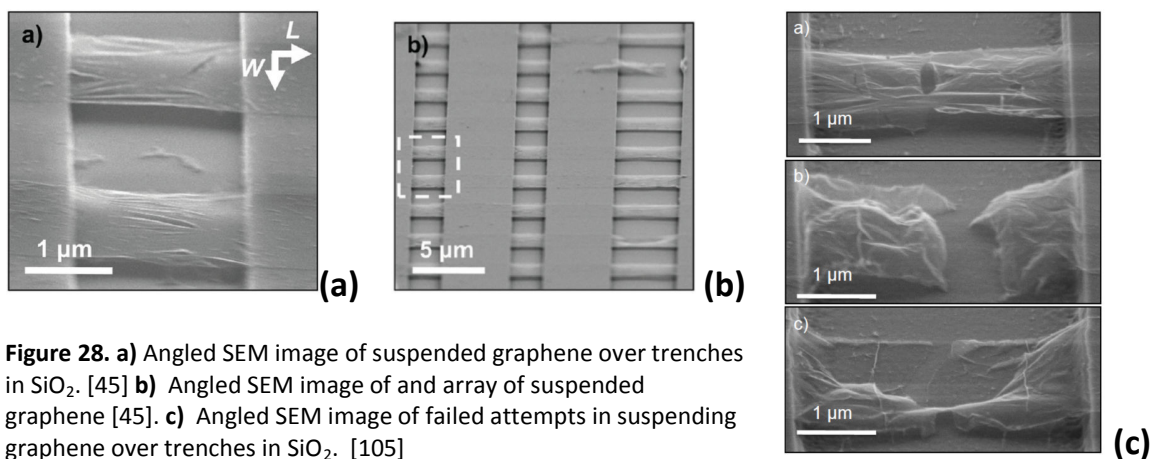
Figure 28. a) Angled SEM image of suspended graphene over trenches in SiO_2. [45] **b)** Angled SEM image of and array of suspended graphene [45]. **c)** Angled SEM image of failed attempts in suspending graphene over trenches in SiO_2. [105]

28

When metal electrodes are used as the etch mask during oxide etching, it is not possible to define a trench in a desired geometry; i.e. the acid will etch the entire wafer surface except under the electrodes. To circumvent this and avoid CPD in the first place, Traversi et al. proposed a sandwich structure of graphene in PMMA as in Figure 29a. A PMMA resist was spincoated on a Si wafer with an oxide layer of 300 nm onto which graphene was exfoliated from HOPG. Flakes in appropriate shapes were spotted by optical microscope. A second layer of PMMA was spincoated over the graphene layer and exposed by ebeam on selected areas into rectangles and developed. Thus, graphene was released in-between PMMA layers. [106]

We mentioned now several times that photo or ebeam resists contaminate graphene. Bao et al., 2010 proposed a resist-free process where they adopted an evaporation technique through Si hard shadow masks as in Figure 29b to realize metallic electrodes. They etched structures in the form of electrodes in Si wafers which was then aligned onto exfoliated graphene flakes for metal deposition. The electrodes served as an etch mask during HF etching and critical point drying. [107]
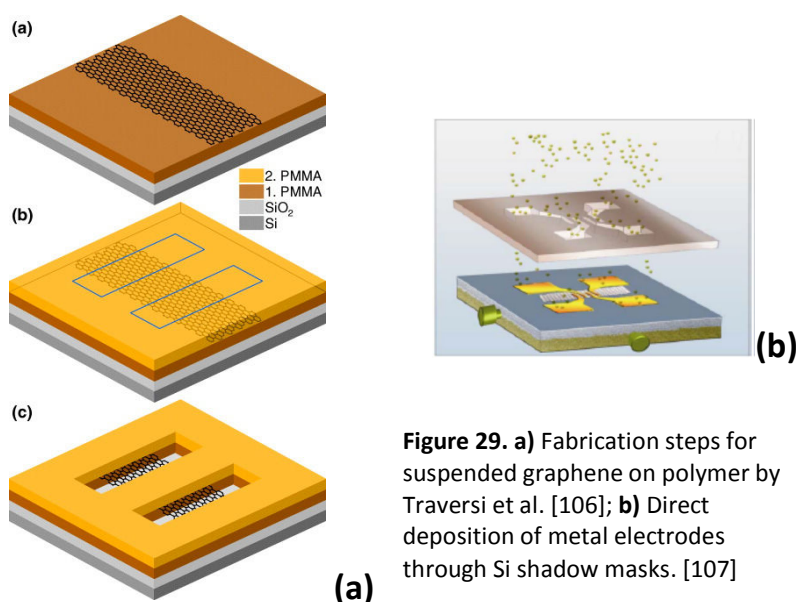
Figure 29. a) Fabrication steps for suspended graphene on polymer by Traversi et al. [106]; **b)** Direct deposition of metal electrodes through Si shadow masks. [107]

Depending on the application, it was shown to be possible to suspend graphene in a transfer-free method. Aleman et al. employ Cu CVD graphene to suspend graphene already at the stage when it is still on the CVD metal. As the nature of CVD process, graphene is grown on both sides of the metal catalyst. The graphene on one side of the metal is usually etched away by oxygen plasma. The authors modified the part of the transfer where the entire metal catalyst is exposed to an etchant and removed. Instead, they placed a photomask onto the etched side of Cu to etch Cu only partially in aqueous $FeCl_3$ into the desired membrane shape. At this step, it was critical to expose the structure to etchant for the correct amount of time to prevent overetching. This was followed by rinsing in water and stripping the resist in acetone giving the structure in Figure 30. [108]
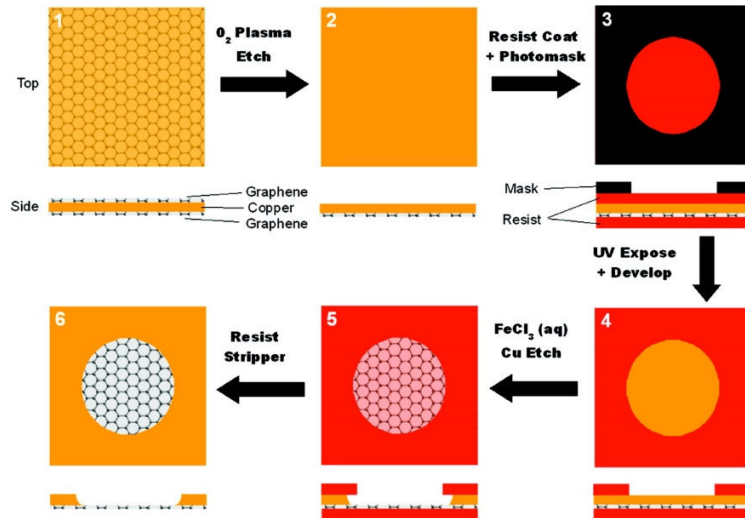
Figure 30. Fabrication mechanism for suspended graphene membrane on Cu. [108]

Another transfer-free technique was proposed by Bharadwaj et al. They deposited Cu on the desired substrate. Since good quality CVD graphene is grown close to the melting temperatures of Cu, the thin film needs to be sufficiently thick, i.e. 400 - 500 nm. To that end, the authors chose electro-deposition of Cu over physical vapor deposition techniques. Growth parameters and heat treatment of the Cu films needed to be optimized. The authors illustrated the subsequent suspending procedure as in Figure 31. CVD graphene was patterned by lithography and mild oxygen plasma. The underlying Cu layer was later etched chemically without stripping the photoresist which was used earlier during oxygen plasma. Graphene pattern was thereon released with the photoresist which supported graphene and prevented stiction - related damage. Finally, graphene pattern was suspended via critical point dryer after resist removal. [109]
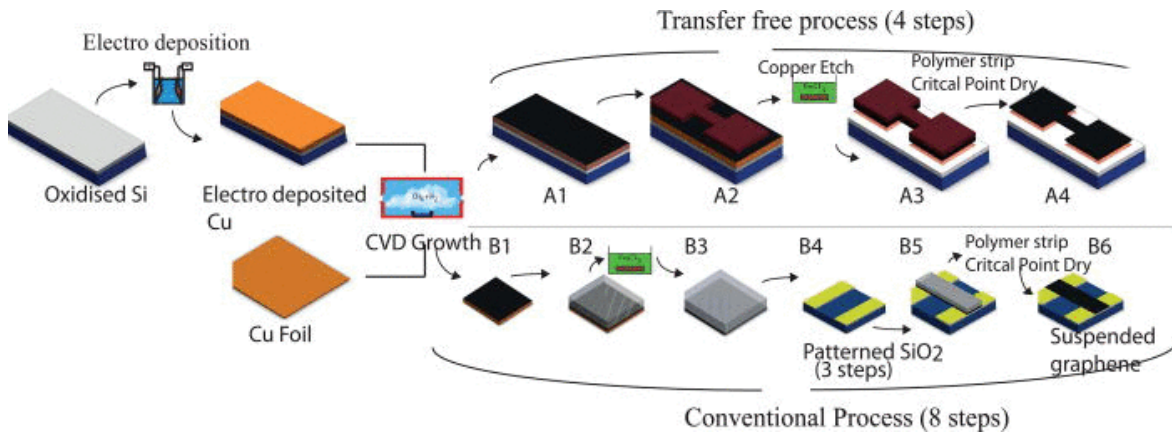
Figure 31. Transfer free process proposed by Bharadwaj et al. and its comparison to conventional process. A1: CVD grown graphene, A2: lithography, A3: suspended polymer and graphene composite, A4: suspended graphene with contacts; B1: graphene on Cu, B2: polymer on graphene/Cu, B3: polymer on graphene, B4: patterned SiO$_2$, B5: polymer and graphene suspended on patterned SiO$_2$, B6: suspended graphene. [109]

We summarized the techniques we reviewed in Table 1. It is intended to give a general idea about how the fabrication evolved over the years.

30

Year	Study	Graphene source	Fabrication
2007	Bunch et al. [48]	exfoliation	Graphene was exfoliated over prepatterned trenches in SiO$_2$.
2007	Frank et al. [93]	exfoliation	Graphene was exfoliated from Kish graphite over trenches in SiO$_2$ by using a probe as a "pencil".
2008	Garcia-Sanchez et al. [91]	exfoliation	Graphene was exfoliated over prepatterned trenches in SiO$_2$.
2009	Bolotin et al. [18]	exfoliation	Rectangular shaped flakes of exfoliated graphene were located. Metal electrodes served as etch mask during HF dipping + CPD.
2009	Shivaraman et al. [103]	SiC	Graphene ribbons were patterned on SiC. SiC was partially etched in electrolyte KOH (1%) under UV source.
2010	Xu et al. [92]	exfoliation	Graphene was exfoliated over prepatterned trenches in SiO$_2$.
2010	van der Zande et al. [45]	CVD	1. Ribbons were patterned while graphene was still on Cu. They were transferred onto Si wafer with predefined trenches. 2. CVD graphene was transferred unpatterned onto a silicon nitride membrane with square holes. The technique was "liquid-free".
2010	Traversi et al. [106]	exfoliation	Graphene was suspended in a PMMA sandwich structure on Si wafer.
2010	Bao et al. [107]	exfoliation	Metal electrodes/etch masks were deposited via shadow masks. The sample was suspended by HF etching + CPD. The fabrication was "resist-free".
2010	Aleman et al. [108]	CVD	Ribbon was patterned and suspended on Cu by etching Cu. The technique was "transfer-free".
2011	Tombros et al. [101]	exfolation	After exfoliation onto LOR/SiO$_2$/Si, graphene was suspended over pillars in LOR. Metal electrodes were realized on the pillars.
2012	Morin et al. [96]	exfoliation	Graphene was exfoliated onto trenches and patterned into suspended ribbons via FIB.
2013	Zhang et al. [98]	CVD	Trenches were realized in Si via DRIE. Graphene was transferred onto trenches and patterned into suspended ribbons via FIB.
2013	Smith et al. [94]	CVD	Graphene was transferred over existing trenches followed by patterning in oxygen plasma.
2013	Dorgan et al. [99]	exfoliation, CVD	Graphene was exfoliated/transferred onto Si wafer followed by patterning. Metal electrodes were realized which serve as etch mask during HF dipping + CPD.
2013	Neuman et al. [102]	exfoliation	After exfoliation onto PMMA/SiO$_2$/Si, graphene was suspended over cross-linked regions of PMMA. Metal electrodes were added as clamps.
2014	Bharadwaj et al. [109]	CVD	Ribbon was patterned on Cu/Wafer by lithography. The resist was not removed. Graphene ribbon/Resist stack was released by etching Cu layer. The technique was "transfer-free".

Table 1. Evolution of the state of art of fabrication techniques for devices with free-standing graphene.

2.5. Driving lines for our process

This review of the fabrication methods of suspended graphene is not exhaustive; yet we can observe how highly varying and creative techniques have been developed so far. When we started this study (in 2010), some of the works presented in this review of the fabrication methods had not yet been published. Moreover, studies on suspended graphene generally focus on presenting or exploiting a particular characteristic; however they hardly investigate the failure mechanisms of fabrication or disclose yield. Thus, we had to develop our own process.

Our objective is to develop a high yield and scalable fabrication route. With this in mind, we followed the following driving rules:

- We categorized the fabrication techniques of state of art in two; transfer over existing trenches and post-patterning substrate etch. Even if it provided the possibility to study certain physical phenomena, the former technique does not allow post-processing. Therefore, we believe that the latter technique is more suitable to industry-oriented device fabrication. Thus, we focus our efforts into the latter.

- We aim to keep the fabrication as simple as possible. In other words, we choose a minimal number of steps for the route and stay within the simplest context of suspended graphene fabrication. For example, we only use standard photoresists and wafers.

- We also attempt to keep the number of times graphene comes into contact with a resist minimal. And when it does, we make sure that there is no additional foreign contaminant other than polymers.

- We focus our experiments on the type of graphene devices which are scalable and compatible with existing Si technologies according to the state of art. Therefore we limit our fabrication to substrate etching techniques where CVD is the source of graphene.

Next section will present the issues encountered during this development. We studied the failure mechanisms and investigated their reasons. And we achieved a process able to provide suspended beams with high yield.

2.6. Proposed synthesis and fabrication techniques

2.6.1. CVD synthesis

We obtain CVD graphene through our collaboration with the group of Prof. Duesberg in CRANN, Trinity College, Dublin. Graphene was synthesized on Cu with a LP-CVD process. Cu was firstly electrochemically polished in phosphoric acid until the surface reached a roughness below 10 nm. Cu foils were heated at 1000°C under a hydrogen flow of 10 sccm for 15 min in a quartz tube furnace followed by a methane flow of 20 sccm at a pressure of 310 mTorr for 20 min. The sample was cooled under hydrogen flow via compressed air. [79] [110]

Raman measurements were employed in CRANN to verify the highly monolayer graphene where certain isolated patches showed formation of double and triple layers. This was explained by the minimal yet present segregation taking place on Cu. Prolonged methane flow lead to additional formation of PyC. [79]

2.6.2. Transfer onto SiO_2/Si

As we explained earlier, polymer assisted transfer is a routine mechanism for processing CVD graphene for electronic applications. The most common choice of polymer is PMMA. Our collaborators from CRANN, Trinity College addressed the contamination issues related to PMMA assisted transfer and responded by employing a modified version of this technique.
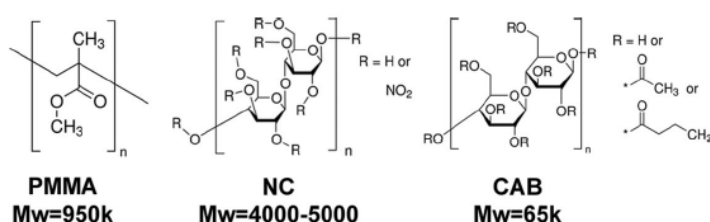
Figure 32. Chemical structure and molecular weights of the polymers employed for transfer. [110]

Conventionally, the stack of PMMA/graphene/Cu catalyst is exposed to $FeCl_3$ or APS solution to remove the Cu layer. The $FeCl_3$ is known to leave residual metal ions which can be electrically interfering while the APS crosslinks PMMA and makes it even more difficult to remove. [111] [112]. One suggested route to eliminate PMMA residues was vacuum annealing of the transferred structure [113] or chemically removing the residues in Choloroform [114]. Alternatively, even more aggressive methods have been adopted such as plasma [115] or annealing in oxygen [116]. Our collaborators, on the other hand, proposed to fully desert PMMA and use cellulose instead for the reasons we will explain. [110]

We had mentioned the difference of the thermal expansion coefficients of Cu and graphene leading to a residual stress in the graphene layer that this stress is relaxed to some extent via wrinkles. Depending on the plasticity of the transfer polymer, stress relaxes into further rearrangement of graphene.

Cellulose nitrate (NC) is a short chain, rigid polymer with bulky groups and ample hydrogen bonding. (Figure 32) It can be smoothly dissolved in acetone and alcohols. Cellulose acetate butyrate (CAB) is a long chain polymer with acetate side chains. Compared to NC, CAB can be polymerized more controllably into longer chains. Hence, it is less rigid than NC.
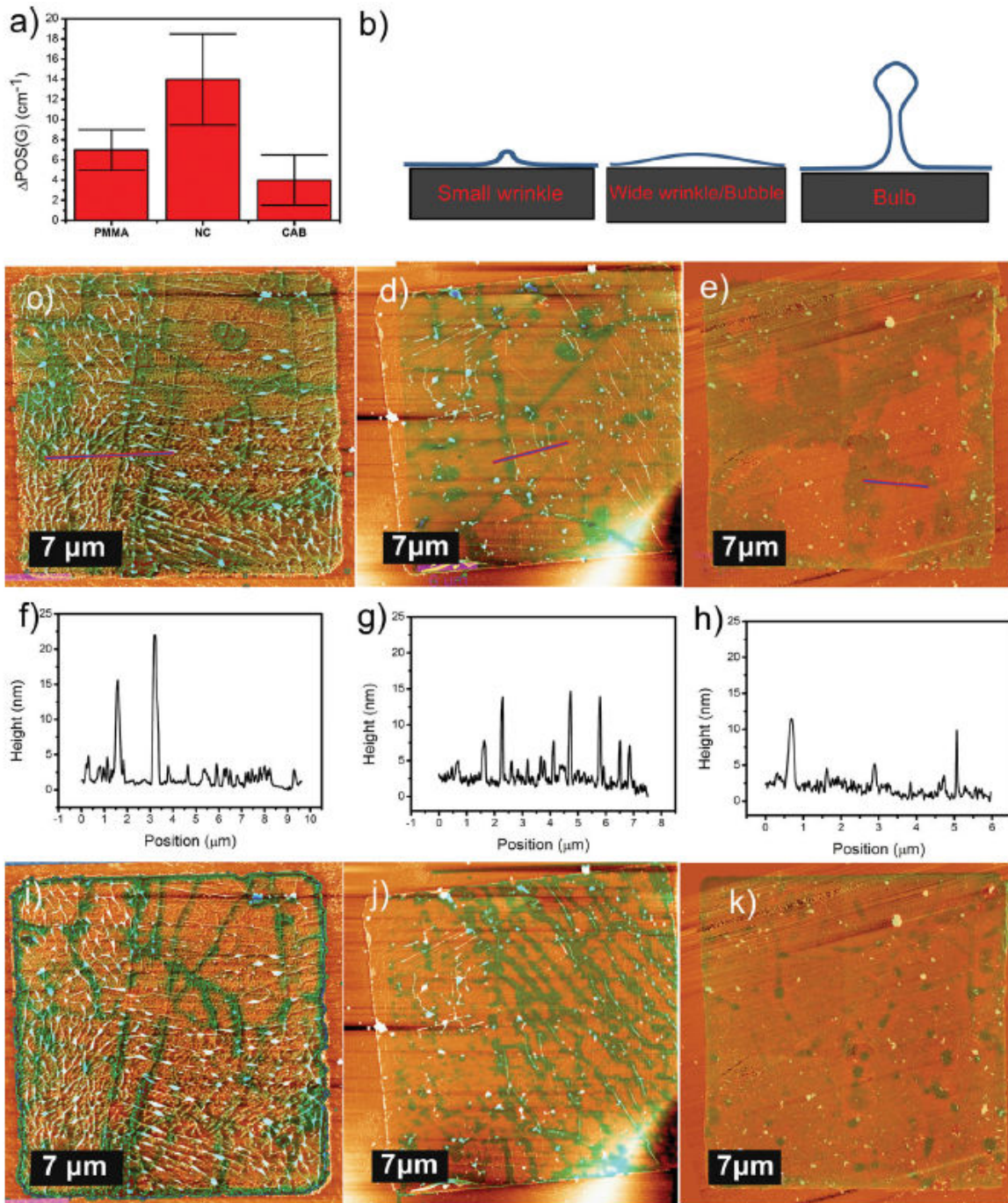
Figure 33. a) Average Raman G band frequency shifts for graphene transferred by PMMA, NC and CAB; **b)** Schematic illustrations of different types of possible folds present; **c-e)** AFM images of graphene transferred by PMMA, NC and CAB with Raman G band frequency shift overlaps; **f-h)** Height profiles of the corresponding AFM images at purple lines; **j-k)** AFM images of graphene transferred by PMMA, NC and CAB with the overlay of Raman intensity ratios of D and G band, I_D/I_G. [110]

The team of Prof. Duesberg compared the two cellulose polymers with PMMA as a candidate for assisting graphene transfer. PMMA, NC and CAB were spincoated as 100 nm films and

rigidized further with thermal tape. Cu was etched in 1M APS for 60 min. The structure was rinsed in DI water for 20 min followed by floating onto the desired destination. The stack was dried in vacuum at 80°C in 0.1 bar. The polymer was stripped in acetone after 8h. Transferred graphene was investigated under AFM and Raman in terms of the differences of stress relaxation through the different transfer polymers. After eliminating the effects from doping, Raman spectra as well as the presence of folds and bubbles revealed the differences between the polymers in terms of stress release. As the most rigid polymer, NC releases less stress in comparison, i.e. there are fewer folds seen in the graphene transferred (Figure 33) In addition, XPS measurements are done on samples to extract the relative amount of sp^2 hybridization which can be directly related to the amount of ratio of residues/graphene. With this, it was possible to conclude that NC and CAB leave much less residues than PMMA does. Thus, for planar applications with little polymeric residue, NC is the right choice for transfer polymer. [110]

2.6.3. Device fabrication

2.6.3.1. Issues with the existing fabrication techniques

The most intuitive method towards a free-standing graphene ribbon is comprised of two steps: i) patterning the graphene into a ribbon and ii) etching the underlying SiO_2 layer in liquid HF. Even though this type of fabrication is quite common in MEMS technologies, it does not follow as smoothly as it sounds in theory. Graphene has indeed a reputation of mechanical stability; however, there are several issues which reduce the yield through tearing and/or collapsing of graphene beams.

The most commonly discussed factor is the capillary forces during air drying. The layer underneath the graphene beam is etched in buffered HF followed by rinsing in water. If the sample is then dried in air or via compressed air/nitrogen strong capillary forces of water pull graphene towards trench walls. Subsequently, the graphene beam sticks to trench walls and tears and/or collapses. This problem is commonly known in MEMS. In fact, this was the driving force towards using critical point driers in MEMS fabrication.

The sole attention to capillary forces will not be sufficient to successfully suspend beams. That is to say, even if one replaces air-drying with CPD, free-standing ribbons are not guaranteed. Our studies show that there is a key player in the fabrication of suspended beams: the interface. During the oxide etch, HF can quickly penetrate into the interface between the etch mask and graphene. This penetration prevents a successfully definition of a step at the wall of the desired trench and therefore results in beam collapse (Figure 34c and Figure 36a) It might go as far as peeling off of the metal contacts. (Figure 34a-b) Any contaminant or residue will act like a bump under the etch-mask facilitating the HF penetration. Therefore, it is crucial to have a clean interface, i.e. a pristine graphene surface.

(a)

(b)

(c)
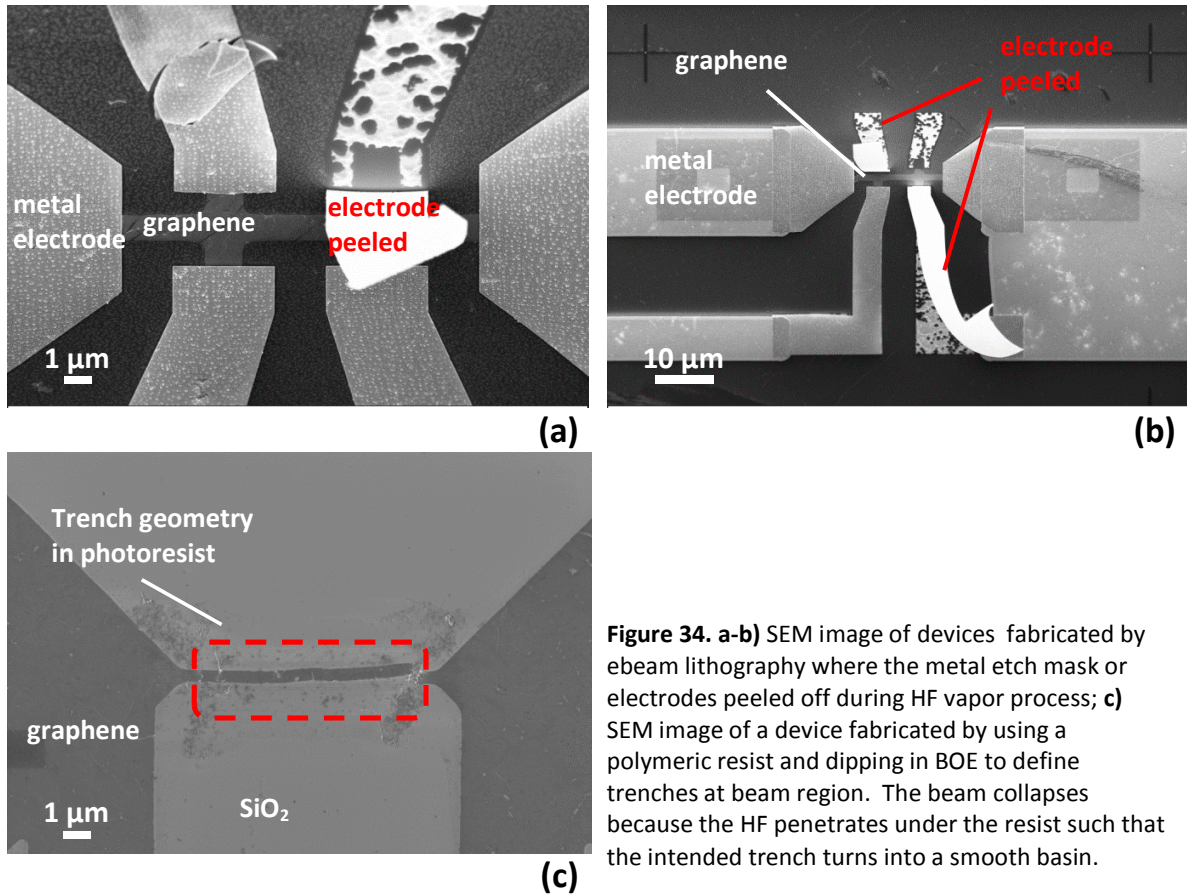
Figure 34. a-b) SEM image of devices fabricated by ebeam lithography where the metal etch mask or electrodes peeled off during HF vapor process; **c)** SEM image of a device fabricated by using a polymeric resist and dipping in BOE to define trenches at beam region. The beam collapses because the HF penetrates under the resist such that the intended trench turns into a smooth basin.

Every time graphene comes into contact with a polymeric resist, it is contaminated. Conventional cleaning methods in MEMS fabrication such as ultrasound or oxygen plasma are too aggressive and can remove graphene as well. Furthermore, the common plasma etching step to pattern graphene can significantly harden the photoresist making it even more difficult to fully remove as observed in Figure 35.
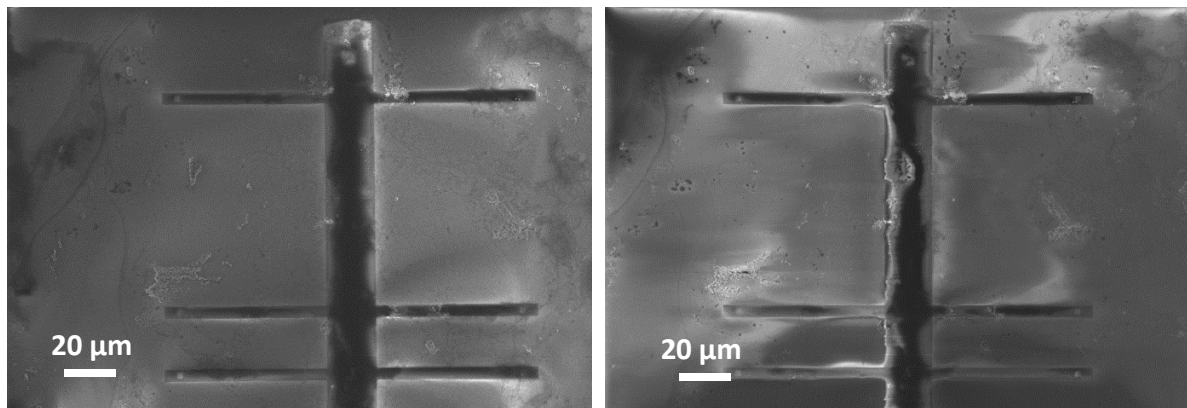
Figure 35. SEM images of graphene patterned by lithography and oxygen plasma. Plasma hardened the polymeric resist and made it impossible to remove by simple immersion in acetone. The plasma-hardened polymeric residues are charging and lead to unclear images.

36

As much as the steps involving polymer coating, imaging needs caution as well. SEM imaging of a device before the final step can result in beam collapse at the final step because it, in fact, interferes with the interface, i.e. graphene surface. For instance, during imaging a device after graphene patterning step, the electron beam can further crosslink the polymeric residues on the graphene and/or lead to carbon deposition. Carbon deposition is a common problem of electron microscopy. While it can be ignored for most applications, here, it can have destroying effects at final fabrication step. In general, we suggest avoiding altogether imaging in-between fabrication steps.
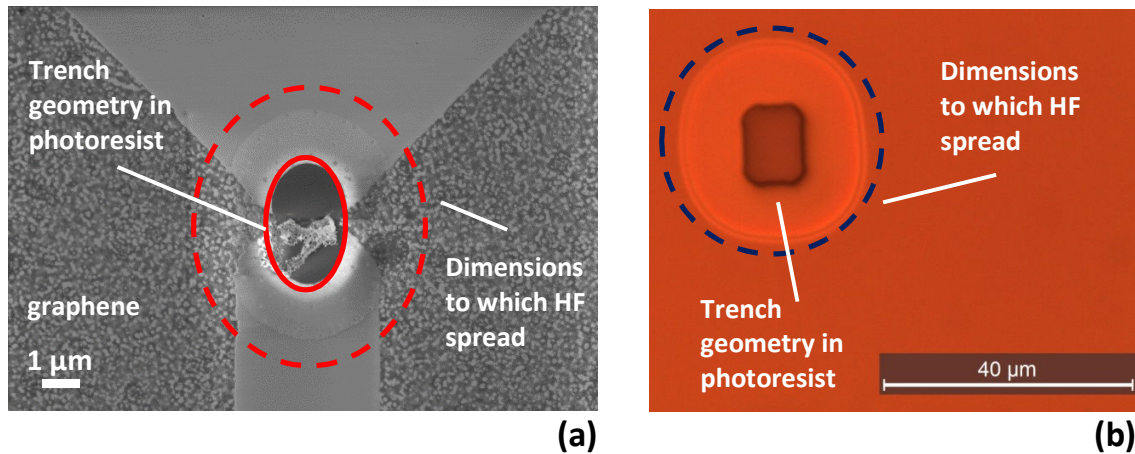
Figure 36. a) SEM image of a device fabricated by using a polymeric resist and dipping in BOE followed by CPD to define trenches at beam region. This device is fabricated in Stanford University with our photomasks during a short collaboration. At the time, a successful route was not achieved. The beam collapses because the HF penetrates under the resist such that the trench is not defined. **b)** Optical image of a test sample where the resist AZ1512 is spun onto an oxidized Si wafer and dipped in BOE for 6 min corresponding to an etch depth of 500 nm. The HF penetrated through the resist/oxide interface.

We now consider a perfectly clean graphene surface with no wrinkles, bubbles or residues to interfere with the resist interface. That is to say, there is no additional bump under the carpet accelerating HF penetration. And we demonstrate how difficult it is to prevent HF penetration even under such circumstances. For starter, there are different types of liquid HF available such as the HF 49% (aq), HF diluted to various degrees and buffered HF. Buffered HF (BHF or BOE) is developed to have control over the oxide etching rate. Another reason for its popularity is its conservation of the photoresist. The mechanism for regular HF etching is predicted as the following:

$$SiO_2 + 4HF \rightarrow SiF_{4(g)} + 2H_2O \text{ or } SiO_2 + 6HF \rightarrow H_2SiF_6 + 2H_2O$$
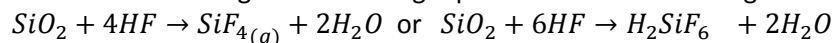
while the reactions that take place during buffered oxide etch are the following:

$$SiO_2 + 4HF \rightarrow SiF_4 + 2H_2O \text{ and } NH_4F \leftrightarrow NH_3 + HF.$$
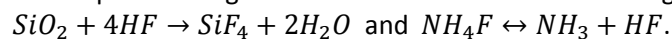
The buffering agent, ammonium fluoride (NH_4F), maintains the HF concentration, controls the pH and aids in keeping the reaction rate constant. Additionally, it minimizes the attack of HF on the photoresist. Figure 36b is an optical image of a test sample where a photoresist is spun and developed to have trenches on a Si wafer with 5μm oxide layer. The sample was dipped in BOE for 6min which corresponds roughly to an oxide etch of 500 nm. As clearly seen in the image, the etching was not confined to the developed area. Even though the surface of the test sample was perfectly clean (the wafers had no processing done on them) BOE penetrated into the resist/substrate interface after 5 min. Therefore, we believe that it is more suitable to use different types of etch mask instead of polymeric resist.

We conclude that suspending graphene needs more care than simply avoiding capillary effects. We propose a fabrication route in the light of solving all the issues we have mentioned, i.e. paying attention to the mask interface.
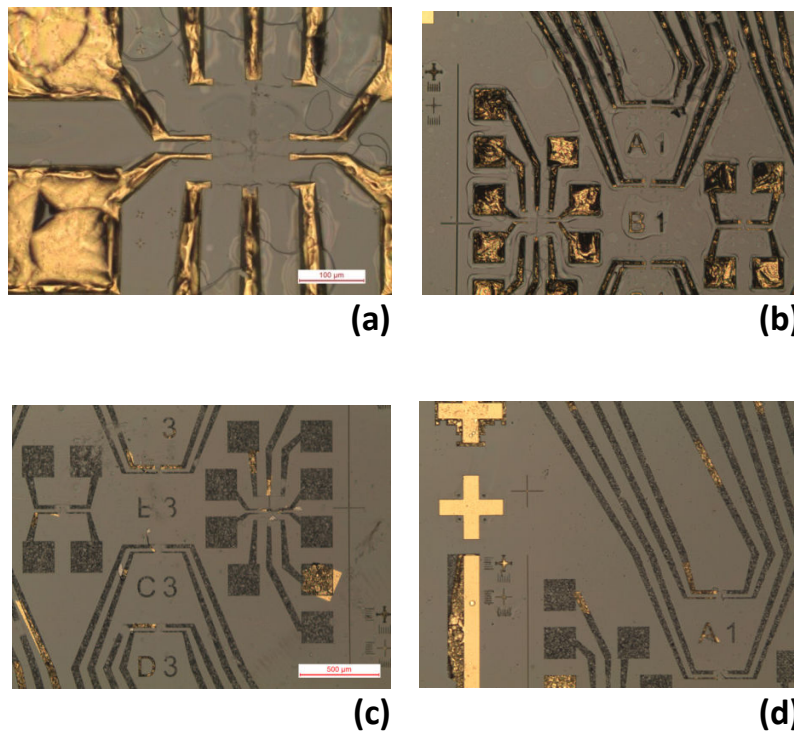
Figure 37. a-b) Optical images of samples which are exposed to the HF vapor equipment with a patterned polymeric resist to etch rectangular trenches under graphene beam. The cycles of ethanol and HF vapor removed the polymeric resist and peeled off the metal electrodes which were deposited after graphene transfer and therefore did not have a tight interface to the wafer surface. **c-d)** The same samples are cleaned in acetone which removed the electrodes entirely. However, the alignment marks stayed. The alignment marks we realized on pristine wafers as a first fabrication step and therefore have a clean interface to the wafer. This underlines once more the importance of interface and adhesion in HF processes.

2.6.3.2. Key process steps developed

All fabrication is done in the clean room facilities of Plateforme Technologique Amont (PTA), Grenoble. At the time of our study, there was no ready recipe for device fabrication from graphene in the facility.

In this section, we firstly discuss each step which we modified and improved. We follow by proposing an exact recipe towards a successful suspending of graphene devices.

Figure 39 illustrates the entire set of fabrication steps.

At the step of transfer

We have explained in Section 2.6.2 how we choose cellulose nitrate over the conventional PMMA to lessen the polymeric residues from transfer. We have also mentioned in Section 2.6.3.1 how graphene is contaminated every time it comes into contact with a polymer. We employ an additional acetic acid cleaning after every immersion step in acetone. This cleaning technique has been initially proposed by Her et al. [117]

At the step of graphene patterning

The energetic ions penetrate into the resist and introduce cross-linking effects into the polymer similar to post-bake via energy transfer. In fact, along with post-baking on a hot plate for a few minutes, a light oxygen plasma is exploited to intentionally strengthen the photoresist for deep reactive ion etching applications and to prevent its easy removal. For the case of optical lithography processes, photoresists are usually sufficiently thick to overcome the hardening issue. We observe that a resist with a thickness over 1μm is sufficient to solve this problem. The ions cannot penetrate all the way into the resist; they are stopped closer to the surface. Thus, acetone can attack the bottom of the resist and remove it. If finer structures are desired, however, it is not possible to use such thick resists in ebeam lithography. Depending on the sought resolution, resist thickness might be required to be reduced down to as little as tens of nanometers. Thus, the resist will easily be hardened in the entire volume. At this point, the first reaction is to forgo the ease of polymeric resists entirely and switch to hard masks. Metal deposition, aluminum in particular, and lift-off are typically adopted as ebeam hard mask. After the plasma treatment the metal mask can be removed via acids. We do not prefer this option since we do not want graphene to come into contact with an additional foreign material considering that it would be nearly impossible to clean it 100%. Residues of metal atoms on graphene could potentially interfere with the electronic properties of graphene. Thus, we move on to a Silicon based ebeam resist: hydrogen silsesquioxane (HSQ). The monomer is a cubic molecule where one Si atom sits in each corner and oxygen atoms link the corners to each other. (Figure 38) This negative ebeam resist is commonly used for high resolution requirements. At the same time, it can be a hard mask for plasma etching. The resist is removed via HF which is not convenient for two reasons: i) HF is a dangerous substance whose manipulation is best minimized when possible, ii) HF would not only remove the HSQ resist, it would also etch the underlying oxide partially or fully which might even lead partial peeling of the some structures on the oxide layer. Bearing all of these in mind, we propose a double layer approach: HSQ + polymeric resist for ebeam lithography. While HSQ layer prevents resist hardening, the polymeric aids easy resist removal in solvents.
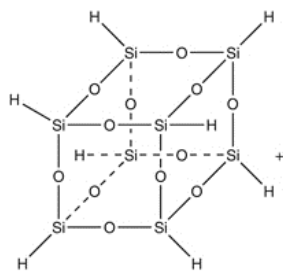
Figure 38. Chemical structure of HSQ. [118]

Here, we find it worth to discuss the step of resist removal in solvent. We emphasize the importance of a slow dissolution. It is known that there is a strong adhesion between graphene and photoresists. At any aggressive attack, the resist can be removed while it still attached to graphene, i.e. taking graphene partially or fully with it. We observe that slow and patient removals result in better yield. Instead of dissolving the resist via hot acetone and/or ultra-sound assistance we prefer to immerse the samples in cold acetone overnight.

Graphene is grown on both sides of Cu foils via CVD processes.

Graphene on the bottom side of the cu foil is etched in oxygen plasma. Cellulose nitrate is spun on graphene on Cu for transfer.

Cu foiled is etched chemically. Cellulose nitrate and graphene are let to float in water for transfer onto Si wafer. Metal contacts are realized by lithography and lift-off on the oxidized Si wafer prior to transfer.

Graphene with polymer is fished out of the water onto the wafer. The structure is heated to evaporate water and ensure graphene adhesion on the wafer.

Polymer is removed in acetone. The resist is spincoated onto graphene depending on the desired beam dimensions. AZ1512 for optical lithography and PMMA/HSQ for ebeam lithography are patterned followed by oxygen plasma etching.

Sample is removed in acetone for 24 h followed by rinsing in isopropanol and immersion in glacial acetic acid for 24 h.

Additional metal layer is patterned by lithography and lift-off to clamp the beam and to serve as etch mask during HF exposure.

The sample is put in the equipment of HF vapor. SiO_2 is etched everywhere except for the areas under metals. Graphene beam is thereof suspended.

Figure 39. Process flow of the proposed fabrication for suspended graphene devices

Additionally, we should address the choice of the resist type as well. Unless there is a special case, such as HSQ, we believe in avoiding any negative resists altogether. Negative resists tend to crosslink further when they are exposed to the plasma energy. Compared to positive resists, they are by nature more difficult to dissolve after processing.

All of the points we mentioned assist having as clean a graphene as possible. The last factor on this subject is the plasma parameters of a reactive ion etching (RIE) system. Graphene is etched away under oxygen environment exceedingly fast. To have control over the etch rate, one can adjust the parameters such as coil power, RF power, flows of the gas mixture O_2/Ar and the etching time. Even when we secure the conditions for a stabilized and light chemical plasma, the exposed time is critical. 30 seconds short or in excess can fail to remove all the desired graphene area or can harden the photoresist too much. Bearing in mind that the plasma conditions can change in the equipment depending on a variety of practical reasons such as cleaning time, plasma stabilization time, recent repairs etc., it is advisable to re-calibrate the plasma time on each new day of plasma etching.

At the step of HF release

The final stage of fabrication is beam release by etching the underneath SiO_2 layer in HF. We have discussed in the Section 2.6.3.1 the challenges of this step. As we said, we firstly desert polymeric resists altogether. Instead, we define a second metal layer through evaporation and lift-off. This Cr/Au layer serves as etch mask as well as clamps to prevent the beam from sliding. For etching, we choose HF vapor. The HF vapor equipment is well-sealed and therefore can be easily manipulated. The vapor phase eliminates any capillary effects already. The HF in the equipment is not buffered, i.e. would attack the resist. Furthermore, the system works on cycles of HF and ethanol flow. Ethanol assists drying the sample from the water which is a side product of the HF and SiO_2 reaction. By clearing away water, the reaction rate is kept under control. However, ethanol dissolves polymeric resist as well. (Figure 37)

Thus, this type of HF vapor equipment is not suitable to use with polymeric resists. In comparison with the wet etching in BOE followed by CPD, HF vapor is simpler as a one-step process. The thickness and area of Cr/Au clamps needs caution as well. The etching in HF vapor is isotropic. Thus, a portion of the metal layer on the sides equal to the amount of the etch depth will be free-standing. The metal area needs to be designed appropriate to the planned etch depth. Depending on the thickness the metals might buckle or peel out. A thickness of ca. 100 nm is sufficient for strongly free-standing metal structures.

2.6.3.3. Mask design

The designs of our devices are presented in Figure 40. First layer (blue) is intended for alignment marks. Second layer is to realize metal electrodes. Third layer is to pattern graphene. Fourth layer add metal clamps which serve as an etch mask during HF etching.

Large structures designed for transmission line measurements are not intended for free-standing devices. Smaller structures are designed in a way that allows 4 probe measurements on SiO_2, i.e. before suspending. The ribbon in-between the source and drain electrodes of the 4 probe device is intended to free-stand at the end of the fabrication steps.
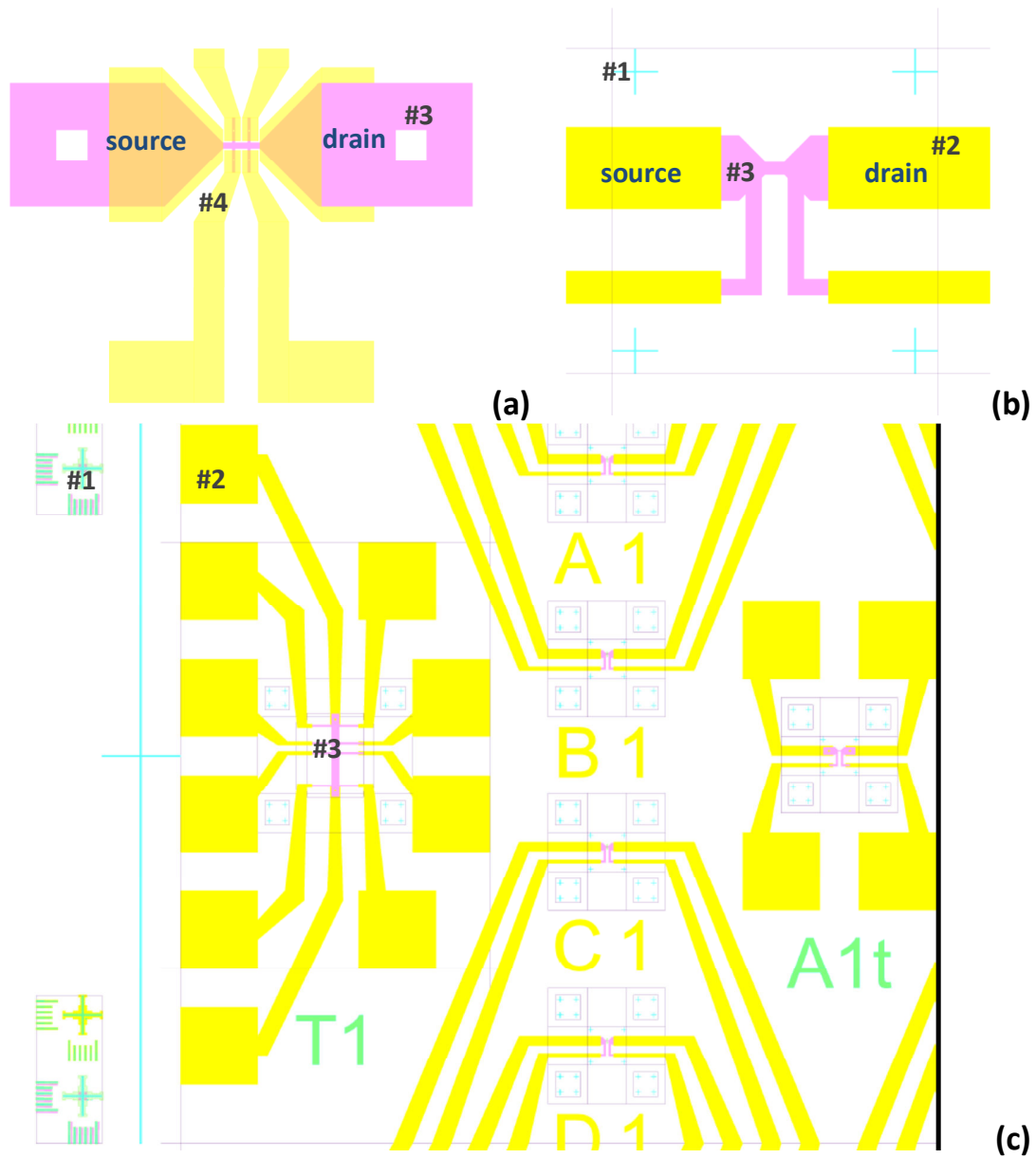
Figure 40. Photomask designs for **a)** ebeam lithography and **b)** optical lithography. **c)** A general look on the device design. Pink is graphene and yellow is metal electrodes. Mask layers are indicated as numbers when applicable. To eliminate contact resistance, we design devices suitable to 4-probe measurements. In addition, we design two large graphene devices per sample which can be used for transmission line measurements (TLM) as well as Hall bar measurements.

2.6.3.4. Final recipe proposed

1. *Alignment marks*

We used two different types of heavily doped Si wafers: i) both sides polished Si wafer ($d = 100 \pm 0.5\ mm; t = 525 \pm 25\ \mu m;\ \sigma = 5 - 10\ \Omega cm$) with a wet thermal oxide of 500 nm, i) both sides polished Si wafer ($d = 100 \pm 0.5\ mm; t = 525 \pm 25\ \mu m;\ \sigma = 5 - 10\ \Omega cm$) with a wet thermal oxide of 5 µm. Alignment marks were realized via ebeam lithography with the resist ZEP 520A for the subsequent optical as well as ebeam lithography steps. ZEP 520A was spin-coated on the wafer with a speed of 4000 rpm for 60 s followed by heating on a hot plate at 180°C for 5 min to evaporate the solvent. These conditions lead to a thickness of ca. 350 nm. The sample was exposed with a beam of 400 µC*cm^2 for 100 kV and developed in a solution of MIBK : IPA [1:1] for 60 s followed by dipping in MIBK : IPA [89:11] for 15 s.

For all the steps involving metal deposition, the metals of choice are gold and chromium. Following the lithography, layers of Cr/Au (10 nm/100 nm) were deposited with rates of 0.2 nm/s and 0.25 nm/s. The vacuum environment in the chamber was $\sim 10^{-8}$ mbar and we kept the pressure in the loadluck at $\sim 10^{-6}$ mbar. Prior to the evaporation, a very short Ar etching was passed on the sample for 10 s at 250 V to ensure well-defined "valleys" and "hills" at the resist. The transferred pattern can have imperfections due to the development which then would result in partial failure of alignment marks. The evaporation was followed by lift-off in sonicated acetone. The wafer was rinsed in isopropanol and dried with compressed air.

Most resist do not adhere well onto an oxidized full size wafer due to the hydrophilic ends of the SiO$_2$ layer. This issue is usually solved by applying hexamethyldisilazane (HMDS) for the case of photolithography. HMDS modifies the SiO$_2$ surface and makes it more hydrophobic. Through that, it improves resist adhesion to wafer surface. For the case of ebeam lithography, it can be solved by using the resist ZEP instead of typical PMMA based materials. ZEP adheres well onto oxide surfaces.

We explained that only a few metals are resistant to HF. This does not only affect the metal choice for the electrodes, but it equally limits the choice for the metals at the alignment marks. Considering that the final stage of the fabrication involves HF, the alignments marks should not peel off. We chose gold for alignment marks as well as electrodes and chromium as adherent layer. And the thickness of the metallic alignment marks was set by the rule of thumb of easy lift-off: evaporated metal thickness needs to be equal to or less than 1/3 of the thickness of the resist.

If graphene devices are integrated at the front end of the line, the drawback of a Cr/Au stack is that it is not compatible with the Si technology. However, changing the metal requires a full study which was beyond the scope of this thesis.

2. *Metal contacts*

Optical lithography was employed at the level of metal contacts. The wafer was spincoated with the commercial photoresist AZ1512 at a rate of 4000 rpm for 60 s leading to a thickness of ca. 1.2 µm. The resist was exposed by the equipment SUSS MicroTech MJB4 under UV for 25 s and developed in the commercial AZ developer for 30 s followed by rinsing well in water. The wafer was dried with compressed air.

Layers of Cr/Au (10 nm/100 nm) were evaporated with rates of 0.2 nm/s and 0.25 nm/s after a 10 s Ar etch at 250 V. The vacuum environment in the chamber was $\sim 10^{-8}$ mbar as the step for alignment marks. But we further lowered the pressure in the loadlock to $\sim 10^{-7}$ mbar. Lift-off was carried out in acetone under ultrasound. The wafer was rinsed in isopropanol and dried with compressed air.

3. *Graphene transfer*

The wafer was cut into pieces of 1x1 cm which correspond to the sizes of graphene sheets produced on Cu by CRANN, Trinity College. Graphene on Cu was transferred onto wafer pieces in CRANN as explained earlier. Cellulose nitrate was removed by immersing the sample in acetone for 24 h followed by rinsing in isopropanol. For additional cleaning, the sample was transferred into glacial acetic acid for 24 h and rinsed in water. The sample was dried by compressed air.

Graphene on the wafer with an oxide layer of 500 nm shows a clear color contrast under optical microscope whereas it is very difficult to differentiate graphene on the wafer with an oxide layer of 5 µm.

4. *Graphene patterning*

We prepared two different sets of samples: i) by optical lithography and ii) ebeam lithography. The width of the beams was varied in the range of 2 – 4 µm for optical lithography and in the range of 200 nm – 1 µm for ebeam lithography. The length of the beams was varied in the range of 6 – 12 µm for optical lithography and in the range of 2 – 4 µm for ebeam lithography.

To fabricate the larger ribbons, we used either the resists AZ1512 or UV5. AZ1512 was spincoated with a rate of 4000 rpm for 60 s resulting in a thickness of 1.2 µm. The resist was exposed by the equipment SUSS MicroTech MJB4 (UV 365, i-line, 8 mW/cm^2) under UV for 25 s and developed in the commercial AZ developer for 30 s followed by rinsing well in water. The sample was dried with compressed air.

UV5 was spun with a rate of 4000 rpm for 60 s leading to a thickness of $\sim$500 nm. Solvents were evaporated by heating at 130°C for 90 s. Sample was exposed under MJB4 Deep UV (240 nm, 4mW/cm^2) for 1.3 s followed by post-exposure bake for 60 s at 130°C. The resist was developed in the commercial AZ326MF for 30 s and well-rinsed in water. The sample was dried with compressed air.

Devices with finer structures were realized by spincoating a layer of the ebeam resist PMMA 4% (by Allresist) at a rate of 2000 rpm for 60 s resulting in a thickness of $\sim$300 nm. The sample was heated at 180°C for 3 min to evaporate the solvent in the resist mixture. After cooling down the sample to room temperature, the ebeam resist HSQ (commercial name: XR1541) was spun on the sample at a rate of 4000 rpm for 60 s leading to a thickness of ca. 130 nm. The sample was heated at 180°C for 3 min. The double layer of ebeam resist was exposed in ebeam and developed in the commercial MF26 for 1min followed by rinsing in water. The sample was dried with compressed air.

44

Patterns were realized by etching graphene under oxygen plasma with an oxygen flow of 20 sccm and an Ar flow of 80 sccm for 75 s. The coil power was kept at 400 W and the RF power is kept at zero. Prior to etching, the chamber was cleaned by oxygen plasma for 10 min followed by applying the graphene etching conditions on a dummy wafer for 10 min for process stabilization. After etching, the sample was immersed in acetone for 24 h to remove the resist, rinsed in isopropanol and put in glacial acetic acid for 24 h.
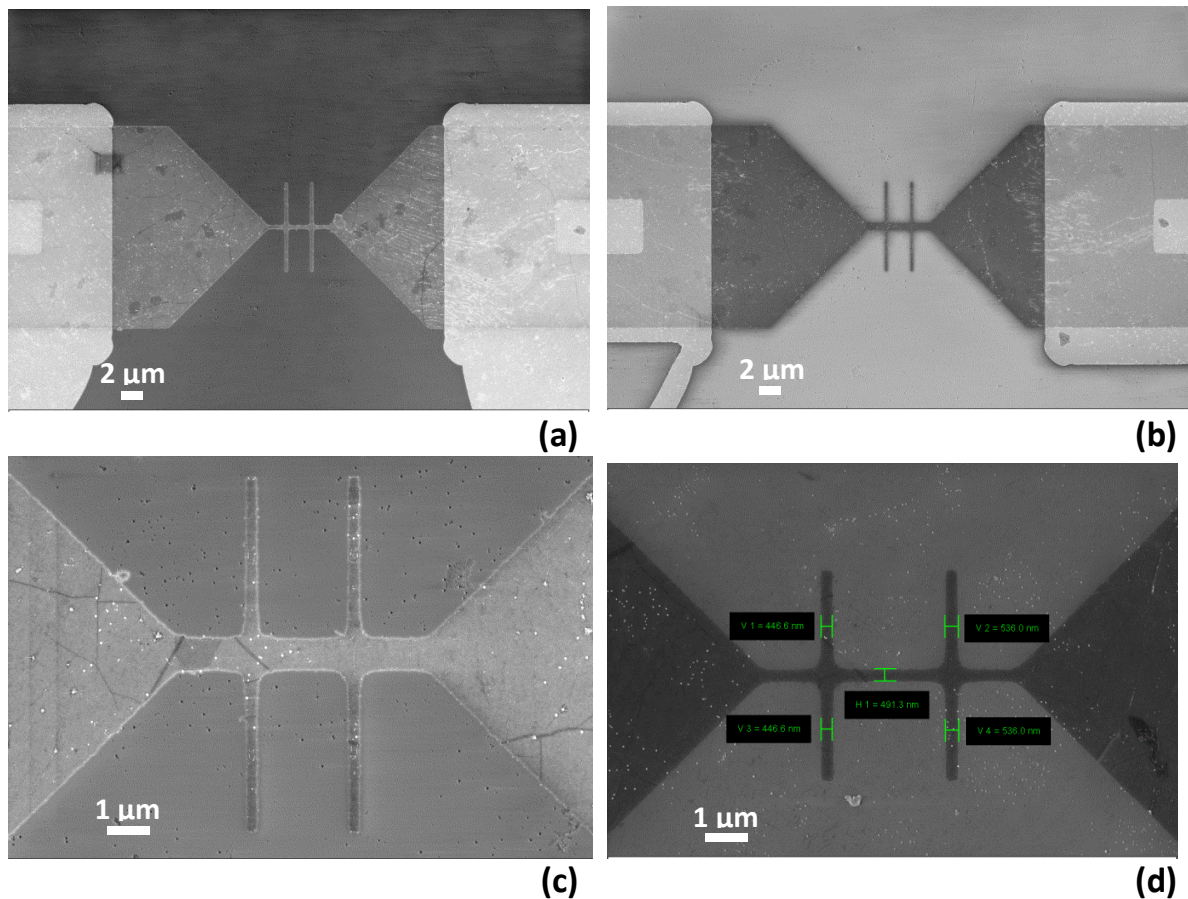
Figure 41. SEM images of devices prepared by ebeam lithography at the stage after graphene patterning.

5. *Metal clamps*

We deposited a second layer of metal to serve as clamps for the beam as well as HF etch mask. As we can see for the samples in Figure 40a, the clamps were very close to each other and therefore cannot afford even small failures of lift-off. After pattering graphene, it was crucial that we do not expose the sample to any aggressive cleaning which even includes sonication in acetone for short time. To ensure that this is not necessary, we aimed to ease the lift-off of this metal layer by using a double layer resist.

We used a double PMMA process to benefit from the uneven resist structure due to the difference in the two molecular weights. PMMA 4% (200K) was spun at a rate of 4000 rpm for 60 s and heated 180°C for 3 min for solvent evaporation. After cooling, PMMA 4% (950K) was spun at a

rate of 4000 rpm for 60 s followed by heating at 180°C for 3 min. The sample was exposed by ebeam lithography and developed in a solution of MIBK:IPA for 45 s and in pure isopropanol for 30 s. The sample was gently dried very with compressed air.

Layers of Cr/Au (10 nm/100 nm or 10 nm/50 nm) were then evaporated with corresponding rates of 0.2 nm/s and 0.25 nm/s. The vacuum environment in the chamber was $\sim 10^{-8}$ mbar and we kept the pressure in the loadlock at $\sim 10^{-7}$ mbar. The evaporation was followed by lift-off in acetone for 24 h. The wafer was rinsed in isopropanol and immersed in glacial acetic acid for 24 h followed by rinse in water. The sample was dried very gently with compressed air.

6. *HF etching*

To etch the oxide layer and release the graphene beam, an HF vapor equipment Primaxx Monarch 3 is employed. An automated recipe is carried out by slow etching in ca. 90 minutes by alternating vapors of HF and ethanol.

2.7. Characterizations

2.7.1. Fabrication yield

We have taken images via SEM and AFM to ensure that our fabrication results in successfully suspended graphene devices. In Figure 42, we present SEM images of all of the 14 devices on one sample. This sample is representative of other samples in the study. All of those images were taken on a tilted sample holder to show clearly if a beam was suspended or collapsed. As we can see, only one of these devices was collapsed. Thus we conclude that this fabrication route has a yield over 90%. We suggested that attention to interface is the key towards successfully free-standing devices through a conventional fabrication. Our results confirm this assumption. The graphene in the sample from Figure 42a-n was patterned by optical lithography. In addition to this, we present more complicated structures with finer dimension in Figure 42o-p which were patterned by ebeam lithography. As observed, even such complicated structures could be suspended by employing this fabrication technique.
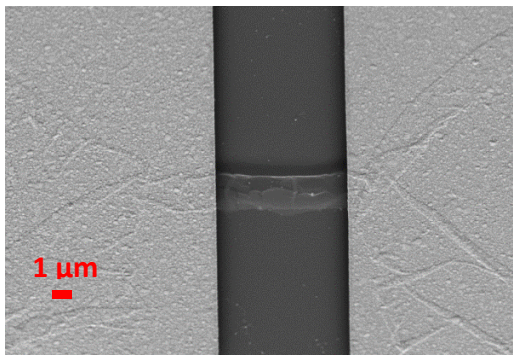
(a)
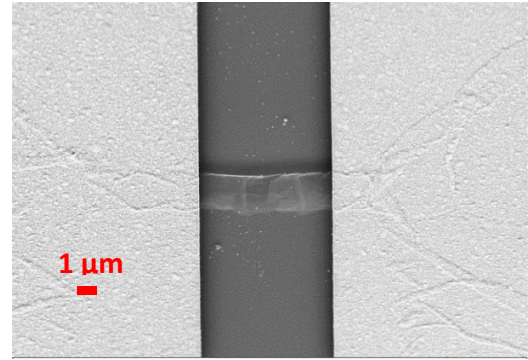
(b)
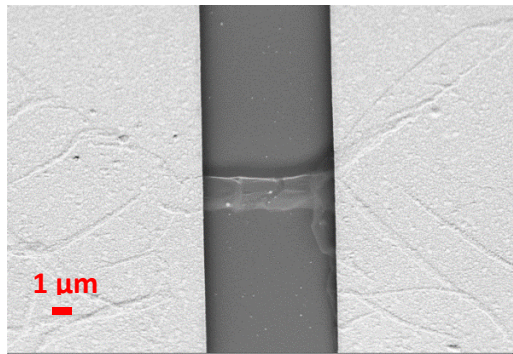
(c)
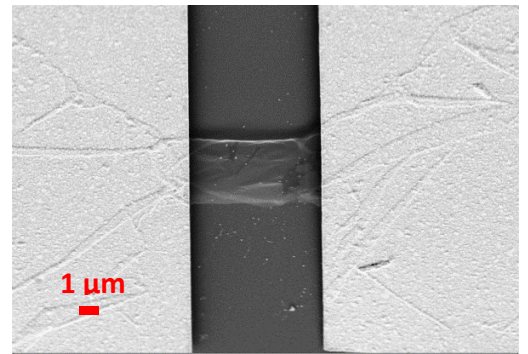
(d)
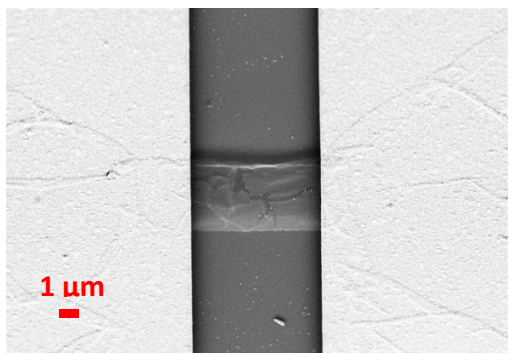
(e)
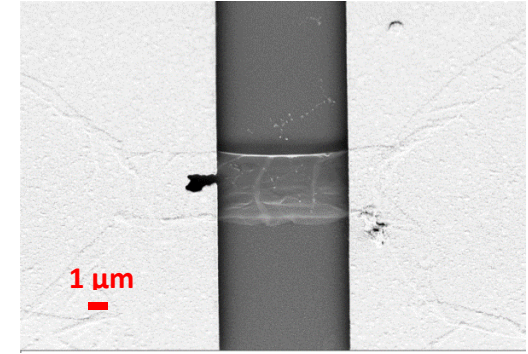
(f)
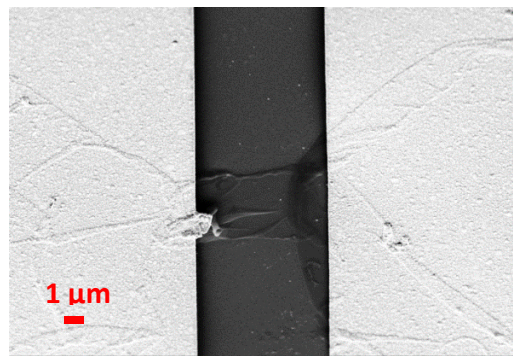
(g)
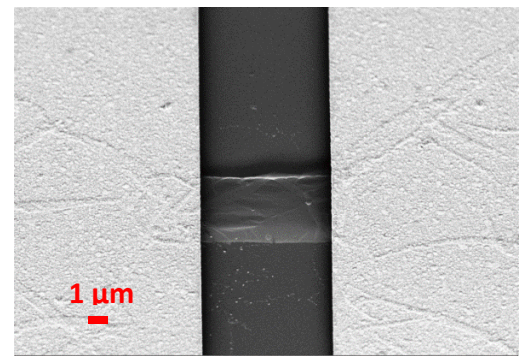
(h)
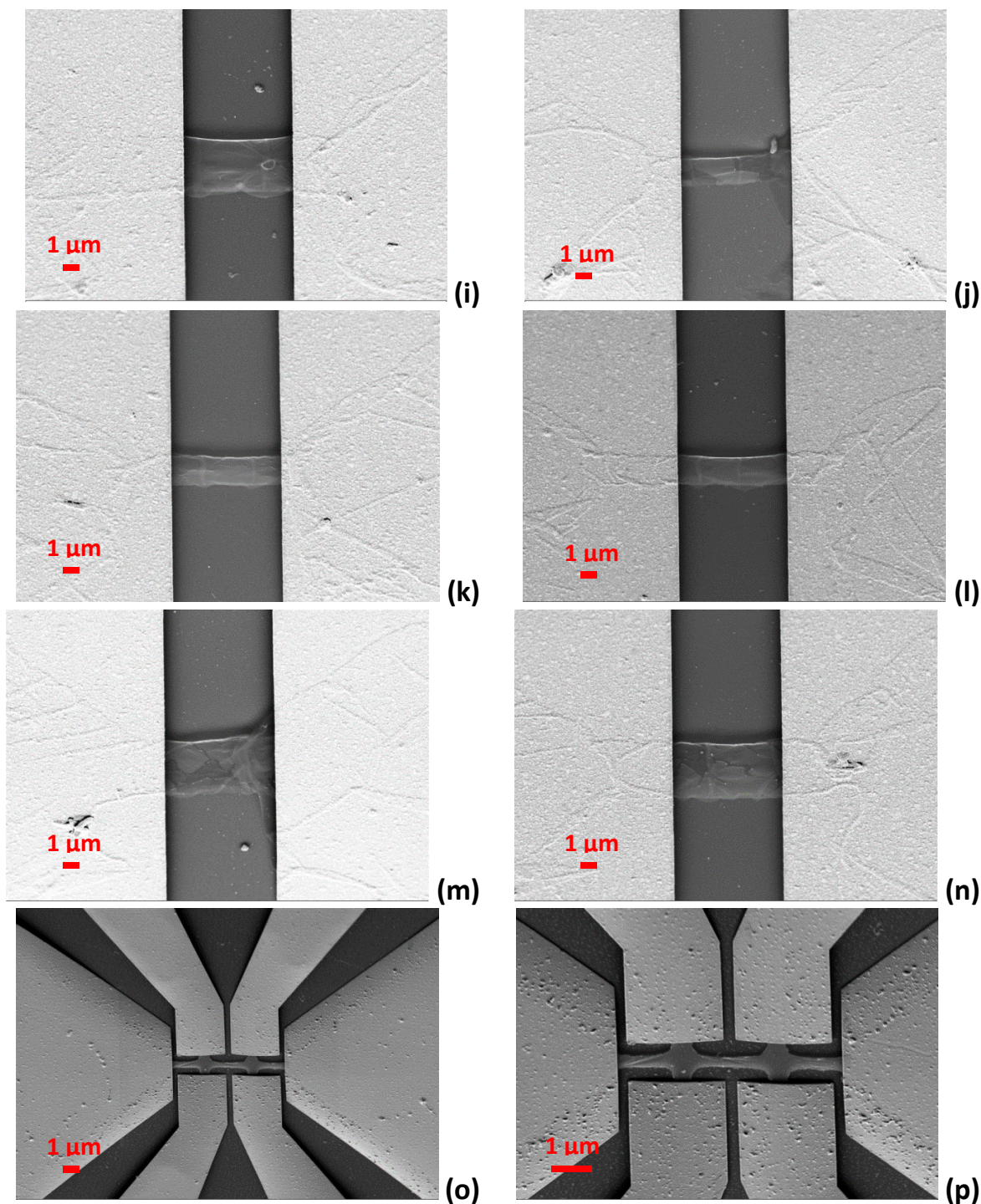
Figure 42. a-n) Tilted SEM images of devices from the same sample to demonstrate the yield of our proposed route. Each 1x1 cm sample is comprised of 14 devices with a graphene beam. As observed, only one graphene beam out of 14 is collapsed. The graphene beams are patterned by optical lithography via the resist UV5. **o-p)** SEM images of suspended devices with more complicated structures. The beams are patterned by ebeam lithography.

To confirm the free-standing structure, we present an AFM image along with a height profile in Figure 43 a and b. The suspended region does not appear clearly due to the fact that the tip interaction at that point is complicated. The blue and red lines indicate where the height profiles are taken from in the AFM image. The difference in the profiles is attributed to the fact that beam is standing higher than the trench bottom. In order to rule out completely the possibility that some residual SiO_2 was still supporting the beam, due to incomplete under-etching, we probed the rigidity of the suspended regions using AFM approach/withdrawal curves. The graphene beam displayed a different behavior from rigid Si surfaces (Figure 43d), with a smaller slope proving that the beam was completely self-supported.
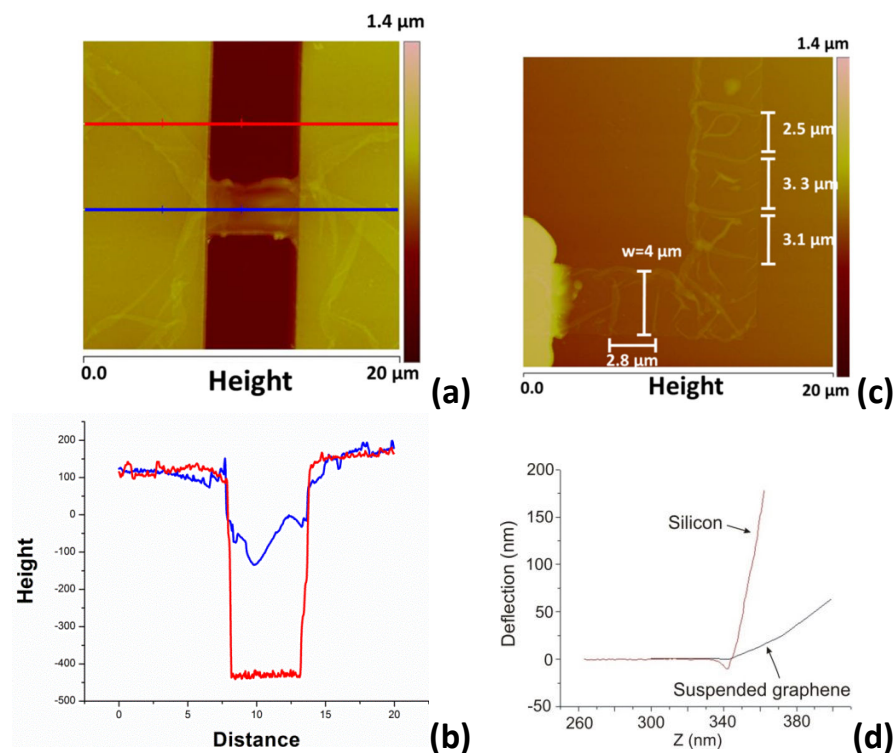
Figure 43. AFM characterization. **a)** Height mapping of a suspended beam, **b)** Cross-sections along the cutlines of 4b, **c)** A supported graphene stripe showing a regular folds pattern, **d)** deflection curves on rigid region (blue) and at the middle of the suspended beam (red) confirming that the graphene beam is fully self-supported.

We investigated the influence of acid treatment by comparing AFM images of two samples, one subjected to acetone cleaning only while the second one is additionally cleaned by acetic acid as well. In Figure 44, we deliberately set the color scale to 50 nm for a better demonstration of the two different sets of height distribution. In Figure 44a, next to the traditional folds of CVD graphene, we observe circular structures most of which are higher than 50 nm (therefore out-of-scale). We interpret them as polymeric residues still present on graphene after a thorough acetone cleaning during transfer process. In contrast to this, there are no such structures present in Figure 44b. Thus, we conclude that the acetic acid treatment is an effective tool to further remove polymeric residue on graphene.

Acetone alone / *Acetone + acetic acid*

(a) **(b)**

(c)
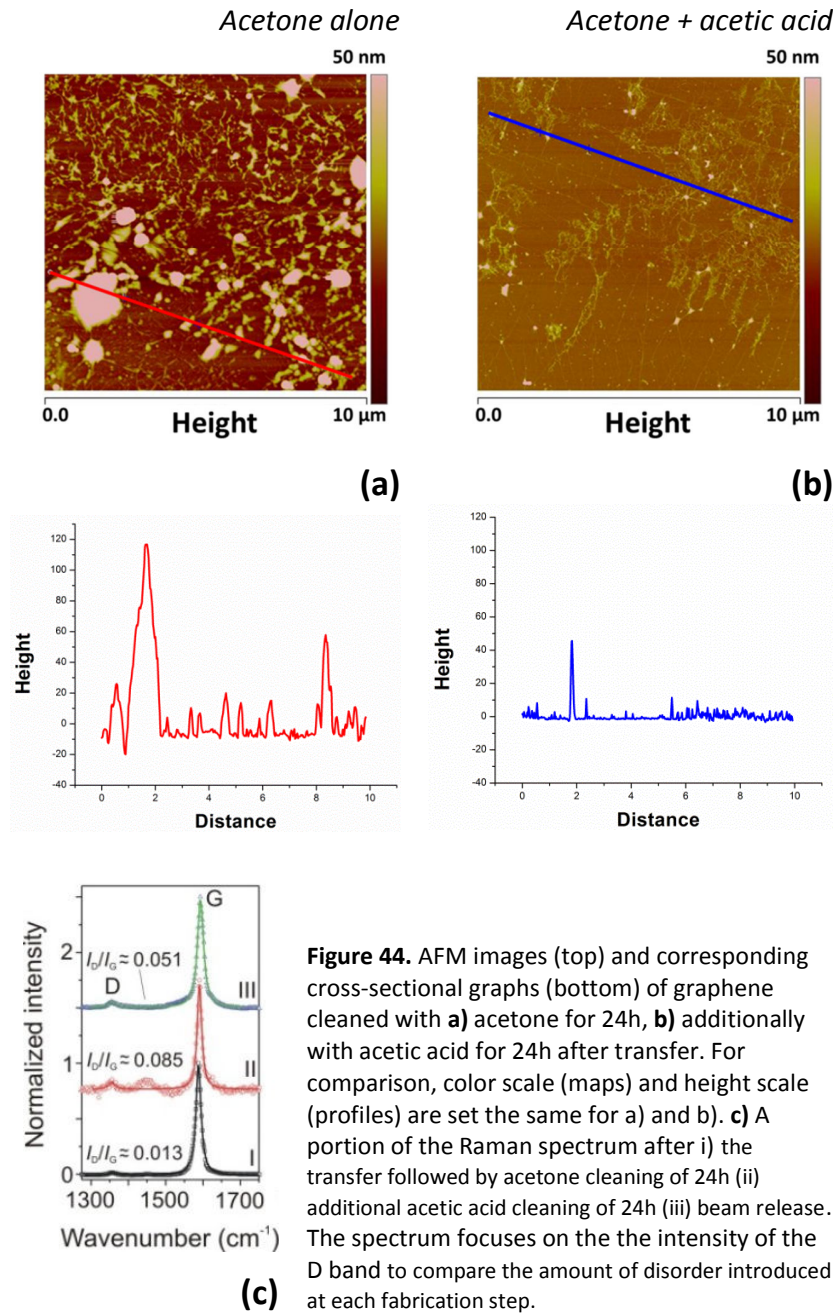
Figure 44. AFM images (top) and corresponding cross-sectional graphs (bottom) of graphene cleaned with **a)** acetone for 24h, **b)** additionally with acetic acid for 24h after transfer. For comparison, color scale (maps) and height scale (profiles) are set the same for a) and b). **c)** A portion of the Raman spectrum after i) the transfer followed by acetone cleaning of 24h (ii) additional acetic acid cleaning of 24h (iii) beam release. The spectrum focuses on the the intensity of the D band to compare the amount of disorder introduced at each fabrication step.

In addition, we inspected if the acid treatment degraded graphene via Raman spectroscopy. We present an entire chapter on Raman measurements. Here, we only insert an explanation regarding the acid treatment. We explain Raman spectra later more in detail. In the Raman spectrum of graphene, the relative intensity of the D band (I_D/I_G) is taken a useful figure of merit for evaluating disorder in graphene because it only appears in the presence of defects. In Figure 44c, we observe that the acid treatment indeed might have introduced some disorder. However, we find the increase in I_D/I_G not alarming and prefer to benefit from the influence of the acid treatment.

50

Furthermore, a weak D band also appears in the spectrum of the final device. While it can have originated from the fabrication steps, it can as easily come from the ribbon edges. The edges of graphene are comprised of unsatisfied dangling bonds which break the symmetry of the honeycomb lattice. The ribbon dimensions are comparable to the laser spot size. Thus, the edges participate in the measurement. That is to say, even though our fabrication might introduce some amount of defects on graphene, we believe that a significant portion of the D band can be attributed to the beam edges.

2.7.2.   Periodic fold formation
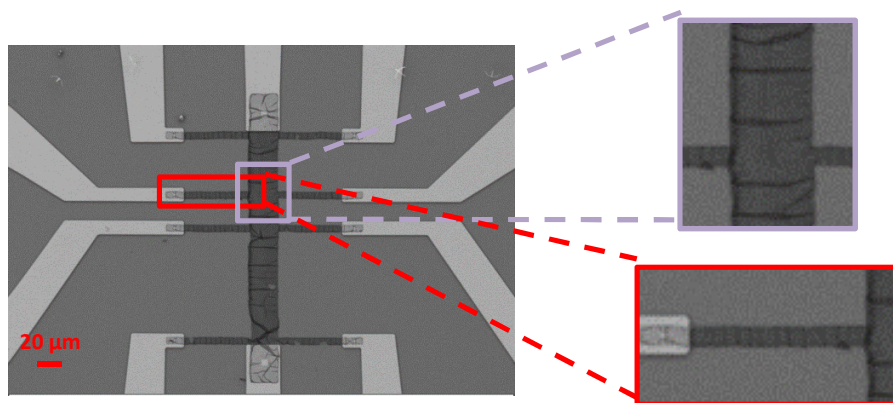
Figure 45. SEM image of a TLM device on the same sample as the one shown in Figure 47. Graphene is patterned with optical lithography using the commercial resist UV5. The samples have undergone thermal Raman measurements, i.e. they were heated up to 200°C and cooled down to room temperature. The suspended beams stay suspended and the systematic folds did not unfold after the thermal treatment. The distance between the folds changes with the ribbon width.

We had explained the formation of wrinkles and folds in CVD graphene in Section 2.3. We believe that their formation is strongly correlated to strain relaxation mechanisms. Figure 43c is the AFM image of the graphene strip in the supported area of a device. We clearly observe systematical folds perpendicular to the length of the strips with a 2 – 4 μm distance from each other. In addition, we see this pattern with quasi-periodic folds in Figure 45. Considering the facts that they are strictly perpendicular to the ribbon length and that the distance in-between the folds change with the ribbon width, they must have undoubtedly formed after or during the graphene patterning step, i.e. once the strip was patterned. Furthermore, we see that these folds are observed on the suspended beams in Figure 42; i.e. they do not unfold after suspending the beam. On the other hand, we show that no such systematic folds are present in the images in Figure 46. At this point, we should underline that the graphene in Figure 42 was patterned with the resist UV5 whereas the graphene in Figure 46 was patterned either with AZ1512 or PMMA/HSQ. Hence, we conclude that the formation of this type of systematic folds perpendicular to the strip length is strongly influenced by the choice of the patterning resist. We already explained that the transfer polymer cellulose nitrate is considerably rigid and does not lead to a full relaxation of the stress built up during the CVD process. Thus, a part of this stress relaxes during patterning with UV5 in the form of such a regular pattern while it does not if AZ1512 or PMMA/HSQ are used instead. We attribute the difference to a variety of factors. Firstly, the adhesion characteristics of UV5 to graphene can be different from the one of AZ1512 or PMMA/HSQ. If the adhesion of graphene to UV5 overcomes its adhesion to the wafer surface, graphene can slide and relax in this fold pattern. Or a difference in the rigidity of the

polymers of UV5, PMMA and AZ1512 can lead to a relaxation for the case of the former while preventing it for the case of the letters. A third explanation can be given by the presence of post exposure baking in the recipe UV5, there is no such baking process for using the other two resists. During this baking at 130°C for 60 s, graphene could have relaxed as well.

(a)

(b)

(c)
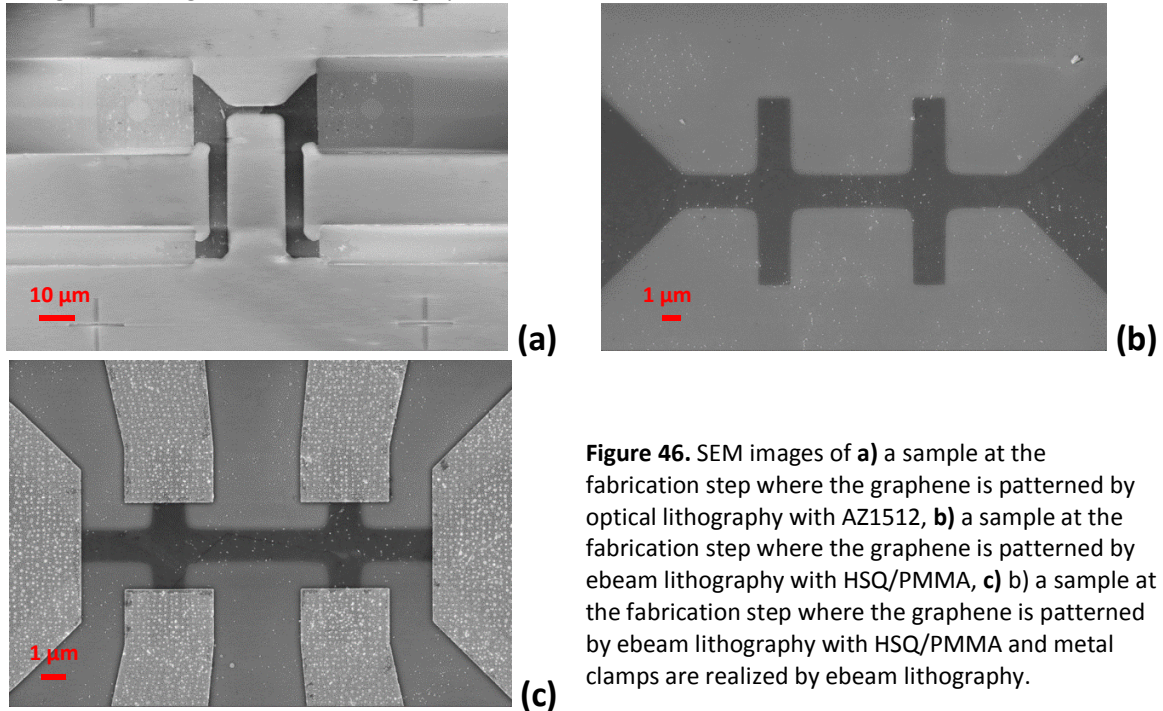
Figure 46. SEM images of **a)** a sample at the fabrication step where the graphene is patterned by optical lithography with AZ1512, **b)** a sample at the fabrication step where the graphene is patterned by ebeam lithography with HSQ/PMMA, **c)** b) a sample at the fabrication step where the graphene is patterned by ebeam lithography with HSQ/PMMA and metal clamps are realized by ebeam lithography.

Figure 47 are the SEM images of several devices belonging to the same sample. Raman measurements are done on the devices of this sample at elevated temperatures; the sample is heated up to 200°C and cooled down to room temperature. Here, we firstly present that the suspended beams did not collapse even after thermal treatments. And secondly, we observe that the fold patterns stayed after thermal treatments as well, on the regions of the suspended beam as well as on the supported regions. In view of strain relaxation as well as in view of interlayer interactions, we believe that the graphene strips with folds present a low energy status of the system. By forming folds, the system is relaxed, i.e. at lower energy. Similarly, when a fold is formed in the form of a bulb in Figure 33b, the graphene monolayer layer interacts with itself such that the system is put to a lower energy as well. Thus, in both perspectives, fold formation appears to be energetically favorable.

(a)
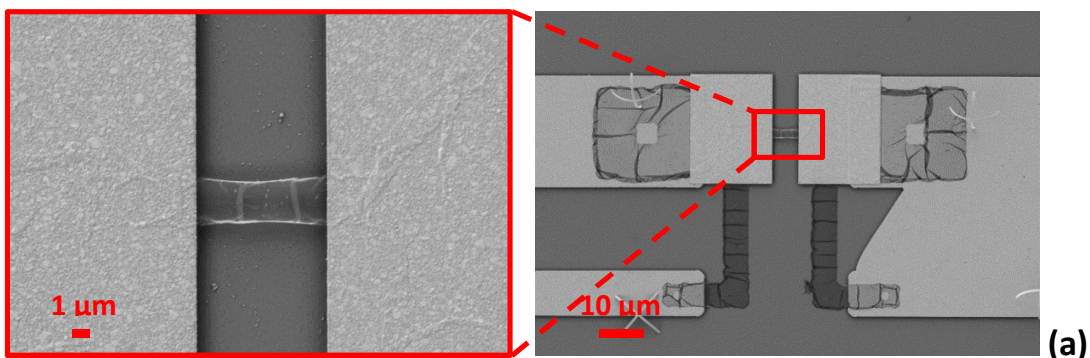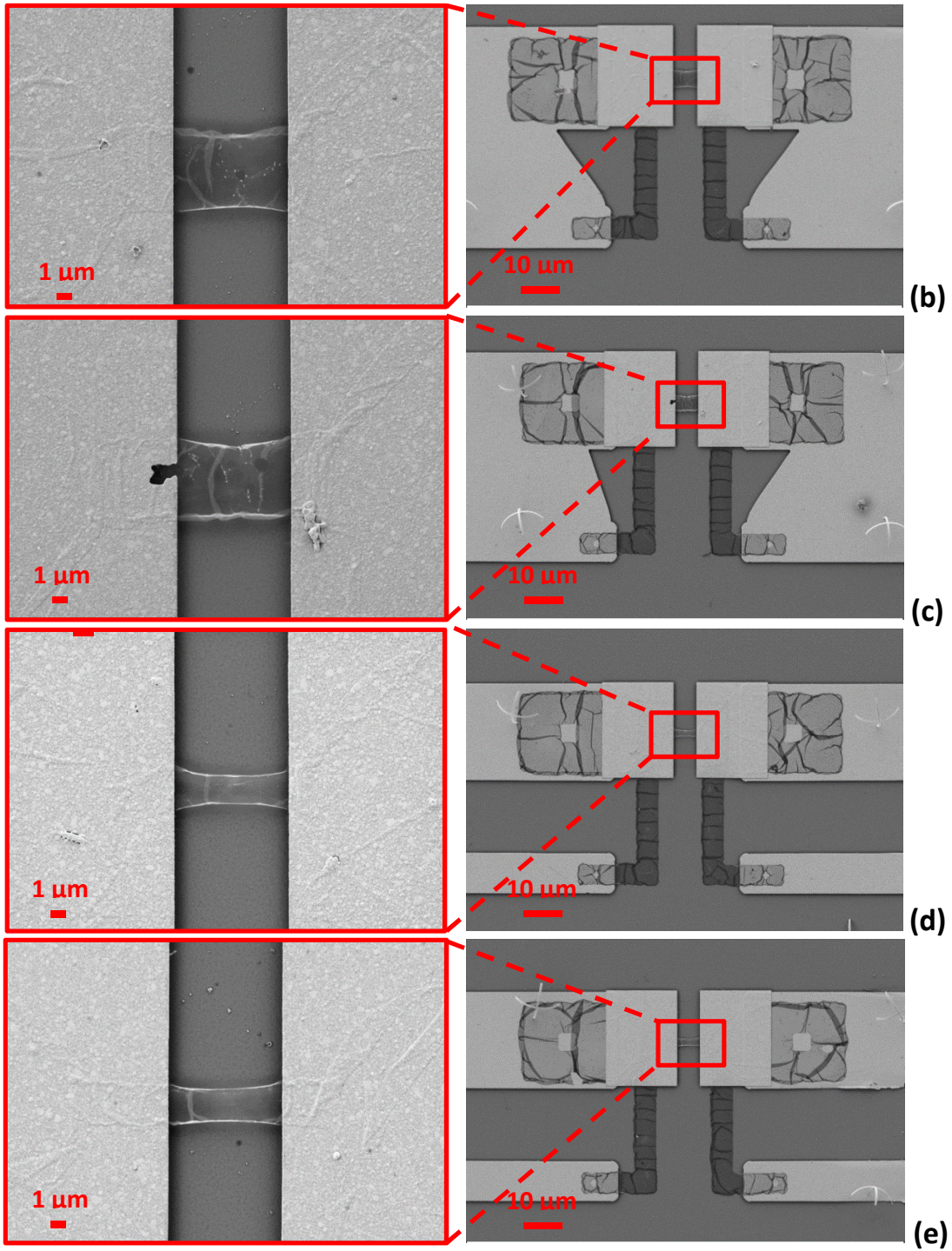
Figure 47. SEM images of devices on the same sample. Graphene is patterned with optical lithography using the commercial resist UV5. The samples have undergone thermal Raman measurements, i.e. they were heated up to 200°C and cooled down to room temperature. The suspended beams stay suspended and the systematic wrinkles did not unfold after the thermal treatment.

2.8. Conclusions

We have presented the state of art of fabricating suspended graphene devices. Suspending graphene is not a straightforward process and this has driven researchers towards employing quite unconventional techniques and materials such as polymer sandwich structures or pillars of LOR. For our route, we preferred keeping to conventional techniques, investigating its issues and proposing solutions. Conventional techniques permit our device fabrication to stay compatible with industrial applications.

The challenge of conventional fabrication lies at the oxide etching step. While most attention has been drawn to overcoming the difficulty of capillary effects by using CPD or vapor HF techniques, we have shown that there is an equally important factor: the etch mask interface. Regardless of the choice of the etch mask, i.e. be it a polymeric resist or a metal layer, we found that the HF penetrates quickly into the graphene/etch mask interface. This does not only prevent the formation of steep edges, it can collapse the beam as well and might go as far as peeling off metal layers. Buffering the etching agent does not help this situation. Therefore, we focused on having a pristine etch mask interface. That is to say, we worked on eliminating impurities which interfere with a perfect adhesion of the etch mask and therefore serve as accelerators of HF penetration.

To that end, we concentrated on having a clean surface after each step of fabrication. We firstly switched to a transfer polymer proven to leave residue, the cellulose nitrate. Then, we added an additional cleaning step, immersion in acetic acid after every time graphene comes into contact with a polymer. After demonstrating that HF penetrates under a polymeric resist even on pristine wafer surfaces after an etch depth of ca. 500 nm, we deserted the idea of polymeric resist entirely and turn to exploiting metal clamps as etch mask. Finally, we used HF vapor equipment over liquid HF followed by CPD due to comparative ease of use as well as smaller number of total fabrication steps. We present that a yield over 90% was possible to achieve through the suggested fabrication route.

Additionally, we discovered that periodic patterns of folds could be formed during the graphene patterning step with a periodicity that depends on the beam width. These folds were very stable and they "survived" suspension or heating. We found that their formation was the result of the choice of resist used for patterning, probably combined with the fact that cellulose nitrate used for transfer leaves a high amount of compressive strain in graphene – as will be discussed more in detail in the next chapter. The fabrication of graphene ribbons with such periodic patterns of folds may present interesting properties which will require further work, beyond the scope of this thesis.

Chapter 3

RAMAN CHARACTERIZATIONS

At first, we would like to introduce Raman spectroscopy. This is followed by the Raman fingerprint of graphene and the different types of information which can be extracted from a graphene spectrum. Finally, we present the Raman spectra of our devices at different fabrication stages and relate spectrum modifications to the presence of the internal and environmental factors such as adsorbates, strain or temperature.

3.1. Introduction to Raman spectroscopy

Raman spectroscopy relies on the inelastic scattering of photons by phonons. The incoming photon causes a time-dependent perturbation on the Hamiltonian of the system. Electrons respond to the fast changing electric field of the photon. It is possible to write the wave functions of the perturbed system with time dependent linear combinations of the unperturbed system where the final energy of the system is increased by $\hbar w_L$ to $E_{GS} + \hbar w_L$ (E_{GS} is the ground state energy) as depicted in Figure 48. This new state is not stationary which is why one talks of a virtual state the system now is in. The system cannot stay in this non-stationary state and therefore falls back to one of it stationary states which can be higher, lower or the same in energy in comparison to the initial unperturbed state by emitting a photon (Figure 48). [119]
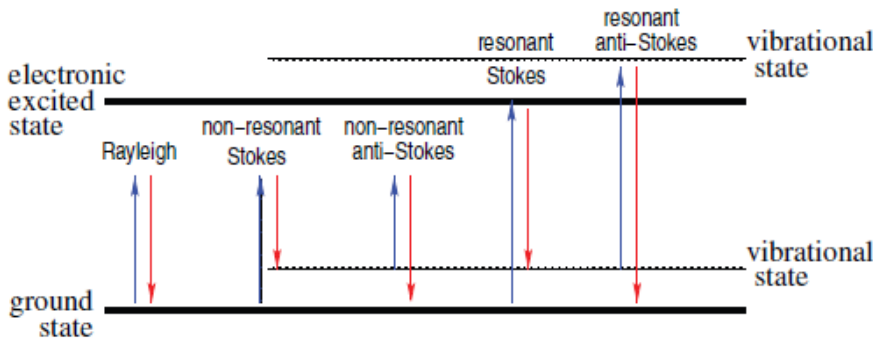
Figure 48. Illustration of Rayleigh and Raman scattering in resonant and non-resonant conditions. [119]

If the system falls back to the initial state, i.e. if the energy of the emitted photon is equal to the energy of the incoming photon, this elastic scattering is called Rayleigh scattering. The photon direction is changed.

With a much lower probability in comparison with Rayleigh scattering, the photon might lose a part of its energy in the interaction with the system. The system does not fall back into the ground state energy level, but it falls to an excited stationary state. The difference between the incident and scattered photon energies therefore correspond to the phonon energy of the excited system:

$$\hbar\omega_L - \hbar\omega_{Sc} = \hbar\Omega \tag{3. 1}$$

This is called Stokes scattering. (Figure 48a) If the system was initially in an excited state, the incident photon can force the state into the vibrational ground state. In this case, the scattered photon leaves the matter with higher energy than the incident photon:

$$\hbar\omega_L + \hbar\omega_{Sc} = \hbar\Omega \qquad (3.\ 2)$$

This is called Anti-Stokes scattering. Raman measurements make use of these two types of inelastic scattering processes: Stokes and Anti-Stokes. [119]

Considering that it is more likely to find the matter in the vibrational ground state than in an excited state, Raman measurements are conventionally done by taking the Stokes shift into account. The intensity of the scattered light is plotted against the energy difference of the incident photon and the scattered photon, i.e. the Raman shift, as an indication of the phonon energies in the system. Instead of energy units, Raman measurements are plotted with cm^{-1}, which then can be converted to energy with the equation: 1 meV = 8.0655447 cm^{-1}. The ratio of Stokes/Anti-Stokes shift gives an indication of the temperature of the sample analyzed. [120] During an attempt to extract the temperature this way, it is important to consider resonant windows of the material as well. The resonances for the Stokes and anti-Stokes shifts might not be at the same energy interval.

Besides the standard Raman spectroscopy, there are other types of Raman setting developed to provide additional information. The resonant or surface-enhanced Raman spectroscopy are among those. Indeed, for most materials, the total energy of the photon excitation and the initial state of the material does not correspond to a stationary state. However, if it does, the Raman signal is greatly enhanced. If the incident photon energy is chosen in a way that the total energy fits a stationary state, resonant Raman measurements can be performed. [121] Surface-enhanced Raman spectroscopy, on the other hand, exploits the fact that the presence of metals can enhance the Raman signal through surface plasmons. [119]

In the range from IR to UV, the laser energy is too large for purely phononic interactions. The scattering process involves electrons as well, especially for carbon allotropes. Therefore, Raman spectra carry information not only on phonons in the carbon material, but also on its electronic behavior. [122], [123] For instance, graphene can lead to resonances for any laser energy due to its zero-gap linear energy dispersion. [124]

The intensity of Raman scattering depends on the square of the incident field amplitude. Therefore it can be enhanced depending on the chosen substrate as an appropriate spacer. This circumstance corresponds to an "interference-enhanced" Raman scattering. [125] [126] As a result, when intensity ratios are compared, it is important to verify that the compared graphene systems are placed on the same substrate material with the same thickness.

3.2. Raman bands of graphene

A typical Raman spectrum of graphene is shown in Figure 50. Several peaks are marked on the spectrum such as D, G, D', 2D and 2D'. They are directly related to the phonon dispersion of graphene and carry information on the material characteristics of a particular type of graphene.

Interpretations of Raman spectra of graphene are based on the phonon dispersion which is as shown in Figure 49a. It is made of 3 acoustic and 3 optical branches. Graphene has 2 atoms per

unit cell and therefore 6 normal modes at the Brillouin zone center Γ, two of which are degenerate. One acoustic branch and one optical branch are out-of-plane modes (o); i.e. the atomic vibrations are perpendicular to the graphene plane, while two acoustic and two optical branches are in-plane (i) modes. Each in-plane mode has one longitudinal (L) and one transverse (T) mode. The modes are classified with respect to the direction of the nearest neighbors. Thus, the longitudinal modes are vibrations that are parallel to the A-B carbon direction while the transverse modes are perpendicular to the A-B carbon atom direction. Following the high symmetry directions ΓK and ΓM, the 6 branches go as: LO, iTO, oTO, LA, iTA, oTA. [127] [128]

(a) **(b)**
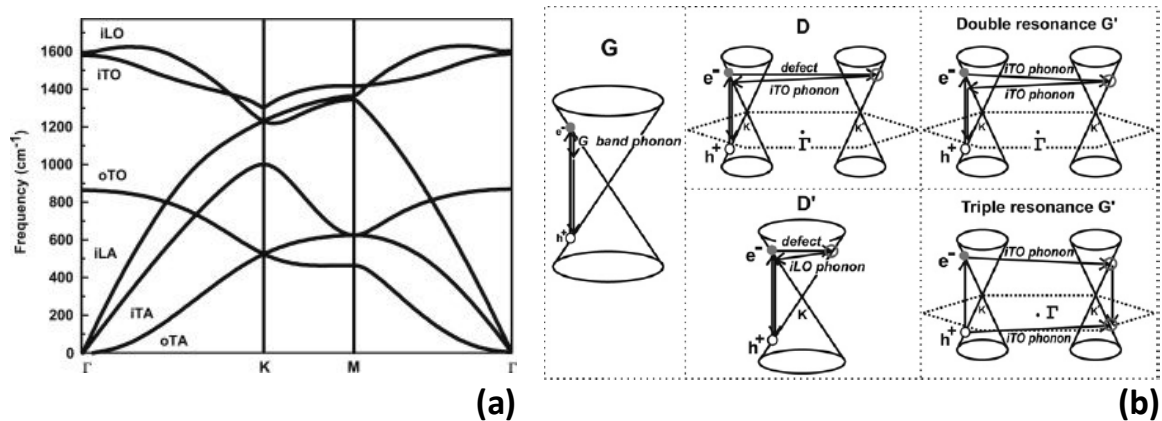
Figure 49. a) Phonon dispersion of single layer graphene. [128] **b)** First order G band process, 1-phonon second order double resonance process giving the intervalley D band and the intravalley D' band, 2-phonon second order process giving the 2D band with a double resonance and triple resonance. 2D band is r as G'. [128]

At the Γ point, i.e. the center of the zone, the two degenerate in-plane optic modes, iTO and LO are the vibrations of the sublattice A against the sublattice B. (Figure 49a) In group theory, these modes are represented as E_{2g}.This is a Raman active mode and results in the G band. [128]

The two other most investigated Raman bands, the D and the 2D bands, originate from the K point. (Figure 49a) The iTO branch is non-degenerate at K point and is represented with the group theory notation D_{3h}. The LO and LA branches, on the other hand, lead to a doubly degenerate phonon. [128]

The phonon dispersions of the iTO and LO branches involve a creation of an electron-hole pair. This electron-phonon coupling leads to this so-called "Kohn anomaly", which is, in fact, the reason for the softening of some phonons at Γ and K points. This will be explained more in detail in Section 3.3.3. [128]

The G band is a normal first order Raman scattering process while the 2D and D bands come from a second-order process including two iTO phonons at K point for the 2D band and one iTO phonon and one defect for the D band. There is a double resonance process for the creation of the D and 2D bands. The wave vectors **q** from the associated phonon couple preferentially to the electronic states with a wave vector **k** where $q \cong 2k$.

The double resonance processes, as shown in Figure 49b, can be broken down as the following: The electron with a wave vector **k** absorbs a photon from the laser. This electron is

scattered inelastically by a phonon (2D band) or a defect (D band) of wave vector **q** and of energy E_{phonon} to a place at K' point with a wave vector **k + q**. Afterwards, the electron is scattered back to a state of **k** while emitting a photon during recombination with a hole at a state of **k**. For D band, the two described scatterings are comprised of one elastic scattering by the defect and one inelastic scattering by photon emission/absorption. For 2D band, the process is done by 2 phonons and there are two inelastic scatterings. These double resonance processes connect two inequivalent points, K and K' in the first Brillouin zone and therefore are called an "intervalley" process. For the creation of the G band, however, the process revolves around the K point and is therefore called an "intravalley" process. (Figure 49b) [128]
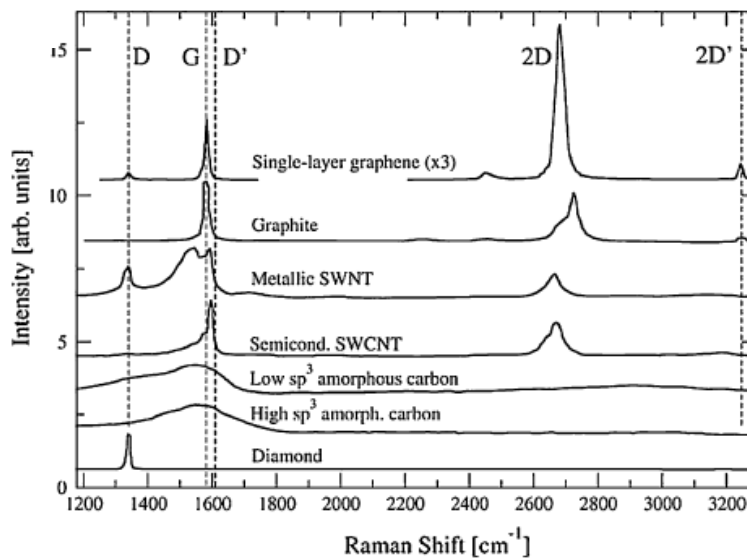
Figure 50. a) Exemplary Raman spectra of single layer graphene, graphite, metallic SWCNT, semiconducting SWCNT, amorphous carbon and diamond. [127]

In Table 2, we present the most relevant peaks that are found in a graphene spectrum (Figure 50). While the given values would help to identify the peaks in a typical graphene spectrum, the positions, line widths and intensities of these bands are strongly affected from a variety of factors. We will address each of them.

	Origin	Position
G band	the doubly degenerate E_{2g} phonon at Γ, the Brillouin zone center	~1580 cm^{-1} [129]
D band	TO phonons at the Brillouin zone corner K Intervalley double resonance process defect required for activation	~1350 cm^{-1} [122] [129] [130] [131]
2D band	overtone of D Intervalley double resonance process with phonons of opposite wave vectors	~2680 cm^{-1} (slightly lower than $2\omega_D$) [119]
D' band	Intravalley double resonance process at K	~1625 cm^{-1} [132] [129]
2D' band	overtone of D'	~3250 cm^{-1} ($2\omega_{D'}$) [119]
D''	defect required for activation can be observed under visible light	~1100 cm^{-1} [133]
D+D''	an overtone	~2450 cm^{-1} ($\omega_D + \omega_{D''}$) [134]

Table 2. Summary of the most relevant peak positions as a guideline for peak identification in a Raman spectrum of graphene.

58

3.3. Factors influencing Raman spectrum of graphene

Several factors can influence the position, intensity and the full width half maximum (FWHM) of the peaks of graphene spectrum. Among those are number of layers, doping, strain and temperature.

3.3.1. Number of layers

In the early stages of especially CVD graphene research, Raman spectroscopy was heavily employed to resolve the number of layers of a grown sample. From a Raman spectrum, it is possible to know if the analyzed graphene is single, double, triple, quadruple or multilayer. As the number of graphene layers increase, the G band shifts with the manner in Figure 51a. In addition, the intensity of the G band increases as well (Figure 51b). This directly changes the I_{2D}/I_G ratio. In a perfect graphene with more than one layer which is under no other effect such as doping, this ratio is expected to be 2. As graphene moves away from single layer, the I_{2D}/I_G ratio moves away from 2. However, neither observation is a clear evidence of the number of layers of the sample. In other words, the number of layers of a graphene sample cannot be determined by solely considering the G band frequency and the I_{2D}/I_G ratio. Both are influenced by factors other than the sample thickness. The intensity ratio can be altered by doping while the position of the G band can be altered by doping or strain. [135] The shape of the 2D band, on the other hand, is a more reliable indicator of the number of layers (up to 4 layers). As in Figure 51c, the 2D of a single layer graphene fits one Lorentzian curve whereas the fitting requires several Lorentzian curves for layers 2-4.

(a)

(b)

(c)
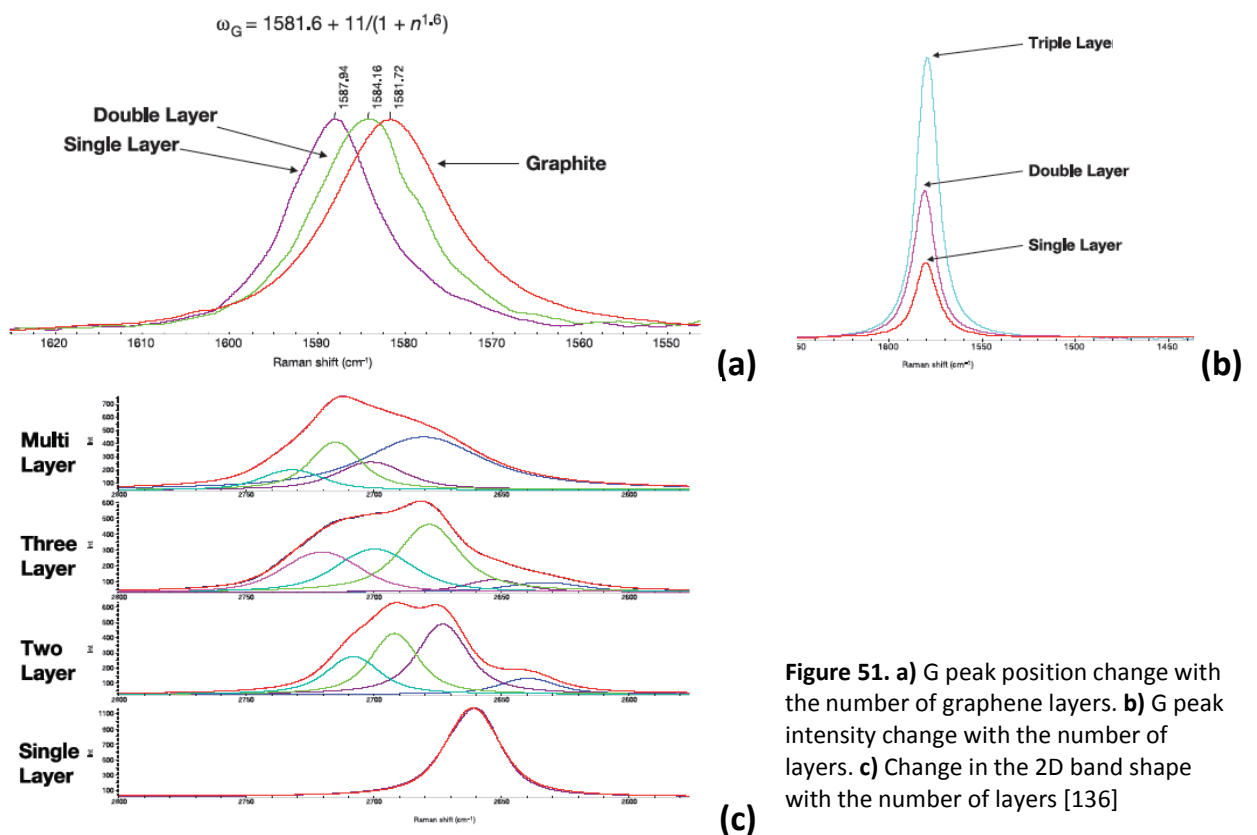
Figure 51. a) G peak position change with the number of graphene layers. **b)** G peak intensity change with the number of layers. **c)** Change in the 2D band shape with the number of layers [136]

3.3.2. Laser energy

The energy of the incident photon can influence the 2D band frequency while it has no effect on the G band. The reason for the influence of the laser energy on the 2D band is the fact that it originates from a double resonance process. [128] The 2D band, which is usually seen in a range of $2680 - 2710$ cm^{-1}, is related to a phonon at **K + Δk** points of the Brillouin zone. The laser energy alters the value of **Δk** due to a double resonance process with the linear dispersion of phonon around **K**. [131] The 2D band frequency changes with the excitation laser wavelength with a slope of $\partial w_{2D}/\partial E_{laser} \cong 100$ eV/cm. [137] [138]

3.3.3. Doping and Kohn anomaly

Graphene is a zero-gap semiconductor and therefore its lattice vibrations are partially screened by electrons. Kohn demonstrated that the screening changes very fast as a function of **q** for the case of phonons with certain wave vectors **q** which then results in a divergence in the phonon dispersion ω(**q**) at such points. This is the so-called "Kohn anomaly". This happens for a vector which fulfills the following condition:

$$q = k_1 - k_2 + b \tag{3.3}$$

where **k₁** and **k₂** belong to electronic states at Fermi level and **b** is a reciprocal state vector which bring the phonon **q** into the first Brillouin zone. For graphene, the wave vectors are the ones at Brilouin zone corners **K** and **K'**. Kohn anomaly happens to certain phonons at points Γ and K which correspond to the G band and the 2D band. In fact, the slope of the phonon dispersion at these points is proportional to the electron-phonon coupling. [128]

Kohn anomaly occurs in graphene where an electron in the valence band absorbs a phonon and is excited to the conduction band by creating an electron-hole pair. The hole and electron recombine and emit a phonon. The frequency and the lifetime of the phonon are heavily influenced by this process. The contribution of this electron-hole process is negative and therefore it results in a softening of the phonon energy compared to an unperturbed phonon. [128]

The effect of doping can be quite dramatic for the case of very high doping levels such that:

$$|E_F| \gg \hbar\omega_L/2 \tag{3.4}$$

Since doping changes the occupations of the electronic state, such a high doping can exclude some regions in k to partake in the Raman process. This stems from the fact that the transition from an empty state or to a filled state is impossible. The destructive interference is suppressed and therefore the G peak is enhanced if:

$$|E_F| = \hbar\omega_L/2 \tag{3.5}$$

The influence of doping on the 2D band is higher than that of the G band. It can, in fact, be completely suppressed if the conduction band is filled at the energy accessed by the laser excitation. The conditions can be broken down as the following, considering that ω$_L$ is the absorbed photon from the laser and ω$_{Sc}$ is the emitted photon and Pos(2D) is the position of the 2D band as:

$$\omega_{Sc} = \omega_L - Pos(2D) \tag{3.6}$$

There are three scenarios:

$$i)\ \omega_L, \omega_{Sc} > 2|E_F|/\hbar \tag{3.7}$$

60

All processes are allowed. The 2D band appears in the Raman spectrum.

$$ii)\ \omega_{Sc} < \frac{2|E_F|}{\hbar} < \omega_L \tag{3.8}$$

The absorption of the photon is allowed. The emission of the phonon is prohibited by Pauli blocking.

$$iii)\ \omega_L, \omega_{Sc} < 2|E_F|/\hbar \tag{3.9}$$

The absorption of the photon and the emission of the phonon is prohibited. As we see that there is a relation between the 2D band, the excitation wavelength and the Fermi level. If the 2D band does not appear for a spectrum taken with a laser at a certain wavelength, it is possible to conclude that Fermi level must be a higher than a certain value. This situation applied to all of the other bands that stem from a double or triple resonance process such as D, D', 2D' and D+D". [119]

The area of the 2D band is very sensitive to the electronic inelastic scattering rate which has contributions both from electron-phonon and electron-electron scattering. Electron-electron scattering increases with carrier concentration, i.e. Fermi level. The 2D band area decreases as the Fermi level moves farther from the Dirac point. The electronic states that mostly take part in the formation of the 2D band are near the $K - M$ direction. And in this direction, the interband part of the electron-electron scattering is inhibited by trigonal warping. [119]

The fact that phonon frequencies and decay rates are influenced from their interaction with π electrons determines their slopes at **Γ** and **K** points. This directly results in a dependence of the phonon frequency and decay rate on the doping level. And this translates to a Raman spectrum as a blueshift of the G band and narrowing of its width. [119]

Frequency shift

In fact, this phonon energy heavily depends on the Fermi level as well. If the Fermi level is moved, the interaction between the phonons and the interband electron-hole pairs decreases. Consequently, this changes the effective force constant of the atomic vibrations. The described Kohn process has a great influence when the Fermi level is at the Dirac point. However, when it is moved more than half of the G-band phonon energy, it can be completely suppressed by the Pauli exclusion principle as depicted in Figure 52a. When the movement is less than half of the phonon energy, there is a logarithmic dependence of phonon softening on the Fermi level. In a real sample, with imperfections and temperature, the logarithmic softening is smoothed out. (Figure 52b) Besides the dependence of the phonon energy, the phonon lifetime is expected to increase because its decay into the electron-hole pair is suppressed. In Figure 52 the dependence of the phonon linewidth is shown with the change in the Fermi level as a consequence of Kohn anomaly. [128]

In fact, the doping-related shift of the Fermi level has two consequences: (i) phonon stiffening or softening with the change of the lattice parameter, (ii) modifying of the phonon dispersion close to Kohn anomalies by the onset of effects beyond the adiabatic Born – Oppenheimer approximation. [139] [140] The excess charge can expand or contract the lattice. Positive doping removes electrons from anti-bonding orbitals, and with that it hardens the G peak while negative doping adds electrons to the anti-bonding orbitals which then softens the G peak. [133]
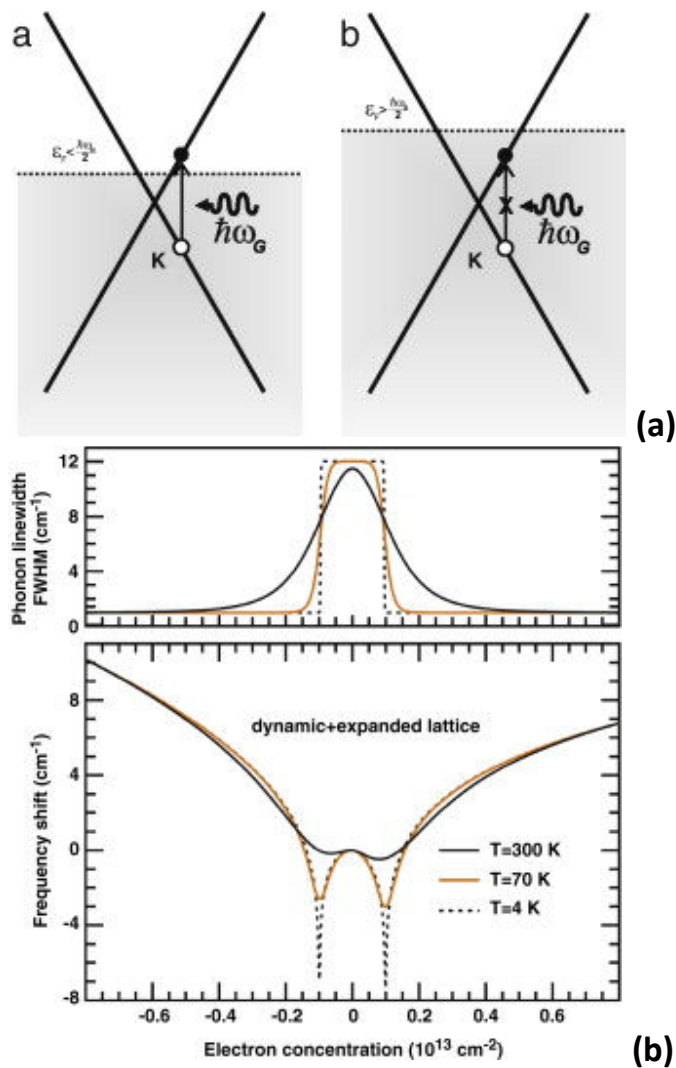
(a)

(b)

We explained how the position of the G and the 2D bands are affected by doping levels due to strong electron – phonon coupling. [141] As demonstrated by Das et al., 2008 in Figure 53a, p-type doping leads to a blueshift of the G and 2D bands while n-type doping leads to a blueshift of the G band and a redshift of the 2D band. [142] [143]

Intensity

Since the positions of the G and 2D bands depend on a variety of factors, one needs another parameter to verify the existence of doping. The intensity ratio of the I_{2D}/I_G is reported to decrease rapidly regardless of the type of carriers as in Figure 53a. It is demonstrated clearly that I_{2D}/I_G is a strong function of the gate voltage. While the absolute intensities might differ in different dielectric environments due to an optical etalon effect, the ratio will not be influenced highly since the scattered phonon wavelengths of the G and 2D bands are very close to each other (such as ~560 and 597 nm respectively). [141] [135] [144] [133]

We recall that the probing of the 2D band of strongly depends on the excitation wavelength. In fact, depending on the amount of doping, the frequency of the adsorbed photon might not be sufficiently high to excite the system to an unfilled electronic state. Consequently, the 2D band might not appear in spectra taken with an energetically lower laser. To make sure that the 2D band is probed even for highly doped graphene, one should abide by the blue and green energies. (Figure 53b) [124]

(b)

(c)

(a)
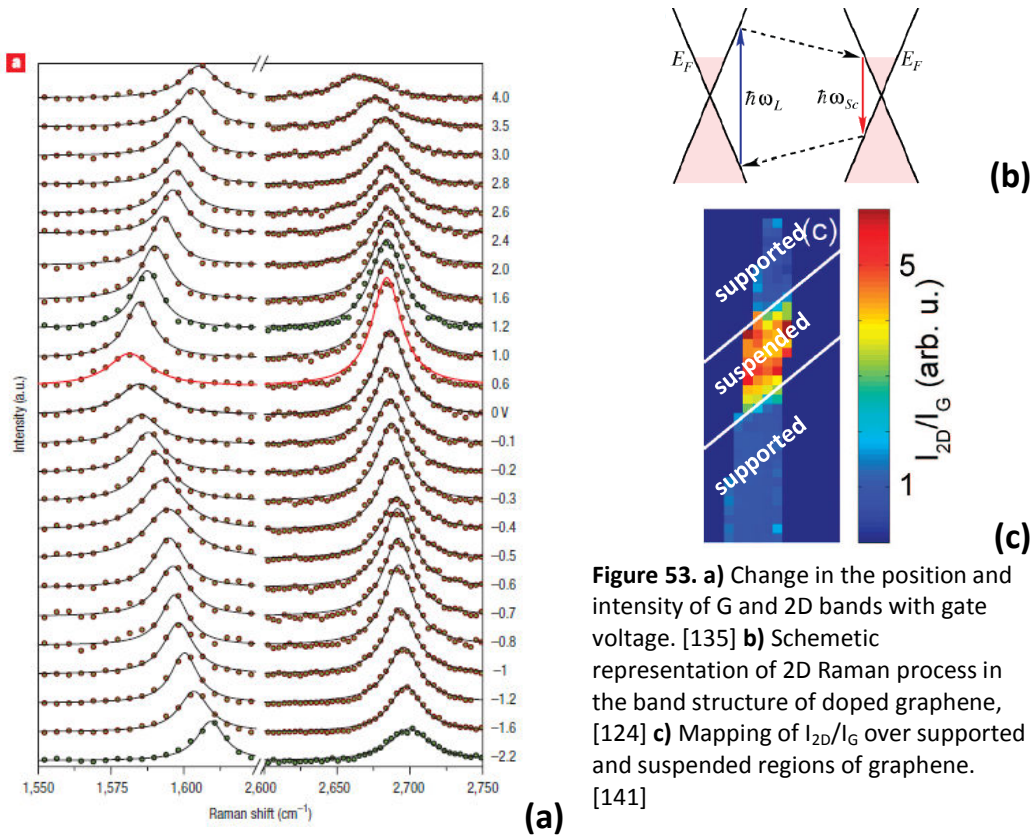
Figure 53. a) Change in the position and intensity of G and 2D bands with gate voltage. [135] **b)** Schematic representation of 2D Raman process in the band structure of doped graphene, [124] **c)** Mapping of I_{2D}/I_G over supported and suspended regions of graphene. [141]

As the intensity of 2D band is strongly suppressed due to the substrate as explained above, the intensity of the G band stays unaffected from the presence of charged impurities. The G band comes from the E_{2g} phonon as explained earlier and has a wave vector of zero. Thus, the process can take place even under non-resonant conditions. [145]

Line width

We also mentioned that not only the frequency of the G band, but also its width is susceptible to changes. The line width of the G band decreases with doping as the G mode phonons stiffen. It is reported that the fwhm(G) increases as the fwhm(2D) decreases at the suspended region in comparison to the supported region regardless of the type of dopants. Berciaud et al. extracted low doping levels using the line width with the following formula:

$$\Gamma_G = \Gamma_0 + \Delta\Gamma[f_T(-\frac{\hbar\omega_G}{2-E_F})] \tag{3.10}$$

63

where $\Delta\Gamma$ is the maximum phonon broadening from electron-hole pair generation (Landau damping) at zero temperature, f_T is the Fermi-Dirac distribution at temperature T, E_F is the Fermi energy relative to the Dirac point and Γ_0 is the contribution to the line width from mainly the phonon – phonon coupling. At room temperature, the maximum contribution to the broadening from the electron-hole pair coupling was reported as $\sim$0.95$\Delta\Gamma$. [141]

So far, there is a consensus on the fact that graphene exhibits p-type doping in devices on an oxidized silicon wafer in ambient conditions. However, there is no agreement on the mechanism of this doping. We find that the explanations from the various studies in this subject show four basic patterns: i) Doping is due to the defects of the SiO_2 surface. ii) Doping is, in fact, related to water layer on the SiO_2 surface. iii) Doping originates from the molecules in air, mainly oxygen. iv) It is the SiO_2 substrate that attracts the oxygen in air. One or all of these mechanisms can be true. And we aim to take all possibilities into account.

3.3.3.1. Substrate-induced doping

Several publications focusing on different types of characterizations demonstrated that exfoliated graphene exhibits inhomogeneous doping on SiO_2 substrates. [141] A series of factors were argued to be involved in the doping mechanism. Sample preparation has an influence on the G band, even in the case of mechanically exfoliated graphene. [146] With impurities of the dangling bonds at the surface, it is believed that the method of growing and/or cleaning process of SiO_2 influences the surface potential. The charge exchange at the graphene/SiO_2 interface leads to a dipole with a direction depending on the contact potential difference at the interface. This inflicts an effective electron injection, i.e. n doping or an effective depletion, i.e. p doping on graphene. [147]

When graphene/SiO_2 is compared with suspended graphene, a blueshift and a decrease in fwhm(G) were observed. Berciaud et al. interpreted this as an indication of substrate related doping of graphene layers where they assumed that the suspended graphene is undoped. They support their claim by the fact that the supported areas of graphene show a systematic decrease in I_{2D}/I_G. [141]

Ni et al. based on their investigation of doping in graphene on the I_{2D}/I_G ratio. The authors explained the decrease in I_{2D}/I_G ratio by the decrease in the 2D intensity. And this decrease is argued to stem from the increase of electron-electron collisions and the increase in inelastic scattering rate with the presence of charged impurities in the SiO_2 layer. $I_{2D} \sim \frac{1}{\gamma^2}$, where 2γ is the inelastic scattering rate of holes or electrons. As the amount of charged impurities increase, the probability of electron – electron collisions and the inelastic scattering rate increase as well. It is known that in suspended graphene, the mobility is enhanced greatly with the absence of long range scattering due to the lack of substrate, i.e. the lack of substrate – related charged impurities. [145]

While we mostly focus on SiO_2/Si as a substrate, we would like to note that the choice of substrate is reported in general to have a direct influence on the Raman spectrum of graphene. In comparison to the typical SiO_2/Si substrate for graphene, ITO as a substrate, for instance, was revealed to cause a slight redshift ($\sim$6 cm^{-1}) of the G band and a large redshift ($\sim$20 cm^{-1}) of the 2D band.

3.3.3.2. Doping by adsorbates

Graphene is entirely made of surface. Any molecule on its surface can directly modify the electronic structure. Adsorbates can be on top or below graphene, i.e. at the graphene/SiO_2 interface. Residual molecules from synthesis and fabrication as well as molecules from air can attach themselves on top of graphene layer. In addition, molecules, especially water, can attach themselves on the SiO_2 surface before graphene transfer. In this case, the electronic structure is influenced by adsorbates, a thin layer of water in particular, from below. The adsorbates are affected from external factors differently due to their location. For instance, air molecules could leave the surface via evacuation whereas heating the sample might help removing the thin water layer at the SiO_2 interface.

O_2 molecules are known to interact with aromatic molecules. Earlier studies on carbon nanotubes show evidence of O_2 adsorption and consequent effective hole doping. Short range distortion of graphene through annealing accentuates reversible or irreversible O_2 binding. Distortion of graphene in the form of ripples distorts the planarity of the π_z orbitals. It is argued that the SiO_2 substrate plays an essential role in the O_2 binding and consequent doping. On the other hand, a study claimed that even suspended graphene showed O_2 doping with or without annealing. [148]

Unless otherwise treated, the surface of an oxidized wafer is terminated by silanol groups which are hydrophilic. The hydrophilic surface attracts water which is then sandwiched between graphene and SiO_2 for supported graphene devices. Just as the adsorbates on top, the water layer is demonstrated to lead to doping of graphene from underneath. [149]

3.3.3.3. Self-doping

It has been argued that defects have the capability of doping graphene. [150] One has to take this into account in analyzing the shift of the G and the 2D bands if, simultaneously, there is an intense D band present.

At the edges of a graphene ribbon or flake, for instance, the shift in the G and 2D band frequencies appear larger due to the so-called "self-doping" effect. This was explained as follows: Dirac fermions have poor screening properties, thus the Coulomb interactions stay long ranged. Consequently, an electrostatic potential forms at the edges. This shifts the position of surface states making the charge transfer to and from them difficult. To remain neutral, the system transfers charge to and from extended defects. The charging stops when the kinetic energy of electrons is paid off by the charging energy of the edges. [151]

3.3.4. Strain

Strain can be detected by Raman spectroscopy since, microscopically, it is the deviation of the crystal lattice out of equilibrium by stretching or compressing. This changes the interaction of phonons with one another or with the incident photon and gives a slightly different response to Raman probing in comparison to what the system in ground state would. We will focus on the responses of the G band and the 2D band under strain.

Tensile (compressive) strain leads to phonon softening (hardening). In other words, tensile strain leads to a redshift of the G and the 2D band positions whereas compression leads to a blueshift of the same band positions. The rate in which the peak positions change with strain is given by Grüneisen parameters. (Figure 54a-c) [129] [152] [137] [119]
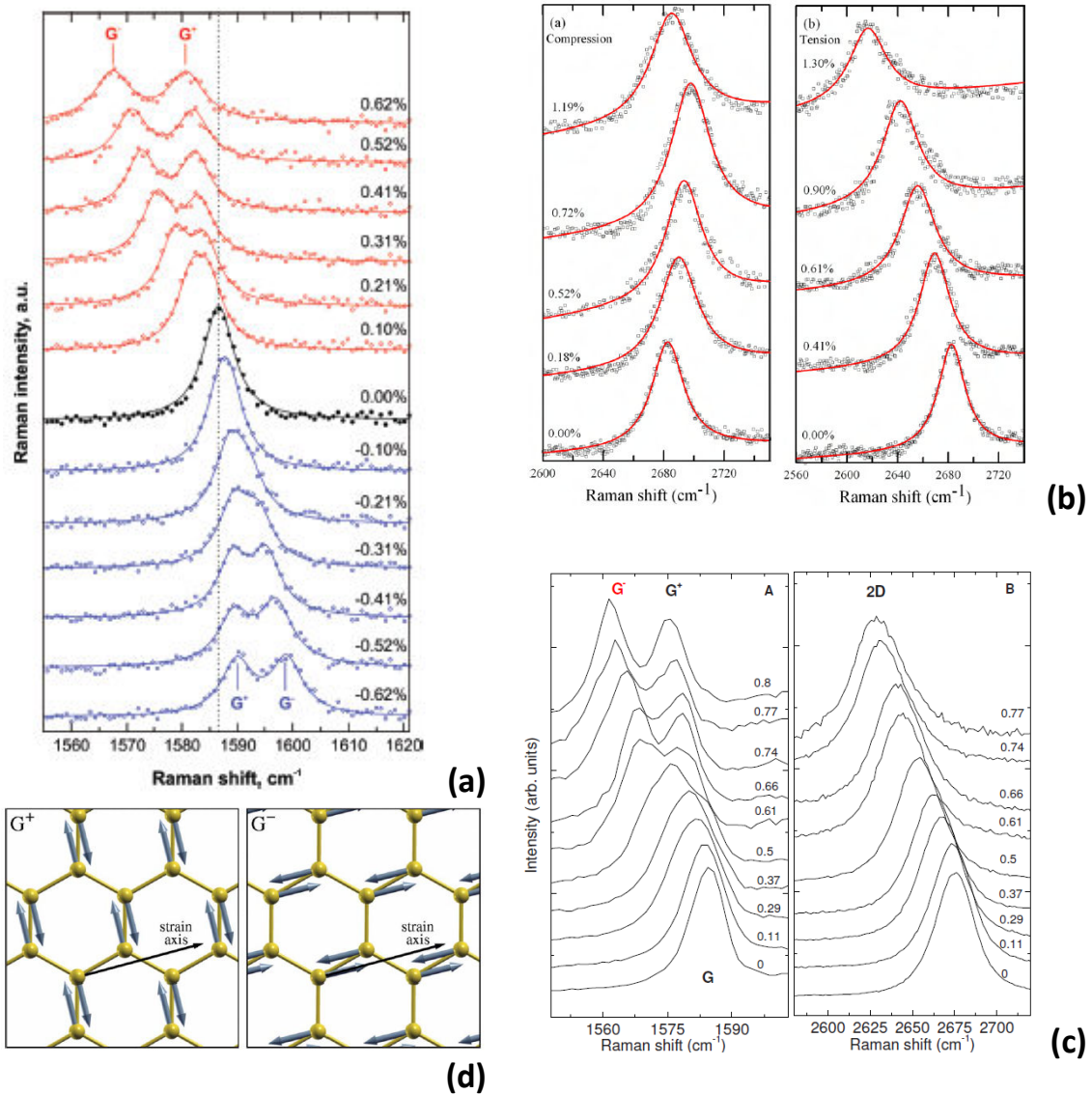
Figure 54. a) Change in the position and intensity of G and 2D bands and G band splitting with uniaxial strain [153] **b)** 2D band plot as a function of compression and tension. [152] **c)** G and 2D peaks as a function of uniaxial strain. [129] **d)** Perpendicular eigenvectors of G^+ G^- modes, G^- is polarized along the strain axis. [129]

In addition, as tension/compression is increased to high values, a splitting in the G band can be observed. More accurately, under uniaxial strain, the doubly degenerate E_{2g} is reported to split in two peaks one of which is polarized along the strain and the other is perpendicular, similar to the G bands of a carbon nanotube. The split bands are commonly referred to as the G^+, located at higher wavenumber and G^-, located at lower wavenumber, analogous to carbon nanotubes. (Figure 54d)

66

The G peak does not split under biaxial strain. [129] [153] One thing to comment on in the two examples of G band splitting in Figure 54 is the actual values of strain. The strain value that split the G band in Figure 54c is 0.66% whereas the strain value that split the G band in Figure 54a is 0.21%. The difference might come from how the strain was evaluated or the fact that built-in strain might not have been taken into account. In any case, this shows that a reverse-engineering to extract the strain values from the G band shift would not be reliable. In other words, looking at our Raman spectrum and deducing quantitative information by using the equations with Gruneisen parameters from these studies would not be dependable.

The phonon vectors E_{2g}^+ and E_{2g}^- are orthogonal as seen Figure 54d. E_{2g}^+ is perpendicular to the strain direction and therefore softens less than the E_{2g}^+ which is parallel to the strain. The G peak splitting can be explained through the loss of degeneracy similarly to the electron confinement and curvature of carbon nanotubes. When graphene is rolled into a tube, the sp^2 bonds become longer in the direction perpendicular to the axis and therefore they soften. With the effect of curvature, nanotubes have a TO G⁻ peak and a LO G⁺ peak. TO G⁻ peak is softer than the latter and more sensitive to diameter changes. [129] In uniaxially strained graphene, The G⁺ originates from a phonon which is perpendicular to the strain and therefore experiences smaller softening. The G⁻ comes from a phonon which is parallel to strain and therefore experiences larger softening. [119]

In addition, the biaxial strain does not change the relative positions of the Dirac cones, uniaxial strain does. This has additional consequences for the phonons which come from double or triple resonance processes such as the 2D band that have intervalley scattering, i.e. from one cone to another. The wave vector is described by the relative distance of the Dirac cones and by the laser energy. At a certain laser energy, when one measures the change 2D band under uniaxial strain, one measures a combination of two effects; from strain and from the relative movement of the Dirac cones. An asymmetric movement of the Dirac cones would broaden the peak and can even split it. [119]

The D and the D' peaks are at the boundaries of the zone and are activated by double resonance as well. Any change which the strain might cause on the double resonance process will change the actual phonon which will be probed. Hence, the D and D' peaks vary with strain in a more complex manner than the G peak does. The D' process connects two points of the same cone around **K** or **K'**, i.e. it is an intravalley process. On the other hand, just as the case of the 2D peak, the D peak is the result of a scattering from the cone at **K** to the cone at **K'**. As a consequence, the relative distance of the Dirac cones has a direct impact on the wave vector of the D peak. The D peak comes from an intervalley process. [129]

We now turn the discussion to 2D and 2D' bands. The 2D' band is also an intravalley process and therefore is not influenced by the relative movement of the Dirac cones. The 2D band, on the other hand, is affected from strain is a more complicated manner. In graphite, the 2D peak varies linearly with strain as opposed to graphene. The difference is attributed to the fact that the graphene layers in graphite are straight while graphene shows wrinkling when it is a single layer. [152] Moreover, the shift of the 2D peak in graphene is two-fold: A portion of the shift comes directly from the uniaxial strain while another portion is related to the relative movement of the Dirac cones which changes the wave vector. In the case of an asymmetric movement of the cones, there is a possibility for the line width to increase. [129]

Raman spectroscopy can help identifying the type of strain further. Anistropic strain can be verified by altering the polarization dependence of the scattered light with respect to the pumped laser. In the presence of anisotropic strain, the G band is expected to appear at different frequencies with the change of polarization. It might go as far as splitting the G band. [141]

The relative intensities of the split peaks of the G band can change with light polarization, i.e. the crystallographic orientation of the probed graphene domain. As explained earlier, the incident light interacts with the graphene phonon via electrons. The electrons sense the crystallographic directions to contribute to the G peak. At zero strain, the vibrations in two crystallographic directions are equivalent. Under strain, the two subbands are resolved in the spectrum. They are vibrations with different orientation with respect to the strain axis. With that, the spectrum changes with the polarization of the incident light with the contribution from the electrons sensing the crystallographic directions and with phonons defined by the strain direction. Figure 55c is an example of a Raman measurement demonstrating how the relative intensities of the G^+ and the G^- peaks change with the change in polarization. [129]

Polarization can favor certain paths. Incoming light excites the electrons or holes stronger that have a momentum perpendicular to the polarization. The same is true for emission. While the G band splitting under the influence of strain is reported several times, it is not as common to see results showing a splitting in the 2D. Such a splitting was reported by Huang et al. The authors observed that graphene samples with no clear crystallographic orientation showed no 2D band splitting with strain, the band only broadened. However, when large strains were applied along high-symmetry directions, the 2D band splitted. Both for the purely armchair and purely zigzag samples, the 2D band appeared at different positions under both of the circumstances: i) when the incident light polarization was parallel to the applied strain and ii) when it was perpendicular to the applied strain as shown in Figure 55a-b. While the armchair graphene showed no splitting in 2D band, peak splitting was observed for the case of the zigzag graphene. When the angle between the incident light polarization and the large uniaxial strain was varied, the 2D band exhibited changes in the intensities of the $2D^+$ and the $2D^-$ peaks as in Figure 55a-b. The polarization dependence of the 2D peak splitting in the zigzag case was reported to correspond to the relative movement of the Dirac cones with strain. [154]

(a)

(b)

(c)
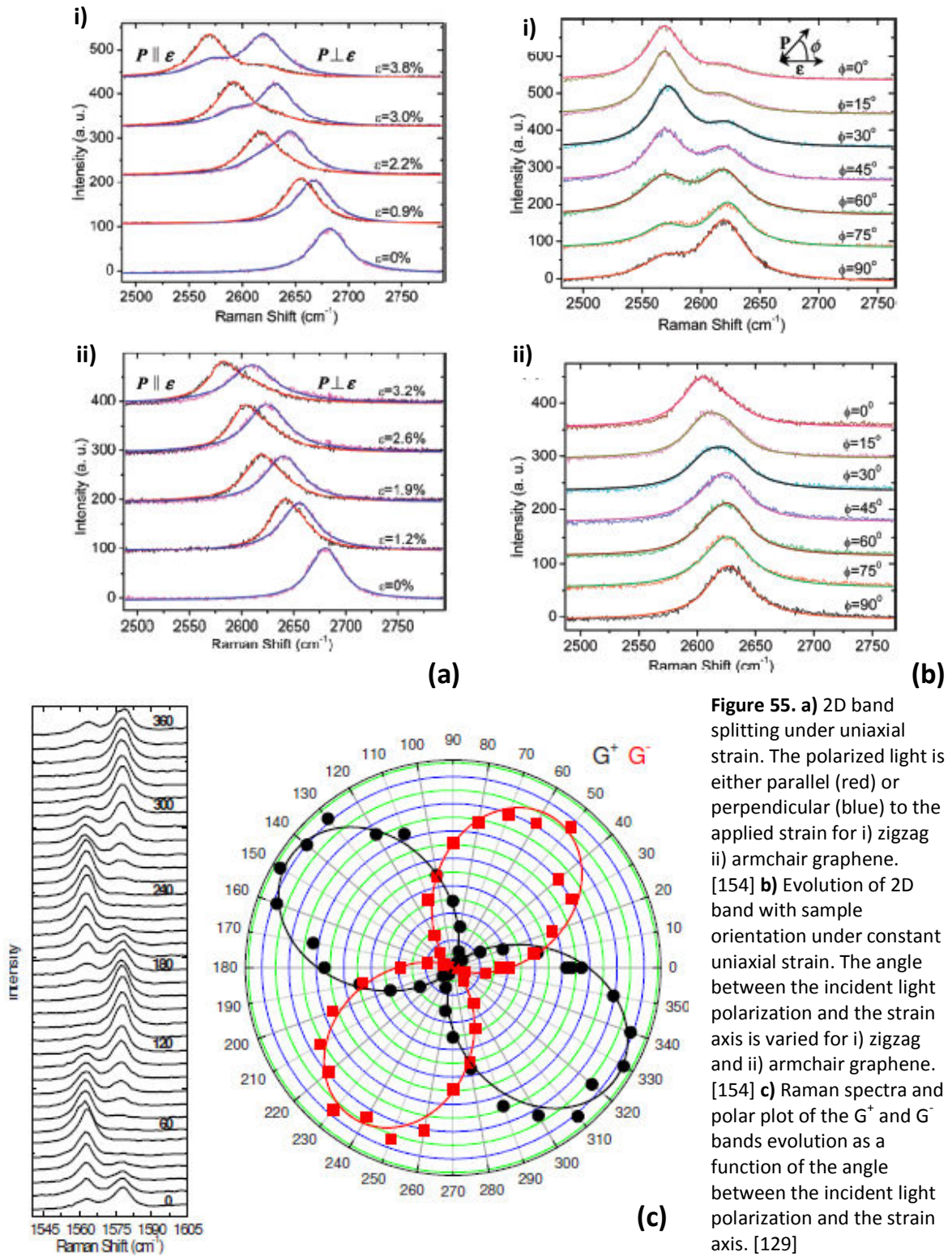
Figure 55. a) 2D band splitting under uniaxial strain. The polarized light is either parallel (red) or perpendicular (blue) to the applied strain for i) zigzag ii) armchair graphene. [154] **b)** Evolution of 2D band with sample orientation under constant uniaxial strain. The angle between the incident light polarization and the strain axis is varied for i) zigzag and ii) armchair graphene. [154] **c)** Raman spectra and polar plot of the G^+ and G^- bands evolution as a function of the angle between the incident light polarization and the strain axis. [129]

3.3.5. Temperature

Theoretically, it is possible to read the actual temperature of a material via Raman spectroscopy. In fact, the temperature can be determined by the ratio of intensities of Stokes and anti-Stokes shifts since this would correspond to the ratio of the ground state vibrational states and the excited vibrational states. And the occupation of these states is directly related to temperature. Therefore, even for the case of a standard Raman measurement (i.e. only the Stokes shift), it would be safe to assume that the band parameters will be influenced by temperature.

When trying to understand the temperature-related effects, it is important to differentiate between the changes in doping and the changes in the lattice parameters in terms of thermal expansion or strain. All of these phenomena happen at the same time when the temperature is increased or when the sample is thermally cycled. Thus, isolating the influence of each factor is not trivial. We present below the studies that have been published on this subject so far. We see that each study looks from a different perspective, makes different assumptions and focuses on a different factor.

Anharmonic effects and phonon-phonon interactions change the positions of the bands and their width when temperature is increased. The line width of the G band has been reported to show a slight decrease at low temperature and an increase for T > 700 K. The width of the G band can be broken into two parts; from the interaction with electron-hole pairs, i.e. electron-phonon coupling and from anharmonic contribution from the interaction with other phonons. Partial Pauli blocking can happen at increased temperature and decrease the damping of the G band phonons due to e-h pair decay. In terms of temperature-dependence, the position of the G band can be broken into two parts; a quasi-harmonic term from thermal expansion and an anharmonic term term from phonon-phonon scattering. [119]

If we assume a "no strain" condition, bands shift with temperature due to elementary anharmonic processes as electron-phonon and phonon-phonon scattering and also due to changes in the lattice parameters with expansion. Anharmonic terms contribute larger at high temperatures.. [127]

In addition, one has to pay attention to the interaction of graphene with the substrate as well. Generally, thermally cycled graphene was reported to exhibit significantly larger G peak shifts on supported regions as opposed to suspended regions. There have been two perspectives to explain this: doping [141] and strain relaxation [155]. We will look at both explanations more in detail.

Calizo et. al made an attempt to model the Raman shift solely due to the temperature as the following:

$$\omega = \omega_0 + \chi T, \text{where} \chi \approx -0.016 \, cm^{-1}/K \text{ [156]} \tag{3.11}$$

for single layer exfoliated graphene on SiO_2. According to Calizo et al., 2007, any higher shift needs to be explained by strain or doping. [156]

3.3.5.1. Heat treatment changes doping levels

If we assume that heating leads to desorption of O_2 molecules and not to the incorporation of them into the crystal lattice of graphene, the p-type doping-related symptoms should decrease at elevated temperatures. Consequently, G band frequency and line width should change. However, heating has a more complicated influence on doping. The G band broadening has two contributions: from electron-phonon coupling and phonon-phonon coupling under heating. Thermal smearing of electron energy distribution increases population above the Dirac point and decreases below. This decreases the width contribution from the electron-phonon coupling at high temperature. Therefore, if the O_2 effect is removed, it is possible to observe temperature-enhanced reduction of electron – phonon coupling at the decrease of G band line width. [157]

Understanding the electron-phonon coupling and phonon anharmonicites is important to predict the performance of graphene devices at high temperatures. Ar annealing, for instance, was reported to result in an increase in the linewidth of G band and a decrease in the G peak frequency. [158] [157] This implied a shift of the Fermi level back towards the Dirac point. Graphene and CNTs are known to have intense electron – phonon coupling when E_F is at Dirac point where this additional scattering broadens the G band. [159] [160] Furthermore, a reduction in the carrier concentration decreases the Fermi surface wavevector k_F and softens w_G by the Kohn anomaly condition $q = 2k_F$, where q is the wavevector of phonons susceptible to electron – phonon coupling. Both behaviors are independent of the type of doping. According to Abdula et al., substrate-related p-type doping originates, in fact, from adsorbant O_2 molecules. That is to say, the SiO_2 substrate enhances the O_2 attachment to graphene. An annealing in Ar is thought to lead to desorption of O_2 and a subsequent decrease in the p-type doping. Blueshifting of the G peak position simultaneously with peak narrowing is argued to stand as evidence to this explanation. [157] If the graphene is heavily doped, Kohn anomaly broadening cannot have a high influence. [157]

The 2D band is not broadened with the electron-phonon coupling because the energy of 2D band phonons is too high. [161] However, the removal of p-type doping is reported to lead to a redshift in the 2D frequency in small amounts. [157]

3.3.5.2. Heat treatment changes strain

Temperature-related changes in the lattice manifest themselves in a Raman spectrum as two different perspectives; changes in phonons and changes in the strain. The former is a direct derivative of the temperature. The latter is a consequence from the combination of built-in strain and interaction with a substrate/trench walls.

Carbon nanostructures have negative thermal expansion, i.e. they contract when they are heated contrary to general 3D materials. [162] [163] Chen et al. estimated the thermal expansion coefficient of graphene as -5.3×10^{-6} K. [155] The authors showed that thermal cycling induces ripples into suspended graphene and claim that they stem from the difference in the thermal expansion coefficients of SiO_2 and graphene. In this example, graphene was suspended over a trench in SiO_2. We explained how the change in tension/compression influences the frequencies of the G and 2D bands. While the strain relaxes in the form of ripples, it can lead to significant shifts in the G band of graphene on the supported region as reported in Figure 56. Suspended graphene was

reported to be tensed at temperatures higher than 600 K with the expansion of SiO_2 substrate and contraction of graphene. [155]

(b)

(a)
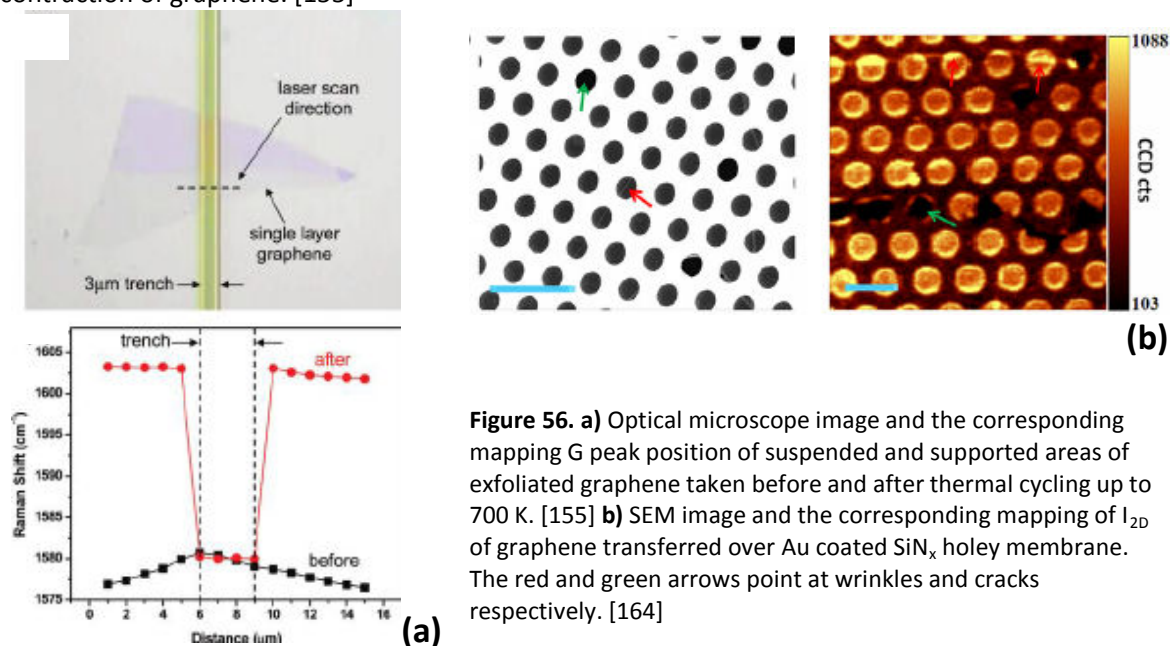
Figure 56. a) Optical microscope image and the corresponding mapping G peak position of suspended and supported areas of exfoliated graphene taken before and after thermal cycling up to 700 K. [155] **b)** SEM image and the corresponding mapping of I_{2D} of graphene transferred over Au coated SiN_x holey membrane. The red and green arrows point at wrinkles and cracks respectively. [164]

Not only, the frequency, but also the width of the G band was claimed to be affected from the temperature. While the broadening of the G band of thermally cycled suspended graphene was taken as evidence for the removal of doping by molecules in, it was attributed to strain phenomena as well by Chen et al. The authors emphasized the ripple formation at the suspended regions of graphene and argued that the Raman frequency was spatially averaged over these ripples considering that the ripple size was smaller than laser spot. Thus, the G band was broadened at the suspended region due to strain relaxation. While the narrowing of the G band for thermally cycled graphene on SiO_2 was argued to be the result of a compression-induced band gap, we believe that this idea is a little far-fetched bearing in mind that such a band gap opening would require significant levels of compression. [155]

As in their previous work, Chen et al. reported that thermally cycled graphene on SiO_2 showed significant amounts of irreversible blueshifts (ca. 25 cm^{-1}) in G and 2D bands while the suspended regions showed no change in peak positions after thermal cycles in air. So far, we talked about two factors, (i) compression induced by the thermal expansion difference between graphene and substrate as well as (ii) doping effects due to trapped surface charge from underlying substrate. In this work, the authors argued that thermal cycling in Ar atmosphere, both suspended and supported regions helped separating between the two types of doping, from the substrate and from gas molecules in air as well as thermally induced strain. The authors reported that the region that was supported on SiO_2 showed significant compression after thermal cycling. [165]

Raman mapping is an efficient method to study graphene, especially CVD graphene, where it serves to identify cracks, wrinkles and suspended regions. An example is shown in Figure 56b where the integrated intensity of the 2D band has been plotted. As we can see, it is possible to identify the locations of wrinkles and cracks in graphene from this Raman mapping. Furthermore, the image of the mapping corresponds exactly to the SEM image with holes in the grid. Thus, it was possible identify the suspended and supported regions of graphene as well. [164]

It is somewhat possible to separate different types of doping, substrate-induced or air-induced by using Ar environment. It is equally necessary to separate the influences of substrate-doping and lattice parameters. Nguyen et al., suggested a method to separate them by applying a gate voltage to graphene while heating in Ar. This way, it was possible to bring the Fermi level back to Dirac point. Under this circumstance, any shift in the peak positions becomes independent of substrate-induced doping. The evolution of G and 2D bands were as in Figure 57a when the Fermi level was kept at the Dirac point. The G band softening at Dirac point due to Kohn anomaly was observed at all temperatures. The first thermal cycle in Ar was argued to remove p-type doping by removing the ambient O_2 molecules. [166]

When the Fermi level was kept at Dirac point, the G band linewidth showed a decrease with heating as in Figure 57b. However, doped graphene showed the opposite trend as in Figure 57b. The G and 2D peak positions of undoped graphene redshifted with heating as in Figure 57a-d, where the frequency shift of the 2D band was half that of the G band. Furthermore, the linewidth of the G band increased irreversibly with annealing. Since the doping factor was eliminated, the increased linewidth was argued to be due to structural deformations due to interaction of graphene with the substrate. The authors showed that the 2D band did not vary largely with the gate voltage, in fact it only showed a shift of 2 cm^{-1}. Therefore, they assigned a large portion of the frequency shifts to structural deformation. Additionally, they showed that 2D band linewidth was slightly broadened with temperature, independent from doping. Pointing at the same cause, the 2D band position was reported to redshift irreversibly by 7 cm^{-1} after cycling. [166]
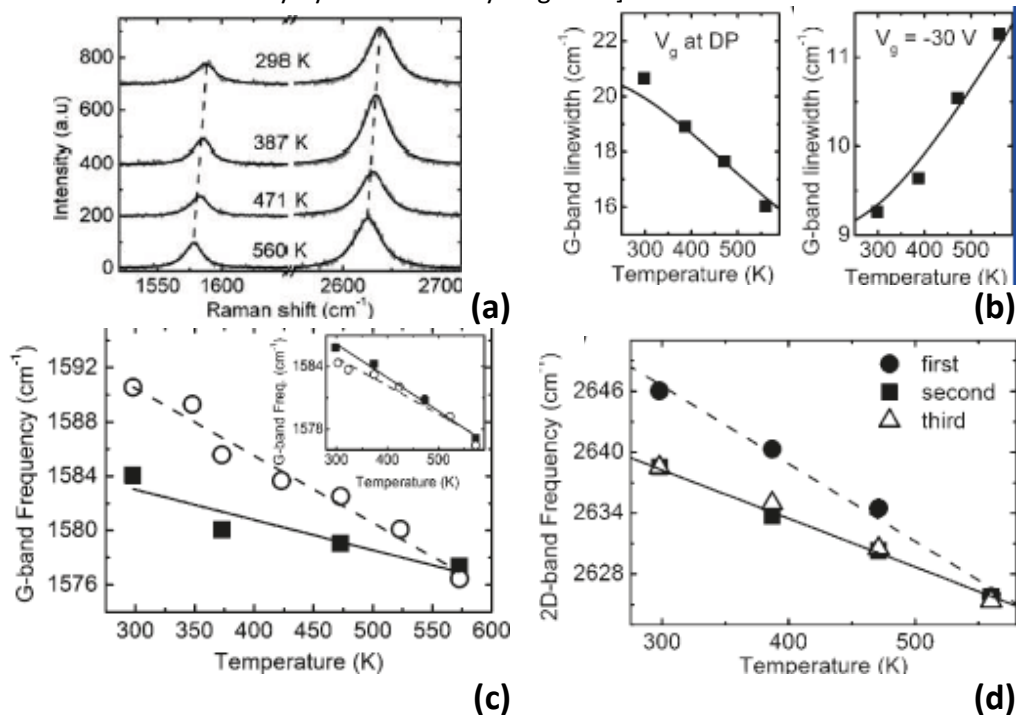
Figure 57. a) G and 2D band shift at the indicated temperatures with the Fermi level fixed at Dirac point by gate voltage **b)** Temperature dependence of the G band linewidth at a gate voltage of -30 V and where the Fermi level is fixed at Dirac point **c)** G band frequency shift with temperature belonging to two different graphene samples **c)** Temperature dependence of the 2D band where the Fermi level is kept at Dirac point, at first, second and third thermal cycles [166]

3.3.5.3. High temperature changes defects

The D band is generally used to verify the defect density in a graphene sample. While the D band can stand for the quality of the analyzed graphene, it can equally originate from the edges of ribbons or flakes. The polarized Raman measurements of Xu et al. demonstrated alterations in graphene edges at temperatures as low as 200°C. The zigzag edges rearranged into armchair segments. The armchair edges dominated up to 500°C. Therefore, attention to the D band can help determining the type of edges present. The exchanged momentum from zigzag edges cannot connect the adjacent Dirac cones as demonstrated in Figure 58. Thus, it cannot fulfill the double resonance condition while the intervalley process from armchair edges does. It is the armchair edges that contribute to the D band intensity. Furthermore, the D band caused by armchair edges is polarization dependent in the following manner:

$$I_D \propto cos^2\theta$$

where θ is the angle between the laser polarization and edge direction. [167] Therefore, while the change in the D band with the temperature can be taken as evidence to degradations in graphene, it can come from edge rearrangements.
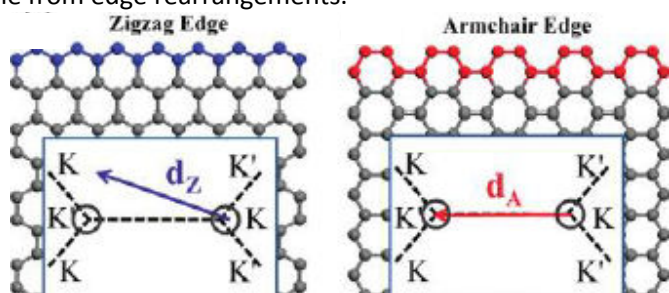
Figure 58. Schematic Illustration of intervalley electron scattering in double resonance process for the case of zigzag and armchair egdes [167]

From all of the studies we presented, we collected some general information in Table 3 to help analyzing a Raman spectrum. We present this as a guideline for distinguishing between the various effects on the spectrum of graphene.

Source	Effect on the Raman spectrum
Number of layers	Redshift of the G band Decrease in the 2D band intensity Change in the shape of the 2D band
Disorder	Appearance of / increase in the intensity of the D band
Any type of doping	Decrease in the line width of the G band Significant decrease in the 2D band intensity
p-type doping	Blueshift of the G and 2D bands
n-type doping	Blueshift of the G band and a redshift of the 2D band
Tensile strain	Redshift of the G and 2D bands
Compressive strain	Blueshift of the G and 2D bands

Table 3. Guideline for analyzing the Raman spectrum of graphene.

3.4. Results & Discussion

We characterized graphene samples with a Raman setup of the grating x1800. The spectra were taken with a 488 nm, the blue line, unless stated otherwise. The laser beam can be focused down to few μm onto the sample. That is to say, the plotted Raman spectrum is an average over the area which the laser beam was interacting with. The utilized objectives were 100x for room temperature measurements and 50x for elevated temperatures. During all measurements, the laser power on sample was kept below 2 mW to avoid laser heating. This limit was set by taking Raman measurements on the same location on graphene and varying the power until the spectrum started showing changes. The compared spectra belong to following samples: i) Graphene transferred on SiO_2/Si, ii) graphene patterned into a ribbon on SiO_2/Si, iii) graphene ribbon on Si, iv) suspended graphene beam. All spectra were normalized according to the intensity of the corresponding G peak. All spectra have undergone baseline correction to eliminate fluorescence, principally belonging to samples at final stage of fabrication, i.e. which have metallic clamps near Raman laser spot. For graphics displayed in this chapter, all spectra were cut in the wavenumber axis to better display the G and 2D bands. We focus on the D, G and 2D bands to infer disorder, doping or strain presence in the sample. The

In the graphs of Raman spectra, the symbols are experimental data and the lines are Lorentzian fits used to extract peak position and line width. Additionally, we inserted SEM or AFM images from the fabrication chapter with a blue spot marking the area of measurement. They do not belong to the same sample the spectrum is taken from. And neither is the blue spot the exact area of the measurement. They are intended to remind the reader of the fabrication stage and clarify the difference between the plots.

3.4.1. Uniformity of Raman spectra of graphene

We took several spectra at different locations of graphene on SiO_2. In addition, we took spectra from different devices on the same sample, both suspended or supported types. This way, we have the chance to firstly investigate the uniformity at different stages of fabrication. We can find out if the CVD and transfer processes or the fabrication method influence the graphene in an inhomogeneous way; i.e. if their influence changes with the location on graphene.

Figure 59 and Figure 60 are Raman spectra representative of different stages of fabrication. It is important to emphasize for both plots that all spectra on the same plot have undergone the exact same fabrication conditions. In other words, each plot was made from one sample.

Figure 59a shows 3 Raman spectra of CVD graphene/SiO_2 measured after transfer and before processing. For each of the plots from Figure 59a-b and Figure 60a-b, the different spectra were taken a different positions on the same sample. Figure 59b plots 3 Raman spectra of CVD graphene patterned into a ribbon on SiO_2. Figure 60a and b belong to different ribbons on the sample after the HF etching step. Therefore, the measured areas were either free-standing between two metal clamp or they laid on Si (not on SiO_2); i.e. the graphene beam was either supported on Si (Figure 60a) or free-standing (Figure 60b)

On each spectrum we drew a "guide to the eye" in the form of a red dashed line. This was designated to give an idea of the frequencies of the G and 2D bands for perfect and pristine graphene according to literature. Furthermore, we included peak positions of the G and 2D bands as Pos(G) and Pos(2D), their line widths in the form of full width at half maximum (fwhm), intensity ratios of I_{2D}/I_G and I_D/I_G. In addition to the red dashed line, these values were intended to help clarifying the interpretations.

When we compare the G and 2D positions, fwhm values and intensity ratios of Figure 61, we see that they vary little for each figure. In Figure 61, the G peak frequencies of different areas on as transferred graphene vary by $2\,cm^{-1}$ as do the fwhm(G). The 2D peak does not vary at all and its fwhm show a difference of $2\,cm^{-1}$. In none of these 3 plots, the G peak frequency varies more than by $3\,cm^{-1}$ while its fwhm changes more than $2\,cm^{-1}$. And the 2D peak position does not vary more than $4\,cm^{-1}$ while its fwhm does not change more than $2\,cm^{-1}$. Thus, we conclude that the spectrum of transferred CVD graphene or supported CVD graphene ribbon measured at one point is likely to represent the entire sample.

In contrast, the suspended beams differ greatly in peak positions, intensity and width as seen in Figure 61,. Therefore, we conclude that each beam is influenced from factors such as doping and strain in a different manner.

3.4.2. Raman signal enhancement

By taking advantage from an appropriate spacer, such as an oxide layer as in the case of optical imaging of graphene, one can enhance the field amplitude and even use the elastic scattering for determining the number of layers. [124] We observe this phenomenon when we compare the signal we get from graphene on SiO_2, on Si and suspended graphene. The intensity we get from suspended samples is significantly larger than the graphene on SiO_2 while graphene on SiO_2 shows significantly higher intensities than graphene on Si. We present normalized data; thus we do not show a direct comparison of these intensities. However, we observe the effects of the enhancement in terms of roughness of plots in Figure 63. The spectral points on the plot of the suspended sample result in the smoothest and clearest peaks while the spectrum of graphene on Si suffers from noise.

3.4.3. Number of layers

The CVD fabrication is developed and practiced in CRANN laboratories, Dublin. The CVD process is already studied in these laboratories in detail. The finalized synthesis results in highly monolayer graphene. [79] [110] Thus, we do not expect that the shifts of G band originate from a multilayer area on the sample. Furthermore, the 2D band shape can be fitted to one Lorentzian curve which indicates monolayer samples as explained before. However, as demonstrated in AFM images earlier, folds can be found on certain samples which can behave as a bilayer or even a multilayer area if they coincide with the Raman laser spot. Averaged over the entire Raman spot including certain folds, a sort of increase in the number of layers could influence the G band position slightly.
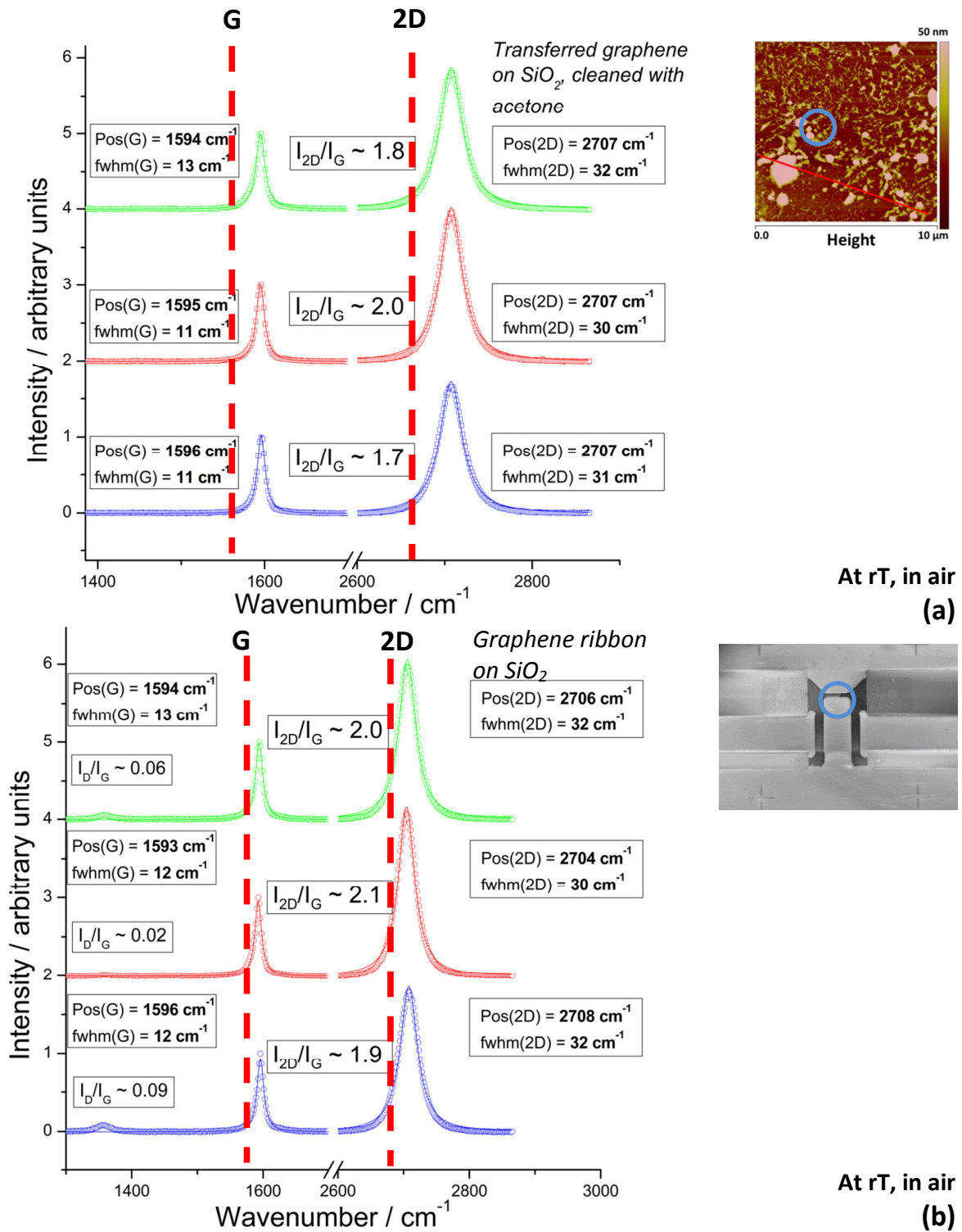
Figure 59. Raman spectra of CVD graphene **a)** transferred onto SiO₂ **b)** and patterned into a beam. Measurements are taken at different areas/beams for statistical analysis.

Graphene ribbon on Si

At rT, in air
(a)

Top graph data (from top to bottom traces):

Pink trace:
Pos(G) = **1593 cm⁻¹**, fwhm(G) = **16 cm⁻¹**
$I_{2D}/I_G \sim 2.5$, $I_D/I_G \sim 0.06$
Pos(2D) = **2708 cm⁻¹**, fwhm(2D) = **30 cm⁻¹**

Green trace:
Pos(G) = **1595 cm⁻¹**, fwhm(G) = **15 cm⁻¹**
$I_{2D}/I_G \sim 2.1$, $I_D/I_G \sim 0.1$
Pos(2D) = **2708 cm⁻¹**, fwhm(2D) = **27 cm⁻¹**

Red trace:
Pos(G) = **1593 cm⁻¹**, fwhm(G) = **15 cm⁻¹**
$I_{2D}/I_G \sim 1.8$, $I_D/I_G \sim 0.06$
Pos(2D) = **2706 cm⁻¹**, fwhm(2D) = **30 cm⁻¹**

Blue trace:
Pos(G) = **1593 cm⁻¹**, fwhm(G) = **14 cm⁻¹**
$I_{2D}/I_G \sim 2.4$, $I_D/I_G \sim 0.06$
Pos(2D) = **2707 cm⁻¹**, fwhm(2D) = **30 cm⁻¹**

At rT, in air
(b)

Bottom graph data (from top to bottom traces):

Magenta trace: *Suspended graphene beam via **ebeam** lithography*
Pos(G) = **1589 cm⁻¹**, fwhm(G) = **22 cm⁻¹**
$I_{2D}/I_G \sim 2.7$, $I_D/I_G \sim 0.2$
Pos(2D) = **2699 cm⁻¹**, fwhm(2D) = **31 cm⁻¹**

Green trace: *Suspended graphene beam via **optical** lithography*
Pos(G) = **1584 cm⁻¹**, fwhm(G) = **22 cm⁻¹**
$I_{2D}/I_G \sim 3.1$, $I_D/I_G \sim 0.01$
Pos(2D) = **2703 cm⁻¹**, fwhm(2D) = **37 cm⁻¹**

Red trace: *Suspended graphene beam via **optical** lithography*
Pos(G) = **1593 cm⁻¹**, fwhm(G) = **20 cm⁻¹**
$I_{2D}/I_G \sim 1.8$, $I_D/I_G \sim 0.07$
Pos(2D) = **2699 cm⁻¹**, fwhm(2D) = **35 cm⁻¹**

Figure 60. Raman spectra of graphene beams after HF etching **a)** at supported regions, i.e. on Si **b)** at suspended regions. Measurements are taken at different positions for statistical analysis.
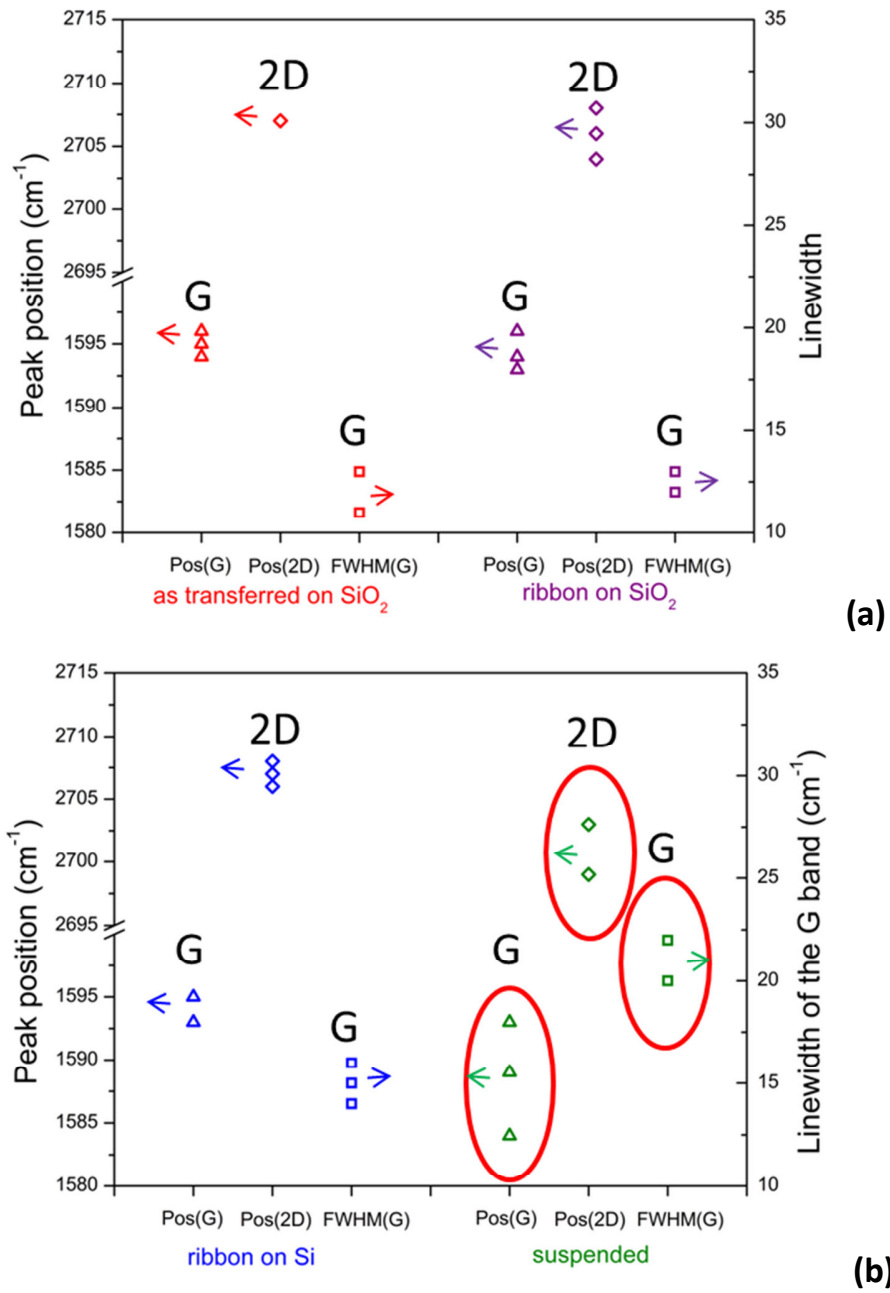
Figure 61. G and 2D peak positions and the G band linewidth are re-plotted from Figure 59 and Figure 60 to better demonstrate the difference in the uniformity at different fabrication stages. While supported graphene is rather uniform at different areas, suspended graphene shows a larger variability in peak positions and linewidth.

3.4.4. Influence of laser energy

The values for the G and 2D peak positions that make up the red dashed line are taken from literature where mostly a green laser line is used. We use a blue line with a wavelength of 488 nm. While we know the laser energy has no influence on the position of the G band, the 2D band position changes with the excitation laser wavelength with a slope of $\partial w_{2D}/\partial E_{laser} \cong 100$ eV/cm. Hence, a portion of roughly 12 cm^{-1} in the deviation from the 2D red dashed line can be attributed to laser energy. To confirm, we took Raman spectra with the green laser as well and the comparison in Figure 62 confirms our calculation. Nonetheless, the plots show a deviation larger than 12 cm^{-1} from the red dashed line. More accurately, after subtracting the laser influence, there is still roughly a deviation of 12 cm^{-1} left to account for.
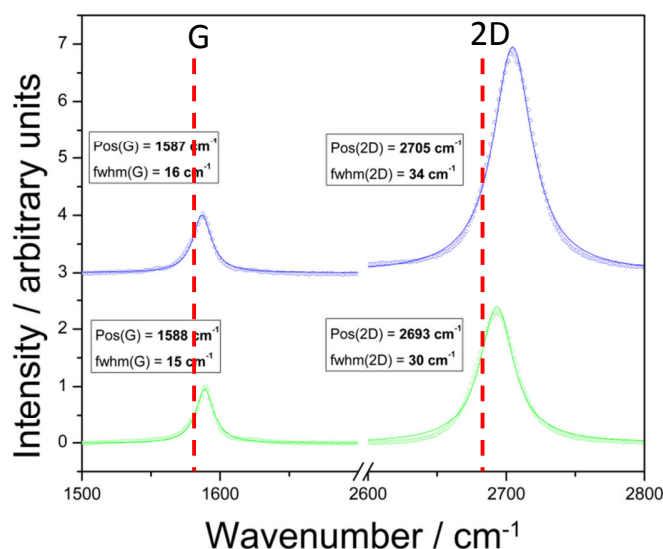
Figure 62 Raman spectra of suspended graphene taken at laser wavelengths of 488 nm (blue) and 512 nm (green).

3.4.5. Defects

As mentioned before, pristine graphene does not show a D band. Thus, its intensity is taken as evidence for the presence of defects. While these defects can be vacancies or impurities, there is equally the chance for the D band to appear due to edges. The edges of graphene are comprised of non-satisfied dangling bonds which are some sort of defects, too. In fact, when we compare the Figure 59a and b, i.e. as-transferred graphene on SiO_2 vs graphene ribbons on SiO_2, there is a general slight increase in the D band intensity. The dimensions of the beams are comparable to the spot size of the laser. Thus, it is safe to assume that the edges took place in the measurement as well. Even though our fabrication might have introduced defects, we believe that a significant portion in the band can be assigned to beam edges. And overall, there is no alarming increase in the D band intensity at the final suspended devices. (Figure 60b) In addition to the D band, a small D' band at 1620 cm^{-1} appears as a shoulder to the G band in samples patterned into a beam. (Figure 60b)

3.4.6. Influence of doping

We mentioned that the substrate or the molecules in air can induce doping in graphene. Doping changes the peak positions of G and 2D band, the G band width as well as intensity ratio.

When we compare the graphene ribbons on Si in Figure 60a and the graphene ribbon on SiO$_2$ in Figure 59b, we see a systematic small decrease of 2 – 4 cm^{-1} in width of the G band for SiO$_2$. The spectra are re-plotted in Figure 63 for better observing the differences and important features are presented in Figure 64. This can be explained by the different influences of substrates. The SiO$_2$ evidently leads to a higher p-type doping than the Si does. On the one hand, this might be due to a higher number of traps at the oxide surface, an enhanced attraction of water or a larger difference in their work potential. On the other hand, we explained that SiO$_2$ promotes the O$_2$ attachment to the graphene surface. P-type doping might have been enhanced through this increase in O$_2$ adsorption. When the substrate is removed, the doping originating from the substrate is removed as well. Thus, the G peak is broadened by 7 – 10 cm^{-1}.
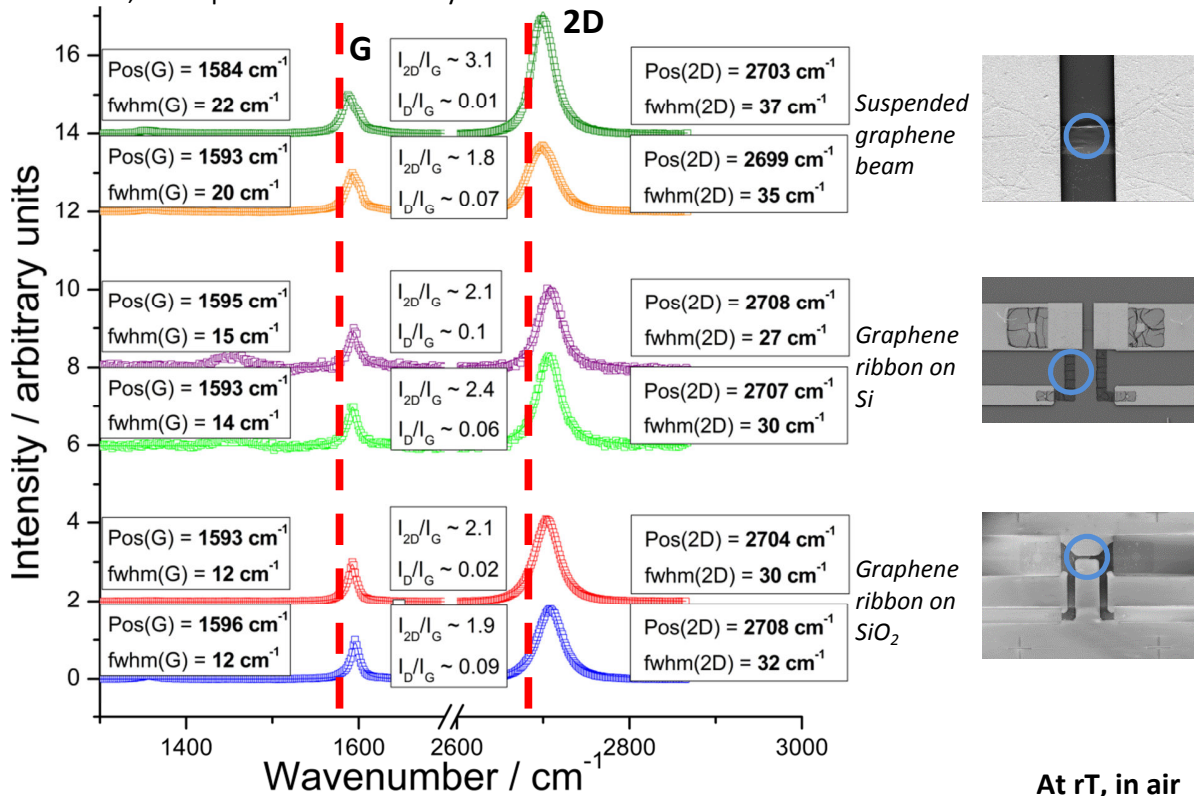
Figure 63 Comparison of Raman spectra of graphene beam on Si, on SiO$_2$ and suspended graphene beam. There are 2 spectra for each type of sample taken at different beams on the same sample.

As we see in Figure 63, there is a deviation towards higher energy from the red dashed lines at all stages of fabrication. The inhomogeneity of values for the suspended samples prevents us from making general conclusions on substrate-related doping. However, if the substrate-related doping was the only cause of blueshift of G and 2D bands, the positions of the red line must coincide with the G and 2D peaks at the suspended region. Yet, compared to the supported regions, the suspended samples show a decrease in the blueshift even though they do not reach the dashed red line. (Figure 64) Additionally, they exhibit a broadening of G band. Thus, the removal of the substrate has indeed a crucial effect on the decrease of doping. Still, there must be more factors causing the deviation of peak positions. Furthermore, we do not observe a suppression of the I$_{2D}$/I$_G$ ratio in relation to doping even though it was shown clearly by the work of Das et al. and explained in Section 3.3.3.
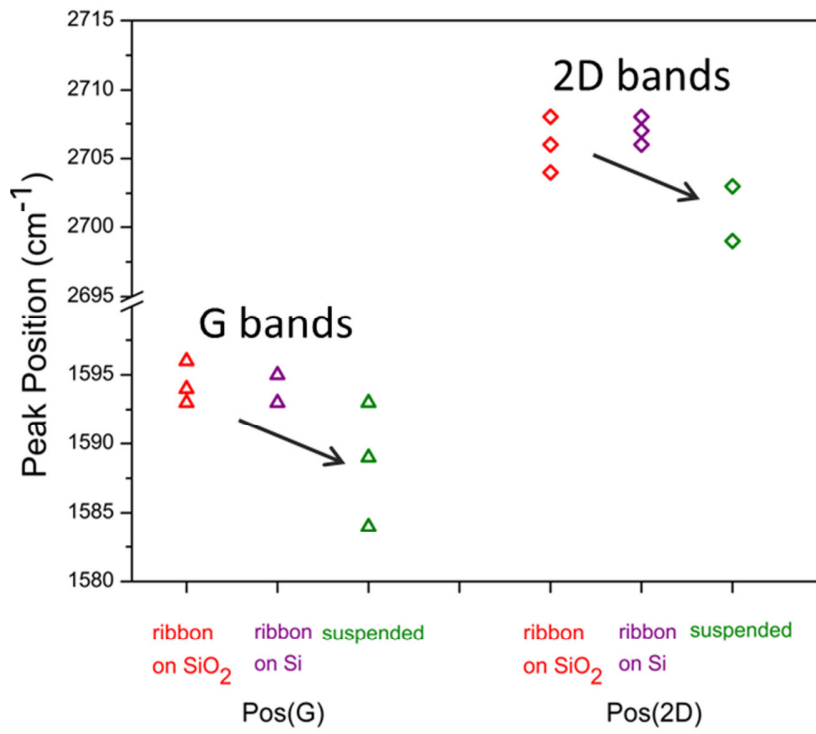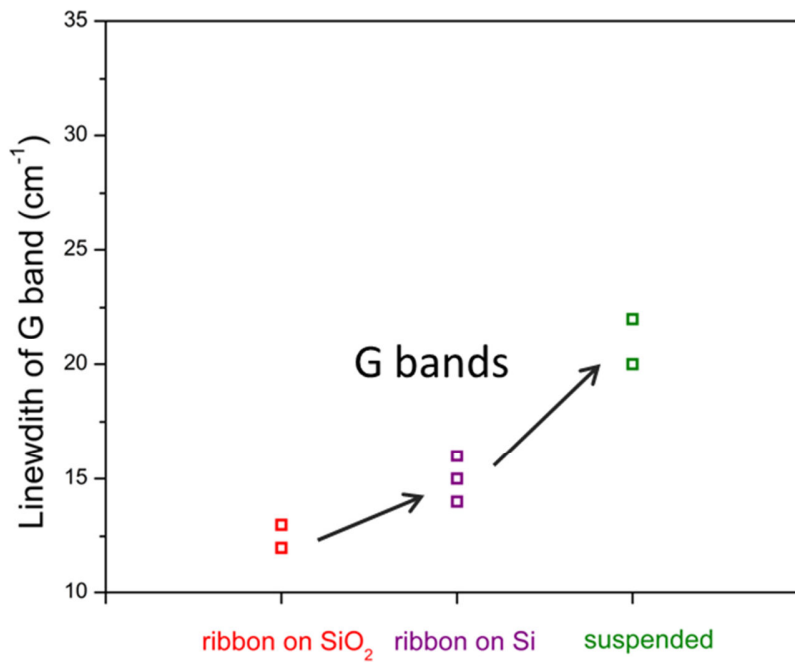
Figure 64. a) G and 2D peak positions and b) the G band linewidth are re-plotted from Figure 63 to better demonstrate the change in doping levels. P-doping is higher on SiO_2 substrate compared to Si substrate. Substrate-induced doping is removed at suspended samples.

Next to the substrate, the O_2 molecules in air are known to lead to doping of graphene as well. This doping is argued to be enhanced by SiO_2 substrate. To verify O_2 doping, we did additional Raman measurements in Ar atmosphere as opposed to air. Figure 65 and Figure 66 compare spectra taken in air and Ar environments for samples on Si or SiO_2 as well as suspended samples. Baring in mind that the values of suspended sample can vary widely, nearly all samples show a systematic decrease in the blueshift of G and 2D band frequencies in Ar compared to their counterparts in air. While the change in peak positions can have different sources, there is a systematic broadening of the G band for every type of sample in Ar compared to samples at the same fabrication stage in air. Therefore, we can conclude that doping via O_2 adsorption is evidently an important factor in our Raman spectra of graphene.

3.4.7. Influence of strain

Suspended graphene beams in Ar (Figure 65c and Figure 66) are, in theory, devoid of the influences of a substrate and O_2 adsorption, i.e. doping. And yet it shows a blueshift of the G and the 2D bands from literature values even after subtracting the shift due to laser energy difference. Thus, we turn to the other source of blueshift; the compressive strain. The blueshift in the G band position with a relatively larger shift in the 2D band position is indicative of compression. Bearing in mind that we do not apply any external compressive stress on the sample, the compression must be internal. In Chapter 2, we explained how CVD process can lead to internal compression. [168] We also talked about the rigidity of the transfer polymer and how it partially prevents strain relaxation during transfer. These Raman spectra confirm the residual compression present in our CVD graphene and demonstrate that it does not fully relax neither during transfer, nor device fabrication or suspending.

Additionally, we think it is worthy to consider the differences in the interaction of graphene with the substrate as well as trench walls. We analyzed the Figure 59a-b, Figure 60a and Figure 65a-b in terms of doping, i.e. we assigned the decrease in blueshifting in suspended samples with respect to the supported samples to the removal of substrate doping. While the sharpening of the G band at graphene/SiO_2 clearly indicates doping, we believe that the change in the shifts must be a combination of the two factors: doping and strain. It is known that the suspended graphene beam is known to attach itself to the trench walls. This can relax part of the compressive strain. This could lead to a decrease in blueshifting, too.

Furthermore, graphene adhesion differs with the type of substrate which would change the strain in graphene. Therefore, the difference in spectra of graphene beam/SiO_2 and graphene beam/Si could also be somewhat influenced both by doping and strain.
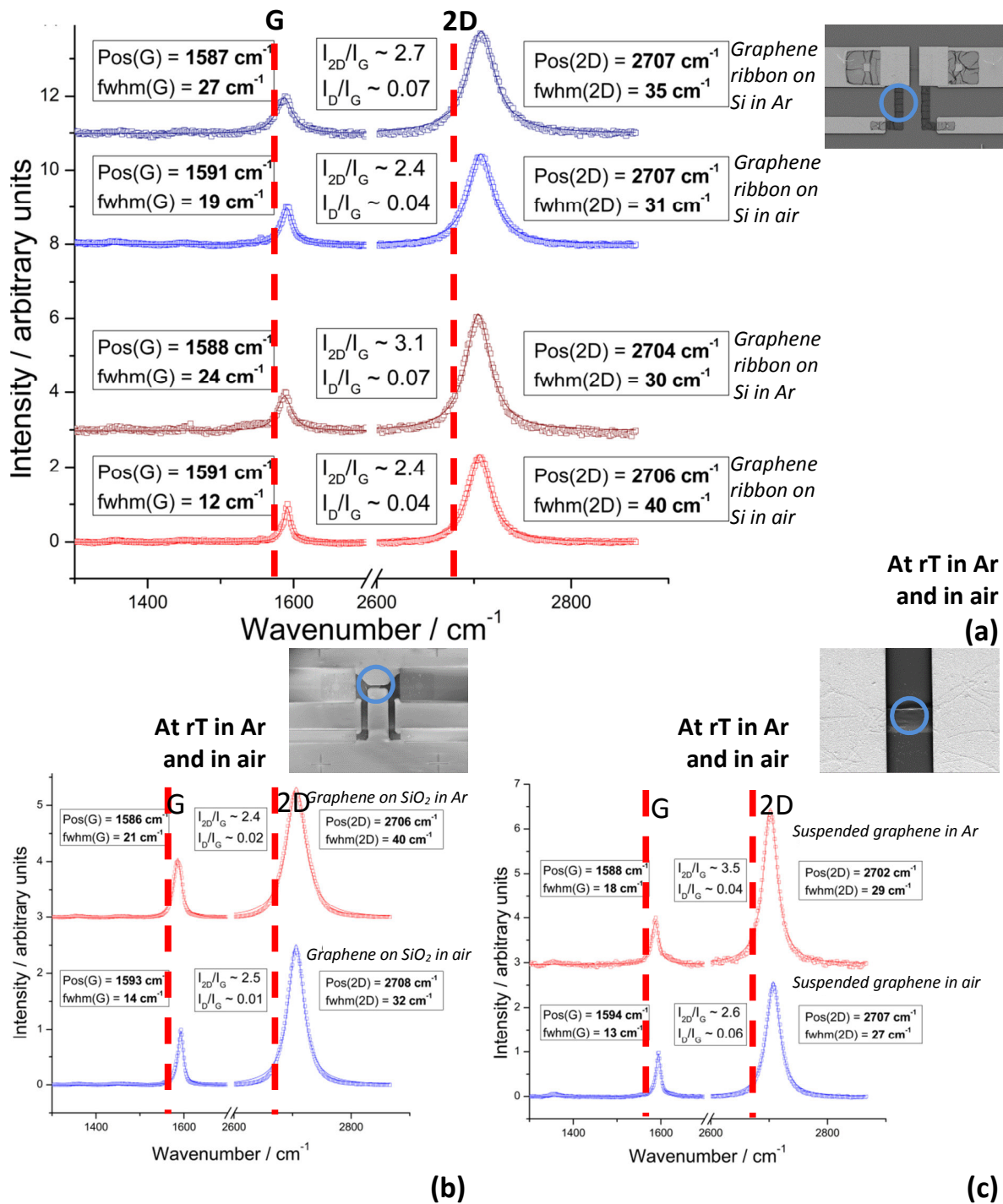
Figure 65. Comparisons of the D, G and 2D bands in Ar and in air, **a)** graphene on Si at two different position on the same sample, **b)** graphene beam on SiO₂ **c)** suspended graphene beam. Each set of 2 plots are taken from roughly the same location on the same sample.

The SEM images show that folds do not unfold during device fabrication or suspending once they are formed. The residual compression must act in a complex manner around folds. Thus, the presence of folds and their interaction with strain might add to the inhomogeneity of the values of G and 2D band positions for suspended graphene beams.
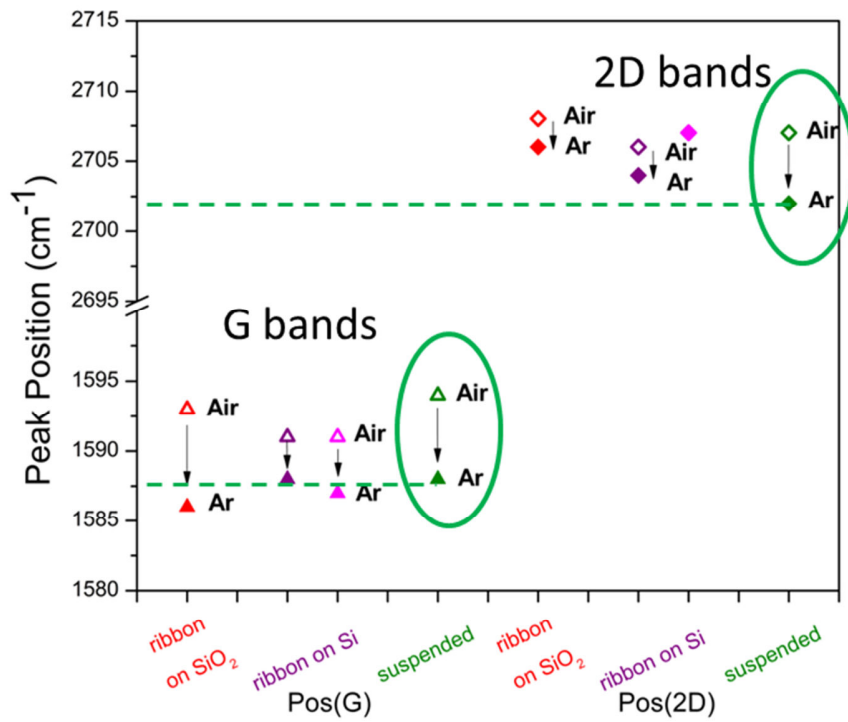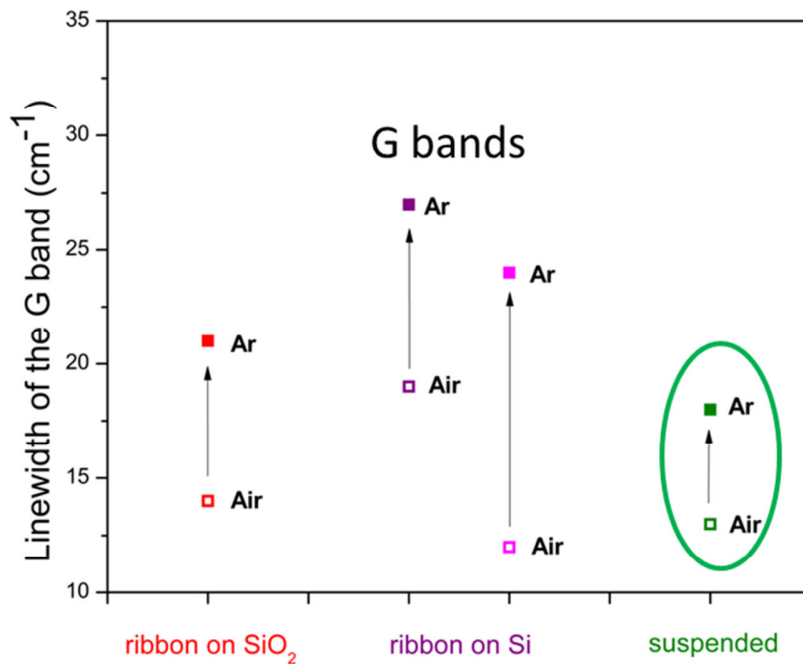
Figure 66 a) G and 2D peak positions and **b)** the G band linewidth are re-plotted from **Figure** 65 to better demonstrate the change in doping levels. In theory, suspended graphene in Ar is no longer under the influence of dopants. The persistent significant blueshift indicates the presence of internal compression.

3.4.8. Influence of temperature

We took additional Raman measurements at elevated temperatures. Bearing in mind the work by Nan et al., which demonstrated that heating graphene in air up to 500°C does not introduce defects, we believe that our samples were safe at temperatures up to 200°C. [169] We compared the behavior of graphene beam on Si and suspended graphene beam at room temperature, at 200°C and after cooling back to room temperature. In addition, we measured graphene beams on SiO_2 in air at room temperature, at 100°C, 200°C, cooled down to 100°C and cooled down to room temperature.

Firstly, we focus on the thermal Raman behavior of graphene ribbons on Si and suspended graphene beam heated under Ar environment. Figure 67a is a comparison of supported graphene before & after thermal treatment up to 200°C in Ar. The samples are measured in air at room temperature before and after heat treatment. However, the heating and cooling is done in Ar atmosphere. We present 3 different graphene beams on Si and 3 different suspended beams from the same sample. It is important to note that the spectra after thermal treatment are taken after letting the sample in air for 24h.

Graphene ribbons on Si in air after thermal cycling in Ar

For ribbons on Si, we firstly observe a systematic and irreversible blueshift of 3 to 6 cm^{-1} in the G band and a blueshift of 2 to 6 cm^{-1} in the 2D band frequency after thermal cycling. (Figure 67a) Additionally, for two out of three ribbons, there is no increase in the fwhm of G bands after heating. (The orange plot appears to show the G band merging with another peak on the lower energy side and therefore we find its fwhm value unreliable for comparison here.) With that, we can make first conclusions about doping. The absence of significant change in the fwhm of G band already hints at no change in doping levels. Hence, the substrates were not significantly altered after thermal cycle. And, while heating the sample under Ar environment surely led to desorption of oxygen and water molecules from top and underneath graphene, the final measurement was taken after 24h in air. That is to say, we believe that there was plenty of time to re-establish the adsorbants on top of graphene. With the lack of significant change in the line width, we do not believe that change is doping is the main factor causing the shift. Doping appears to be restored after the thermal treatment.

The blueshift in both bands accompanied with the lack of change in the fwhm(G) point towards compression as the main factor. We mentioned in Section 3.3.5.2 the difference in thermal expansion coefficients of graphene and the substrate. We also presented studies which demonstrated that supported graphene was argued to leave the thermal cycle with a significant compression. Thus, thermal treatments of graphene, even at as low as 200°C are capable of increasing compression in graphene. This is not only significant in terms of operational temperatures of future graphene devices, but also with regard to the fabrication steps of graphene. During fabrication, it is common to heat graphene shortly at temperatures up to 200°C to evaporate water and increase adhesion to substrate. Thus, this must be done with caution as well.
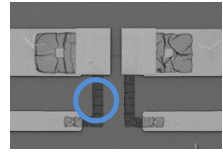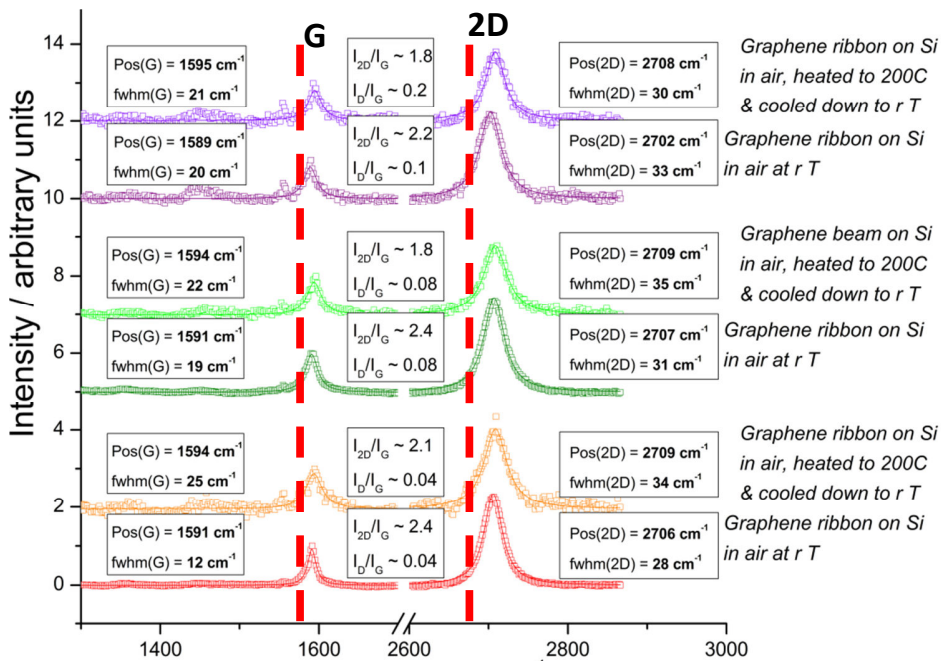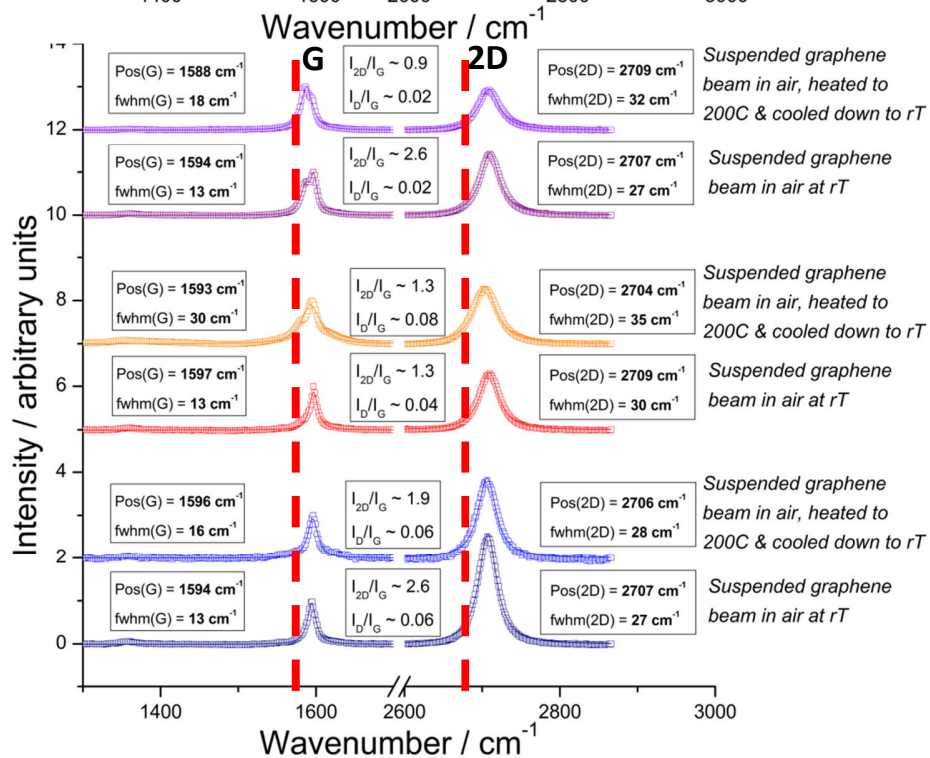
Figure 67. a) Comparisons of G and 2D bands of supported graphene before & after thermal treatment up to 200°C in Ar. 3 upper sets of before & after spectra belong to 3 different graphene beams on Si from the same sample, 1 bottom set belongs to as-transferred graphene on SiO_2. **b)** Comparisons of G and 2D bands of suspended graphene before & after thermal treatment up to 200°C in Ar. 3 sets of before & after spectra belong to 3 different suspended beams from the same sample. All are taken at room temperature in air.

<u>Suspended graphene ribbons in air after thermal cycling in Ar</u>

We now turn to the behavior of suspended samples with temperature shown in Figure 67b. We start by evaluating doping. For all plots, there is a broadening in the G band after thermal cycling. However, we have to be cautious when assigning this broadening directly to the removal of doping in this case. All plots on Figure 67 belong to the same sample which has undergone the same fabrication steps and the thermal cycling conditions. We talked about how the line widths of the supported ribbons did not change indicating that there were no changes in doping levels. Thus, we do expect that the line broadening in suspended beams are due to doping. Besides, for both water and oxygen doping, there were strong arguments in literature saying that they are attracted because of the SiO_2 substrate in the first place. With the lack of the SiO_2 substrate under the Ar environment, we do not believe that doping can have a high impact. Thus, we assign this broadening to strain. In Section 3.3.5.2, we refer to a study which argued that averaging of the G band over an area can lead to its broadening. We believe that thermal cycling led to inhomogeneous stress relaxation in the measured ribbon. The folds are known to be temperature-robust while ripples can form during thermal cycling as we presented in Section 3.3.5.2. This resulted in a complicated strain which varied over the ribbon.

Furthermore, at suspended samples, we observe a redshift of $4-6\ cm^{-1}$ in the G peak frequency for the first two sets caused by thermal treatment in Ar. The third set displays a small blueshift of $2\ cm^{-1}$. And the first and third plots show a small blueshift in the 2D band of $1-2\ cm^{-1}$ while the second one has a redshift of $5\ cm^{-1}$. The lack of uniformity in the shifts of Figure 67b tells us that the thermally induced strain relaxation has a much more complex behavior in suspended samples. Structural deformations are not resolved in a spatially averaged signal of a complex behavior. Raman mapping over these beams would be desired to have a more in depth analysis.

<u>Graphene ribbons on SiO_2 in air after thermal cycling in air</u>

In the two out of three sets of graphene ribbons on SiO_2 in Figure 68a, we observe a significant broadening in the line width of $3-6\ cm^{-1}$ after thermal cycling. Doping must have been indeed reduced during this thermal treatment. Thermal treatments would mainly lead to desorption of molecules; oxygen and water in this case. The fact that this change is more visible for the samples on SiO_2 then for the samples on Si, even if the treatment for the case of SiO_2 was done in air, shows that the substrate SiO_2 indeed has an important role in the attachment of molecules on graphene surface.

Furthermore, there is a blueshift of $4-8\ cm^{-1}$ in the G band and a blueshift of $3-6\ cm^{-1}$ in the 2D band for ribbons on SiO_2 after thermal cycling. This is consistent with the compression induced during thermal cycling on supported samples in Section 3.3.5.2. as well as our samples on Si. Therefore we conclude that any heat treatments such as annealing for device improvement should be done with caution. While it can indeed improve mobility and decrease doping, it can also add a significant amount of compressive stress on graphene.
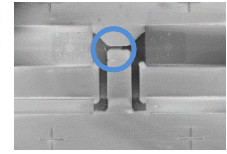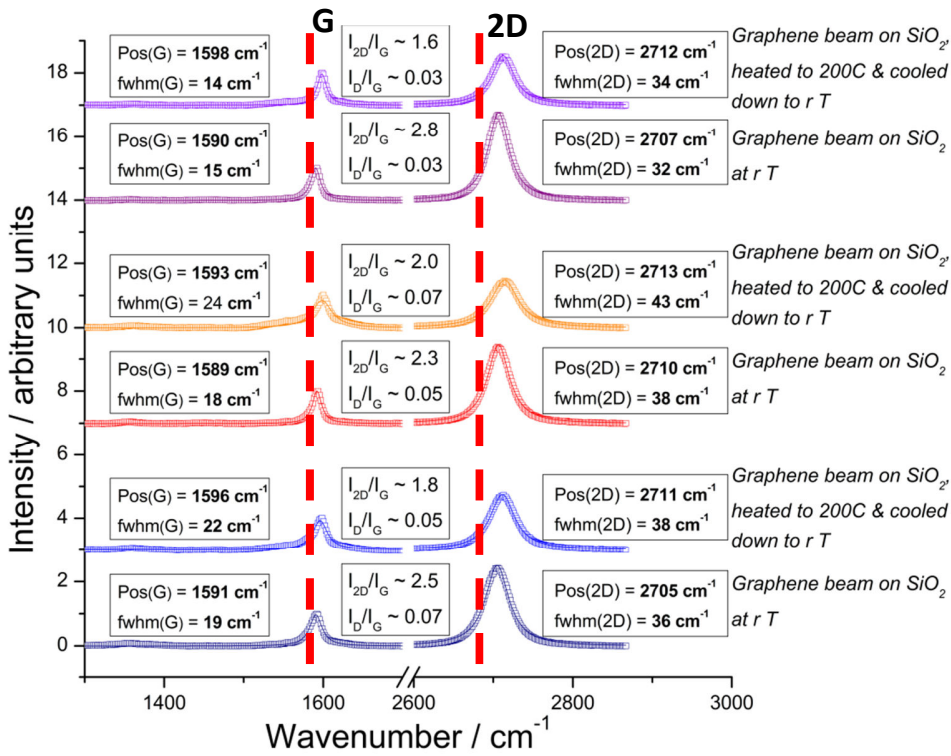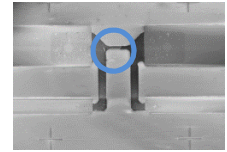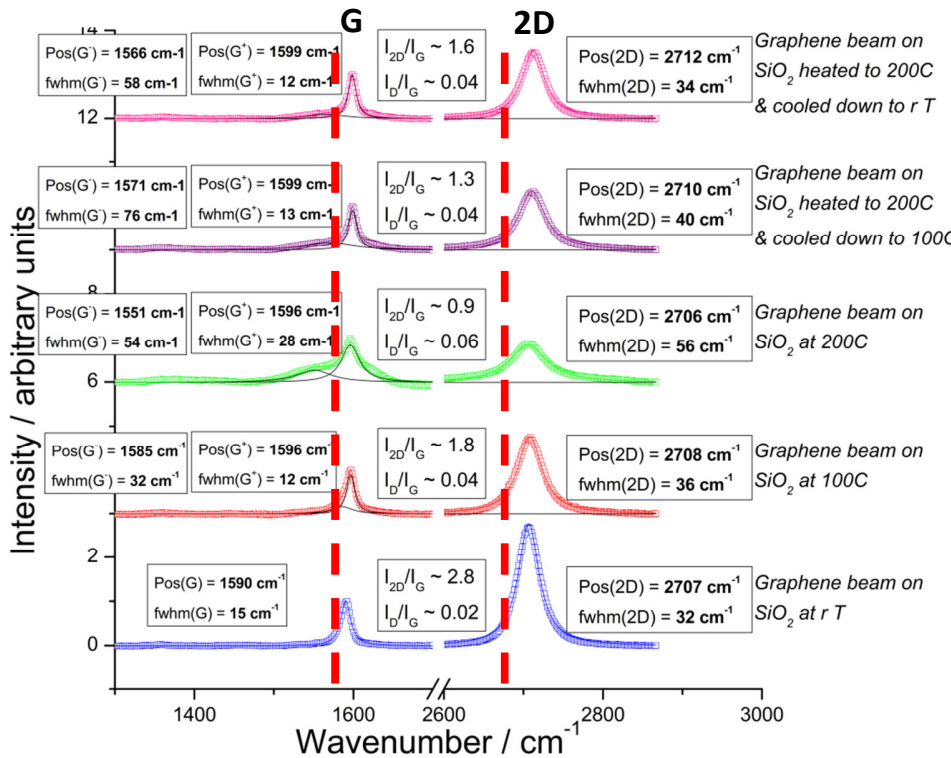
Figure 68. a) Comparisons of G and 2D bands of graphene beam on SiO_2 before & after thermal treatment up to 200°C in air. 3 sets of before & after spectra are taken at 3 different beams on the same sample. **b)** Evolution of G and 2D bands of graphene beam on SiO_2 during thermal treatment up to 200°C in Ar. All spectra are taken in air.

Graphene ribbons at high temperature

In Figure 68b and Figure 69a-b, we study the behavior of the Raman spectra at elevated temperatures. One common feature we observe for ribbons on Si or SiO_2 or suspended beams is the suppression of the 2D band at 200°C. The fact that the intensity is restored once the sample is cooled down to room temperature hints at reversible temporary changes at high temperature as the source of this suppression. The 2D band is generated by a double resonance process which we explained in Section. And therefore, it is very sensitive to the changes in the relative distances of the Dirac cones which can be moved due to anharmonic effects at high temperatures. Therefore, the double resonance process is inhibited leading to a smearing of the 2D band.

G band, however, can occur under non-resonant conditions. We expect a general broadening of the peaks due to anharmonic effects and electron-phonon coupling at elevated temperatures. Thermal smearing of electron energy distribution increases population above the Dirac point and decreases below. It is expected to observe a damping of the E_{2g} phonons due to partial Pauli blocking with the decay in electron – hole pairs at high temperature. [170] [128] The broadening is restored for all ribbons when they are cooled back to room temperature. (In Figure 68b and Figure 69a-b)

While this general pattern is true for the different types of ribbons, the ribbons on SiO_2 differ in one aspect in Figure 69b. There is a gradual splitting of the G band as the temperature is increased. The split bands recombine after cooling down to room temperature. The lower energy band is lower in in intensity and is more smeared out compared to the higher energy band. To analyze this, we first recall that the main difference between the ribbons on SiO_2 and the rest is the fact that it displays higher doping levels and that it is influenced from doping changes more pronouncedly. The G band is created when an electron in the valence band absorbs a phonon and is excited to the conduction band by creating an electron-hole pair. Therefore, it is very sensitive to the spatially inhomogeneous thermal smearing of the electron energy distribution around the Fermi level.

90
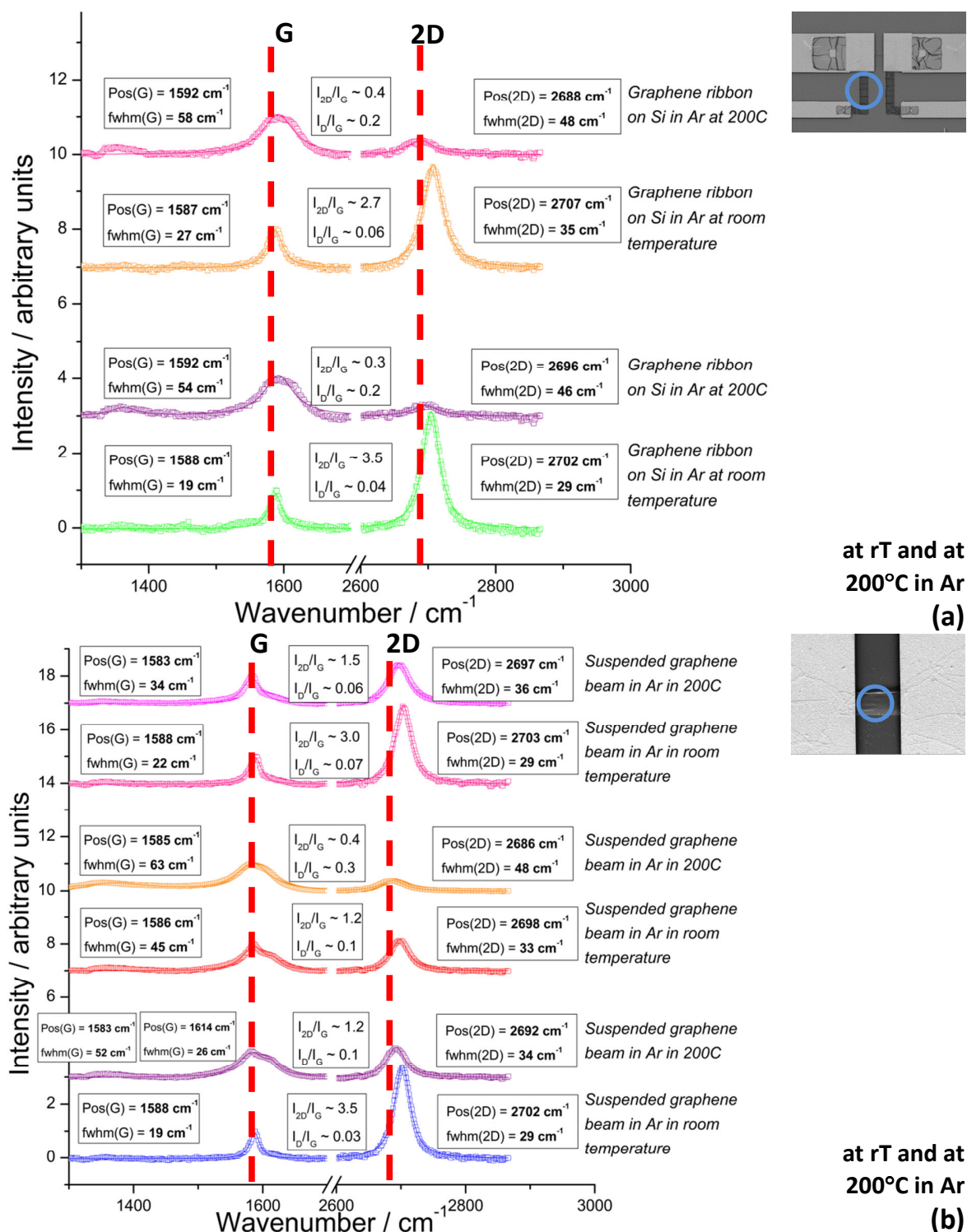
Figure 69. a) Comparisons of G and 2D bands of supported graphene at room temperature (rT) and at 200°C in Ar. 3 upper sets of rT and 200°C belong to 3 different graphene beams on Si from the same sample, 1 bottom set belongs to as-transferred graphene on SiO$_2$. **b)** Comparisons of G and 2D bands of suspended graphene at room temperature (rT) and at 200°C in Ar. 3 sets of rT and 200°C belong to 3 different suspended beams from the same sample.

3.5. Conclusion

We analyzed the fabrication stages as well as the final devices via Raman spectroscopy. The measurements allowed us to have an idea about the influence of fabrication and environmental factors on graphene. We took spectra of as-transferred graphene, graphene ribbon on SiO_2, graphene ribbon on Si and suspended graphene samples and studied them in terms of the G and 2D band frequency, the I_{2D}/I_G intensity ratio and the D band intensity. We experimented by changing the atmosphere to Ar and inspected the consequences. Additionally, we evaluated the temperature-dependent changes of graphene in air and Ar. For that, we chose to increase the temperature up 200°C which is a relevant range in terms of device fabrication and operation; but low enough not to significantly degrade graphene. All of these measurements permitted us to understand the interplay of doping and strain on a Raman spectrum.

The SiO_2 substrate clearly has an important role in the p-type doping of graphene. Be it from its attraction of oxygen or water, we observed significant broadening of the G band once the substrate was removed. Already, compared to the Si substrate, the SiO_2 substrate showed evidence of increased doping each time in the same environment, air or Ar. Considering that the conditions for adsorbates were similar, the triumph of SiO_2 over Si in doping indeed points towards the enhanced attraction of adsorbates by SiO_2.

Recent studies address stress building in CVD graphene due to the high thermal budget during synthesis. This stress is partially relaxed during polymer-assisted transfer or lithography processes depending on the rigidity of the polymers used. The suspended regions in our final devices under Ar atmosphere are largely devoid of doping effects. And yet again, the spectra showed deviations in the frequencies of certain bands. As doping is eliminated, we believe that it is safe to assign the deviations to built-in strain. It appears that the residual strain from the CVD process does not fully relax during fabrication despite wrinkle and fold forming. The folds of the ribbon unfold neither when suspended nor heated. Even the suspended ribbon in the final device is slightly under compression.

Graphene can be heated up to 200°C during device fabrication or up to even higher temperatures during annealing for device improvement. The studies on annealing vary on the subject if it decreases doping or if improves mobility. We observed that heating graphene on s substrate even to temperatures as low as 200°C introduced significant compression. Therefore, we believe that heating graphene even up to temperatures as low as 200°C should be done with caution.

Chapter 4

ELECTRICAL CHARACTERIZATION

We studied the electrical properties of graphene devices. Room temperature measurements were done to assess the electrical operation of the devices; in particular to extract contact resistance and verify hysteresis in electrical properties. Because our devices feature no top gate and either no back gate (suspended beams) or a very thick back-gate oxide (supported beams), current control capability was limited. Therefore, we extracted information about carrier density and mobility by Hall measurements at low temperatures. In addition, Hall measurements have the advantage of allowing independent extraction of the two.

4.1. Contact Resistance

4.1.1. Measurement configuration

To measure the real channel resistance or to extract the contract resistance, several methods are developed among which are the four-probe technique and transmission line method (TLM). The TLM technique is based on measuring the two-probe resistance of devices with different contact separation. Contact resistance can be obtained by extrapolating the two probe resistance from devices with different contact-contact lengths to L=0. The four-probe technique, on the other hand, has two outer current-carrying electrodes and two inner voltage-sensing electrodes. The force current generates a voltage drop across the channel which is measured by the two inner voltage probes. This allows to separate channel properties from contact properties. This is the method we used to extract contact resistance in our devices. (Figure 70)

In a four-probe device, contact resistance can be obtained with the following simple set of formula. The voltage drop across the current leads can be measured with Ohm's law:
$$V = IR \tag{4. 1}$$

The two-probe resistance of a graphene device is the following:
$$R_{2p} = 2R_C + R_G \tag{4. 2}$$

where R_C is the contact resistance, R_{2p} is the total resistance in 2 probe measurement and R_G is the resistance from graphene as:
$$R_G = \rho_G L/W \tag{4. 3}$$

Our devices are fabricated in the pattern from Figure 70. Their four-probe geometry permits us to distinguish between channel and contact properties. We characterized supported devices where graphene is patterned by optical lithography as described in Chapter 2 and our metal stack of choice for electrodes is Cr/Au.

(a) **(b)**
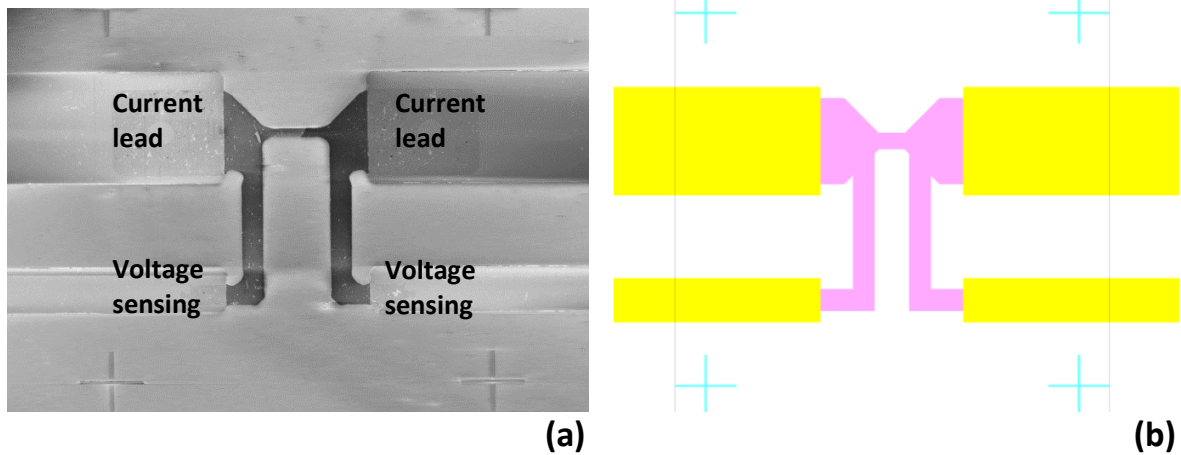
Figure 70. a) SEM image of a sample at the fabrication step where the graphene is patterned by optical lithography with AZ1512, **b)** Photomask design for optical lithography. Pink is graphene and yellow is metal electrodes.

4.1.2. Contact resistance on graphene

Contact resistance in graphene electronics is in general considered as a potential performance killer for both analog and future possible digital applications by limiting the on-current. [36] [171] In graphene optoelectronics, however, it is a strong source of photocurrent due to large band bending at metal-graphene junction. [172] [173]

Due to the limited density of states (DOS) in graphene, current injection from the metal can be suppressed. The linear dispersion relation of graphene leads to a high Fermi velocity of $\sim 10^8$ cm/s and a very small DOS around the Fermi energy. Thus, even though the carriers have high mobility, the very small DOS can restrain current. [174]
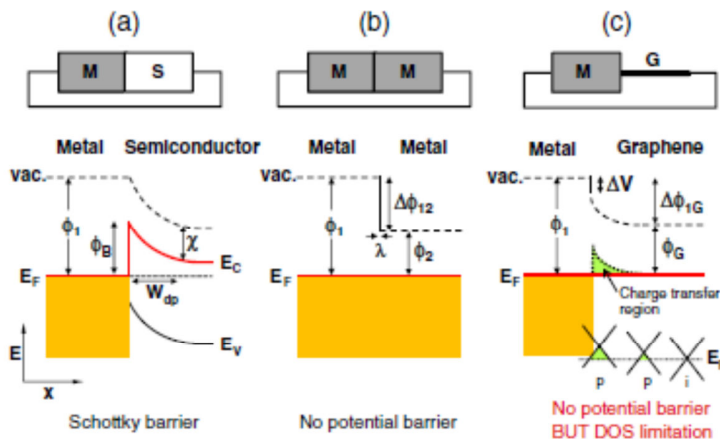
Figure 71. Energy band diagrams at contacts of **a)** metal/semiconductor, **b)** metal/metal and **c)** metal graphene. E_C and E_V are energies of conduction and valence bands respectively. ϕ is the work function of the corresponding material. χ is the electron affinity. [174]

To address the influence of the DOS of graphene on contact resistance, Nagashio et al. looked at the contact of metal/metal, metal/semiconductor firstly and compared these to the case of metal/graphene as in Figure 71. When a metal and a semiconductor come into contact where an external wire permits the Fermi levels to equilibrate, a Schottky barrier forms as:

94

$$\phi_B = \phi_1 - \chi \tag{4.4}$$

where ϕ_1 is the work function of the metal and χ is the electron affinity of the semiconductor. In Figure 71, a depletion layer of w_{dp} appears since the semiconductor has lower carrier density. In contrast to this, no barrier forms at the metal/metal contact except for the screening of a small redistribution of the electron cloud due to the large carrier density. The screening length is defined as:

$$\lambda = [4\pi N(E_F)]^{-1/2} \tag{4.5}$$

where $N(E_F)$ is the DOS at the Fermi level. This length is as short as less than 1 nm in metals. Similar to a metal, graphene does not have a band gap. Figure 72 illustrates the charge transfer at the metal-graphene interface. As one moves away from the interface, the amount of charge transfer from graphene into metal decreases. (Figure 71c) Even a very small transfer of charge changes the Fermi level in graphene powerfully. This transfer leads to a dipole layer at the interface of which the potential difference is shown as ΔV in Figure 71c. The small DOS results in a large screening length. The potential difference ΔV at the metal/graphene interface is not the same as:

$$\phi_{1G} = \phi_1 - \phi_G, \tag{4.6}$$

but it depends on the interaction of the graphene and metal. [174]
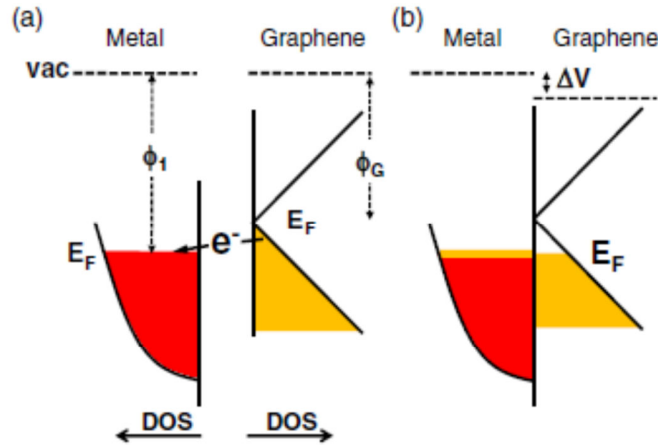
Figure 72. The influence of DOS on the energy bands at the vicinity of the metal/graphene contact **a)** before the contact and **b)** after the contact. [174]

In Figure 73, Nagashio et al. sketched the band diagram of a graphene FET including the charge transfer region in the case of hole-doping. The dash-dotted and dash-double-dotted lines are the evolution of the Dirac point at different gate voltages in Figure 73b. In Figure 73c, the change in the resistivity is shown. In the case of a positive gate voltage, a p-n-p junction can be seen at the contact which adds to the resistance. This increase does not take place in the case of a negative gate voltage since no p-n-p junction is formed. Such difference gives the asymmetric behavior of resistivity with the change of gate voltage depicted in Figure 73d. [174]
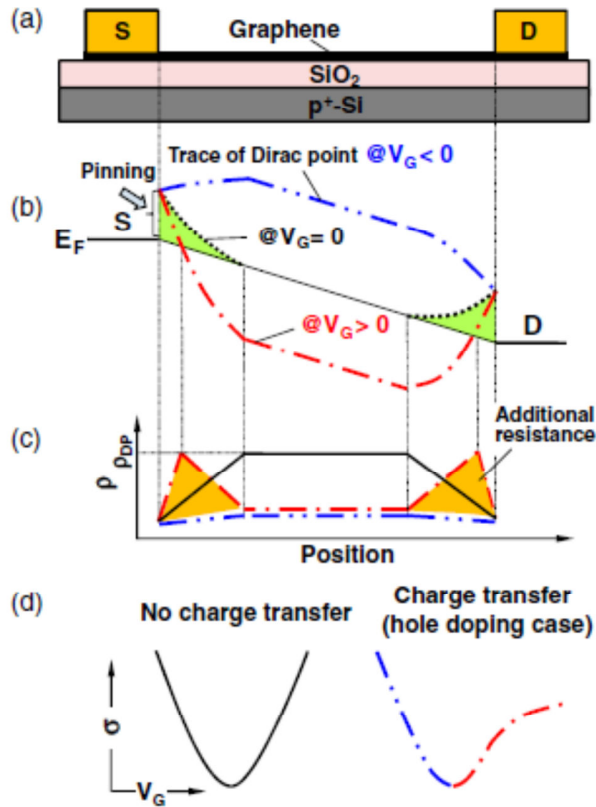
Figure 73. a) Illustration of a graphene device on Si wafer with back-gating. **b)** Energy band diagram of the illustrated device to demonstrate the influence of metallic contacts. The broken line, the dash-dotted line and the dash-double-dotted line represent Dirac points at different color-coded gate voltages. **c)** The change in resistivity is represented corresponding to the areas in the device. **d)** Conductivity for the case with no charge transfer (left) and with charge transfer (right) The additional resistance from the p-n junction leads to the asymmetry in the conduction curve. [174]

Contact resistivity is defined by the contact resistance and the contact area or the contact width. Therefore, understanding the current flow path is important when deducing contact resistivity from contact resistance. It is shown that the current mainly flows from the edge of the metal contact into graphene layer. Contact resistivity is thereof better defined by the channel width as:

$$\rho_C^w = R_C w \tag{4.7}$$

instead of contact area as:

$$\rho_C^A = R_C A \tag{4.8}$$

Nagashio et al. argued that in reality, the current does not exactly flow at the contact edge. They estimated a transfer length through the magnitude of the resistance of the channel and the contact resistivity via a cross-bridge Kelvin probe structure. In Figure 74, they plotted the change in the transfer length with gate voltage for low and high mobility cases. As we see, the transfer length is $\sim 1\ \mu m$. And current crowding was reported for contacts larger than the transfer length. For devices where the contact length was shorter than the transfer length, area conduction and therefore area resistivity needed to be taken into account. [174] Here, we present another perspective by Gong et al. which argued that the metal (Pd an Ti) is not simply deposited as a layer onto graphene. According to them, the metal either undergoes a strong chemical intercalation resulting in a metal-carbide; or it is driven into oxidation and carbidization by the oxygen or carbon in the evaporation chamber or by graphene resulting in a metal-oxide or a metal-carbide graphene contact. [175]

96

There has been a variety of conclusions on the gate voltage dependence of the contact resistivity. For instance, the ρ_c measured by TLM was reported to be constant with gate voltage for Ti/Au and Ni contacts where all contacts were assumed equivalent. [176] [177] On the other hand, Nagashio et al. observed a negative branch of the ρ_c when gate voltage was swept. They explained this with schematics from Figure 75. When four-probe measurements were used to determine total resistance R_{total} and channel resistance R_{ch}, the Dirac points for the total device area and the channel area do not always coincide. When they do not, they give way to the situation in Figure 75a where ρ_c is negative at one side of the Dirac point. If the Dirac points do coincide ρ_c behavior has the shape in Figure 75b. [174]
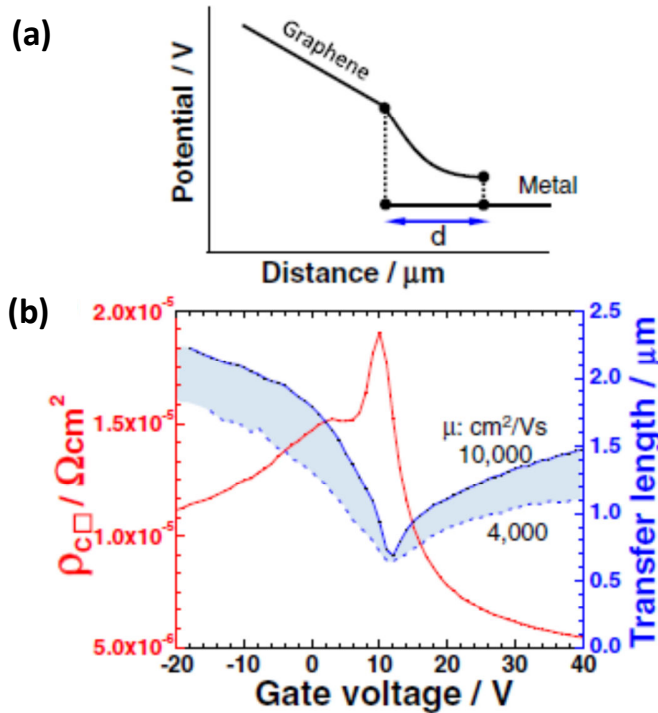
Figure 74. a) A schematic of the electric potential drop at the graphene/metal contact. **b)** the contact resistivity and transfer length determined as a function of gate voltage. [174]

A variety of factors have been reported to influence the magnitude of contact resistance in a graphene device. They can be listed as the following: i) The mobility of the chosen graphene is one of the factors. Higher mobility can lead to better carrier injection efficiency from metal to graphene. [178] ii) The choice of metal or metal stack for the contacts was reported to have a large influence as well. Metals leading to a higher metal-induced doping concentration in the area of graphene under the contact can improve contact properties. [178] For instance, a stack of Ti/Pd/Au is demonstrated to perform better than Ti/Au or Ni/Au contacts. [179] Additionally, Ni was claimed to be a good choice in reducing the contact resistance due to its comparatively high work function. The contact resistivity for Ti/Au and Cr/Au contacts were generally reported as largely varying as 10^3 to 10^6 Ω μm. Ni contacts, on the other hand showed a low and uniform resistivity. [174] [180] iii) The method of choice for the realization of the contacts is another factor. Sputtering was claimed to produce significantly larger contact resistance in comparison to evaporation. The explanation was given by the fact that sputtered metal atoms have higher kinetic energies which remove carbon atoms from graphene; i.e. introduce defects into the graphene layer. [175] And the parameters of the evaporation technique have an influence as well. Russo et al. showed that lower background pressure during metal evaporation led to lower contact resistance for contacts involving Ti. They argued that molecule adsorption on graphene before evaporation or the partial oxidation of Ti during evaporation are possible explanations. As the background pressure, metal deposition rate is

another parameter of contact realization. The deposition rate leads to a [176] certain grain size for each type of metal. Watanabe et al. argued that metal grain size affects the contact area where smaller grains have more contact area with graphene and therefore lead to an improved contact. [181] iv) Another factor is the interface. Graphene surface can have polymeric residues from fabrication which interfere with the contact. In the work by Hsu et al., a sacrificial layer of Al was deposited in-between the photoresist layer and graphene such that the graphene was prevented from coming into contact with polymers. The authors showed that eliminating photoresist residues led to a fourfold decrease of contact resistance. [182]
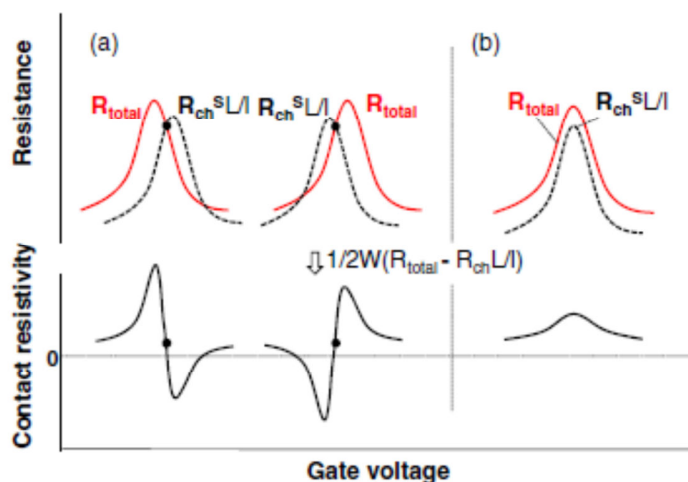
Figure 75. Representations of different types of contact resistivity change with gate voltage. **a)** The relative positions of Dirac points are different for the total resistance and the channel resistance. **b)** They are almost equal. [174]

4.1.3.   Measurement results

Figure 76 is a representative two-probe I-V measurement from our devices. The linear behavior states that there were good Ohmic contacts between the metal and graphene. The voltage was swept up and down for two cycles where all measurements followed each other perfectly, i.e. no hysteresis was observed during I_d/V_d measurements.

We extracted a contact resistance of $\sim 100 - 150\ \Omega$. We base the subsequent calculation of contact resistivity on the Equation 4.7, considering that the current in graphene was reported to flow mainly at the edge of the contact. Our devices demonstrated a channel resistivity of 0.9 - 2.1 kΩ/□ and a contact resistivity of approximately $\sim 2 - 3 \times 10^3\ \Omega$ μm where the voltage is swept from -1 to 1 mV.

In Section 4.1.2, we mentioned that the contact resistivity of Cr/Au has been reported to vary between $\sim 10^3 - 10^6\ \Omega$ μm. Our fabrication clearly resulted in a contact resistivity at the lower end of this variation. We believe that low contact resistance is achieved by two main effects from our fabrication method. In the same section, we summarized several opinions and studies on the influence of the interface and electrode realization on the contact resistance of the final device. As we explained while describing the fabrication process in Chapter 2, the methods we employed have a particular focus on the improvement of the interface. While this was intended to successfully suspend the graphene ribbon, it also decreased the polymeric residues at the graphene/metal contact. Avoiding the influence of plasma hardening on the resist and adding the acetic acid cleaning helped towards a pristine interface. In addition to the interface, we talked about a study which discussed the effect of chamber pressure on the metal evaporation. Molecule adsorption on

graphene before evaporation or the partial oxidation of Ti during evaporation can deteriorate the electrode partially under insufficient vacuum levels. The standard user parameters for our evaporation equipment involve a pressure of $\sim 10^{-8}$ mbar in the evaporation chamber and a pressure of 10^{-6} mbar in the load lock. To improve contact properties, we further decreased the load lock pressure down to 10^{-7} mbar such that it interferes with the chamber pressure even less at the transfer of sample holder. Additionally, we deposited 20 nm of Ti while the shutter is closed, i.e. Ti did not land on the sample. Ti is known to trap the remaining oxygen atoms and further improve the chamber vacuum. Thus, we believe that these measures along with the care of the interface resulted in the low contact resistance of our devices.
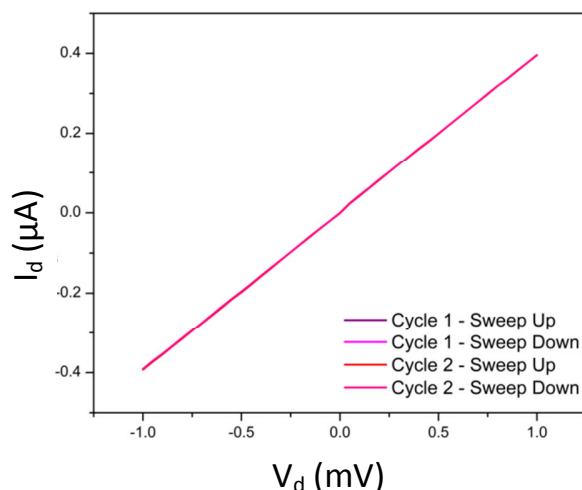
Figure 76. I-V curve of a 2-probe measurement from a representative graphene device on SiO_2. The voltage is swept from -1 mV to 1 mV in increments of 0.5 µV in two cycles. The cycles coincide perfectly and the linear relation of I_d/V_d indicates good Ohmic contacts.

4.2. Hysteresis

4.2.1. Possible origins for hysteresis from literature

Ideally, the charge neutrality point (CNP) of graphene must be located at zero gate voltage. Under ambient conditions and on a SiO_2 substrate, however, graphene devices demonstrate p-type doping as we mentioned during the analysis of Raman measurements in Section. The origin of this doping has often been related to adsorbates on top and underneath graphene. [149] [183]

It is possible to observe hysteresis in either direction as sketched in Figure 77. The CNP can move towards negative voltages or towards more positive voltages. Wang et al. suggested two mechanisms which explain the CNP movement in each direction: capacitive gating and charge transfer. Capacitive gating occurs when there is a dipole layer between graphene and the back-gate. Usually, this layer is made of adsorbed water molecules under ambient conditions which lead to charge trapping. The accumulation of charge in trap centers, such as the surface states between graphene and the oxide, can screen the electric field of the back-gate. [183] A study by Lee et al. showed that the surface states at Si/SiO_2 and the bulk states in SiO_2 do not participate in such trapping. [184] As illustrated in Figure 77c. charges can move to graphene and align in dipoles under external electric field. Through this, the electrical field in graphene is enhanced locally which attracts even more majority carriers from metal contacts. Thus, the carrier density of graphene is higher and a hysteresis shift is observed in the form of Figure 77d. Capacitive gating is observed commonly in devices that are gates by electrolytes. [183]

Figure 77. Illustrations for the two mechanisms which affect the carrier density and hysteresis in graphene devices. **a)** Sketch of the charge transfer mechanism which leads to the type of hysteresis [183] depicted in **b)**. If a charge is transferred from graphene towards charge traps at the interface the conductance upshifts as shown in **b)**. **c)** Sketch of the capacitive mechanism [183] which leads to the type of hysteresis depicted in **d)**. A charged ion modifies the local electrostatic potential around graphene which attracts more positive charges from metal contacts.

Charge transfer, on the other hand, leads to a hysteresis in the opposite direction as in Figure 77b. When back-gating at negative voltage regime, the holes in graphene get trapped in trap centers such that in time, graphene "feels" a more positive gate voltage than the applied gate voltage. These charges lead to an opposite-doping of graphene as in Figure 77a. Thus, in negative regime, the gate voltage sweeping downshifts the CNP as represented in Figure 77b. Following this, the gate voltage sweeping in the positive regime injects electrons into the traps centers leading to an upshifting of the CNP. The charges continue being trapped until the gate polarity is reversed in direct current. When a total charge Δq is transferred to or from graphene a positive shift of conductance takes places as in $\Delta q = C\Delta V$, where C is the dielectric capacitance. [183]

Charge transfer is related to the dissociation of oxygen and water on graphene surface. When water is in equilibrium with air, it is slightly acidic with a pH of 6. The electrochemical potential of graphene is therefore higher than that which leads to electron transfer from graphene. Dissolved oxygen assists this transfer. Thus, if the pH is increased, the transfer could be reversed to opposite direction. The redox reaction, which is the origin of the unintentional p-doping of graphene FETs, is affected by the back-gate. There is a disagreement on the charge transfer mechanism on if the charge transfer takes place directly between graphene and water or if there is a mediating neighbor such as an oxide or polymeric residues which present the hydroxyl groups. Such a neighbor can give or take protons to and from the solution resulting in a bound surface charge. Furthermore, gate voltage has been observed to be capable of changing the pH of the water layer next to an oxide. Veligura et al. argued that, regardless of the type, both mechanisms lead to a hysteresis with the same direction. (Figure 77b) [185]
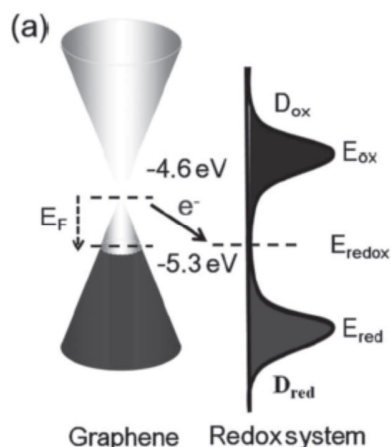
Figure 78. Illustration of the doping mechanism in graphene from O_2/H_2O. The arrow shows the direction of charge transfer. [186]

It is commonly known that on the surface of a SiO_2, hydroxyl groups couple to dangling bonds of Si and result in the hydrophilic silanol groups on SiO_2 layer. Lafkioti et al. argued that loosely bound molecules such as water attached to the silanol groups must be the source of doping and hysteresis since both can be suppressed when graphene is pumped to vacuum atmosphere without additional heating. [149]

Xu et al. emphasized that a mixture of O_2 and H_2O exposure brings heavier doping than the species individually under the same partial pressures. They further argued that a lone exposure to either O_2 or H_2O results in no doping. In contrast to Lafkioti et al., the authors added that simple evacuation cannot remove the doping after H_2O exposure and that heating is indeed necessary. They further added that the presence of SiO_2 is vital for doping to occur; the authors claimed that they observed no doping for the case of free-standing graphene devices. This supports their claim that the doping species O_2 and H_2O are placed in-between graphene and SiO_2 instead of on top of the hydrophobic graphene. Also, in a theoretical perspective, the electron affinity of O_2 (0.44 eV) is significantly lower than the Fermi level of graphene (4.6 eV). Thus, a direct charge transfer is not favorable. Instead, a mechanism has been proposed which involve O_2/H_2O and graphene as a redox couple. The Fermi level of graphene (-4.6 eV) is higher than the electrochemical potential of the redox couple O_2/H_2O. This was presented as the necessary driving force to transfer electrons from graphene into the unoccupied states of O_2/H_2O as depicted in Figure 78. While a direct charge exchange is not expected to lead to hysteresis, redox reactions of O_2/H_2O and graphene give way to hysteresis. [186]

The two mechanisms of charge transfer and capacitive gating have been suggested to be competing in a graphene device. Moreover, they are influenced by gate sweeping rate differently. Slow gate sweeping can enhance the hysteresis due to charge trapping and suppress the hysteresis due to capacitive gating. [183]

Current annealing can be a method which helps suppressing hysteresis. [183] Additionally, ensuring that there is no water layer accumulating in-between the graphene and SiO_2 interface is another method. Depositing a layer of HMDS before graphene transfer, which is a substance leading to hydrophobicity, can be of assistance in decreasing hysteresis as well as p-type doping. [149]

4.2.2. Measurement results

We back-gated a device in the same pattern as in Figure 70. This device had an oxide layer of 500 nm on each side of the Si wafer which decreased the influence of the back-gate significantly. 100 V is the highest value our equipment can safely go up to, thus our measurements were restricted to $\mp$ 100 V for the back-gate voltage. As expected from graphene devices on SiO_2 under ambient conditions, the device was clearly far from the CNP and in the p-type doping regime (Figure 79). As the device was depleted in holes, i.e. in the positive regime of V_{bg}, (Figure 79a) the conductance decreased. We presented several theories on the doping mechanism of graphene with a combined influence from the SiO_2 surface and the O_2/H_2O adsorbants below or above graphene. These findings were consistent with our interpretations of the behavior of the G and 2D bands in Raman spectra from Section.

In general, a non-annealed graphene device shows little current modulation with back-gating. [183] Therefore, along with the rather thick oxide layer on our samples, the lack of annealing led to the expected limited modulation of current. (Figure 79)

(a)   **(b)**
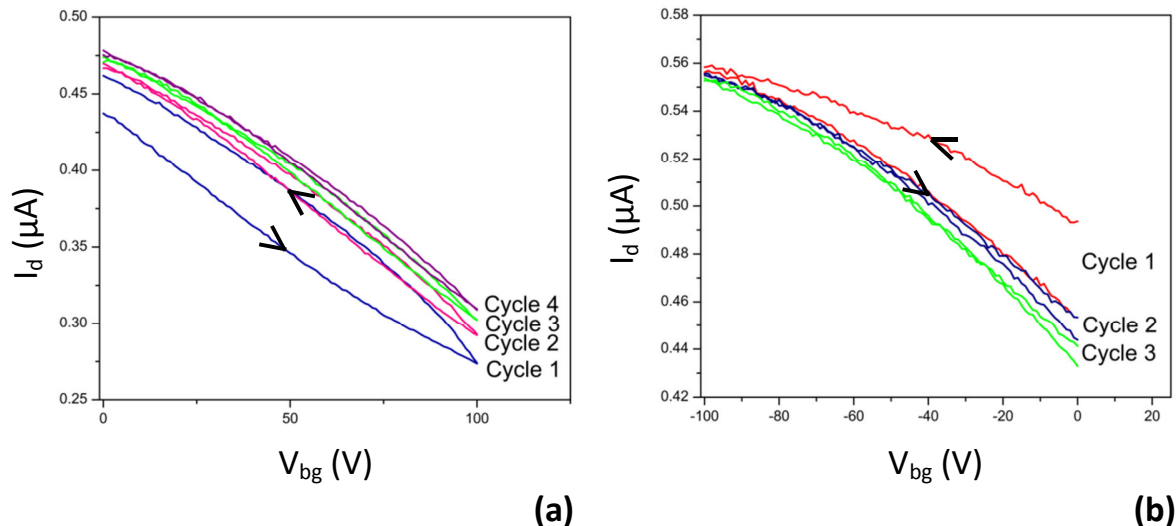
Figure 79. Hysteresis I_d/V_{bg} curves from a back-gated device **a)** where the gate voltage is swept from 0 V to 100 V and **b)** where the gate voltage is swept in opposite direction from 0 V to -100 V. The arrows show the direction of the sweeping. For the cycles in **a)**, the curve that is higher in I_d follows the curve that is lower in I_d. For the cycles in **b)**, the curve that is lower in I_d follows the curve that is higher in I_d.

The charges continued being trapped as long as the gate voltage direction was preserved. This explains the lack of the large hysteresis for cycles after the first one, both in Figure 79a and b. In both graphs, the cycles after the first one follow the backwards sweeping curve from the first cycle. This supports the idea of holding the charges trapped in the gate voltage region of the same polarity.

Hysteresis can be clearly observed at the first cycle both at the positive (Figure 79a) or negative (Figure 79b) gate voltage regime. For both regimes, the hysteresis disappears at later cycles. Even though the device was far from the CNP, the decrease/increase in the conductance enables us to distinguish the dominating mechanism causing the hysteresis. The behavior of conductance at the hole depletion/injection regions is similar to the sketch from Figure 77b. Thus, charge transfer must be the origin of hysteresis. At negative gate voltages, the device was exposed

to a more positive voltage when holes from graphene were trapped in trap centers. It was explained earlier that the O_2/H_2O attached to the silanol groups of the oxide layer have the capability of obtaining/donating protons. The system then most likely created a redox couple with graphene as explained and functions as a charge trap center.

One solution that is generally proposed to suppress hysteresis is annealing. However, we did not anneal our devices. At this moment, there is not a consensus on the influence of annealing on the doping of graphene devices. While it can clearly be efficient in removing adsorbates such as oxygen and water molecules as well as reducing the amount of fabrication residues from graphene surface and the SiO_2/graphene interface, it can suppress or promote p-type doping. Therefore, we believe that we need to characterize the devices thoroughly before introducing annealing into our fabrication steps. In Chapter 3, we found out that heating up to 200C did decrease doping for a device on SiO_2, however it also added significant compression. Moreover, annealing is proposed to be carried out in Ar, N_2 or vacuum atmospheres, even traces of oxygen at elevated temperatures can degrade graphene partially. Therefore, annealing is only safely implemented under ultra-high vacuum (UHV) conditions. Even if access to UHV furnaces is considerably difficult in comparison to flowing Ar or N_2 in a furnace, it is the most secure choice.

4.3. Hall mobility at low temperature

4.3.1. Mobility in graphene

Mobility is often taken as a figure of merit of graphene. When comparing the mobility from different devices, the first point to factor in is the substrate. The substrate is known to generally interfere with transport properties of graphene. [187] This has been proven when Bolotin et al. showed that suspended devices from exfoliated graphene can reach to mobilities of 200 000 $cm^2V^{-1}s^{-1}$.

We focus on the mobility of devices on SiO_2 with graphene from two different sources by giving some numbers as guidance for graphene/SiO_2. Mobility for exfoliated graphene has been reported as approximately 10 000 $cm^2V^{-1}s^{-1}$. [8] Mobility for CVD can vary greatly depending on the cleaning methods, annealing and grain size. Reported values differ between $800 - 5000$ $cm^2V^{-1}s^{-1}$. [188] [189] [190] [191] In comparison to exfoliated graphene, devices made of CVD graphene exhibited lower mobility, higher impurity doping and higher asymmetry between electron and hole conduction. [192]

CVD graphene devices are known to have three main sources of disorder: i) grain boundaries due to synthesis conditions, ii) contamination due to fabrication conditions and iii) point defects, Grain boundaries have the greatest influence on lowering mobility. [188] Graphene grows on metal catalytic surface at random nucleation points which then merge to form a continuous surface. Grain boundaries are line defects between disoriented grains and can act as barriers with a width of a few nm which interfere with the propagation of charge carriers, both for electrons and holes. [193] The influence of grain boundaries on the mobility has been investigated by growing grains which are significantly larger than the device size (of ca. 250 μm). Mobility extracted from the devices made of such large grains has been compared against mobility from devices made of small grains. In other words, devices with and without grain boundaries were compared. This comparison came to revealing that the grain boundary has indeed a large effect on mobility. Another study defined two

types of mobility in devices made of CVD graphene as "inter-domain" and "intra-domain" mobility. It was revealed that the latter is 3 times as high as the former reaching the values of devices made of exfoliated graphene. [194] This was taken as evidence that the grain boundary is the main factor in lowering mobility.

Another study had a different perspective on the effect of grain boundaries. It interpreted the behavior of mobility at grain boundaries as "n-type inversion channels" in p-type graphene on SiO_2 leading to p-n junctions. The Dirac point has been mapped over CVD graphene via measuring the spatial distribution of tunnel conductivity (LDOS) minima. The study revealed that the Dirac point was located at a pronounced n-type region over grain boundaries in contrast to the p-doped grains. The origin of this behavior has been debated; it is argued to originate from self-doping through a charge transfer between the line defects and the defect-free area or adsorbates which preferably attach themselves to grain boundaries. [193] A line defect can disrupt the sp^2 bonding and enhance the surface chemical activity, i.e. promote surface reactions with adsorbates. [195]

The influence of point defects were compared against the one of line defects on lowering mobility. Graphene solely with point defects is produced by treating exfoliated graphene with oxygen plasma. Exfoliated graphene is taken for comparison since it is single crystal, i.e. with no grain boundaries. The increase in point defects by plasma is verified through Raman measurement by measuring the I_D/I_G ratio. [188]

The most common procedure to increase mobility has been proposed to be annealing. It has been often employed to improve the transport qualities of graphene which has undergone fabrication processes. During fabrication, contaminants from photoresists cannot always be fully removed from the hydrophobic graphene surface by conventional solvents. These can act as external scattering centers and degrade transport properties. Heating at $300 - 400°C$ in Ar/H_2 [196] atmosphere or nitrogen atmosphere [188] or in ultrahigh vacuum [197] is among proposed processes. Another method is Joule heating where current is conducted through graphene with the intention of removing contaminants. [198] However, it has also been reported that this heating process increased the interaction between graphene and the SiO_2 substrate. This added to the existing p-type doping by intensifying the influence of charged impurities at substrate interface. However, the opposite has been proposed as well. Heating was reported to clearly restore charge neutrality point, but actually lead to lower mobility. [188]

4.3.2.   Mobility extraction from Hall measurements

When a magnetic field is applied to an electrical conductor perpendicular to the current, there is a voltage drop across the conductor transverse to the current. In Figure 80b, when magnetic field is applied in the z-direction during a current flow in x-direction, the resulting Lorenz force accelerates electrons in the (–y) direction. This voltage is called the Hall voltage and the behavior is called the Hall effect. The effect can be used to extract carrier mobility and carrier concentration separately. We use a 3D example as sketched in Figure 80 to demonstrate mobility extraction from classical Hall effect.
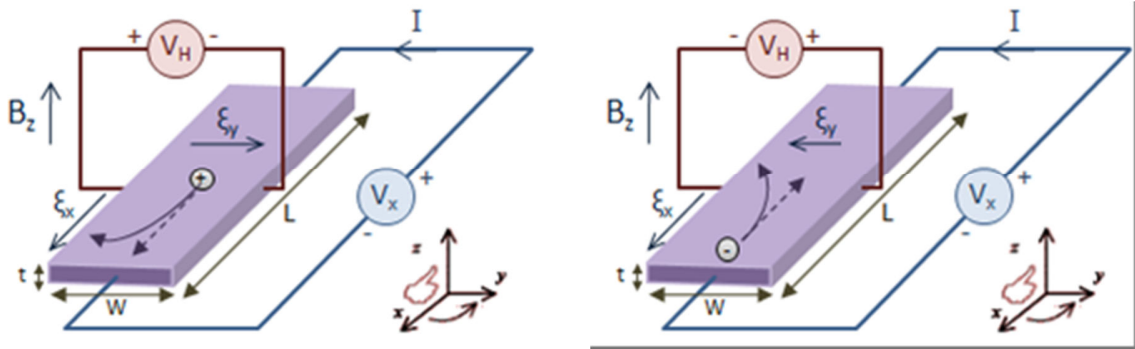
Figure 80. Hall measurement setup for **a)** holes and **b)** electrons. V_x is the longitudinal voltage, V_H is the Hall voltage. B_z is the external magnetic field, ξ_x and ξ_y are the electrical field in the corresponding directions. [199]

The Lorenz force is defined for electrons (n) and for holes (p) as the following:

$$\overrightarrow{F_{Hn}} = -q(\vec{v}_n x \vec{B}_z) \qquad (4.9)$$

$$\overrightarrow{F_{Hp}} = +q(\vec{v}_p x \vec{B}_z) \qquad (4.10)$$

$\vec{F}_H$ is the Lorentz force, q is the charge, υ is the carrier velocity and B is the magnetic field. The Lorenz force is countered by a force originating from the Hall voltage leading to a zero net force on the carriers. For electrons, the following holds true:

$$\vec{F}_y = (-q)\vec{\xi}_y + (-q)[\overrightarrow{v_n} \, x \, \overrightarrow{B_z}] = 0 \qquad (4.11)$$

$$\xi_y = v_x B_z \qquad (4.12)$$

Introducing the electron sheet density n_s (integral of electron concentration n on the film thickness t), the electron current is described as follows:

$$I = -q n_s v_x w \qquad (4.13)$$

where w is the width as shown in Figure 80. When the carrier velocity $υ_x$ from equation 4.12 is introduced into the Equation 4.13 and keeping in mind that

$$\xi_y = V_H/w \qquad (4.14)$$

it is possible to obtain electron sheet concentration as:

$$n_s = -\frac{IB_z}{qV_h} \qquad (4.15)$$

Usually, n_s is thus extracted from the slope of V_H variation with magnetic field, which is expected to be linear. A similar equation holds for holes. Mobility is then extracted from the simultaneous measurement of the resistivity or –rather in the case of thin films– of the sheet resistivity ρ_s measured in Ohms per square, $\Omega/\square$. (per units of L/W).
Indeed, following,

$$V_x = \mu_0 E_x = -\mu_n \rho_{ns} I/W \qquad (4.16)$$

which can be equaled to the value deduced from 4.12

$$V_x = \frac{V_H}{WB_z} \qquad (4.17)$$

This allows mobility to be extracted as:

$$\mu_n = -\frac{V_{Hn}}{\varrho_{ns}IB} \qquad (4.18)$$

Similarly, it is possible to obtain the hole mobility μ_p as:

$$\mu_p = -\frac{V_{Hp}}{\varrho_{ns}IB} \qquad (4.19)$$

where ϱ_{ns} and ϱ_{ps} are the sheet resistivity for electrons and holes, respectively. For 2D materials, the thickness t is discarded. Instead, the resistivity is defined in the units of Ω per square instead of Ω cm.

4.3.3. Measurement results

We have fabricated Hall bar structures with the methods we explained in the Chapter 4. An SEM of the device type we used to extract mobility is shown in Figure 81a. We could only mount two samples in the cryostat and had time to measure one. On this device, we performed electrical measurements in the presence of magnetic field at low temperatures. We swept the magnetic field from -5 T to 11 T back and forth while measuring the longitudinal resistance R_{xx} between contacts 3-5 and the Hall resistance R_{xy} between contacts 3-4 and passing current through 1-2 at 4 K and 20 K. These measurements give us an insight on the mobility and magnetoresistance of our samples.
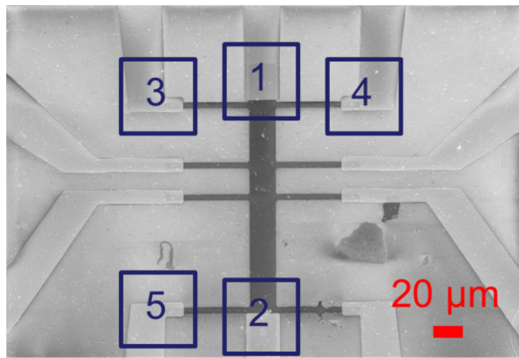
(a)
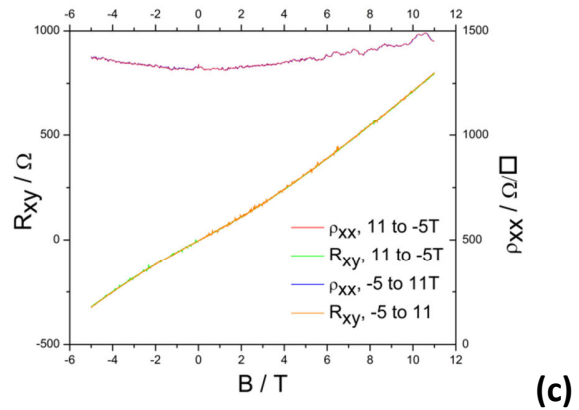
(c)
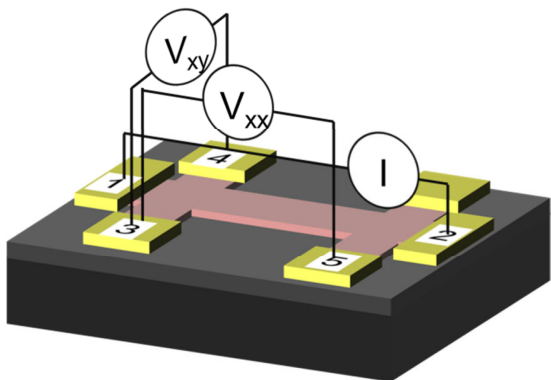
(b)

Figure 81. a) SEM image of a Hall bar structure. Numbers correspond to **b)** the sketch for Hall bar measurements. **b)** Electrodes are illustrated to explain the way Hall mobility is extracted. **c)** Hall resistance and longitudinal resistivity are plotted against magnetic field at 4 K. Magnetic field is swept from -5 to 11 T passing through zero field for corrections. The grids in the left and right y-axis have the same scale.

We present the raw data from our measurements at 4 K in Figure 81c. When ρ_{xx} and R_{xy} were plotted with the same grid space in y-axis, the ρ_{xx} appears sufficiently flat to calculate mobility from carrier density. Considering that for a 3D material:

$$R_{xy} = \frac{V_H}{I} = \frac{B}{nte} \qquad (4.\,20)$$

where e is the elementary charge, it is possible to extract the carrier concentration n from the slope the Hall resistance as a function of magnetic field as dR_{xy}/dB. And by inserting the carrier concentration into equation 4.17, we obtained Hall mobility.

Our device displayed a carrier density of 9×10^{12} cm^{-2} and through that a mobility of ~ 500 cm^{2}V^{-1}s^{-1}. Here, we must point to a necessary correction. In Figure 81a we can observe that the contacts 3 and 4 were fairly close to the contact 1. Therefore, the Hall voltage measured at the vicinity of the current contact did not correspond to the maximum Hall voltage in the ribbon. That is to say, corrections were necessary. We simulated the variation of the Hall voltage across the Hall bar ribbon via Finite Element Method (FEM) in software FlexPDE based on the classical Drude's model as in Figure 82 and calculated the necessary correction for the Hall voltage and through that the Hall resistivity. For the calculation we needed to take into account the uncertainty of the distance 3 and 4 from the contact 1 due to alignment error during lithography process. We came to a corrected mean value of $3.6 * 10^{12}$ cm^{-2} for carrier density and 1200 cm^{2}V^{-1}s^{-1} for mobility where the minimum necessary correction was calculated as $5.6 * 10^{12}$ cm^{-2} for carrier density and 800 cm^{2}V^{-1}s^{-1} for mobility.

Among graphene devices on a substrate, it is known that the mobility of CVD devices cannot compare to the ones made of exfoliated graphene. [188] Impurities and defects are possible reasons recognized for low mobility. Among those are surface contaminants, point defects and grain boundaries, or in other words "line defects". The formers can be introduced during any step of device production from all types of graphene while the latter, grain boundaries, are intrinsic to CVD synthesis. [188] [194] We have mentioned earlier that Song et al., 2012 have demonstrated that the presence of grain boundaries have the largest impact on mobility. These line defects are described to act like a high resistivity potential barrier. [194] Therefore, regardless of how clean and defect-free the graphene is in our samples, the devices will have a comparatively low mobility as long as the graphene source is polycrystalline.

Our sample was heavily p-doped as expected for graphene on SiO$_2$ in air. Several mechanisms have been proposed to cause p-type doping for graphene on SiO$_2$ among which there are charge-transfer doping from H$_2$O and O$_2$ molecules, [200] increase in the number of scattering sites with polymeric residue [196] [197] and influence of metal contacts. [201] It is worthy to add that no annealing has been done to our samples which could help removing adsorbants/impurities and bringing the charge neutrality point closer to Dirac point.
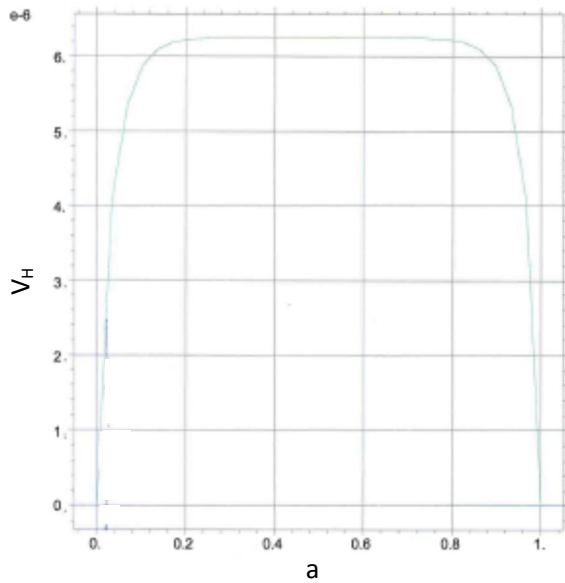
Figure 82. Simulation results for the Hall voltage variation over the ribbon length. 'a' represents the position along the ribbon, normalized to its entire length. The absolute value of V_H depends on the resistivity chosen but its relative variation with respect to the maximum value does not.

The longitudinal resistivity appears rather flat in Figure 81c. When it is expanded, however, we observe reproducible features, both at low and high magnetic fields. We will categorize and address them in the next section.

4.4. Observation of quantum effects in magnetoresistance

We expanded the scale of magnetoresistivity ρ_{xx} in Figure 87a and we see some features at the vicinity of zero magnetic field, large amplitude oscillations towards higher magnetic fields and small amplitude oscillations at all magnetic field values. To identify these, we introduce some basic phenomena stemming from quantum interference and quantum confinement effects.

4.4.1. Weak localization

4.4.1.1. Theory and weak localization in graphene

Weak localization is a phenomenon observed at fairly low temperatures in disordered electronic systems where the transport is diffusive instead of ballistic. That is to say, the carrier passes through random scattering events while it moves in a straight line. The resistivity of a material is directly derived from the probability of a carrier to travel from point A to point B. The probability of travelling from point A to point B is comprised of two parts: the classical part which is the sum of the probabilities of the diffusive paths connecting the two points and the quantum mechanical part which is the interference of the amplitudes belonging to different paths. The classical part gives the Drude formula for the case of metallic conductivity. The interference part can induce a difference in the travelling where the path is identical, but the direction is different. Weak localization stems mainly from this part.
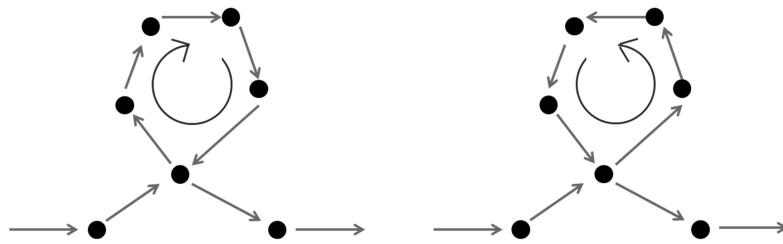
Figure 83. Illustration of weak localization. The electron waves entering a loop of scatterers have the possibility of travelling in either direction.

No lattice is perfect. At higher temperatures, vibrations distort the lattice. Dislocations are present at the least in the form of static disorder which remains present even at low temperatures. At high temperatures, it is not necessary to take into account the wave-like properties of electrons since inelastic scattering coming mainly from phonons prevents the electrons from keeping phase coherence over distances longer than the mean free path. This inelastic scattering is suppressed at low temperatures and elastic scattering dominates. This allows electrons to retain phase coherence over larger distances.

In a three dimensional material, a large amount of disorder leads to electron localization at low temperature whereas a small amount will not. In a two dimensional material, even the presence of a small amount of disorder results in localization.

If the wave function of an electron enters an array of point scatterers, it scatters isotropically off of every point. The scattered waves will scatter from other defect points leading to second, third order etc. waves. The sum of all of these wave functions in a chosen direction will be incoherent and give the net scattering probability. However, this changes when we consider the case of waves depicted in Figure 83 where they travel the same closed loop but with opposite directions. At the exit of the loop, the outgoing waves are in phase since the travelled loop is identical even though the directions are different. This interference of these coherent paths added together gives rise to a large amount of backscattering. This value needs to be added to the mentioned isotropic scattering and it implies a lowering of conductivity. If the wave function of electrons stay phase-coherent over a long distance, then a certain amount of isotropic scatterers can result in more backscattering compared to the rest of the directions.

To verify the presence of weak localization, one needs to insert a factor which influences the phase coherence without changing anything else in the system. If a magnetic field is applied perpendicular to the sheet, it will add a phase to both wave paths which is negative for one path and positive for the other. That is to say, under sufficient magnetic field, the phase coherent contribution to resistivity is removed.

At low temperatures, the elastic scattering time is very short in comparison to the inelastic dephasing time. In fact, heat breaks down this localization effect just as the magnetic field does. And so does spin. Introducing spin-related effects can lead to weak "anti"-localization. In fact, for a set of electrons to stay truly in phase, their spins must be in phase as well. The two main factors affecting this are the spin-orbit coupling and the spin-flip interaction. The former is an interaction between the orbital angular momentum of an electron (between the scatterer and the electron) and its spin. During the conservation of the angular momentum, it can pass between the orbital and spin degrees of freedom. Thus, this changes the spin and with that, the coherence of backscattering. On the other hand, the angular momentum can also be passed between the scatterer and the electron (i.e.

without the orbital angular momentum). This is a spin-flip interaction. Light elements are expected to be influenced by spin-orbit scattering.

Weak localization should depend only on the absolute magnitude of B and not its sign. Thus, it is of interest to verify negative field values as well.

<u>Weak localization in graphene</u>

In fact, perfect graphene is expected to demonstrate weak antilocalization. The interference in graphene is influenced by chirality from pseudo-spin and through that the unconventional Berry phase of π. [9] In conventional metals, the Berry phase is 2π which leads to constructive interference. This way backscattering in enhanced. However, for the case of graphene, negative magnetoresistance and with that weak antilocalization is observed. We cannot stress enough that this is unique to the case of defect-free or suspended graphene. Ripples, grain boundaries and dislocations lead to weak localization instead. [202] [203] [204] The appearance of weak localization is interpreted as dominating intervalley scattering stemming from atomically sharp defects and impurities. The intervalley scattering takes place between the two Dirac cones (with opposite pseudo-spins). It is safe to say that the weak (anti)localization in graphene is directly related to the nature of defects. [205]

A large amount of elastic intervalley scattering recovers weak localization. Chirality is reversed between the two valleys and therefore if a scattering involves intervalley scattering there is zero phase difference between the self-intersecting paths. Zero phase difference translates to constructive interference, i.e. weak localization. [206]

Weak localization in graphene is not only sensitive to inelastic phase-breaking processes, but it is also influenced by elastic scattering. [203] McCann et al. proposed a formula for fitting weak (anti)localization in graphene as the following:

$$\Delta\rho(B) = -\frac{e^2\rho^2}{\pi h}\left[F\left(\frac{\tau_B^{-1}}{\tau_\varphi^{-1}}\right) - F\left(\frac{\tau_B^{-1}}{\tau_\varphi^{-1}+2\tau_i^{-1}}\right) - 2F\left(\frac{\tau_B^{-1}}{\tau_\varphi^{-1}+\tau_*^{-1}}\right)\right] \quad\quad (4.21)$$

$$\text{where } F(z) = \ln z + \psi\left(\frac{1}{2} + \frac{1}{z}\right) \quad\quad (4.22)$$

and ψ is the digamma function. The formula takes into account contribution from different scattering terms such as dephasing rate τ_φ and elastic intervalley scattering rate τ_i from atomically sharp scattering and device edges. Also, it considers the inelastic intervalley trigonal warping and the elastic intravalley chirality symmetry breaking from dislocations and topological effects. The magnitude of the weak localization is defined by the decoherence length. For the interference to take place, phase coherence needs to be kept where τ_φ controls the size of the loop in Figure 83. The formula predicts that no weak localization is observed when the intervalley scattering is slow such as $\tau_i > \tau_\varphi$. When intervalley scattering is fast such as $\tau_i < \tau_\varphi$, the equation can be fitted to the weak localization peak. (Figure 84) [207] [206]
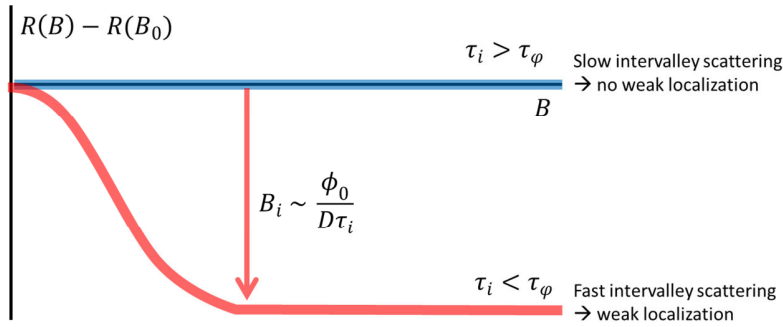
Figure 84. Sketch to demonstrate the formula fitting from the equation of McCann et al. When the intervalley scattering is slow such as $\tau_i > \tau_\varphi$, the equation predicts no weak localization. When intervalley scattering is fast such as $\tau_i < \tau_\varphi$, the equation can be fitted to the weak localization peak.

The elastic intervalley scattering length strongly depends on device characteristics since it stems from short-range, atomically sharp scatterers and edges of the device. If no gating is present, charge carrier density is directly related to such defects. Highly doped CVD graphene samples show low elastic intervalley scattering lengths due to charged defects. [206]

The sum of all the sublattice symmetry breaking terms is mostly influenced by the elastic intravalley trigonal warping (distortion of the dispersion relation at finite energy [208] scattering term and other chirality breaking terms. The degree of trigonal warping depends on the Fermi level. Therefore, increase in the carrier density leads to an increase in the trigonal warping term. The chirality breaking term is not influenced by carrier density; it is mainly influenced by topological effects. Temperature decreases this dephasing rate τ_φ. Therefore both localization types disappear at higher temperatures. [206] [208]

4.4.1.2. Discussion of our results

In Figure 87a and Figure 85a, we plotted the evolution of longitudinal resistivity with magnetic field at 4 K and 20 K. We swept the magnetic field well through zero field to make corrections to magnetic field shift if necessary. Firstly, we focus on the behavior of resistivity at low magnetic fields. Figure 85b depicts low magnetic field behavior of the curves where an overall negative magnetoresistance is immediately observed at low B. We had explained that such behavior is interpreted as weak localization which occurs when electrons regain phase coherence at low temperature. In fact, the so called "Berry's phase" in graphene adds a phase difference of π to these paths and thus resulting in destructive interference, i.e. leading to weak antilocalization which we do not observe. We have explained that the presence of strong intervalley scattering in graphene restores weak localization. [206] Thus, it is safe to say that intervalley scattering dominates in our samples among the scaterring mechanisms which include elastic intravalley trigonal warping scattering and elastic intravalley chirality breaking scattering. Intervalley scattering is known to originate mainly from grain boundaries in CVD graphene. [193]

Additional to the conventional weak localization in graphene, we observe side peaks near the zero magnetic field. (Figure 85a) These symmetrical peaks are partially suppressed at 20 K, however they are still present, i.e. they are robust with temperature and direction of magnetic field. Thus, we conclude that they are magnetically activated states. However, they prevent us from fitting the weak localization decay to the equation from the Section 4.4.1.1 to extract the different scattering times as described theoretically in [207].

Universal conductance fluctuations can be recognized as reproducible oscillations in Figure 85a for curves sweeping B up and down. They disappear partially at higher temperature as expected. (Figure 87a) [16]

(a) **(b)**
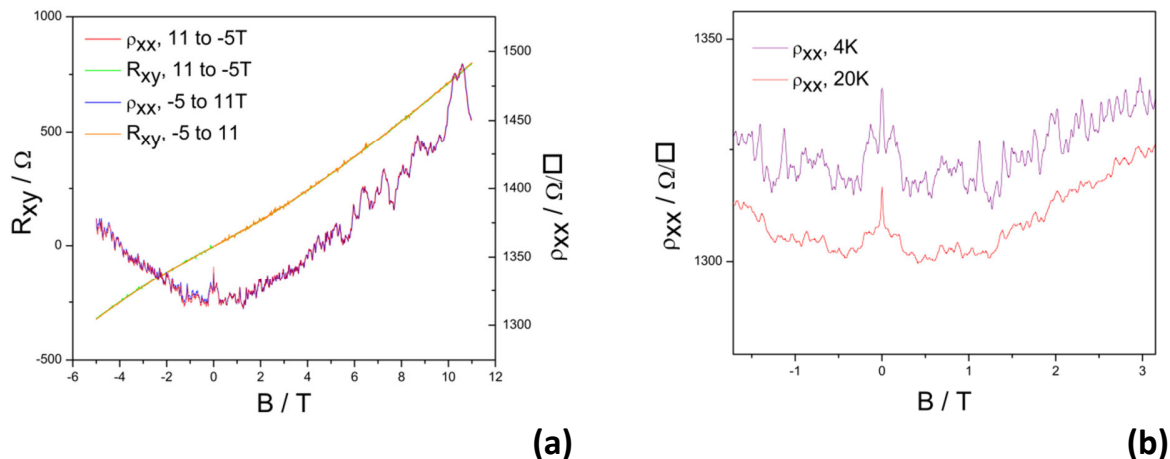
Figure 85. a) Hall resistance and longitudinal resistivity are plotted against magnetic field at 4 K. Magnetic field is swept from -5 to 11 T passing through zero field for corrections. The scale for the longitudinal resistivity is expanded to better demonstrate the features. The oscillations of the curves up and down follow each other closely. **b)** Detail from plot b is shown to better demonstrate weak localization.

4.4.2. Quantum Hall Effect

4.4.2.1. Theory and quantum Hall effect in graphene

The Hall conductance is quantized in two dimensional systems usually at low temperature and under strong magnetic fields. The quantized values are defined as the following:

$$\sigma = \frac{I_{channel}}{V_{Hall}} = \nu \frac{e^2}{h} \tag{4.23}$$

"ν" is known as the "filling factor" which can be integer or certain fractional values depending on which the effect takes the name "integer" quantum Hall effect or "fractional" quantum Hall effect. The integer QHE originates from single-particle orbitals of an electron in a magnetic field. The fractional QHE stems from electron-electron interactions. (Figure 86)

Electrons of two dimensional systems have circular cyclotron orbits in magnetic field. The energy levels of such orbits are called Landau levels and are quantized as the following:

$$E_N = \hbar\omega_c(N + 1/2) \text{ with } \omega_c = eB/m. \tag{4.24}$$

At low magnetic fields, Landau levels lead to Shubnikov de Haas oscillations. At high magnetic fields, the levels are highly degenerate since the number of electrons per level is proportional to the applied field.

One can observe the quantum Hall effect in graphene at liquid He temperatures above a magnetic field of 1 T. [15] If higher magnetic fields are applied, it is possible to observe the effect at even higher temperatures. For instance, under a magnetic field of 45 T, the QHE appears at room temperature. In comparison, it is not easy to detect the fractional QHE as it is for the integer QHE. It

requires temperatures lower than 1 K. Up to 20 K, it is still possible to observe it under the condition that the sample is ultraclean. [209]

(a)

(c)

(b)

(d)
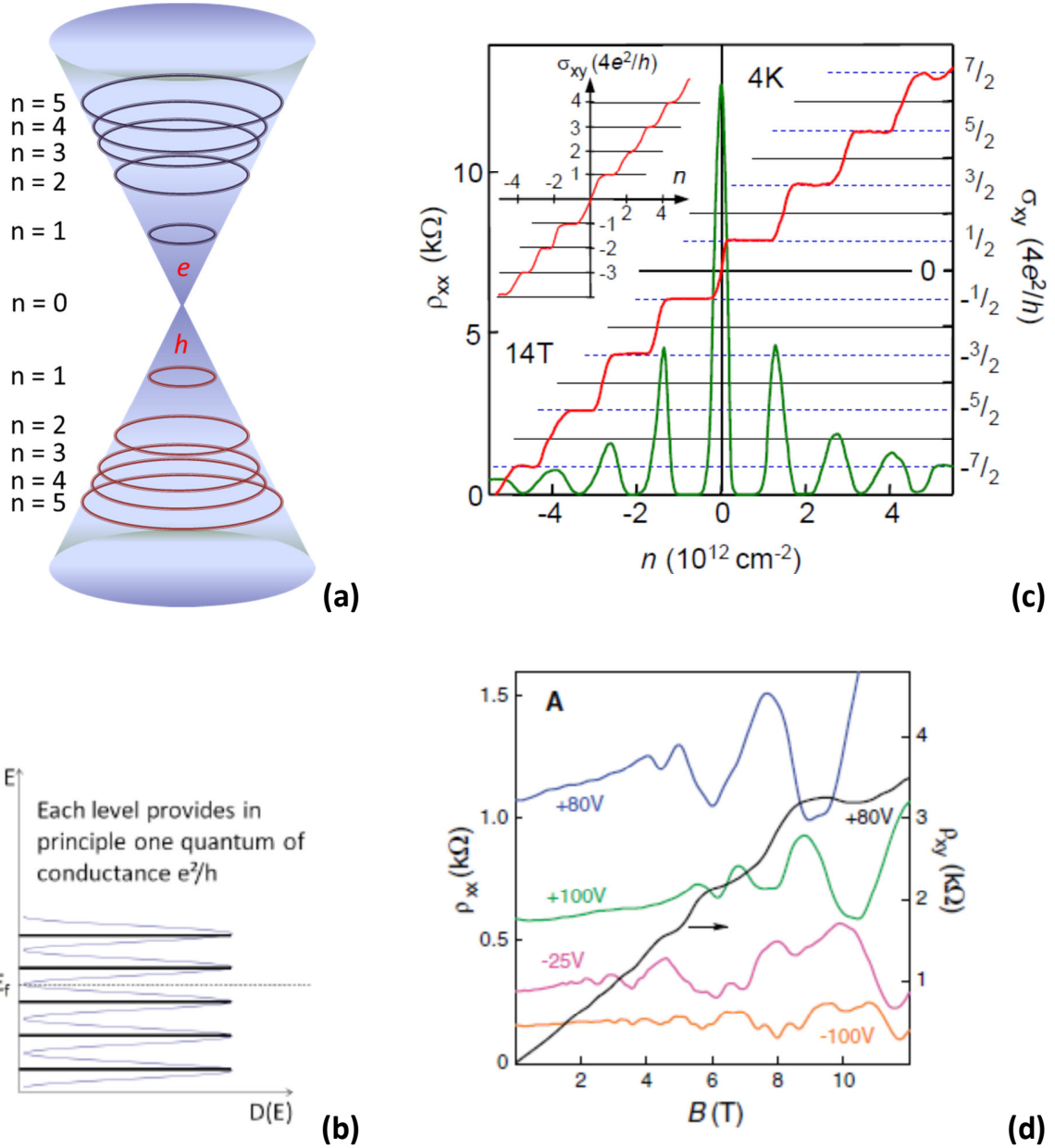
Figure 86. a) Illustration of Landau levels in the electronic band structure of graphene. **b)** Representation of quantized Hall conductance in graphene. DOS have peaks at Landau levels and they are broadened by disorder. [210] **c)** Quantum Hall effect. Hall conductivity σ_{xy} and longitudinal resistivity ρ_{xx} plotted against carrier concentration at B=14 T. [15] **c)** First measurements of Shubnikov de Haas oscillations in longitudinal resistivity ρ_{xx} and plateaus in Hall resistivity ρ_{xy} from exfoliated few layer graphene. [8]

The energy levels of graphene are quantized under magnetic fields in the following way:

$$E_N = sgn(N)\sqrt{2e\hbar v_F^2 |N|}, \ N = 0, \mp 1, \mp 2, \dots \qquad (4.25)$$

In practice, Landau levels lead to Shubnikov de Haas oscillations in resistivity. These oscillations appear in longitudinal resistivity by changing carrier density under magnetic field.

The minima of the peaks correspond to gaps in-between the quantized Landau levels. The carriers contributing to the current are solely on the edge states at the Fermi level. Additionally, in magnetic field the edges carry current in opposite directions. The scattering is suppressed since the carrier has to go from one edge to another for backscattering to happen which is not possible.

At the integers where a minimum is found in longitudinal resistivity, one observes plateaus in Hall resistance as shown in Figure 86c. The plateaus are where ρ_{xy} stays constant as a multiple v^{-1} of h/e^2, where v is the filling factor. The filling factor stands for the levels up to the Fermi energy. [210] In the absence of backscattering, the quantum Hall effect is represented as:

$$\upsilon = \frac{h}{R_{xy}e^2} \qquad (4.26)$$

Under low magnetic field, the even filling factors appear because the Landau levels can be occupied by both with spin up and spin down electrons. Thus, $\upsilon = 2, 4, 6, 8 \dots$ At high magnetic field, it is possible to remove this degeneracy through Zeeman interaction and observe all of the filling factors.

Figure 86c is an example of QHE in graphene. The filling factor sequence goes as $\upsilon = \mp 2, \mp 6, \mp 10 \dots$ The fact that both holes or electrons can be activated in graphene is the origin of positive as well as negative signs of filling factors. Due to the extra valley degeneracy, added to the spin degeneracy, the QHE plateaus appear with a factor of $4e^2/h$ instead of $2e^2/h$. Furthermore, the absence of a plateau at zero carrier density confirms the Landau state at N=0 both for electrons and holes. [210]

4.4.2.2. Observation of Landau levels in our measurements

Resistivity is expected to show oscillations under magnetic field corresponding to Landau levels of graphene. In Figure 85a and Figure 87a, we plotted longitudinal resistivity and Hall resistance against magnetic field. As we see, the clear oscillations in ρ_{xx} with high amplitudes stemming from Landau levels are not present and neither are the plateaus of Hall resistance against magnetic field. We attribute the lack of them to disorder. We mentioned that defects in graphene are reported to break down the quantum Hall effect. Landau level broadening depends on the magnetic field and disorder, and it has a significant impact on the excitation gaps. [211] Even if they are not as clear as observed in exfoliated graphene samples as we have shown, [8] we observe temperature robust peaks in Figure 87a. Furthermore, peak positions show a linear trend against 1/B. (Figure 87b) We approximated Landau levels with the equation:

$$E_n = 31.59 \ T^{-1/2} meV \sqrt{nB} \qquad (4.27)$$

from the work by Cresti et al. [212] We believe that the general disorder originating from CVD synthesis and device fabrication prevents us to observe Landau states. In any case, we believe that

the peaks are sufficiently robust to be interpreted as magnetic states of the material additionally due to the fact that in Figure 87b the peak maxima show a linear behavior.

(a)   **(b)**
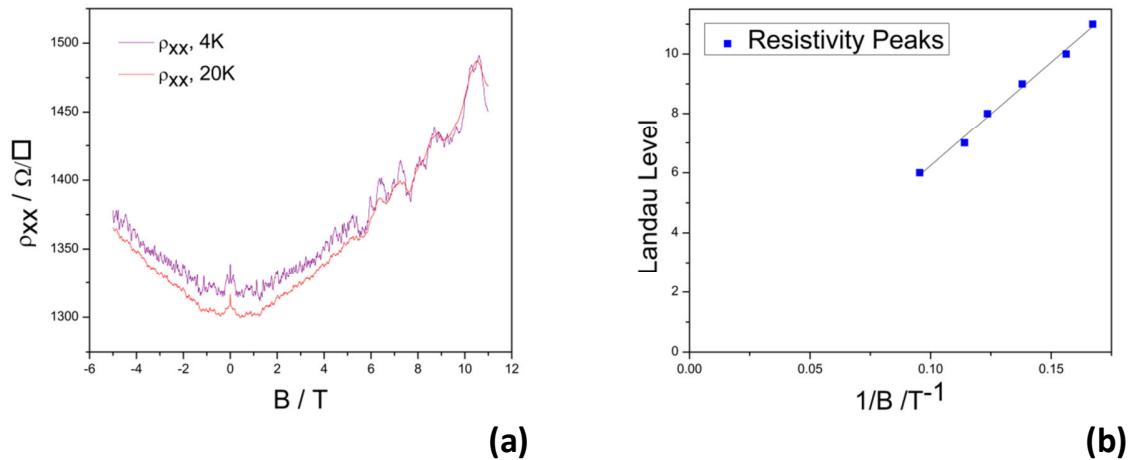
Figure 87. a) Longitudinal resistivity is plotted against magnetic field at 4 K and 20 K. Temperature-robust states are pointed out. **b)** Resistivity peaks from plot b are plotted in the form of 1/B against equidistant numbers to demonstrate linear dependence.

4.5. Temperature dependence

The influence of temperature on the transport properties directly gives the fingerprint of scattering in graphene. Several mechanisms are competing to shape the temperature-dependence of graphene.

4.5.1. Scattering mechanisms in graphene

It is possible to deduce on the quality and crystallinity of graphene through the behavior of mobility with temperature. While certain scattering mechanisms are enhanced at low temperature, some are suppressed and others remain uninfluenced. [194]

We categorize the scattering mechanisms in graphene in two types according to their origin: i) from phonons and ii) from defects. Phonon-induced scattering in graphene can occur due to the acoustic and optical phonons in graphene while they can also be due to the surface optical phonons of the SiO_2 substrate. At low temperature phonons behave as if they are "frozen" such that mobility and thereof the conductivity of the device increases. Furthermore, linear dispersion relation of graphene predicts that the resistivity originating from isotropic scatterers such as phonons does not depend on carrier density. [213]. This is the dominant mechanism of scattering in a perfect exfoliated graphene. (Figure 88a)

Acoustic phonon scattering, which leads to a linear temperature dependence, has been reported to contribute a small amount to resistivity unless for the case of graphene with high mobility and high carrier density. Additionally, it has been already known that transport in graphene is strongly coupled to surface optical phonons of the polar SiO_2. Thus, when the temperature is sufficiently increased to absorb and emit phonons, surface phonons scattering has a large contribution to resistivity. [214]

We look at resistivity vs temperature plots from studies published as guidance. [213] [214] Figure 88a is a study on exfoliated graphene on SiO_2 which demonstrated the change in resistivity with temperature. Taking into account the contribution from acoustic phonons and surface phonons from the substrate, the equation fitted the observed data well.
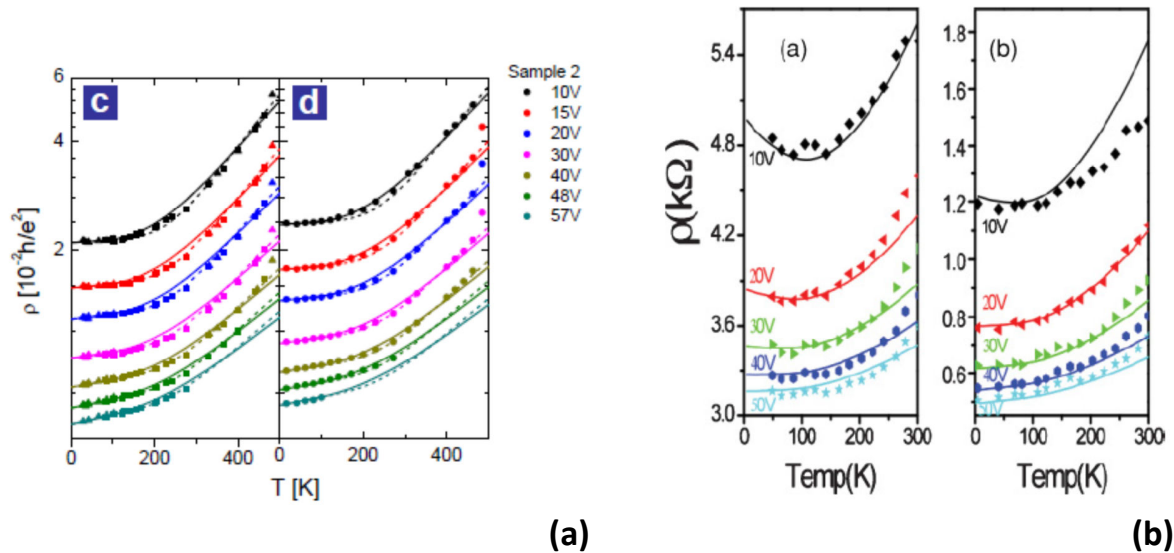
Figure 88. a) Resistivity is plotted against temperature at logarithmic scale for 7 different gate voltages. Solid lines are fits with an equation from [213] which includes acoustic phonon scattering in graphene and optical phonon scattering from SiO_2 substrate. [213] **b)** Resistivity is plotted against temperature at different gate voltages for CVD graphene samples. Lines are calculations fitting to data. [214]

"Defects" is an umbrella term for a series of different types of scattering sources in graphene. One of them is charged impurities. They contribute to shaping the temperature-dependence of resistivity in two manners: i) charged impurity screening and ii) creating potential fluctuations. High carrier concentrations are known to result in the screening of charged impurities. This type of scattering is commonly referred as Coulomb scattering.

The potential fluctuations which can stem from adsorbants, inhomogeneities in graphene or at the substrate interface to name a few.

Grain boundaries are another type of defects, otherwise referred as "line defects". They are independent of temperature, too. Ogawa et al. presented a study proving this point for the case of graphene. The authors separated intra-domain and inter-domain mobility in CVD graphene and looked at their behavior with temperature. Similar to exfoliated devices, the intra-domain mobility has been found to decrease with temperature pointing towards dependence on mainly phonon scattering. On the other hand, inter-domain mobility is influenced by temperature in a weaker manner than the intra-domain mobility does. This mobility involves transport over grain boundaries. Tunneling as well as thermally activated hopping of the carriers over the defect region are expected to participate in transport through grain boundaries. [194]

At low temperature regions, if the resistivity shows no dependence on temperature, this can be taken as an indication of the possibility of inter-grain transport even though the thermal energy is not sufficiently high to overcome the grain boundary potential. The proposed mechanism is tunneling. [215] [216]

116

There can be many other sources for defects such as roughness or edge inhomogeneities, for instance. In this section, with no intention to exclude those, we particularly focus on those that form the temperature dependence of the resistivity of graphene.

Figure 88b is a study on CVD graphene. As observed, the low temperature behavior differs from exfoliated graphene where the resistivity has a negative slope with temperature at low values. Since the main difference between exfoliated and CVD graphene originates from defects, it is safe to relate the difference of the low temperature resistivity to defects. Heo et al. described that phonons give way to a "metallic" behavior, i.e. the resistivity has a positive slope with temperature, while carrier activation across fluctuating potentials lead to an "insulating" behavior, i.e. the resistivity has a negative slope with temperature. [214]

In CVD graphene, three mechanisms have been reported to compete: i) thermal activation of carriers in electron-hole puddles created by charged impurities, ii) temperature-dependent screening of charged impurities and iii) phonon scattering. At low carrier densities and low temperature, the dominating factor is the carrier activation across potential fluctuations originating from random charged impurities. The strength of the "insulating" behavior depends on the strength of the potential fluctuation which, in return, is proportional to charged impurity density and inversely proportional to mobility. [214]

4.5.2. Measurement Results

In Figure 89, we plotted the resistivity change during heating to room temperature after measurements at 4 K. Three features can be observed; i) a resistivity decrease at low temperature, ii) followed by a plateau in a wide range of temperature and ii) the subsequent resistivity increase after 250 K. Just as in previous works before us as in Section 4.5.1, we refer to these two different regions as "insulating" or "metallic" depending on whether the slope dρ/dT is negative or positive. The resistivity behaves in an "insulating" way at very low temperature and in a "metallic" way as the temperature reaches room temperature. We explained in Section 4.5.1, that a combination of the two behaviors is characteristic to low mobility graphene devices with a high carrier density. The low mobility device is well in the diffusive regime.

As expected from CVD graphene, different scattering mechanisms appear to be competing which are as follows: i) charged impurity screening, ii) thermal activation of carriers over potential fluctuations and iii) phonon scattering. At low temperatures, the dominating mechanism is the thermal activation of carriers over the fluctuations created by charged impurities. Furthermore, we believe that the plateau region is dominated by scattering due to grain boundaries and other uncharged structural defects. While they have often been reported to have significant influence in CVD graphene transport, they are also uninfluenced by temperature. At high temperatures, phonon scattering mechanisms prevail. Regardless of the graphene source, exfoliated or CVD, acoustic phonons from graphene and surface phonons from SiO_2 result in an increase in the resistivity with increased temperature. In addition, charged impurity screening must be taking part in shaping the high temperature behavior considering that the device is heavily doped.
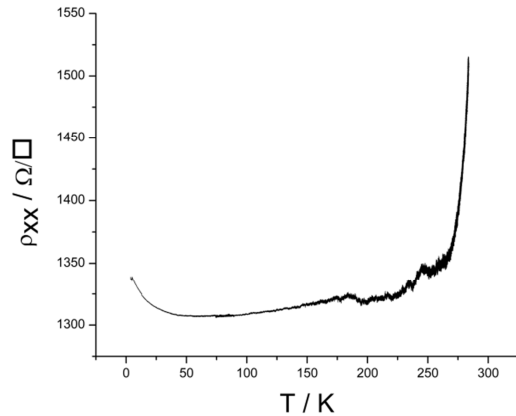
Figure 89. Sample is heated from 4 K to room temperature while longitudinal resistivity is measured. Increase in resistivity is observed for low and high temperature.

4.6. Conclusion

We characterized devices from graphene ribbons on SiO_2 electrically at room temperature as well as at low temperatures. At room temperature we extracted a channel resistivity of 0.9 - 2.1 kΩ/□ and contact resistance of $\sim 100 - 150$ Ω which corresponds to a contact resistivity of $\sim 2 - 3 \times 10^3$ Ω μm. This value is on the lower end among the reported contact resistivity range for Cr/Au contacts which is $\sim 10^3$ - 10^6 Ω μm. We believe that we owe such low contact resistance values to two main effects from our fabrication process: i) our care of the interface which is originally intended for successful suspending, ii) our attempt in keeping the chamber pressure low during metal contact evaporation by depositing Ti into the chamber. Additionally, we characterized same type of devices via back-gating. The results confirmed our interpretation of p-type doping from the Raman spectra despite the little gate modulation due to high oxide thickness and the lack of annealing. P-type doping is expected for graphene devices on SiO_2 under ambient conditions. The direction of the hysteresis helped us to determine that the dominating mechanism in our devices was charge transfer. A O_2/H_2O layer attached to the silanol groups on the oxide could be acting as charge traps where the charges were transferred to from graphene depending on the polarity of the gate voltage.

At temperatures as low as 20 K and 4 K, we characterized Hall bar structures while sweeping the magnetic field in both directions up to 11 T. We extracted average carrier density and mobility values as via the semi-Drude model as 9×10^{12} cm^{-2} and 500 cm^{2}V^{-1}s^{-1} respectively. The low mobility of devices of CVD graphene has generally been attributed largely to the presence of grain boundaries and lesser to fabrication-related defects. In addition, plotting the magnetoresistance enabled us to comment on weak localization and Landau levels of graphene. Even though weak antilocalization phenomenon is expected to appear in graphene at low magnetic field with the addition of a phase difference of π due to the so called "Berry's phase", we observed weak localization instead which has been reported to be restored under the condition of strong intervalley scattering. As for resolving the Landau levels, we did not observe the clear oscillations in longitudinal resistivity ρ_{xx} with high amplitudes or the plateaus of Hall resistance. We attributed the lack of them to disorder. Even if the peaks were not as clearly resolved, we could identify temperature-robust peaks and showed that the peak maxima had a linear behavior against 1/B. This indicates that they can indeed be stemming from Landau levels. Following these measurement, we additionally plotted the change in the resistance of the device as we heated it back to room temperature. The graph

demonstrates two distinct behaviors characteristic to low mobility graphene devices. At low temperature, we observe insulating behavior which we attributed to thermal activation of charge carriers over potential fluctuations. As the temperature is increased, on the other hand, to room temperature, the resistivity behaves more "metallic" influenced by the acoustic phonons in graphene as well as the closely coupled surface phonons from SiO_2.

120

Chapter 5

CONCLUSIONS & PROSPECTS

During this thesis, we developed a fabrication route for scalable suspended graphene devices. This process was developed in the PTA clean room and in collaboration with Proof. Georg Duesberg for CVD graphene growth and transfer on our pre-processed wafers. The processing was then followed up in Grenoble again where we devised a route for two different sample types including ebeam lithography and optical (UV) lithography. The former is intended for narrower structures while the latter is a more conventional process. It is worth recalling that at the time where we started this thesis, there were only few publications about CVD graphene device fabrication. To help graphene's pathway into industry, we kept to conventional methods from MEMS technologies and studied their interaction with graphene during fabrication. We studied the issues involved and suggested solutions. We identified that one of the key factors to high yield is a good interface between the etch mask and graphene during HF etch. By this way, we were able to reach a fabrication yield over 90%. Additionally, we showed that intentional periodical fold formation is possible in ribbons. The interplay between the photoresists and CVD process can lead to systematic folds during fabrication which are perpendicular to the ribbon length. Furthermore, we found that they do not unfold after thermal cycles. Although the role of these folds needs to be further explored, the fact that it is possible to control their formation by the choice of the process steps and their period by the choice of the ribbon width is an important result. It is promising to control strain relaxation in the final device. Additionally the presence of a periodical network of transverse folds along the beam may have interesting outcomes in the future.

Raman spectroscopy permitted us to have insight on materials properties at different fabrication steps as well as at final devices. Firstly, we had the evidence that our fabrication technique did not introduce significant damage to graphene itself. We also concluded that the SiO_2 is indeed responsible for a great portion of the p-type doping in supported graphene devices. By mostly eliminating the substrate, i.e. suspending graphene and changing the atmosphere from air to Ar, we had the opportunity to study the strain in Raman spectra. We observed that the built-in strain from the high thermal budget of CVD was not fully relaxed even at the stage of suspended beam. Additionally, the factors influencing Raman spectra led to a complex interplay for suspended devices such that the suspended beams varied greatly in their Raman spectra while the Raman spectra from supported graphene, be it on Si or SiO_2, were quite uniform. We heated our samples to 200°C in Ar and air which led us to believe that thermal treatments of graphene during fabrication or post-fabrication, with the intention of device improvement, are better done with caution. Even if 200°C did not degrade our graphene, it did not improve in removing the p-type doping. In fact, it even hinted at a possible slight increase in p-doping.

In addition to being the key of a safe and reproducible process, our insistence on having a clean surface after each step of fabrication was rewarded with a low contact resistance. We characterized supported devices electrically and observed a contact resistance of $\sim100-150\,\Omega$ which corresponds to a contact resistivity of $\sim2-3\times10^3\,\Omega\,\mu m$. The devices showed Ohmic behavior with a channel resistivity of 0.9 - 2.1 kΩ/□. The fact that our devices have a rather thick oxide layer did not permit us to modulate current highly via back-gating. However, the type of hysteresis we

observed through the limited current modulation pointed that charge transfer was the origin which involved a combination of oxygen from air and water at the SiO_2 interface for doping mechanism.

We further studied the magnetoresistivity data from sweeping the magnetic field up to 11 T at 20 K and 4 K while well-passing zero. From this study, we were able to firstly extract the Hall mobility of a device as 500 $cm^2V^{-1}s^{-1}$ and a carrier concentration of 9 x 10^{12} cm^{-2} at low temperature Although they are far from the records that have been obtained for exfoliated graphene, this values are in the range of published values for CVD graphene (especially for non-annealed samples). The grain boundaries of CVD graphene has been in general accounted for the low mobility. The high p-doping is also consistent with what is expected for a device on SiO_2. It is also consistent with our Raman measurements which pointed to the same conclusion, with a high p-doping for supported structures. Moreover, even if our device was far from perfect, considering that it has grain boundaries and fabrication-induced impurities and even if we failed to see a clear quantum Hall effect, we observed temperature-robust features which we interpreted as quantum interference and quantum confinement effects. We were able to fit Landau levels to the high magnetic field oscillations of the magnetoresistivity. In addition, we identified the low magnetic field behavior as weak localization which pointed towards strong intervalley scattering in our device.

Finally, we looked at the behavior of the resistivity during heating after the low temperature measurements and observed two distinct behaviors in our first measurement. We concluded that the resistivity was strongly influenced by thermal activation of carriers over potential fluctuations at low temperatures. And at high temperatures, acoustics phonons from graphene and surface optical phonons from the SiO_2 substrate along with charged impurity screening dominated the increase of resistivity. Between the two, a plateau was observed in a large range of resistivity. In this region, scattering with defects is probably the main limiting phenomenon.

Based on these results, and especially the reliable and reproducible fabrication route along with control over fold patterns, several studies can now be carried out.

First follow-ups of this work will continue by exploring the systematic folds. Furthermore, we plan on making more complicated structures such as entirely suspended Hall bars and study their electronic properties at room and low temperature, with and without folds. These devices will be fabricated with a thinner oxide to increase current modulation capabilities.

We aim to study these folds under Raman spectroscopy, preferably by mapping. This way, we can gain insight of the influence of such folds on the distribution of strain in the ribbon and the interaction with the substrate. Additionally, we would like to study them at suspended regions as well. The devices will be characterized electrically in order to analyze the influence of the folds on the electrical and magnetoelectrical properties. In addition, we plan on studying the influence of annealing on our devices, particularly the suspended ones.

Moreover, we intend to combine in the same experiment electrical measurements and Raman spectroscopy. By applying gate voltage we want to investigate the changes in Raman spectra and better separate the effects of doping and strain.

Conferences & Publications

O. I. Aydin, T. Hallam, J.L. Thomassin, M. Mouis, and G.S. Duesberg, *Interface and strain effects on the fabrication of suspended CVD graphene devices*, Solid-State Electronics: Special Issue ULIS (2014) to be published.

O. I. Aydin, T. Hallam, A. Cresti, M. Mouis, B. Piot, J.L. Thomassin and G.S. Duesberg*, Low temperature characterizations of CVD graphene devices fabricated with a scalable process route*, WOLTE 2014, Grenoble (2014)

O. I. Aydin, T. Hallam, J.L. Thomassin, M. Mouis, and G.S. Duesberg*, Challenges in Suspending CVD Graphene: More than Capillary Effects,* ULIS 2014, Stockholm (2014)

A. Delamoreanu, O.I. Aydin, C. Rabot, C. Vallee, M. Mouis, A. Zenasni, *Large area CVD growth and characterization of graphene for transparent electrodes and electromechanical devices*, Lavoisier Discussions (2011)

Chapter 6

REFERENCES

[1]   R. Chang, «Essential Chemistry, 2/e,» 2000. [En ligne]. Available: http://www.mhhe.com/physsci/chemistry/essentialchemistry/flash/hybrv18.swf. [Accès le August 2014].

[2]   L. Pauling, The Nature of the chemical bond and the structure of molecules and crystals: An introduction to modern structural chemistry, Cornell University Press, 1960.

[3]   «Carbon: allotropes,» [En ligne]. Available: http://www.webelements.com/carbon/allotropes.html. [Accès le August 2014].

[4]   «Allotropes of carbon,» [En ligne]. Available: http://en.wikipedia.org/wiki/Allotropes_of_carbon. [Accès le August 2014].

[5]   H. Kroto, J. Heath, S. O'Brien, R. Curl et R. Smalley, «C60: Buckminsterfullerene,» *Nature 318,* p. 162, 1985.

[6]   S. Iijima, «Helical microtubules of graphitic carbon,» *Nature 354,* p. 56, 1991.

[7]   L. Landau, «Zur Theorie der Phasenumwandlungen II,» *Physikalische Zeitschrift der Sowjetunion 11,* p. 26, 1937.

[8]   K. Novoselov , A. Geim, S. Morozov, D. Jiang, Y. Zhang, S. Dubonos, I. Grigorieva et A. Firsov, «Electric field effect in atomically thin carbon films,» *Science 22,* p. 666, 2004.

[9]   Y. Zhang, Y.-W. Tan, H. Stormer et P. Kim, «Experimental observation of the quantum Hall effect and Berry's phase in graphene,» *Nature 438,* p. 201, 2005.

[10]   C. Berger, Z. Song, T. Li, X. Li, A. Ogbazghi, R. Feng, Z. Dai, A. Marchenkov, E. Conrad, P. First et W. de Heer, «Ultrathin epitaxial graphite- 2D electron gas properties and a route toward graphene-based nanoelectronics,» *Journal of Physical Chemistry B 108,* p. 19912, 2004.

[11]   C. Berger, Z. Song, T. Li, X. Li, A. Ogbazghi, R. Feng, Z. Dai, A. Marchenkov, E. Conrad, P. First et W. de Heer, «Ultrathin epitaxial graphite: 2D electron gas properties and a route toward graphene-based nanoelectronics,» *Journal of Physical Chemistry B 108,* p. 19912, 2004.

[12]   X. Li, W. Cai, J. An, S. Kim, J. Nah, D. Yang, R. Piner, A. Velamakanni, E. Tutuc, S. Banerjee, L. Colombo et R. Ruoff, «Large-area synthesis of high quality and uniform graphene films on copper foils,» *Science 324,* p. 1312, 2009.

[13]   R. Saito, G. Dresselhaus et M. Dresselhaus, Physical properties of carbon nanotube, Imperial College Press, 1998.

[14]   A. Castro Neto, F. Guinea, N. Peres, K. Novoselov et A. Geim, «The electronic properties of graphene,» *Reviews of modern physics 81,* p. 109, 2009.

[15]   K. Novoselov, A. Geim, S. Morozov, D. Jiang, M. Katsnelson, I. Grigorieva, S. Dubonos et A. Firsov, «Two-dimensional gas of massless Dirac fermions in

graphene,» *Nature 438,* p. 197, 2005.

[16] A. Geim et K. Novoselov, «The rise of graphene,» *Nature Materials 6,* p. 183, 2007.

[17] S. Morozov, K. Novoselov, M. Katsnelson, F. Schedin, D. Elias, J. Jaszczak et A. Geim, «Giant intrinsic carrier mobilities in graphene and its bilayer,» *Physical Review Letters 100,* p. 016602, 2008.

[18] K. Bolotin, K. Sikes, Z. Jiang, M. Klima, G. Fudenberg, J. Hone, P. Kim et H. Stormer, «Ultrahigh electron mobility in suspended graphene,» *Solid State Communications 146,* p. 351, 2008.

[19] C. Berger, Z. Song, X. Li, X. Wu, N. Brown, C. Naud, D. Mayou, T. Li, J. Hass, A. Marchenkov, E. Conrad, P. First et W. de Heer, «Electronic confinement and coherence in patterned epitaxial graphene,» *Science 312,* p. 1191, 2006.

[20] K. Novoselov, E. McCann, S. Morozov, V. Fal'ko, M. Katsnelson, U. Zeitler, D. Jiang, F. Schedin et A. Geim, «Unconventional quantum Hall effect and Berry's phase of 2π in bilayer graphene,» *Nature 2,* p. 177, 2006.

[21] E. McCann, «Asymmetry gap in the electronic band structure of bilayer graphene,» *Physical Review B 74,* p. 161403, 2006.

[22] M. Han, B. Ozyilmaz, Y. Zhang et P. Kim, «Energy band-gap engineering of graphene nanoribbons,» *Physical Review Letters 98,* p. 206805, 2007.

[23] Z. Chen, Y. Lin, M. Rooks et P. Avouris, «Graphene nano-ribbon electronics,» *Physica E 40,* p. 228, 2007.

[24] S. Zhou, G.-H. Gweon, A. Fedorov, P. First, W. de Heer, D.-H. Lee, F. Guinea, A. Castro Neto et A. Lanzara, «Substrate-induced bandgap opening in epitaxial graphene,» *Nature Materials 6,* p. 770, 2007.

[25] A. Sakhee-Pour, «Elastic properties of single-layered graphene sheet,» *Solid State Communications 149,* p. 91, 2009.

[26] C. Lee, X. Wei, J. Kysar et J. Hone, «Measurement of the elastic properties and intrinsic strength of monolayer graphene,» *Science 321,* p. 385, 2008.

[27] A. Kuzmenko, E. Heumen, F. Carbone et D. Marel, «Universal optical conductance of graphite,» *Physical Review Letters 100,* p. 117401, 2008.

[28] V. Kravets, A. Grigorenko, R. Nair, P. Blake, S. Anissimova, K. Novoselov et A. Geim, «Spectroscopic ellipsometry of graphene and an exciton-shifted van Hove peak in absorption,» *Physical Review B 81,* p. 155413, 2010.

[29] C. Lau, W. Bao et J. Velasco Jr., «Properties of suspended graphene membranes,» *Materials Today 15,* p. 238, 2012.

[30] K. Zakharchenko, M. Katsnelson et A. Fasolino, «Finite temperature lattice properties of graphene beyond the quasiharmonic approximation,» *Physical Review Letters 102,* p. 046808, 2009.

[31] S. Ghosh, W. Bao, D. Nika, S. Subrina, E. Pokatilov, C. Lau et A. Balandin, «Dimensional crossover of thermal transport in few-layer graphene,» *Nature Materials 9,* p. 555, 2010.

[32] W. Cai, A. Moore, Y. Zhu, X. Li, S. Chen, L. Shi et R. Ruoff, «Thermal Transport in suspended and supported monolayer graphene grown by chemical vapor deposition,» *Nano Letters 10,* p. 1645, 2010.

126

[33] J. Seol, I. Jo, A. Moore, L. Lindsay, Z. Aitken, M. Pettes, X. Li, Z. Yao, R. Huang, D. Broido, N. Mingo, R. Ruoff et L. Shi, «Two-dimensional phonon transport in supported graphene,» *Science 328,* p. 213, 2010.

[34] S. Banerjee, L. Register, E. Tutuc, D. Basu, S. Kim, D. Reddy et A. MacDonald, «Graphene for CMOS and beyond CMOS applications,» *Proceedings of the IEEE 98,* p. 2032, 2010.

[35] X. Wang, Y. Ouyang, X. Li, H. Wang, J. Guo et H. Dai, «Room temperature all semiconducting sub 10 nm graphene nanoribbon field effect transistors,» *Physical Review Letters 100,* p. 206803, 2008.

[36] Y.-M. Lin, C. Dimitrakopoulos, K. Jenkins, D. Farmer, H.-Y. Chiu, A. Grill et P. Avouris, «100-GHz transistors from wafer-scale epitaxial graphene,» *Science 5,* p. 662, 2010.

[37] H. Happy, N. Meng, R. Fleurier, E. Pichonat, D. Vignaud et G. Dambrine, «Graphene nano ribbon field effect transistor for high frequency applications,» *2011 Proceedings of 41st European Microwave Conference (EuMC 2011). IEEE. 2011,* 2011.

[38] H. Wang et H. Al, «Graphene Electronics for RF Applications,» *IEEE Microwave Magazine 13,* p. 114, 2012.

[39] W. Zhu, V. Perebeinos, M. Freitag et P. Avouris, «Carrier scattering, mobilities and electrostatic potential in monolayer, bilayer and trilayer graphene,» *Physical Review B 80,* p. 235402, 2009.

[40] K. Kim, Y. Zhao, H. Jang, S. Lee, J. Kim, K. Kim, J.-H. Ahn, P. Kim, J.-Y. Choi et B. Hong, «Large-scale pattern growth of graphene films for stretchable transparent electrodes,» *Nature 457,* p. 2009, 2009.

[41] B. Wang, M. Bocquet, S. Marchini, S. Günther et J. Wintterlin, «Chemical origin of a graphene moiré overlayer on Ru(0001),» *Physical Chemistry Chemical Physics 10,* p. 3530, 2008.

[42] C. Chen et J. Hone, «Graphene nanomechanical systems,» *Proceedings of the IEEE 101,* p. 1766, 2013.

[43] T. Lee, S. Bhunia et M. Mehregany, «Electromechanical computing at 500c with silicon carbide,» *Science 329,* p. 1316, 2010.

[44] M. Bagheri, M. Poot, M. Li, W. Pernice et H. Tang, «Dynamic manipulation of nanomechanical resonators in the high-amplitude regime and non-volatile mechanical memory operation,» *Nature Nanotechnology 6,* p. 726, 2011.

[45] A. van der Zande, R. Barton, J. Alden, C. Ruiz-Vargas, W. Whitney, P. Pham, J. Park, J. Parpia, H. Craighead et P. McEuen, «Large-scale arrays of single-layer graphene resonators,» *Nano Letters 10,* p. 4869, 2010.

[46] V. Singh, S. Sengupta, H. Solanki, R. Dhall, A. Allain, S. Dhara, P. Pant et M. Deshmukh, «Probing thermal expansion of graphene and modal dispersion at low-temperature using graphene nanoelectromechanical systems resonators,» *Nanotechnology 21,* p. 165204, 2010.

[47] C. Chen, S. Rosenblatt, K. Bolotin, W. Kalb, P. Kim, I. Kymissis, H. Stormer, T. Heinz et J. Hone, «Performance of monolayer graphene nanomechanical resonators

with electrical readout,» *Nature Nanotechnology 4,* p. 861, 2009.

[48] J. Bunch, A. van der Zande, S. Verbridge, I. Frank, D. Tanenbaum, J. Parpia, H. Craighead et P. McEuen, «Electromechanical resonators from graphene sheets,» *Science 315,* p. 490, 2007.

[49] F. Schedin, A. Geim, S. Morozov, E. Hill, P. Blake, M. Katsnelson et K. Novoselov, «Detection of individual gas molecules adsorbed on graphene,» *Nature Materials 6,* p. 652, 2007.

[50] J. Fowler, M. Allen, V. Tung, Y. Yang, R. Kaner et B. Weiller, «Practical chemical sensors from chemically derived graphene,» *ACS Nano 3,* p. 201, 2009.

[51] C. Shan, H. Yang, J. Song, D. Han, A. Ivaska et L. Niu, «Direct electrochemistry of glucose oxidase and biosensing for glucose based on graphene,» *Analytical Chemistry 81,* p. 2378, 2009.

[52] A. Alwarappan, A. Erdem, C. Liu et C. Li, «Probing the electrochemical properties of graphene nanosheets for biosensing applications,» *Journal of Physical Chemistry C 113,* p. 8853, 2009.

[53] J. Li, S. Guo, Y. Zhai et E. Wang, «Nafion-graphene nanocomposite film as enhanced sensing platform for ultrasensitive determination of cadmium,» *Electrochemistry Communications 11,* p. 1085, 2009.

[54] J. Wu, H. Becerril, Z. Bao, Z. Liu, Y. Chen et P. Peumans, «Organic solar cells with solution-processed graphene transparent electrodes,» *Applied Physics Letters 92,* p. 263302, 2008.

[55] X. Wang, L. Zhi et K. Mullen, «Transparent conductive graphene electrodes for dye-sensitized solar cells,» *Nano Letters 8,* p. 323, 2008.

[56] X. Wang, L. Zhi, N. Tsao, Z. Tomovic, J. Li et K. Muellen, «Transparent carbon films as electrodes in organic solar cells,» *Angewandte Chemie International Edition 47,* p. 2990, 2008.

[57] F. Wang, Y. Zhang, C. Tian, C. Girit, A. Zettl, M. Crommie et Y. Shen, «Gate-variable optical transitions in graphene,» *Science 11,* p. 206, 2008.

[58] F. Xia, T. Mueller, Y.-M. Lin, A. Valdes-Garcia et P. Avouris, «Ultrafast graphene photodetector,» *Nature Nanotechnology 4,* p. 839, 2009.

[59] N. Varghese, U. Mogera, A. Govindaraj, A. Das, P. Maiti, A. Sood et C. Rao, «Binding of DNA nucleobases and nucleosides with graphene,» *ChemPhysChem 10,* p. 206, 2009.

[60] S. Paek, E. Yoo et I. Honma, «Enhanced cyclic performance and lithium storage capacity of SnO/graphene nanoporous electrodes with three-dimensionally delaminated flexible structures,» *Nano Letters 9,* p. 72, 2009.

[61] D. Wang, D. Choi, J. Li, Z. Yang, Z. Nie, R. Kou, D. Hu, C. Wang, L. Saraf, J. Zhang, I. Aksay et J. Liu, «Self-Assembled TiO2–Graphene Hybrid Nanostructures for Enhanced Li-Ion Insertion,» *ACS Nano 3,* p. 907, 2009.

[62] P. Blake, E. Hill, A. Castro Neto, K. Novoselov, D. Jiang, R. Yang, T. Booth et A. Geim, «Making graphene visible,» *Applied Physics Letters 91,* p. 063124, 2007.

[63] S. Park et R. Ruoff, «Chemical methods for the production of graphenes,» *Nature Nanotechnology 5,* p. 309, 2009.

[64] P. First , W. de Heer, T. Seyller, C. Berger, J. Stroscio et J.-S. Moon, «Epitaxial graphenes on silicon carbide,» *MRS Bulletin 35,* p. 296, 2010.

[65] C. Mattevi, H. Kim et M. Chhowalla, «A review of chemical vapor deposition of graphene on copper,» *Journal of Materials Chemistry 21,* p. 3324, 2011.

[66] P. Somani, S. Somani et M. Umeno, «Planer nano-graphenes from camphor by CVD,» *Chemical Physics Letters 430,* p. 56, 2006.

[67] G. Ruan, Z. Sun, Z. Peng et J. Tour, «Growth of graphene from food, insects, waste,» *ACS Nano 5,* p. 7601, 2011.

[68] Z. Sun, Z. Yan, J. Yao, E. Beitler, Y. Zhu et J. Tour, «Growth of graphene from solid carbon sources,» *Nature 468,* p. 549, 2010.

[69] R. Munoz et C. Gomez-Aleixandre, «Review of CVD synthesis of graphene,» *Chemical Vapor Deposition 19,* p. 297, 2013.

[70] L. Gao, W. Ren, H. Xu, L. Jin, Z. Wang, T. Ma, L.-P. Ma, Z. Zhang, Q. Fu, L.-M. Peng, X. Bao et H.-M. Cheng, «Repeated growth and bubling transfer of graphene with milimetre-size single crystal grains using platinum,» *Nature Communications 3,* p. 1, 2012.

[71] L. Gao, J. Guest et N. Guisinger, «Epitaxial graphene on Cu(111),» *Nano Letters 10,* p. 3512, 2010.

[72] Y. Ogawa, B. Hu, C. Orofeo, M. Tsuji, K.-I. Ikeda, S. Mizuno, H. Hibino et H. Ago, «Domain structure and boundary in single-layer graphene grown on Cu(111) and Cu(100) films,» *Journal of Physical Chemistry Letters 3,* p. 219, 2012.

[73] S.-Y. Kwon, C. Ciobanu, V. Petrova, V. Shenoy, J. Bareno, V. Gambin, I. Petrov et S. Kodambaka, «Growth of semiconducting graphene on Palladium,» *Nano Letters 9,* p. 3985, 2009.

[74] H. Wang, G. Wang, P. Bao, S. Yang, W. Zhu, X. Xie et W.-J. Zhang, «Controllable synthesis of submilimeter single-crystal monolayer graphene domains on copper foils by suppressing nucleation,» *Journal of the American Chemical Society 134,* p. 3627, 2012.

[75] Q. Yu, J. Lian, S. Siriponglert, H. Li, Y. Chen et S.-S. Pei, «Graphene segregated on Ni surfaces and transferred to insulators,» *Applied Physics Letters 93,* p. 113103, 2008.

[76] Y. Zhang, L. Zhang et C. Zhou, «Review of chemical vapor deposition of graphene and related applications,» *Accounts of Chemical Research 46,* p. 2329, 2013.

[77] I. Vlassiouk, M. Regmi, P. Fulvio, S. Dai, P. Datskos, G. Eres et S. Smirnov, «Role of hydrogen in chemical vapor deposition growth of large single-crystal graphene,» *ACS Nano 5,* p. 6069, 2011.

[78] M. Losurdo, M. Giangregorio, P. Capezzuto et G. Bruno, «Graphene CVD growth on copper and nickel: role of hydrogen in kinetics and structure,» *Physical Chemistry Chemical Physics 13,* p. 20836, 2011.

[79] S. Kumar, N. McEvoy, H.-Y. Kim, K. Lee, N. Peltekis, E. Rezvani, H. Nolan, A. Weidlich, R. Daly et G. Duesberg, «CVD growth and processing of graphene for electronic applications,» *Physica Status Solidi B 248,* p. 2604, 2011.

[80] C. Lee et J. Choi, «Direct growth of nanographene on glass and postdeposition size

control,» *Applied Physics Letters 98,* p. 183106, 2011.

[81] X. Ding, G. Ding, X. Xie, F. Huang et M. Jiang, «Direct growth of few layer graphene on hexagonal boron nitride by chemical vapor deposition,» *Carbon 49,* p. 2522, 2011.

[82] M. Rummeli, A. Bachmatiuk, A. Scott, F. Borrnert, J. Warner, V. Hoffman, J.-H. Lin, G. Cunibert et B. Buchner, «Direct low-temperature nanographene CVD synthesis over a dielectric insulator,» *ACS Nano 4,* p. 4206, 2010.

[83] A. Ismach, C. Druzgalski, S. Penwell, A. Schwartzberg, M. Zheng, A. Javey, J. Bokor et Y. Zhang, «Direct chemical vapor deposition of graphene on dielectric surfaces,» *Nano Letters 10,* p. 1542, 2010.

[84] M. Levendorf, C. Ruiz-Vargas, S. Garg et J. Park, «Transfer-free batch fabrication of single layer graphene transistors,» *Nano Letters 9,* p. 4479, 2009.

[85] T. Terasawa et K. Saiki, «Growth of graphene on Cu by plasma enhanced chemical vapor deposition,» *Carbon 50,* p. 869, 2012.

[86] K. Zhang et M. Arroyo, «Adhesion and friction control localized folding in supported graphene,» *Journal of Applied Physics 113,* p. 193501, 2013.

[87] K. Kim, Z. Lee, B. Malone, K. Chan, B. Aleman, W. Regan, W. Gannett, M. Crommie, M. Cohen et A. Zettl, «Multiply folded graphene,» *Physical Review B 83,* p. 245433, 2011.

[88] T. Kollie, «Measurement of the thermal-expansion coefficient of nickel from 300 to 1000 K and determination of the power-law constants near the Curie temperature,» *Physical Review B 16,* p. 4872, 1977.

[89] J. Nelson et D. Riley, «The thermal expansion of graphite from 15C to 800C: part I. Experimental,» *Proceedings of the Physical Society 57,* p. 477, 1945.

[90] W. Bao, F. Miao, Z. Chen, H. Zhang, W. Jang, C. Dames et C. Lau, «Controlled ripple texturing of suspended graphene and ultrathin graphite membranes,» *Nature Nanotechnology 4,* p. 562, 2009.

[91] D. Garcia-Sanchez, A. van der Zande, A. San Paulo, B. Lassagne, P. McEuen et A. Bachtold, «Imaging mechanical vibrations in suspended graphene sheets,» *Nano Letters 8,* p. 1399, 2008.

[92] Y. Xu, C. Chen, V. Deshpande, F. DiRenno, A. Gondarenko, D. Heinz, S. Liu, P. Kim et J. Hone, «Radio frequency electrical transuction of graphene mechanical resonators,» *Applied Physics Letters 97,* p. 243111, 2010.

[93] I. Frank, D. Tanenbaum, A. van der Zande et P. McEuen, «Mechanical properties of suspended graphene sheets,» *Journal of Vacuum Science & Technology B 25,* p. 2558, 2007.

[94] A. Smith, S. Vaziri, F. Niklaus, A. Fischer, M. Sterner, A. Delin, M. Ostling et M. Lemme, «Pressure sensors based on suspended graphene membranes,» *Solid-State Electronics 88,* p. 89, 2013.

[95] J. Bunch, S. Verbridge, J. Alden, A. van der Zande, J. Parpia, H. Craighead et P. McEuen, «Impermeable atomic membranes from graphene sheets,» *Nano Letters 8,* p. 2458, 2008.

[96] A. Morin, D. Lucot, A. Ouerghi, G. Patriarche, E. Bourhis, A. Madouri, C. Ulysse, J.

Pelta, L. Auvray, R. Jede, L. Bruchhaus et J. Gierak, «FIB carving of nanopores into suspended graphene films,» *Microelectronics Engineering 97,* p. 311, 2012.

[97] J. Gierak, «Focused ion beam technology and ultimate applications,» *Semiconductor Science and Technology 24,* p. 043001, 2009.

[98] S. Zhang, X. Wan, Y. Xu et J. Chen, «Fabrication of large-scale suspended graphene clamp-clamp beam by FIB cutting,» *Proceedings of the 13th IEEE International Conference on Nanotechnology,* p. 644, 2013.

[99] V. Dorgan, A. Behnam, H. Conley, K. Bolotin et E. Pop, «High-field electrical and thermal transport in suspended graphene,» *Nano Letters 13,* p. 4581, 2013.

[100] N. Tombros, A. Veligura, J. Junesch, M. Guimaraes, I. Vera-Marun, H. Jonkman et B. van Wees, «Quantized conductance of a suspended graphene nanoconstriction,» *Nature Physics 7,* p. 697, 2011.

[101] N. Tombros, A. Veligura, J. Junesch, J. van den Berg, P. Zomer, M. Wojtaszek, I. Vera Marun, H. Jonkman et B. van Wees, «Large yield production of high mobility freely suspended graphene electronic devices on a polydimethylglutarimide based organic polymer,» *Journal of Applied Physics 109,* p. 093702, 2011.

[102] I. Neumann, J. van de Vondel, G. Bridoux, M. Costache, F. Alzina, C. Sotomayor Torres et S. Valenzula, «Electrical detection of spin precession in freely suspended graphene spin valves on cross-linked poly(methyl methacrylate),» *Small 9,* p. 156, 2013.

[103] S. Shivaraman, R. Barton, X. Yu, J. Alden, L. Herman, M. Chandrashekhar, J. Park, P. McEuen, J. Parpia, H. Craighead et M. Spencer, «Free-standing epitaxial graphene,» *Nano Letters 9,* p. 3100, 2009.

[104] M. Kato, M. Ichimura, E. Arai et P. Ramasamy, «Electrochemical etching of 6H-SiC using aqueous KOH solutions with low surface roughness,» *Japanese Journal of Applied Physics 42,* p. 4233, 2003.

[105] A. van der Zande, R. Barton, J. Alden, C. Ruiz-Vargas, W. Whitney, P. Pham, J. Park, J. Parpia, H. Craighead et P. McEuen, «Large-scale arrays of single-layer graphene resonators - Supporting Information,» *Nano Letters 10,* p. 4869, 2010.

[106] F. Traversi, F. Guzman-Vazquez, L. Rizzi, V. Russo, C. Casari, C. Gomez-Navarro et R. Sordan, «Elastic properties of graphene suspended on a polymer substrate by e-beam exposure,» *New Journal of Physics 12,* p. 023034, 2010.

[107] W. Bao, G. Liu, Z. Zhao, H. Zhang, D. Yan, A. Deshpande, B. LeRoy et C. Lau, «Lithography-free fabrication of high quality substrate-supported and freestanding graphene devices,» *Nano Research 3,* p. 98, 2010.

[108] B. Aleman, W. Regan, S. Aloni, V. Altoe, N. Alem, C. Girit, B. Geng, L. Maserati, M. Crommie, F. Wang et A. Zettl, «Transfer-free batch fabrication of large-area suspended graphene membranes,» *ACS Nano 4,* p. 4762, 2010.

[109] B. Bharadwaj, R. Pratap et S. Raghavan, «Transfer free suspended graphene devices on silicon using electrodeposited copper,» *Journal of Vacuum Science & Technology B 32,* p. 010603, 2014.

[110] T. Hallam, N. Berner, C. Yim et G. Duesberg, «Strain, bubbles, dirt and folds: A study of graphene polymer-assisted transfer,» *Advanced Materials Interfaces ,* p.

1400115, 2014.

[111] D. Zhan, L. Sun, Z. Ni, L. Liu, X. Fan, Y. Wang, T. Yu, Y. Lam, W. Huang et Z. Shen, «FeCl3-based few-layer graphene intercalation compounds: Single linear dispersion electronic band structure and strong charge transfer doping,» *Advanced Functional Materials 20,* p. 3504, 2010.

[112] A. Pirkle, J. Chan, A. Venugopal, D. Hinojos, C. Magnuson, S. McDonell, L. Colombo, E. Vogel, R. Ruoff et R. Wallace, «The effect of chemical residues on the physical and electrical properties of chemical vapor deposited graphene transferred to SiO2,» *Applied Physics Letters 99,* p. 122108, 2011.

[113] Z. Ni, H. Wang, Z. Luo, Y. Wang, T. Yu, Y. Wu et Z. Shen, «The effect of vacuum annealing on graphene,» *Journal of Raman Spectroscopy 41,* p. 479, 2010.

[114] Z. Cheng, Q. Zhou, C. Wang, Q. Li, C. Wang et Y. Fang, «Toward intrinsic graphene surfaces: A systematic study on thermal annealing and wet-chemical treatment of SiO2-supported graphene devices,» *Nano Letters 11,* p. 767, 2011.

[115] N. Peltekis, S. Kumar, N. McEvoy, K. Lee, A. Weidlich et G. Duesberg, «The effects of downstream plasma treatments on graphene surfaces,» *Carbon 50,* p. 395, 2012.

[116] K. Kumar, Y.-S. Kim et E.-H. Yang, «The influence of thermal annealing to remove polymeric residue on the electronic doping and morphological characteristics of graphene,» *Carbon 65,* p. 35, 2013.

[117] M. Her, R. Beams et L. Novotny, «Graphene transfer with reduced residue,» *Physics Letters A 377,* p. 1455, 2013.

[118] F. Huang, F. Huang, Y. Zhou et L. Du, «Preparation and properties of bismaleimide resins modified with hydrogen silesquioxane and dipropargyl ether and their composites,» *Polymer Journal 42,* p. 261, 2010.

[119] A. Ferrari et D. Basko, «Raman spectroscopy as a versatile tool for studying the properties of graphene,» *Nature Nanotechnology,* p. 235, 2013.

[120] P. Yu et M. Cardona, Fundamentals of Semiconductors, Berlin: Springer, 2005.

[121] R. Martin et L. Falicov, Resonance Raman scattering, In light scattering in solids I, Berlin: Springer, 1983.

[122] D. Basko, S. Piscanec et A. Ferrari, «Electron-electron interactions and doping dependence of the two-phonon Raman intensity in graphene,» *Physics Review B 80,* p. 165413, 2009.

[123] C. Faugeras, «Tuning the electron-phonon coupling in multilayer graphene with magnetic fields,» *Physical Review Letters 81,* p. 155436, 2010.

[124] A. Ferrari et D. Basko, «Raman spectroscopy as a versatile tool for studying the properties of graphene - Supporting Information,» *Nature Nanotechnology,* p. 235, 2013.

[125] D. Yoon, H. Moon, Y.-W. Son, J. Choi, B. Park, Y. Cha, Y. Kim et H. Cheong, «Interference effect on Raman spectrum of graphene in SiO2/Si,» *Physical Review B 80,* p. 125422, 2009.

[126] Y. Wang, Z. Ni, Z. Shen, H. Wang et Y. Wu, «Interference enhancement of Raman signal of graphene,» *Applied Physics Letters 92,* p. 043121, 2008.

[127] N. Ferralis, «Probing mechanical properties of graphene with Raman spectroscopy,» *Journal of Materials Science 45,* p. 5135, 2010.

[128] L. Malard, M. Pimenta, G. Dresselhaus et M. Dresselhaus, «Raman spectroscopy in graphene,» *Physics Reports 473,* p. 51, 2009.

[129] T. Mohuiddin, A. Lombardo, R. Nair, A. Bonetti, G. Savini, R. Jalil, N. Bonini, D. Basko, C. Galiotis, N. Marzari, K. Novoselov, A. Geim and A. Ferrari, "Uniaxial strain in graphene by Raman spectroscopy: G peak splitting, Grüneisen parameters and sample orientation," *Physical Review B 79,* p. 205433, 2009.

[130] J. Yan, Y. Zhang, P. Kim et A. Pinczuk, «Electric Field Effect Tuning of Electron-Phonon Coupling in Graphene,» *Physical Review Letters 98,* p. 166802, 2007.

[131] S. Piscanec, M. Lazzeri, F. Mauri, A. Ferrari et J. Robertson, «Kohn Anomalies and Electron-Phonon Interactions in Graphite,» *Physical Review Letters 93,* p. 185503, 2004.

[132] A. Nazarov, S. Gordienko, P. Lytvyn, V. Strelchuk, A. Nikolenko, A. Vasin, A. Rusavsky, V. Lysenko et V. Popov, «Characterization of graphene layers by Kelvin probe force microscopy and micro-Raman spectroscopy,» *Physica Status Solidi C 10,* p. 1172, 2013.

[133] M. Kalbac, A. Reina-Cecco, H. Farhat, J. Kong, L. Kavan et M. Dresselhaus, «The Influence of Strong Electron and Hole Doping on the Raman Intensity of Chemical Vapor-Deposition Graphene,» *ACS Nano 4,* p. 6055, 2010.

[134] C. Casiraghi, S. Pisana, K. Novoselov, A. Geim et A. Ferrari, «Raman fingerprint of charged impurities in graphene,» *Applied Physics Letters 91,* p. 233108, 2007.

[135] A. Das, S. Pisana, B. Chakraborty, S. Piscanec, S. Saha, U. Waghmare, K. Novoselov, H. Krishnamurthy, A. Geim, A. Ferrari et A. Sood, «Monitoring dopants by Raman scattering in an electrochemically top-gated graphene transistor,» *Nature Nanotechnology 3,* p. 210, 2008.

[136] M. Wall, «The Raman spectroscopy of graphene and the determination of layer thickness,» Thermo Scientific, [En ligne]. Available: www.fisher.be.

[137] O. Frank, M. Mohr, J. Maultzsch, C. Thomsen, I. Riaz, R. Jalil, K. Novoselov, G. Tsoukleri, J. Parthenios, K. Papagelis, L. Kavan et C. Galiotis, «Raman 2D-Band Splitting in Graphene: Theory and Experiment,» *ACS nano 5,* p. 2231, 2011.

[138] Y. Wang, D. Alsmeyer et R. McCreery, «Raman Spectroscopy of Carbon Materials: Structural Basis of Observed Spectra,» *Chemistry of Materials 2,* p. 557, 1990.

[139] S. Pisana, M. Lazzeri, C. Casiraghi, K. Novolesov, A. Geim, A. Ferrari et F. Mauri, «Breakdown of the adiabatic Born–Oppenheimer approximation in graphene,» *Nature Materials 6,* p. 198, 2007.

[140] J. Yan, Y. Zhang, P. Kim et A. Pinczuk, «Electric field effect tuning of electron–phonon coupling in graphene,» *Physical Review Letters 98,* p. 166802, 2007.

[141] S. Berciaud, S. Ryu, L. Brus et T. Heinz, «Probing the Intrinsic Properties of Exfoliated Graphene: Raman Spectroscopy of Free-Standing Monolayers,» *Nano Letters 9,* p. 346, 2009.

[142] A. Das, S. Pisana, B. Chakraborty, S. Piscanec, S. Saha, U. Waghmare, K. Novoselov, H. Krishnamurthy, A. Geim, A. Ferrari et A. Sood, «Monitoring dopants

by Raman scattering in an electrochemically top-gated graphene transistor.,» *Nature Nanotechnology 3,* p. 210, 2008.

[143] C. Huang, B.-J. Lin, H.-Y. Lin, C.-H. Huang, F.-Y. Shih, W.-H. Wang, C.-Y. Liu et H.-C. Chui, «Surface-enhanced Raman scattering of suspended monolayer graphene,» *Nanoscale Research Letters 8,* p. 480, 2013.

[144] C. Huang, B.-J. Lin, H.-Y. Lin, C.-H. Huang, F.-Y. Shih, W.-H. Wang, C.-Y. Liu et H.-C. Chui, «Surface-enhanced Raman scattering of suspended monolayer graphene,» *Nanoscale Research Letters 8,* p. 480, 2013.

[145] Z. Ni, T. Yu, Z. Luo, Y. Wang, L. Liu, C. Wong, J. Miao, W. Huang et Z. Shen, «Probing charged impurities in suspended graphene using Raman spectroscopy,» *ACS Nano 3,* p. 569, 2009.

[146] A. Das, B. Chakraborty et A. Sood, «Raman spectroscopy of graphene on different substrates and influence defects,» *Bulletin of Materials Science 31,* p. 579, 2008.

[147] Y. Shi, X. Dong, J. Wang et L.-J. Li, «Effective doping of single-layer graphene from underlying SiO2 substrates,» *Physical Review B 79,* p. 115402, 2009.

[148] S. Ryu, L. Liu, S. Berciaud, Y.-J. Yu, H. Liu et P. Kim, «Atmospheric Oxygen Binding and Hole Doping in Deformed Graphene on a SiO2 Substrate,» *Nano Letters 10,* p. 4944, 2010.

[149] M. Lafkioti, B. Krauss, T. Lohmann, U. Zschieschang, H. Klauk, K. von Klitzing et J. Smet, «Graphene on a hydrophobic substrate: doping reduction and hysteresis suppression under ambient conditions,» *Nano Letters 10,* p. 1149, 2010.

[150] N. Peres, F. Guinea et A. Castro Neto, «Electronic properties of disordered two-dimensional carbon,» *Physical Review B 73,* p. 125411, 2006.

[151] A. Castro Neto et F. Guinea, «Electron-phonon coupling and Raman spectroscopy in graphene,» *Physical Review B 75,* p. 045404, 2007.

[152] G. Tsoukleri, J. Parthenios, K. Papagelis, R. Jalil, A. Ferrari, A. Geim, K. Novoselov et C. Galiotis, «Subjecting a Graphene Monolayer to Tension and Compression,» *Small 5,* p. 2397, 2009.

[153] O. Frank, G. Tsoukleri, J. Parthenios, K. Papagelis, I. Riaz, R. Jalil, K. Novoselov et C. Galiotis, «Compression behavior of single-layer graphenes,» *ACS Nano 4,* p. 3131, 2010.

[154] M. Huang, H. Yan, T. Heinz et J. Hone, «Probing Strain-Induced Electronic Structure Change in Graphene by Raman Spectroscopy,» *Nano Letters 10,* p. 4074, 2010.

[155] C. Chen, W. Bao, J. Theiss, C. Dames, C. Lau et S. Cronin, «Raman spectroscopy of ripple formation in suspended graphene,» *Nano Letters 9,* p. 4172, 2009.

[156] I. Calizo, A. Balandin, W. Bao, F. Miao et C. Lau, «Temperature dependence of the Raman spectra of graphene and graphene multilayers,» *Nano Letters 7,* p. 2645, 2007.

[157] D. Abdula, T. Ozel, K. Kang, D. Cahill et M. Shim, «Environment-induced effects on the temperature dependence of Raman spectra of single-layer graphene,» *Physical Chemistry Letters C 112,* p. 20131, 2008.

[158] I. Calizo, S. Ghosh, D. Teweldebrhan, W. Bao, F. Miao, C. Lau et A. Balandin,

«Raman nanometrology of graphene on arbitrary substrates and at variable temperature,» *Proc. SPIE 7037, Carbon nanotubes and associated devices, 70371B,* 2008.

[159] S. Pisana, M. Lazzeri, C. Casiraghi, K. Novoselov, A. Geim, A. Ferrari et F. Mauri, «Breakdown of the adiabatic Born–Oppenheimer approximation in graphene,» *Nature Materials 6,* p. 198, 2007.

[160] A. Ferrari, «Raman spectroscopy of graphene and graphite: Disorder, electron–phonon coupling, doping and nonadiabatic effects,» *Solid State Communications 143,* p. 47, 2007.

[161] A. Das, S. Pisana, B. Chakraborty, S. Piscanec, S. Saha, U. Waghmare, K. Novoselov, H. Krishnamurthy, A. Geim, A. Ferrari et A. Sood, «Monitoring dopants by Raman scattering in an electrochemically top-gated graphene transistor,» *Nature Nanotechnology 3,* p. 210, 2008.

[162] Y. Kwon, S. Berber et D. Tomanek, «Thermal expansion of carbon structures,» *Physical Review B 68,* p. 035425, 2003.

[163] D. Yoon, Y.-W. Son et H. Cheong, «Negative thermal expansion coefficient of graphene measured by Raman spectroscopy,» *Nano Letters 11,* p. 3227, 2011.

[164] S. Chen, Q. Li, Q. Zhang, Y. Qu, H. Ji., R. Ruoff et W. Cai, «Thermal conductivity measurements of suspended graphene with and without wrinkles by micro-Raman mapping,» *Nanotechnology 23,* p. 365701, 2012.

[165] C.-C. Chen, W. Bao, C.-C. Chang, Z. Zhao, C. Lau et S. Cronin, «Raman spectroscopy of substrate-induced compression and substrate doping in thermally cycled graphene,» *Physical Review B 85,* p. 035431, 2012.

[166] K. Nguyen, D. Abdula, C.-L. Tsai et M. Shim, «Temperature and gate voltage dependent Raman spectra of single-layer graphene,» *ACS Nano 5,* p. 5273, 2011.

[167] Y. Xu, D. Zhan, L. Liu, H. Suo, Z. Ni, T. Nguyen, C. Zhao et Z. Shen, «Thermal dynamics of graphene edges investigated by polarized Raman spectroscopy,» *ACS Nano 5,* p. 147, 2011.

[168] G. Troppenz, M. Gluba, M. Kraft, J. Rappich et N. Nickel, «Strain relaxation in graphene grown by chemical vapor deposition,» *Journal of Applied Physics 114,* p. 214312, 2013.

[169] H. Nan, Z. Ni, J. Wang, Z. Zafar, Z. Shi et Y. Wang, «The thermal stability of graphene in air investigated by Raman spectroscopy,» *Journal of Raman Spectroscopy 44,* p. 1018, 2013.

[170] N. Bonini, M. Lazzeri, N. Marzari et F. Mauri, «Raman anharmonicities in graphite and graphene,» *Physical Review Letters 99,* p. 176802, 2007.

[171] F. Xia, D. Farmer, Y.-M. Lin et P. Avouris, «Graphene field-effect transistors with high on/off current ratio and large transport band gap at room temperature,» *Nano Letters 9,* p. 1039, 2009.

[172] E. Lee, K. Balasubramanian, R. Weitz, M. Burghard et K. Kern, «Contact and edge effects in graphene devices,» *Nature Nanotechnology 3,* p. 486, 2008.

[173] F. Xia, T. Mueller, R. Golizadeh-Mojarad, M. Freitag, Y.-M. Lin, J. Tsang, V. Perebeinos et P. Avouris, «Photocurrent imaging and efficient photon detection in a

graphene transistor,» *Nano Letters 9,* p. 1039, 2009.

[174] K. Nagashio et A. Toriumi, «Density-of-states limited contact resistance in graphene field-effect transistors,» *Japanese Journal of Applied Physics 50,* p. 070108, 2011.

[175] C. Gong, S. McDonnell, X. Qin, A. Azcatl, H. Dong, Y. Chabal, K. Cho et R. Wallace, «Realistic metal-graphene contact structures,» *ACS Nano 8,* p. 642, 2014.

[176] S. Russo, M. Craciun, M. Yamamoto, A. Morpurgo et S. Tarucha, «Contact resistance in graphene-based devices,» *Physica E 42,* p. 677, 2010.

[177] A. Venugopal, L. Colombo et E. Vogel, «Contact resistance in few and multilayer graphene devices,» *Applied Physics Letters 96,* p. 013512, 2010.

[178] F. Xia, V. Perebeinos, Y.-M. Lin, Y. Wu et P. Avouris, «The origins and limits of metal-graphene junction resistance,» *Nature Nanotechnology 6,* p. 179, 2011.

[179] B.-C. Huang, M. Zhang, Y. Wang et J. Woo, «Contact resistance in top-gated graphene field-effect transistors,» *Applied Physics Letters 99,* p. 032107, 2011.

[180] K. Nagashio, T. Nishimura, K. Kita et A. Toriumi, «Systematic investigation of the intrinsic channel properties and contact resistance of monolayer and multilayer graphene field-effect transistor,» *Japanese Journal of Applied Physics 49,* p. 051304, 2010.

[181] E. Watanabe, A. Conwill, D. Tsuya et Y. Koide, «Low contact resistance metals for graphene based devices,» *Diamond & Related Materials 24,* p. 171, 2012.

[182] A. Hsu, H. Wang, K. Kim, J. Kong et T. Palacios, «Impact of graphene interface quality on contact resistance and RF device performance,» *IEEE Electron Device Letters 32,* p. 1008, 2011.

[183] H. Wang, Y. Wu, C. Cong, J. Shang et T. Yu, «Hysteresis of electronic transport in graphene transistors,» *ACS Nano 4,* p. 7221, 2010.

[184] Y. Lee, C. Kang, U. Jung, J. Kim, H. Hwang, H.-J. Chung, S. Seo, R. Choi et B. Lee, «Fast transient charging at the graphene/SiO2 interface causing hysteretic device characteristics,» *Applied Physics Letters 98,* p. 183508, 2011.

[185] A. Veligura, P. Zomer, I. Vera-Marun, C. Jozsa, P. Gordiichuk et B. van Wees, «Relating hysteresis and electrochemistry in graphene field effect transistors,» *Journal of Applied Physics 110,* p. 113708, 2011.

[186] H. Xu, Y. Chen, J. Zhang et H. Zhang, «Investigating the Mechanism of Hysteresis Effect in Graphene Electrical Field Device Fabricated on SiO2 Substrates using Raman Spectroscopy,» *Small 8,* p. 2833, 2012.

[187] W. de Heer, C. Berger, X. Wu, P. First, E. Conrad, X. Li, T. Li, M. Sprinkle, J. Hass, M. Sadowski, M. Potenski et G. Martinez, «Epitaxial graphene,» *Solid State Communications 143,* p. 92, 2007.

[188] H. Song, S. Li, H. Miyazaki, S. Sato, K. Hayashi, A. Yamada, N. Yokoyama et K. Tsukagoshi, «Origin of the relatively low transport mobility of graphene grown through chemical vapor deposition,» *Scientific Reports 2,* p. 337, 2012.

[189] H. Cao, Q. Yu, L. Jauregui, J. Tian, W. Wu, Z. Liu, R. Jalilian, D. Benjamin, Z. Jiang, J. Bao, S. Pei et Y. Chen, «Electronic transport in chemical vapor deposited graphene synthesized on Cu: Quantum Hall effect and weak localization,» *Applied Physics Letters 96,* p. 122106, 2010.

136

[190] J. Suk, A. Kitt, C. Magnuson, Y. Hao, S. Ahmed, J. An, A. Swan, B. Goldberg et R. Ruoff, «Transfer of CVD-Grown Monolayer Graphene onto Arbitrary Substrates,» *ACS Nano 5,* p. 6916, 2011.

[191] D. Wei, Y. Liu, Y. Wang, H. Zhang, L. Huang et G. Yu, «Synthesis of N-doped graphene by chemical vapor deposition and its electrical properties,» *Nano Letters 9,* p. 1752, 2009.

[192] N. Petrone, C. Dean, I. Meric, A. van der Zande, P. Huang, L. Wang, D. Muller, K. Shepard et J. Hone, «Chemical vapor deposition-derived graphene with electrical performance of exfoliated graphene,» *Nano Letters 12,* p. 2751, 2012.

[193] L. Tapaszto, P. Nemes-Incze, G. Dobrik, K. Yoo, C. Hwang et L. Biro, «Mapping the electronic properties of individual graphene grain boundaries,» *Applied Physics Letters 100,* p. 053114, 2012.

[194] Y. Ogawa, K. Komatsu, K. Kawahara, M. Tsuji, K. Tsukagoshi et H. Ago, «Structure and transport properties of the interface between CVD-grown graphene domains,» *Nanoscale 6,* p. 7288, 2014.

[195] X. Li, C. Magnuson, A. Venugopal, J. An, J. Suk, B. Han, M. Borysiak, W. Cai, A. Velamakanni, Y. Zhu, L. Fu, E. Vogel, E. Voekl, L. Colombo et R. Ruoff, «Graphene films with large domain size by a two-step chemical vapor deposition process,» *Nano Letters 10,* p. 4328, 2010.

[196] M. Ishigami, J. Chen, W. Cullen, M. Fuhrer et E. Williams, «Atomic structure of graphene on SiO2,» *Nano Letters 7,* p. 1643, 2007.

[197] A. Pirkle, J. Chan, A. Venugopal, D. Hinojos, C. Magnuson, S. McDonnell, L. Colombo, E. Vogel, R. Ruoff et R. Wallace, «The effect of chemical residues on the physical and electrical properties of chemical vapor deposited graphene transferred to SiO2,» *Applied Physics Letters 99,* p. 112108, 2011.

[198] J. Moser, A. Barreiro et A. Bachtold, «Current-induced cleaning of graphene,» *Applied Physics Letters 91,* p. 163513, 2007.

[199] «Wikipedia,» [En ligne]. Available: http://en.wikipedia.org/wiki/Electron_mobility. [Accès le 10 August 2014].

[200] P. Levesque, S. Sabri, C. Aguirre, J. Guillemette, M. Siaj, P. Desjardins, T. Szkopek et R. Martel, «Probing charge transfer at surfaces using graphene transistors,» *Nano Letters 11,* p. 132, 2011.

[201] G. Giovanetti, P. Khomyakov, G. Brocks, V. Karpan, J. van den Brink et P. Kelly, «Doping Graphene with Metal Contacts,» *Physical Review Letters 101,* p. 026803, 2008.

[202] S. Morozov, K. Novoselov, M. Katsnelson, F. Schedin, L. Ponomarenko, D. Jiang et A. Geim, «Strong suppression of weak localization in graphene,» *Physical Review Letters 97,* p. 016801, 2006.

[203] F. Tikhonenko, D. Horsell, R. Gorbachev et A. Savchenko, «Weak localization in graphene flakes,» *Physical Review Letters 100,* p. 056802, 2008.

[204] A. Morpurgo et F. Guinea, «Intervalley scattering, long-range disorder, and effective time-reversal symmetry breaking in graphene,» *Physical Review Letters 97,* p. 196804, 2006.

[205] X. Miao, S. Tongay et A. Hebard, «Strain-induced suppression of weak localization in CVD-grown graphene,» *Journal of Physics: Condensed Matter 24,* p. 475304, 2012.

[206] A. Baker, J. Alexander-Webber, T. Altebaeumer, T. Janssen, A. Tzalenchuk, S. Lara-Avila, S. Kubatkin, R. Yakimova, C.-T. Lin, L.-J. Li et R. Nicholas, «Weak localization scattering lengths in epitaxial, and CVD graphene,» *Physical Review B 86,* p. 235441, 2012.

[207] E. McCann, K. Kechedzhi, V. Fal'ko, H. Suzuura, T. Ando et B. Altshuler, «Weak localization magnetoresistance and valley symmetry in graphene,» *Physical Review Letters 97,* p. 146805, 2006.

[208] D. Horsell, F. Tikhonenko, R. Gorbachev et A. Savchenko, «Weak localization in monolayer and bilayer graphene,» *Philosophical Transactions of the Royal Society A 366,* p. 245, 2008.

[209] K. Novoselov, Z. Jiang, Y. Zhang, S. Morozov, H. Stormer, U. Zeitler, J. Maan, G. Boebinger, P. Kim et A. Geim, «Room-temperature quantum Hall effect in graphene,» *Science 9,* p. 1379, 2007.

[210] D. Cooper, B. D'Anjou, N. Ghattamaneni, B. Harack, M. Hilke, A. Horth, N. Majlis, M. Massicotte, L. Vandsburger, E. Whiteway et V. Yu, «Experimental review of graphene,» *ISRN Condensed Matter Physics 2012,* p. 501686, 2012.

[211] D. Abergel, V. Apalkov, J. Berashevich, K. Ziegler et T. Chakraborty, «Properties of graphene: A theoretical perspective,» *Advances in Physics 59,* p. 261, 2010.

[212] A. Cresti, G. Grosso et G. Parravicini, «Electronic states and magnetotransport in unipolar and bipolar graphene,» *Physical Review B 77,* p. 115408, 2008.

[213] J.-H. Chen, C. Jang, S. Xiao, M. Ishigami et M. Fuhrer, «Intrinsic and extrinsic performance limits of graphene and devices on SiO2,» *Nature Nanotechnology 3,* p. 206, 2008.

[214] J. Heo, H. Chung, S.-H. Lee, H. Yang, D. Seo, J. Shin, U.-I. Chung, S. Seo, E. Hwang et S. Das Sarma, «Nonmonotonic temperature dependent transport in graphene grown by chemical vapor deposition,» *Physical Review B 84,* p. 035421, 2011.

[215] A. Kumari, N. Prasad, P. Bhatnagar, P. Mathur, A. Yadav, C. Tomy et C. Bhatia, «Eletrical transport properties of polycrystalline CVD graphene on SiO2/Si substrate,» *Diamond & Related Materials 45,* p. 28, 2014.

[216] T. Minari, T. Nemoto et S. Isoda, «Temperature and electric-field dependence of the mobility of a single-grain pentacene field-effect,» *Journal of Applied Physics 99,* p. 034506, 2006.